

RUHR  
UNIVERSITÄT  
BOCHUM

**RUB**



**Fakultät Maschinenbau**

*fortschritt studieren*

# **Atomic-scale characterisation of grain boundary structure and segregation in bcc-iron**

Dissertation

zur

Erlangung des Grades

PhD

der Fakultät für Maschinenbau

der Ruhr-Universität Bochum

von

**Ali Ahmadian**

aus Herat, Afghanistan

Bochum 2022

Dissertation eingereicht am:	20.08.2022
Tag der mündlichen prüfung:	17.10.2022
Vorsitz:	Univ.-Prof. Dr.-Ing. Detlef Gerhard
Erstgutachter:	Prof. Dr. Gerhard Dehm
Zweitgutachter:	Prof. Dr. Christian Kübel

I, Ali Ahmadian, declare that this thesis titled, “Atomic-scale characterisation of grain boundary structure and segregation in bcc-iron” and the work presented in it are my own. I confirm that:

- This work was done wholly while in candidature for a research degree at this University.
- Where I have consulted the published work of others, this is always clearly attributed.
- Where I have quoted from the work of others, the source is always given. With the exception of such quotations, this thesis is entirely my own work.
- I have acknowledged all main sources of help.
- Where the thesis is based on work done by myself jointly with others, I have made clear exactly what was done by others and what I have contributed myself.

Signed:

---

Date:

---



*“Knowledge is better than wealth, because knowledge protects you while you have to protect wealth, and wealth decreases by (its) spending, while knowledge increases when you spend it.”*

*“Be like the flower, who even gives its fragrance to the hand that crushes it.”*

– Imam Ali ibn Abi Talib (a.s.)

## Abstract

Body-centered cubic (bcc) Fe is the basis for all ferritic steels used in the automotive and construction sectors. These metals have a polycrystalline nature, i.e. they contain grain boundaries (GBs). The structure and composition of the boundaries determines their cohesive strength, which in turn regulates the macroscopic deformation behavior of the material under load. The cohesion strength of the GB can be changed by segregation of impurities or solutes. Depending on how strong the bonds of the atoms at the GB are, the material can either become brittle or ductile along the GB. Technologically relevant is to prevent the segregation of those elements, which would reduce the cohesion strength and lead to intergranular fracture. This can be achieved using cohesion enhancing elements, which can have a strong impact on the segregation behavior of detrimental solutes.

In this work, I have explored the segregation behavior of the detrimental elements Al, Zn and Mn in bcc-Fe in the presence of B and C. The latter ones are known to strengthen the grain boundary. All investigation were done on a Fe-4 *at.*%Al bicrystal with a  $\Sigma 5[001](310)$  tilt GB. The bicrystal was grown in house by the Bridgman method and it contained 4 *at.*% Al to stabilize the bcc phase. The structure and chemical composition of the GB was analyzed by using scanning transmission electron microscopy (STEM) and its various analytical techniques including energy dispersive spectroscopy (EDS) and electron energy loss spectroscopy EELS). Atom probe tomography (APT) measurements were applied to give insights into the 3D-distribution of the enriched solutes and impurities. My experimental observations were complemented by first-principles based density functional theory (DFT) calculations, which shed light onto the segregation mechanism and the properties of the grain boundary before and after segregation.

First, I studied the structure and composition of the initial bicrystal, i.e. without Zn or Mn. With high-resolution STEM imaging I was able to reveal the arrangement of the atoms at the boundary to be kite-type. However, the structure of the GB showed local distortions, whose origin could be GB dislocations. From compositional studies it was found that Al is depleted by  $\approx 2$  *at.*% at the GB. This Al depletion was due to the strong repulsive interaction with B and C, which enriched the boundary first. Further, B and C showed a different segregation pattern. While B uniformly enriched the boundary reaching a peak of 1.8 *at.*%, the segregation of C showed a complex non-uniform pattern with local concentration variations between 1.5 *at.*% and 2.3 *at.*%. This variation in C can be attributed to local GB defects, which act as sinks for C atoms. My experimental studies were confirmed by the DFT calculations of cooperation partners. The DFT simulations also showed that substitutional segregation of B could distort locally the GB structure, which resembled the distorted kites I observed.

In a second step I studied the segregation behavior of Zn, which is typically used as a coating layer on steel to avoid the corrosion of the material. However, Zn has a strong embrittling effect on Fe GBs when it liquefies e.g. during welding processes. This phenomenon is known as liquid metal embrittlement (LME). In this complex

process the liquid Zn preferentially diffuses and segregates to the GB promoting a weakening of the atomic bonds. In order to understand the segregation behavior of Zn in the presence of the cohesion enhancing elements B and C, comparative studies of a Zn-rich and a Zn-poor region were carried out. The Zn-rich region with a bulk concentration of  $\approx 5.5 \text{ at.}\%$  for Zn showed nanometer size spaced clustering of Zn at the GB. The concentration of this clusters were  $\geq 20 \text{ at.}\%$  inducing complex structural modifications. The B and C did not correlate with this clusters but their concentration reduced to  $\leq 0.5 \text{ at.}\%$ . This low concentration is attributed to a broadening of the concentration profiles due to a possible migration of the GB after Zn segregation. The Zn-poor region with a bulk concentration of  $\approx 0.5 \text{ at.}\%$  for Zn showed no clear Zn segregation. On the other hand, the GB concentrations of B and C were symmetric and narrow reaching peak values of  $1.8 \text{ at.}\%$  and  $1 \text{ at.}\%$ , respectively. From the atomistic simulations, we found out that the presence of B and C reduces the segregation tendency of Zn and therefore its detrimental effect on GB cohesion strength. The nonuniform segregation of Zn clusters suggests a local, periodic weakening along the GB.

In the last step, I studied the segregation behavior of Mn. Our goal was to observe a phase transformation of the GB, since Mn is a typical austenite stabilizer, i.e. it transforms bcc-Fe into a face-centered cubic (fcc) Fe. However, the electron beam deposited Mn film onto the bicrystal promoted the formation of internal nanoscale oxides in the bulk as well as at the GB after annealing in a high-vacuum furnace at  $700^\circ\text{C}$ . Compositional studies of the GB oxides showed a core-shell structure. The core consist of  $\text{Al}_2\text{O}_3$ , while the shell is Mn-rich indicating the formation of  $\text{FeMnO}$ . The phase of the  $\text{Al}_2\text{O}_3$  core was analysed by ELNES showing similarities of  $\delta\text{-Al}_2\text{O}_3$ . Investigation of the structure of the GB oxide core revealed a nanocrystalline structure with preferential orientation to the bcc-Fe matrix. Outside the precipitates no Al and Mn was found at the GB.

My presented studies highlight the effect of co-segregation and the impact of impurities on the disastrous materials failure due to GB segregation of embrittling solutes. Although my investigations were limited to a single  $\Sigma 5$  tilt GB, the results can be qualitatively transferred to general GBs.

The main results and discussion contained within this thesis are based on the following publications/manuscripts:

### Publication 1

#### **Aluminum depletion induced by co-segregation of carbon and boron in a bcc-iron grain boundary**

A. Ahmadian, D. Scheiber, X. Zhou, B.Gault, L. Romaner, C. H. Liebscher and G. Dehm

*Nature Communications* 12 (2021): 6008

### Publication 2

#### **Impurity segregation outweighs liquid metal embrittlement in iron**

A. Ahmadian, D. Scheiber, X. Zhou, B.Gault, L. Romaner, G. Dehm and C. H. Liebscher

*Unpublished*

### Publication 3

#### **Formation of nanocrystalline grain boundary oxides in a bcc-Fe-4 at.%Al bicrystal promoted by Mn diffusion**

A. Ahmadian, C. H. Liebscher and G. Dehm

*Unpublished*



# Contents

	<b>iii</b>
<b>1 Introduction</b>	<b>3</b>
1.1 Motivation . . . . .	3
1.2 Objectives . . . . .	5
<b>2 Theory</b>	<b>9</b>
2.1 Grain boundaries in metals . . . . .	9
2.1.1 Macroscopic and microscopic degrees of freedom . . . . .	10
2.1.2 Coincidence site lattice . . . . .	11
2.1.3 O-lattice model . . . . .	12
2.1.4 Structural unit model . . . . .	13
2.2 Grain boundary composition . . . . .	15
2.2.1 Equilibrium segregation . . . . .	16
2.2.2 Non-equilibrium segregation . . . . .	25
2.2.3 Diffusion induced grain boundary migration . . . . .	26
2.2.4 Liquid metal embrittlement . . . . .	28
2.2.5 Grain boundary precipitation . . . . .	30
<b>3 Experimental Methods</b>	<b>33</b>
3.1 Fabrication of bicrystals . . . . .	33
3.2 Scanning electron microscopy . . . . .	34
3.2.1 Secondary electrons and their detection . . . . .	36
3.2.2 Energy dispersive X-ray spectroscopy . . . . .	36
3.2.3 Backscattered electrons: Imaging and diffraction . . . . .	40
3.3 Scanning transmission electron microscopy . . . . .	44
3.3.1 General description . . . . .	44
3.3.2 Image formation in TEM . . . . .	45
3.3.3 Image formation in STEM . . . . .	52

3.3.4	Aberration correction . . . . .	56
3.3.5	STEM-EDS vs. SEM-EDS . . . . .	57
3.4	Electron energy loss spectroscopy . . . . .	58
3.5	Atom probe tomography . . . . .	60
<b>4</b>	<b>Experimental details</b>	<b>65</b>
4.1	Bicrystal growth . . . . .	65
4.2	Diffusion couple . . . . .	66
4.3	Sample preparation and characterization in SEM . . . . .	67
4.4	Sample preparation for TEM and APT . . . . .	68
4.5	(S)TEM and APT characterization . . . . .	68
4.6	Atomistic simulations . . . . .	69
<b>5</b>	<b>Results and Discussion</b>	<b>71</b>
5.1	Aluminum depletion induced by co-segregation of carbon and boron in a bcc-iron grain boundary . . . . .	72
5.2	Introduction . . . . .	72
5.3	Results . . . . .	75
5.4	Conclusion . . . . .	95
5.5	Impurity segregation outweighs liquid metal embrittlement in iron . . . . .	96
5.6	Introduction . . . . .	96
5.7	Results . . . . .	98
5.8	Discussion . . . . .	104
5.9	Conclusion . . . . .	105
5.10	Formation of nanocrystalline grain boundary oxides in a bcc-Fe-4 <i>at.</i> %Al bicrystal promoted by Mn diffusion . . . . .	116
5.11	Introduction . . . . .	116
5.12	Results . . . . .	118
5.13	Conclusion . . . . .	124
<b>6</b>	<b>Summary and outlook</b>	<b>127</b>

# List of Figures

1.1	Fe-Al phase diagram . . . . .	6
2.1	Rotation of two crystals . . . . .	10
2.2	Construction of CSL boundary in bcc structure . . . . .	11
2.3	DSC-lattice model . . . . .	13
2.4	Structural Unit model . . . . .	16
2.5	Segregation of tin in ferritic iron . . . . .	19
2.6	The Fowler isotherm . . . . .	21
2.7	GB segregation of foreign elements . . . . .	22
2.8	GB energy vs tilt angle . . . . .	24
2.9	Schematic representation of DIGM in bulk samples . . . . .	27
2.10	GB dislocation climbing . . . . .	29
2.11	GB precipitation and its growth . . . . .	31
3.1	Bicrystal growth in a Bridgman furnace . . . . .	34
3.2	Principle of an scanning electron microscope . . . . .	35
3.3	Energy dispersive X-ray spectrum of Fe . . . . .	38
3.4	Formation of EBSD pattern . . . . .	43
3.5	Ray diagram for a TEM and STEM . . . . .	46
3.6	The effect of the spherical aberration of a real lens . . . . .	49
3.7	PCTF of TEM . . . . .	51
3.8	Schematic representation for STEM imaging . . . . .	54
3.9	Resolution in STEM . . . . .	56
3.10	A typical EEL spectrum . . . . .	59
3.11	Schematic representation of an APT . . . . .	62
4.1	Zn diffusion into the Fe bicrystal . . . . .	67
5.1	Overview images of the GB . . . . .	76
5.2	Global characterization of the GB . . . . .	77

## List of Figures

5.3	Atomic structure of the GB . . . . .	78
5.4	High resolution imaging of distorted GB structure . . . . .	79
5.5	Grain boundary nano-facetting in close vicinity to a GB precipitate . . . . .	80
5.6	Formation of precipitates at the GB . . . . .	81
5.7	Elemental distribution of Al at the GB . . . . .	82
5.8	Correlative STEM-APT study of the GB . . . . .	83
5.9	Distribution of C and B along the GB . . . . .	85
5.10	Solute segregation energies at the GB . . . . .	87
5.11	Disorder at the GB for B at substitutional segregation sites . . . . .	88
5.12	Solute interactions at GB . . . . .	89
5.13	Computed grain boundary segregation kinetics . . . . .	92
5.14	Overview BSE images of the GB . . . . .	100
5.15	Microstructural characterisation . . . . .	107
5.16	High resolution STEM-EDS at different acceleration voltages . . . . .	108
5.17	Segregation of Zn, B, C and depletion of Al at the GB of region 1 . . . . .	109
5.18	Segregation of Zn, B and C at the GB of region 1 . . . . .	110
5.19	Segregation of Zn, B, and C at the GB of region 2 . . . . .	111
5.20	HAADF-STEM of the from region 1 and 2 . . . . .	112
5.21	Atomic structure of the GB . . . . .	113
5.22	Influence of annealing on GB structure . . . . .	114
5.23	Modelling of Zn segregation to GB with and without B . . . . .	115
5.24	SEM-EDS analysis of the GB . . . . .	119
5.25	Overview HAADF-STEM image . . . . .	120
5.26	STEM-EDS analysis of the GB precipitates . . . . .	120
5.27	EELS analysis of GB oxide. . . . .	121
5.28	HRTEM imaging and corresponding FFTs of the GB precipitate core . . . . .	122
5.29	Atomic structure of the GB . . . . .	123

# List of Tables

- 4.1 Wet chemical analysis of the Fe bicrystal showing the bulk concentrations . . . . . 66
- 5.1 Diffusion data employed for the segregation kinetics simulations . . . 91



# List of Abbreviations

<b>ABF</b> .....	<b>A</b> nnular <b>B</b> right <b>F</b> ield
<b>APT</b> .....	<b>A</b> tom <b>P</b> robe <b>T</b> omography
<b>bcc</b> .....	<b>b</b> ody- <b>c</b> entered <b>c</b> ubic
<b>BET</b> .....	<b>B</b> runauer <b>E</b> mmet and <b>T</b> eller
<b>BF</b> .....	<b>B</b> right <b>F</b> ield
<b>BSE</b> .....	<b>B</b> ack- <b>S</b> cattered <b>E</b> lectron
<b>CBED</b> .....	<b>C</b> onvergent <b>B</b> eam <b>E</b> lectron <b>D</b> iffraction
<b>CCD</b> .....	<b>C</b> harge- <b>C</b> oupled <b>D</b> evice
<b>CMOS</b> .....	<b>C</b> omplementary <b>M</b> etal- <b>O</b> xide- <b>S</b> emiconductor
<b>CSL</b> .....	<b>C</b> oincidence <b>S</b> ite <b>L</b> attice
<b>CTEM</b> .....	<b>C</b> onventional <b>T</b> ransmission <b>E</b> lectron <b>M</b> icroscopy
<b>DF</b> .....	<b>D</b> ark <b>F</b> ield
<b>DFT</b> .....	<b>D</b> ensity <b>F</b> unctional <b>T</b> heory
<b>DIGM</b> .....	<b>D</b> iffusion <b>I</b> nduced <b>G</b> rain boundary <b>M</b> igration
<b>DSC</b> .....	<b>D</b> isplacement <b>S</b> hift <b>C</b> omplete
<b>EBSD</b> .....	<b>E</b> lectron <b>B</b> ackscattered <b>E</b> lectron <b>D</b> iffraction
<b>EDS</b> .....	<b>E</b> nergy <b>D</b> ispersive <b>X</b> -ray <b>S</b> pectroscopy
<b>EELS</b> .....	<b>E</b> lectron <b>E</b> nergy <b>L</b> oss <b>S</b> pectroscopy
<b>ELNES</b> .....	<b>E</b> nergy <b>L</b> oss <b>N</b> ear <b>E</b> dge <b>S</b> tructure

*0 List of Abbreviations*

<b>fcc</b> .....	<b>f</b> ace- <b>c</b> entered <b>c</b> ubic
<b>FEG</b> .....	<b>F</b> ield <b>E</b> mission <b>G</b> un
<b>FFT</b> .....	<b>F</b> ast <b>F</b> ourier <b>T</b> ransform
<b>FIB</b> .....	<b>F</b> ocused <b>I</b> on <b>B</b> eam
<b>FWHM</b> .....	<b>F</b> ull <b>W</b> idth of <b>H</b> alf <b>M</b> aximum
<b>GB</b> .....	<b>G</b> rain <b>B</b> oundary
<b>GBD</b> .....	<b>G</b> rain <b>B</b> oundary <b>D</b> islocation
<b>HAADF</b> .....	<b>H</b> igh <b>A</b> ngle <b>A</b> nnular <b>D</b> ark <b>F</b> ield
<b>HR</b> .....	<b>H</b> igh <b>R</b> esolution
<b>IE</b> .....	<b>I</b> nterfacial <b>E</b> xcess
<b>LAADF</b> .....	<b>L</b> ow <b>A</b> ngle <b>A</b> nnular <b>D</b> ark <b>F</b> ield
<b>LME</b> .....	<b>L</b> iquid <b>M</b> etal <b>E</b> mbrittlement
<b>OA</b> .....	<b>O</b> bjective <b>A</b> perture
<b>SAED</b> .....	<b>S</b> electd <b>A</b> rea <b>E</b> lectron <b>D</b> iffraction
<b>SDD</b> .....	<b>S</b> ilicon <b>D</b> rift <b>D</b> etector
<b>SE</b> .....	<b>S</b> econdary <b>E</b> lectron
<b>SEM</b> .....	<b>S</b> canning <b>E</b> lectron <b>M</b> icroscopy
<b>STEM</b> .....	<b>S</b> canning <b>T</b> ransmission <b>E</b> lectron <b>M</b> icroscopy
<b>SU</b> .....	<b>S</b> tructural <b>U</b> nit
<b>TEM</b> .....	<b>T</b> ransmission <b>E</b> lectron <b>M</b> icroscopy
<b>TOF</b> .....	<b>T</b> ime <b>O</b> f <b>F</b> light



# 1 Introduction

## 1.1 Motivation

Most engineering materials have a polycrystalline microstructure, i.e. they consist of many single crystallites or grains with different orientations to each other. The interfaces separating the grains are called **grain boundaries (GBs)**. GBs are planar defects and they play an important role in determining the macroscopic physical and mechanical properties of the polycrystal. A famous example is the strengthening effect of the GBs, where the GB hinders the motion of dislocations. Reducing the grain size or increasing the fraction of GBs leads to an increase of the strength. This is described by the Hall-Petch model [1–3], which relates the dislocation-GB interaction with the resulting yield stress. However, the Hall-Petch model assumes all GBs to be the same. This is not the case, since the interaction between the dislocation and a GB depends on the **GB structure** [4, 5]. As the GB separates the adjoining grains, its structure will be different from the structure of the grains [6]. Especially the GB energy and cohesion strength depend on the underlying structure. Observations on discontinuous changes of the GB structure, its composition and properties at critical values of thermodynamic parameters suggested that GBs behave like two-dimensional phases. [7–9]. Therefore, phase transformations can occur upon accumulation of solutes or impurities in the form of a solid solution. The process of enrichment of foreign elements at GBs is called **GB segregation** [10].

The origin of GB segregation is the reduction of the total energy of the system. GB segregation is known to affect the properties of the GB and thus the overall properties of the material. Even small amount of a certain element can cause the material to become ductile or brittle. It is known that impurities such as phosphorous (P) or sulfur (S) have a detrimental effect on iron (Fe) GBs [11–17], while carbon (C) and boron (B) show a beneficial effect by enhancing the cohesion strength of the GB [17–23]. Therefore theoretical models were developed to understand GB segregation.

## 1 Introduction

The most well-known Langmuir-McLean model was proposed in 1957 [24] to predict the segregation tendency of a solute and estimate GB concentration at a specific bulk concentration.

However, it should be mentioned that the thermodynamic process of GB segregation becomes more complex when two or more solutes/impurities tend to enrich the GB. Site-competition and attractive/repulsive interaction between segregating atoms has to be taken into account. These co-segregation effects can be used to cancel out or prevent the detrimental effect of certain elements [12]. Attractive interaction at the GB would enhance the segregation tendency.

Besides the effect on GB cohesion, GB segregation can also influence the mobility of the GB. This becomes important during unwanted grain coarsening. The solute atoms can retard the mobility of the boundary and the phenomenon is known as *solute drag effect* [25]. It is originally proposed that a migrating GB will interact with segregating solutes, which apply a drag force onto the boundary and retard its velocity. The strength of the drag force depends on the velocity of the GB. Hillert [26] showed that coherency stresses could revert the solute drag force and induce GB migration. The process is termed as *diffusion induced GB migration (DIGM)*.

GB segregation is studied since several decades starting with Auger electron spectroscopy (AES) [27–31]. Nowadays atom probe tomography (APT) is used due to its higher chemical sensitivity [32, 33]. As mentioned before, GB segregation depends on the underlying structure of the GB and its energy. With the development of aberration-corrected scanning transmission electron microscopes (STEM) it is possible to observe the atomic structure of the GB. Additional analytical techniques in STEM such as energy dispersive spectroscopy (EDS) and electron energy loss spectroscopy (EELS) it is also possible to extract compositional information of the GB at the nm-scale. Recently, the structure and composition of several tilt GBs were studied by STEM [34–36]. Once the structure and composition of the GB is identified, theoretical simulations are needed to extract information about the mechanism of (co-) segregation, the cohesion strength and other GB properties. First-principles based density functional theory (DFT) is mostly used to calculate the interaction between the atoms and simulate GB segregation of solutes and impurities [16, 19, 20]. A combination of STEM investigations, APT measurements and DFT calculations would unravel the GB structure and composition upon segregation.

## 1.2 Objectives

The goal of this work is to understand how the GB structure and composition are correlated with the GB energy and cohesion strength. As a host material the body-centered cubic iron (bcc-Fe) was chosen. Fe is the second most common element in the earth crust and Fe-based alloys denoted as steels are the most important metals in human history used in different engineering fields such as the automotive as well as the energy sector. It has been used by humans for thousands of years and has contributed to the development of societies. The industrial revolution would not have been possible without Fe. At room temperature pure bcc-Fe has a lattice parameter of 2.87 Å, a density of 7.87 g/cm<sup>3</sup>, a melting point at 1536°C and it is ferromagnetic up to 768°C [37]. Therefore, bcc-Fe is also known as ferrite or  $\alpha$ -Fe. The bcc-Fe has an allotropic property, i.e. upon annealing to a temperature above 911°C the  $\alpha$ -Fe transforms to  $\gamma$ -Fe, which has a face-centered cubic (fcc) structure and is known as austenite [37]. In order to be able to grow bcc-Fe bicrystal, the  $\gamma$ -phase region has to be avoided during heating or cooling. Al is a good candidate to stabilize the bcc-phase of Fe [38]. Figure 1.1 shows the Fe-Al binary phase diagram in the composition range up to 50 at.% Al. From the phase diagram it becomes clear that Al is a good ferrite stabilizer as it shrinks the  $\gamma$ -phase loop (denoted as A1) [39]. A minimum content of  $\approx 1.95$  at.% Al maintains the disordered bcc-phase [40], denoted as A2, over the whole temperature range. The A2 phase is a solid solution. It should be noted that Al shows a high solubility in  $\alpha$ -Fe up to  $\approx 45$  at.% at 1318°C, but its solubility decreases to  $\approx 12.5$  at.% at 200°C [40]. This is important because GB segregation is always related to the solubility of foreign atoms [41].

Here, we studied a bcc-Fe-4 at.%Al bicrystal, which was grown in-house by the Bridgman method. The bicrystal contained a  $\Sigma 5$  tilt GB. Even so pure Fe and Al were used to grow the bicrystal, impurity elements in the ppm range will always be present. Typical impurities in Fe are manganese (Mn), silicon (Si), S, P, C and B [42]. Additional alloying elements can be introduced through deposition and subsequent annealing. Special focus was on elements, which have a detrimental effect on the GB cohesion and would embrittle the GB. Preventing GB embrittlement with the help of cohesion enhancing impurities would open the path to design new materials. However, the mechanism of GB segregation of two or more elements is still not fully resolved. One reason is the lack of experimental observations on the exact GB structure before and after the segregation process. It is necessary to study

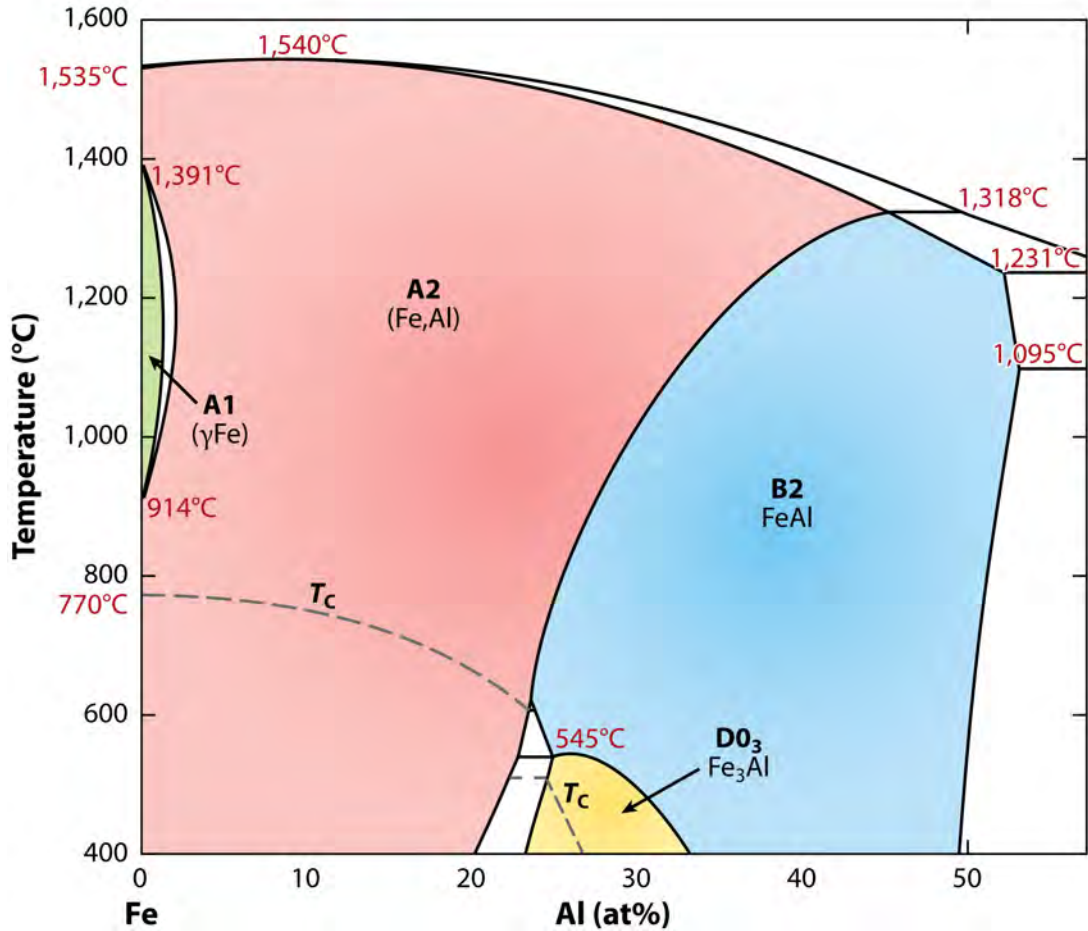


**Figure 1.1: Fe-Al phase diagram** Fe-rich binary Fe-Al phase diagram highlighting the ranges of the disordered bcc solid solution A2 and the ordered bcc intermetallic phases DO<sub>3</sub> and B2. Taken from [38]

systematically the GB structure and composition from the micron scale down to the atomic scale so that GB defects occurring at different length scales will not be overseen.

Correlative microscopy studies combining aberration-corrected STEM and APT were applied on a symmetric  $\Sigma 5$  [001] (310) GB in bcc-Fe-4 at.%Al to extract the atomic structure and composition. The observed information were used as an input for DFT calculations to determine the GB energy and cohesion. After profound studies on the segregation behavior of Al in the presence of B and C, other solutes were introduced into the bicrystal.

The first element of interest was Zn. Zn is often used to protect advanced high strength steels from corrosion. However, Zn has a very low melting point of 419.5°C

[42] and high temperature processes such as resistance spot welding would liquefy the Zn. The liquid Zn will penetrate along the GBs into the steel matrix. Mechanical stress would cause intergranular cracking. This liquid Zn induced GB embrittlement limits the structural application [43, 44]. Since the complex process involves many mechanisms, we limit our studies on the initial stage before cracking occurs. Special focus is the interplay between C, B and Zn.

Finally, the GB segregation of Mn was studied. The motivation for Mn is its character to induce phase transformation of ferrite to austinite Fe. This is the reason why Mn is heavily used in austinite steels. Low concentrations of Mn result in a duplex phase microstructure. However, Mn is alike Zn a GB embrittler and therefore it is of great interest to observe its segregation in correlation with B and C.

In the following, an outline of the work is given: Chapter 2 gives an overview of theoretical models to describe GB structure and segregation. Experimental and theoretical evidence found in the literature are limited only on bcc-Fe. Consequences of GB segregation are discussed in the light of diffusion induced GB migration (DIGM) and GB precipitation. Chapter 3 introduces the different experimental methods, which were used in this thesis. The focus is on STEM, which was the main tool for the investigations. Chapter 5 will show the results obtained on GB segregation of Al, Zn and Mn. The results are based on three publications/manuscripts. Finally, chapter 6 will summarize and give a short outlook.



## 2 Theory

This chapter introduces the theoretical background of grain boundaries (GBs) necessary for understanding the experimental results as well as their discussion. It is divided into two parts. The first part deals with GB structure. In a first step, the crystallographic parameters called *degrees of freedom* (DOF) are introduced to describe the geometry of GBs. Next, different models used to classify GB structures are shown. These models are based on the macroscopic or microscopic parameters. The focus will be placed on high angle GBs and their energy. In the second part the GB composition is described with the main focus on GB segregation. Models are presented to describe the equilibrium and non-equilibrium segregation processes. In the context of co-segregation, the effect of interactive segregation and site-competition is necessary to understand real materials. Finally, some consequences of GB segregation such as diffusion induced GB migration, liquid metal embrittlement and GB precipitation are discussed briefly. Detailed information about the various models can be found in textbooks such as [6, 10, 45].

### 2.1 Grain boundaries in metals

Most engineering metals have a polycrystalline nature, i.e. they consist of many crystallites (grains), which are misoriented with respect to each other. The interface separating two regions of the same crystal structure but with different orientation, is known as a grain boundary (GB). Because GBs are described as 2D structural defects, they are sites with a higher energy compared to the perfect crystals. As such they have a significant amount of influence on the macroscopic material properties such as strength, conductivity or diffusion. This can be explained by the structural differences of the GBs compared to the neighboring grains.

### 2.1.1 Macroscopic and microscopic degrees of freedom

A GB represents the orientation transition from grain A to grain B. It can be described by five macroscopic degrees of freedom (DOFs). Three DOFs describe the relative orientation of the adjoining grains and are determined by the rotation angle  $\theta$  (one DOF) and the rotation axis  $\mathbf{r}$  (two DOFs). The remaining two DOFs describe the orientation of the GB plane through the GB plane normal ( $\mathbf{n}_A$ ,  $\mathbf{n}_B$ ). By using Miller indices for the vectors, each GB can be described as:

$$\Theta^\circ [h_r k_r l_r] (h_A k_A l_A) / (h_B k_B l_B) \quad (2.1)$$

In general the misorientation can be split into a tilt and twist component. Pure tilt and twist rotations are schematically shown in Figure 2.1. For a pure tilt GB (Fig. 2.1 a), the rotation axis  $\mathbf{r}$  is perpendicular to the boundary plane normal  $\mathbf{n}_{A,B}$  and for a pure twist boundary (Fig. 2.1 b) the rotation axis is parallel to the GB plane normal. The number of DOFs can be further reduced by defining special types of GBs. If the miller indices of the GB plane are identical in both grains, i.e.  $\mathbf{n}_A = \mathbf{n}_B$ , the GB is called symmetric.

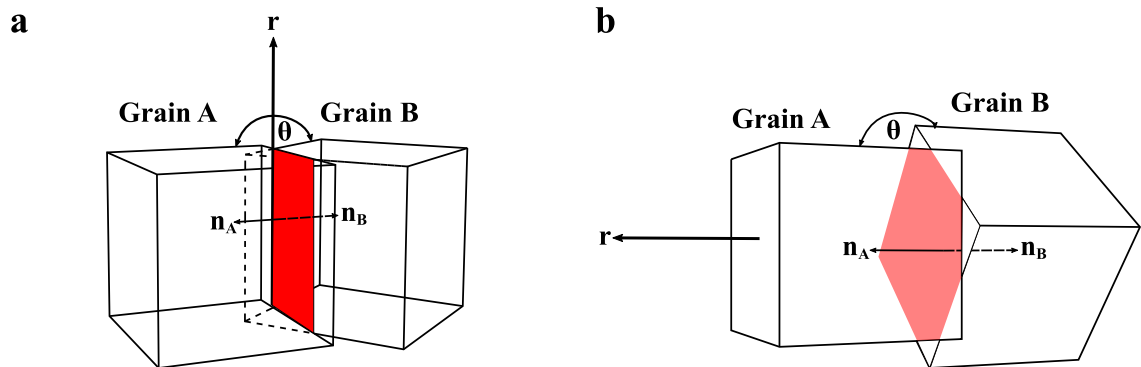


**Figure 2.1: Rotation of two crystals by  $\Theta$ .** **a** For a pure tilt GB, the common rotation axis  $\mathbf{r}$  is perpendicular to the GB plane normal  $\mathbf{n}_A$ ,  $\mathbf{n}_B$ . **b** For a pure twist GB, the rotation axis is parallel to the plane normal.

Besides the five macroscopic DOFs, there are three microscopic DOFs, which are described by the rigid body translation of grain A with respect to grain B. While the macroscopic DOFs depend on the geometric constraints, the microscopic DOFs usually depend on temperature, pressure or chemistry at the GB. Therefore the microscopic DOFs are chosen by nature such that the energy of the GB is minimized.



### 2.1.2 Coincidence site lattice

The most-widely used formalism to describe the structure of high angle GBs ( $\Theta \geq 15^\circ$ ) is the *coincidence site lattice* (CSL) model, developed by Kronberg and Wilson [46]. As shown in Figure 2.2 a, when two interpenetrating cubic lattices (red and blue) are rotated around the same  $[001]$  axis, certain rotation angles can lead to the occurrence of a dichromatic pattern and coincidence points (black points). Due to the periodic arrangement of the adjacent crystals, these coincident points span a superlattice - the CSL. The reciprocal density of coincidence sites is defined by  $\Sigma$ . However, this  $\Sigma$  value does not describe the position of the GB plane. Figure 2.2 b depicts the formation of a  $\Sigma 5$  CSL by rotating two bcc structures  $36.87^\circ$  with respect to each other around the  $[001]$  axis. The lattice parameter of the CSL is  $\sqrt{5}a$  with  $a$  the crystal lattice parameter. A GB can be placed such that it runs through a large number of coincidence sites. This is energetically preferred. The underlying idea is that less number of bonds are broken, if a density of lattice points coincide. Therefore low- $\Sigma$  boundaries are supposed to be special with respect to their properties [47]. Exemplary, the  $\Sigma 5 [001] (310)$  symmetric tilt GB is shown in Fig. 2.2 where  $\mathbf{n}_A = \mathbf{n}_B$ .

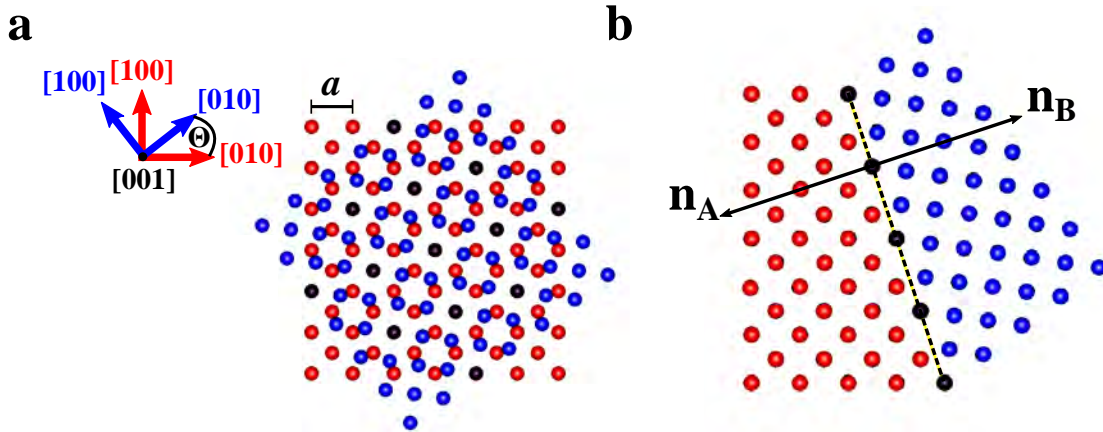


**Figure 2.2: Formation of CSL boundary in bcc crystals.** **a** Rotation of the blue lattice by  $\Theta = 36.87^\circ$  around the  $[001]$  axis with respect to the red lattice. The lattice parameter is  $a$  and the rotation creates a dichromatic/ Moirée pattern. The black points indicate coincident sites, where blue and red lattice points overlap. These points span the CSL with lattice parameter  $\sqrt{5}a$ . The GB passes through the coincident points. **b** Example for a  $\Sigma 5 [001] (310)$  GB (dashed black line). The GB plane normal  $(\mathbf{n}_A, \mathbf{n}_B)$  into the right and left grain are symmetric.

It should be noted that the CSL model is a purely geometrical model. Any slight change of the rotation angle or even an infinitesimal shift of one lattice with respect

to the other would destroy the coincidence principle and therefore the  $\Sigma$  value. Therefore, Bollmann generalized the CSL concept to the O-lattice model [48].

### 2.1.3 O-lattice model

It is known from low-angle GBs ( $\Theta \leq 15^\circ$ ), that small differences in orientation between perfect crystals is accommodated by an array of dislocations [49]. This concept can be applied to high angle GBs, too. In order to maintain the CSL, deviations from the ideal coincidence are compensated by dislocations [48]. These dislocations must contain a Burgers vector  $\mathbf{b}$ , which does not destroy the CSL. It is possible that the Burgers vector is a vector of the crystal lattice or even the CSL. However, the elastic energy of dislocations increases quadratically with the Burgers vector length. Small vectors are sufficient to preserve the coincidence. Such dislocations are referred to as *secondary GB dislocations* to distinguish them from the primary lattice dislocations. The set of all translation vectors, which meet these conditions constitute the so-called *displacement shift complete* (DSC) lattice or O-lattice. The density of secondary GB dislocations is related to the deviation angle  $\Delta\Theta$ , which in turn is inversely related to  $\Sigma$  by  $\Delta\Theta = \frac{\Theta_0}{\Sigma}$  with  $\Theta_0 \approx 15^\circ$  (Brandon criterion) [47, 50]. As shown in Figure 2.3, the DSC lattice (green) contains all lattice points in both crystals. A secondary dislocation with a Burgers vector magnitude of  $b_{DSC} = \frac{1}{5}\sqrt{5}a$ , i.e. one-fifth of the CSL length would shift one crystal along the other, but the number of coincidence sites remains constant. Thus, the DSC translation vector preserves the CSL symmetry. Further, introducing a secondary GB dislocation would cause a step in the boundary plane. This principle can be used to explain faceting of the GB through a an array of GB dislocations.

Similar to the CSL model, the O-lattice concept is based on geometric considerations and does not take into account interatomic interactions. This is important when calculating the GB energy to determine the atomic structure of the GB. This can be illustrated when comparing the GB energy of the same  $\Sigma 9$  GB in fcc metals and silicon [45]. In order to get the information about the equilibrium position of the atoms, an atomic relaxation is applied. This relaxation can destroy the coincidence but it retains the periodicity of the CSL. High resolution electron microscopy and computer simulation show that the atoms in the GB arrange in characteristic repeating polyhedra, which are referred as *structural units*.

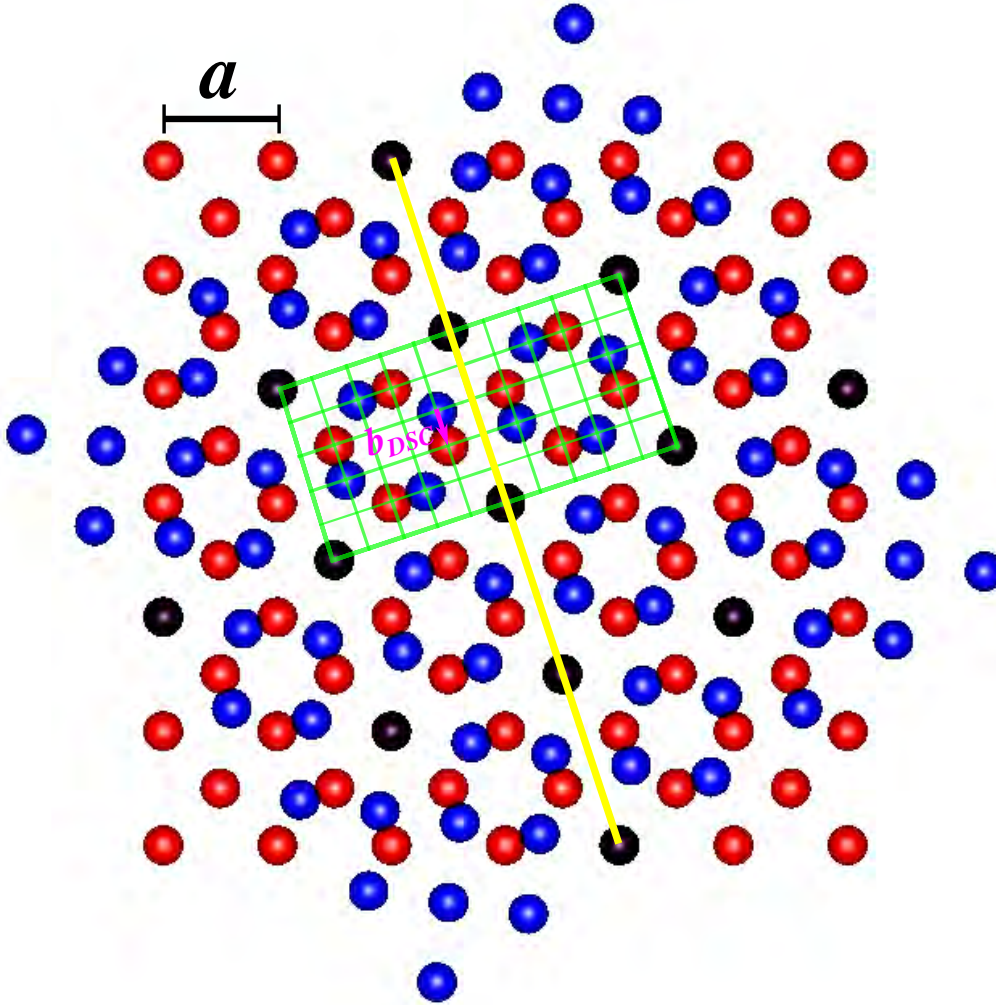


**Figure 2.3: DSC-lattice model.** The DSC lattice (green lines) for a  $\Sigma 5$  configuration with lattice parameter  $b_{DSC} \frac{1}{5} \sqrt{5} a$ . Displacing the blue lattice by the vector  $\mathbf{b}_{DSC}$  shifts the coincident points but preserves their density, i.e. the  $\Sigma$  configuration.

#### 2.1.4 Structural unit model

The *structural unit* (SU) model describes the structure of a GB by a periodic arrangement of the atoms in certain configurations. Sutton and Vitek [51] studied the structure of a series of symmetric tilt GBs in copper and aluminum up to  $\Sigma = 411$  using molecular statics simulations. Their analysis showed that some GBs consist of one type of SU. These boundaries are referred as *delimiting* or *favored* boundaries. All non-favored GBs consist of a mixture of the favored boundaries. This corresponds to the O-lattice model of secondary GB dislocations. The structure of

## 2 Theory

a favored GB is mainly governed by the interaction potential and thermodynamic principle of energy minimization. Figure 2.4 shows the core structure of symmetric tilt GBs viewed along the  $[001]$  tilt axis. The SUs are highlighted in blue. For  $\Sigma = 1$  ( $\Theta_A = 0^\circ$ ), the GB consists of A-units corresponding to squares (Fig. 2.4 a)). The next delimiting boundary is the  $\Sigma = 5$  at a misorientation of  $\Theta_B = 36.87^\circ$  having a triangular or kite-type SU as shown in Fig. 2.4 b). Now, all GBs with  $\Theta_A < \Theta < \Theta_B$  are represented by a combination of A-units and B-units. Exemplary, this is shown for  $\Sigma = 37a$  (Fig.2.4 c)) occurring at a misorientation of  $\Theta = 18.92^\circ$ , respectively. Closer inspection of the  $\Sigma 37a$  reveals that the GB structure contains mainly B-units and a minority of A-units. According to Bishop and Chalmers [52], the SU model and the GB dislocation model [48, 53] are just different ways to describe the same GB structure. Therefore, the minority A-units can be described by an intrinsic secondary dislocation with a Burgers vector  $b_b$  of the DSC-lattice of the B-unit with [45]

$$b_b = \nu_A \sin(\Theta_B - \Theta_A)/2$$

where  $\nu_A$  is the length of the minority A-unit. It should be noted that these dislocations create a strong hydrostatic stress field. Calculation of these stress fields agree with the stress fields associated with a secondary GB dislocation. Thus, they can be used to localize the secondary GB dislocation. [51, 54].

We have seen that the GB structure is related to its energy and the hydrostatic stress field can distort the atomic structure and thus change its energy. Atomic relaxations are necessary to minimize these distortions as well as the energy [45]. Therefore, the SU model was first developed upon atomistic simulations using reliable interatomic potentials through relaxation of the secondary GB dislocations [51].

The GB energy or specific excess free energy  $\gamma$  (energy per unit area) of the GB is defined as the difference in the Gibbs free energy  $G$  of the material with and without the GB divided by the GB area  $A$ :

$$\gamma = \left( \frac{\partial G}{\partial A} \right)_{T,p,N} \quad (2.2)$$

with  $T$  the temperature,  $p$  the pressure and  $N$  the number of atoms. The GB energy depends strongly on the four microscopic DOFs. They have to be optimized through

local relaxation of each atom at the interface to obtain the equilibrium ground state of the GB structure. In this manner, one crystal is allowed to shift (rigid body translation) with respect to the other and the atoms at the interface may occupy positions away from the coincidence sites. The z-component of the translation vector (parallel to the GB plane normal) is very important as it describes the *GB expansion*  $\delta V$ .

One way to compute the GB energy is called  $\gamma$ -surface approach, derived from the principle of stacking fault or  $\gamma$ -surface energy calculation. In the case of a symmetrical CSL GB, where the SUs are periodically repeated, this simplifies the calculation of the GB energy. Once the energy of each individual SU is known, then the energy of all GBs is simply the sum of these groups. According to the SU model, asymmetrical boundaries consist of steps (facets) composed of symmetrical segments. In this model it is considered that some boundaries have a single-type SU (favored GB) and serve as reference for other GBs. Computer simulations have shown that favored GBs have a low energy. Slight changes in the orientation relationship causes the formation of other SUs, which can be regarded as secondary dislocations. Therefore the SU model is a supplement of the O-lattice and CSL model [55, 56].

So far we have only looked at the interface structure in pure (single-element) systems. In reality, however, there may be local variations in GB chemistry. In multi-element systems, segregation effects play a crucial role, especially in the case of diffusion studies. Theoretical models describing GB segregation - starting with a pure binary system and later extended to multi-elements systems are introduced in the following section.

## 2.2 Grain boundary composition

In binary or multicomponent systems segregation of solute or impurity elements can change GB composition. In general, segregation describes the local enrichment of solute atoms or molecules at specific sites such as surfaces, dislocations or GBs. For historical reasons, the term “adsorption” is used for surface segregation. This is the reason why thermodynamic concepts of surface adsorption are used to describe GB segregation. A distinction is also made between equilibrium and non-equilibrium segregation.

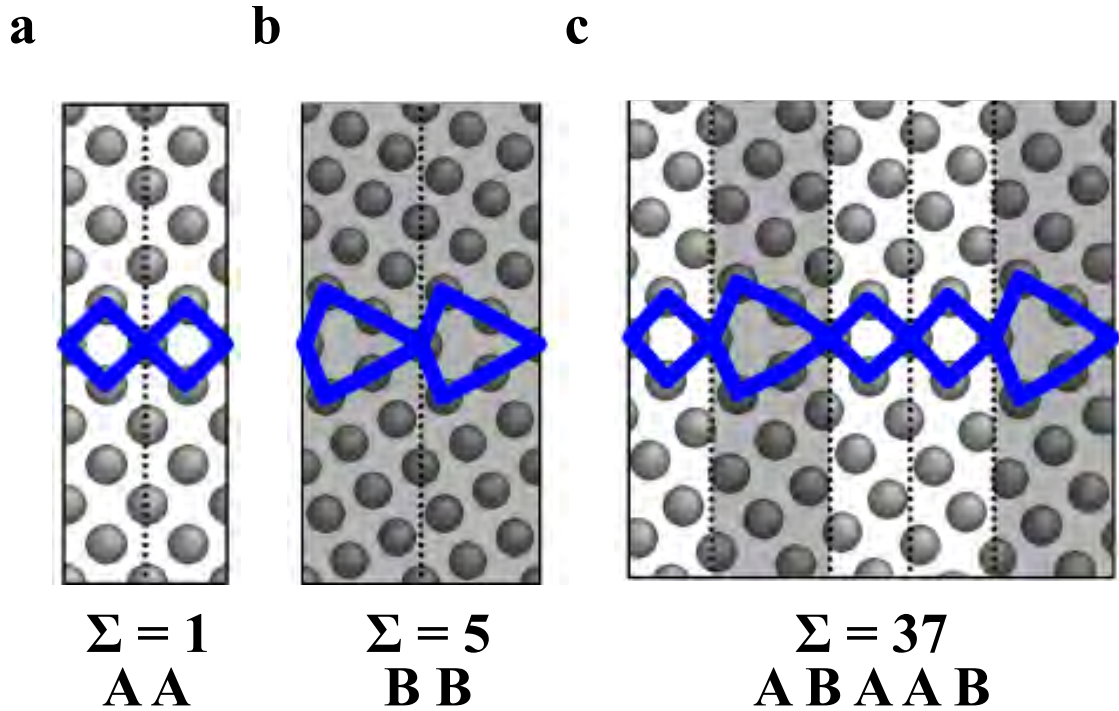


**Figure 2.4:** Structural unit model for different  $\Sigma$ -GBs in bcc-Fe viewed along  $[001]$  tilt axis. **a** The  $\Sigma = 1$  boundary structure (at  $\Theta = 0^\circ$  misorientation) consist of squares rotated by  $45^\circ$ . **b** The  $\Sigma = 5$  at  $\Theta = 36.87^\circ$  consists of triangular or kite-type SU. **c** The SU of the  $\Sigma = 37$  at  $\Theta = 18.92^\circ$  is a combination of the previous SUs. Image was taken from [55].

### 2.2.1 Equilibrium segregation

Equilibrium segregation, which is defined by the fact that the width of the segregation zone depends exclusively on the structural width of the interface. Since this only extends over a few atomic layers, the equilibrium segregation is limited to one or two atomic layers at the interface. It is therefore given quantitatively by the degree of coverage  $X_b$ , the fraction of the coverage of a monolayer. The free energy, which is a measure of the unsaturated atomic bonds of the disordered interface structure, is generally used for the thermodynamic description of interfaces. Minimization of the interfacial Gibbs free energy is the driving force for segregation. McLean was the first to derive the free energy of a system in which dissolved foreign atoms segregate to the GB. His model is based on Gibbs' idea [57] on surface adsorption.

### Langmuir-McLean model

The Gibbs free energy, which depends largely upon the number of unsaturated atomic bonds in the GB structure, is generally used for the thermodynamic description of interfaces. At constant temperature  $T$ , the free energy will be at minimum and is therefore the driving force for equilibrium segregation. The segregated atoms occupy specific positions in order to minimize the atomic binding energies and to lower the free energy of the boundary. McLean [24] was the first to derive an expression for the total free enthalpy of a system in which solute atoms segregate to the GB. For this purpose he proposed a model that differentiates the GB area from the surrounding bulk. Suppose there are  $N$  lattice sites in the bulk occupied by  $P$  solute atoms and  $n$  lattice sites at the GB with  $p$  solute atoms among them, then the total free energy of the system is [58]:

$$G_{tot} = H - TS_{config} \quad (2.3)$$

$$= pe + PE - Tk_B\{\ln(n!N!) - \ln(n-p)!p!(N-P)P!\} \quad (2.4)$$

with  $H$  the enthalpy and  $S_{config}$  the configurational entropy. Further,  $k_B$  is the Boltzmann constant and  $e$  and  $E$  denote the distortion energies of the solute atoms at the GB and the bulk. The minimum of Eq. 2.4 at constant  $T$  and  $p + P$  is obtained by:

$$\left(\frac{\partial G_{tot}}{\partial p}\right) = 0 \quad (2.5)$$

$\Leftrightarrow$

$$\frac{p}{n-p} = \frac{P}{N-P} \exp\left(\frac{E-e}{k_B T}\right) \quad (2.6)$$

With  $X_c = P/N$  the concentration of solute atoms in the bulk,  $X_b = p/n$  the concentration of solute atoms at an interface site Eq. 2.6 becomes

$$\frac{X_b}{X_b^0 - X_b} = \frac{X_c}{1 - X_c} \exp\left(-\frac{\Delta G}{k_B T}\right) \quad (2.7)$$

with  $X_b^0$  the saturation limit of  $X_b$ . This formalism is analogue to the Langmuir adsorption isotherm, which was developed for free surfaces. Therefore Eq. 2.7 is referred as the **Langmuir-McLean equation**. The term  $\Delta G = e - E$  is the free adsorption energy per mole of solute [59]. A negative value means that the atom

has a tendency for segregation. Furthermore, the segregation behavior is stronger with increasing  $X_c$  (bulk solute concentration) and decreasing temperature  $T$ . The GB enrichment ratio is determined by  $\beta = \frac{X_b}{X_b^0}$ .

The problem with the Langmuir-McLean model is its assumption that the probability of occupation is the same for all sites within the interface. Even if all GBs were identical, from the previous section it is known that defects such as GB dislocations may alter the atomic arrangement and could generate new possible positions for the solute elements. This would result in an anisotropic segregation tendency. A further effect on the driving force for segregation is the size difference between solute and solvent atoms. Smaller solute atoms rather match in sites which are already compressed, while larger atoms would occupy lattice sites which are already expanded. The size effect is mainly relevant for *interstitial* segregation. The GB expansion or excess volume  $\delta V$  is an important factor that often predetermines the type and amount of segregation [24].

### Seah-Hondros model

The pioneering work of McLean [24] proposed that segregation of certain solute atoms to the GB would result in intergranular embrittlement of the material. However, the validity of the McLean model is limited to a saturated segregation ( $X_b = 1$  in Eq. 2.7) in the submonolayer regime due to the assumption of a free energy of segregation  $\Delta G$  that is independent of the coverage. Further, the probability of occupation is same for all boundary sites and the interaction between neighboring segregated atoms is neglected in this model.

First of all, there is no physical reason why solute enrichment at the GB should be limited to the saturation coverage. As shown in Figure 2.5 [60], tin segregation to  $\alpha$ -iron GBs can exceed one atomic monolayer depending on the bulk content. This could not be explained by the McLean model. Hondros and Seah [59] used the BET-theory (**B**runauer, **E**mmett and **T**eller)[61], to modify the Langmuir-McLean equation (Eq. 2.7) to

$$\frac{X_b}{X_b^0 - X_b} = \frac{X_c}{X_c^{SS}} \exp\left(-\frac{\Delta G}{k_B T}\right) \quad (2.8)$$

with  $X_c^{SS} = \exp\left(\frac{\Delta G_{sol}}{k_B T}\right)$  the bulk solute concentration at solid solubility, where  $\Delta G_{sol}$  is the free energy of precipitation. The Seah-Hondros model links the GB segregation with solid solubility of alloying elements. Further, it can be used to estimate



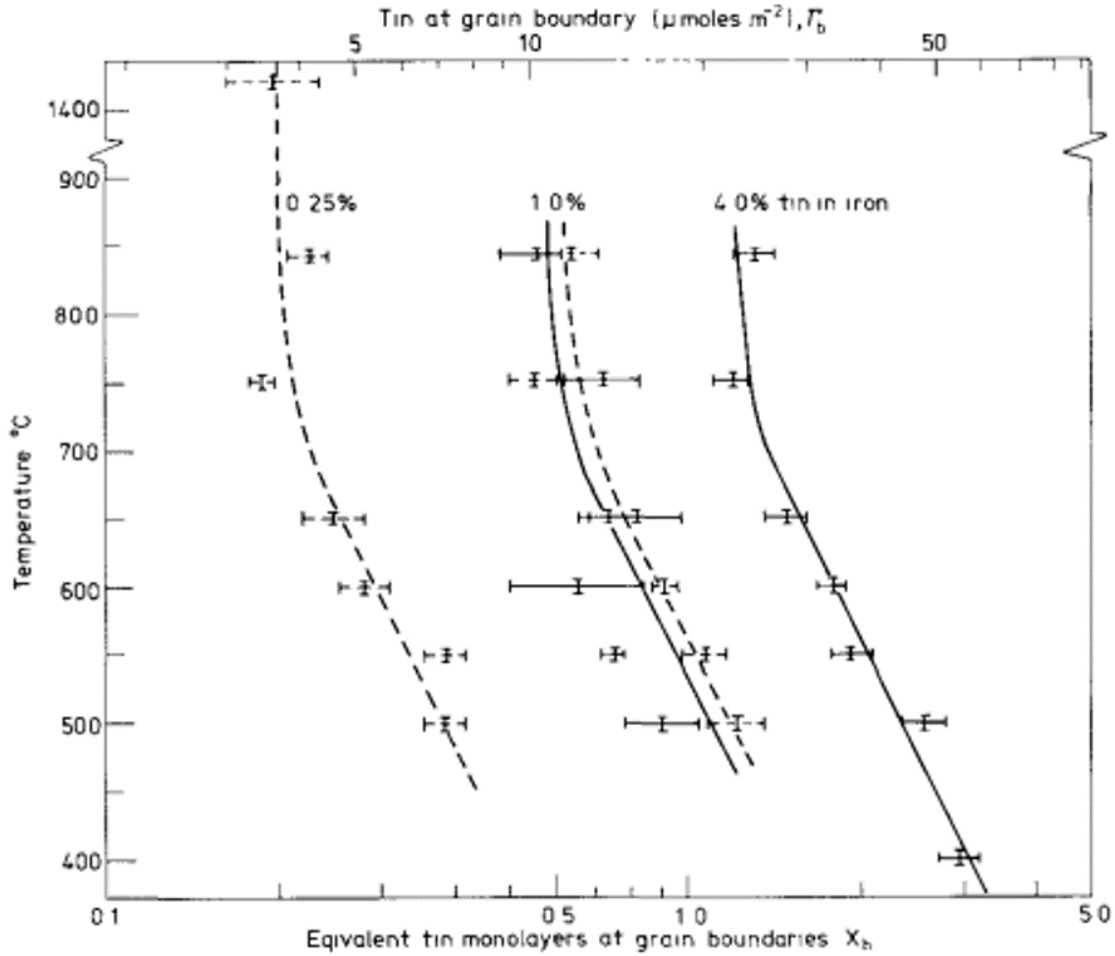


**Figure 2.5: Segregation of tin in ferritic iron** Increasing the bulk tin content from 0.25 *at.*% to 4 *at.*% means that the GB coverage exceeds one monolayer at ambient temperatures. Taken from [60]

precipitation from the bulk solute concentration. This solubility limit can also be changed e.g. through addition of a third element. Although the Seah and Hondros model was successfully applied to segregation of sulfur, tin [60] and carbon [62] in ferritic iron, at high concentration levels, the solute-solute interaction causes deviations from the ideal Seah-Hondros as well as Langmuir-McLean model.

Further, within the Langmuir-McLean as well as Seah-Hondros models interactions between solute atoms at the GB are neglected, whereby  $\Delta G$  becomes constant. Considering a very low concentration of solute atoms (e.g. in a dilute alloy), this assumption is correct. For higher concentration or for multi-element material systems, the Fowler-Guggenheim or Guttman model [63] needs to be used.

### Fowler-Guggenheim model

In a multicomponent system, where two or more elements tend to segregate to the GB, the interaction between them needs to be taken into account. In the **Fowler-Guggenheim** adsorption theory [63] an additional term  $\omega$  is introduced, describing the interaction energy of segregating atoms. Following the McLean model, the total free energy (see Eq- 2.4 of the binary system is then given by

$$G_{tot} = pe + \frac{1}{2}\left(\frac{p^2}{n}\right)Z_1\omega PE + \frac{1}{2}\left(\frac{P^2}{N}\right)Z_1\omega - Tk_B\{\ln(n!N!) - \ln(n-p)!p!(N-P)!P!\} \quad (2.9)$$

with  $Z_1$  the coordination number of solute atoms in the GB and  $\omega$  the interaction energy. Obviously  $\omega$  is related to the fraction of segregated solutes. The differential derivative of  $G$  at constant  $T$  and  $p + P$  gives the GB adsorption isotherm:

$$\frac{X_b}{X_b^0 - X_b} = \frac{X_c}{1 - X_c} \exp\left(-\frac{\Delta G^0 - Z_1\omega(X_b/X_b^0)}{k_B T}\right) \quad (2.10)$$

For  $\omega = 0$  Eq. 2.10 reduces to the Langmuir-McLean model. A similar trend is observed for  $X_b$  close to zero, which corresponds to the early stage of segregation. For  $\omega > 0$ , the interaction is repulsive, while for  $\omega < 0$  it is attractive. The latter case would enhance the total segregation energy. The more  $\omega$  becomes negative, the segregation rises steeper with decreasing temperature. The increase is stronger than in the Langmuir-McLean model until a critical temperature  $T_{crit} = \frac{Z_1\omega}{2k_B}$  is reached, where the segregation curve become discontinuous. Figure 2.6 shows the Fowler adsorption isotherm as a function of  $X_c \exp\left(\frac{\Delta G_{seg}}{k_B T}\right) = X_c K$  for different interaction terms  $Z_1\omega$ . Additionally, experimental results of Pichard et al. [64] on selen (Se) and tellurium (Te) segregation in Fe at 800° were included for  $\frac{Z_1\omega}{k_B T} = 2.5$  and 4. The Fowler-Guggenheim model correlates well with the experimental data. For a large interaction term  $\frac{-Z_1\omega}{k_B T} \leq 4$  the GB concentration  $X_b$  jumps from low to high coverage level. This is shown by the dotted curve in Fig. 2.6 for  $Z_1\omega = -6k_B T$ . In this case the segregation level changes discontinuously from A to B.

### Guttman model

For ternary and higher order systems, Guttman advanced the Fowler-Guggenheim model, allowing interactions between co-segregating elements [66]. This is very important especially for the engineering materials such as Fe, which is often alloyed

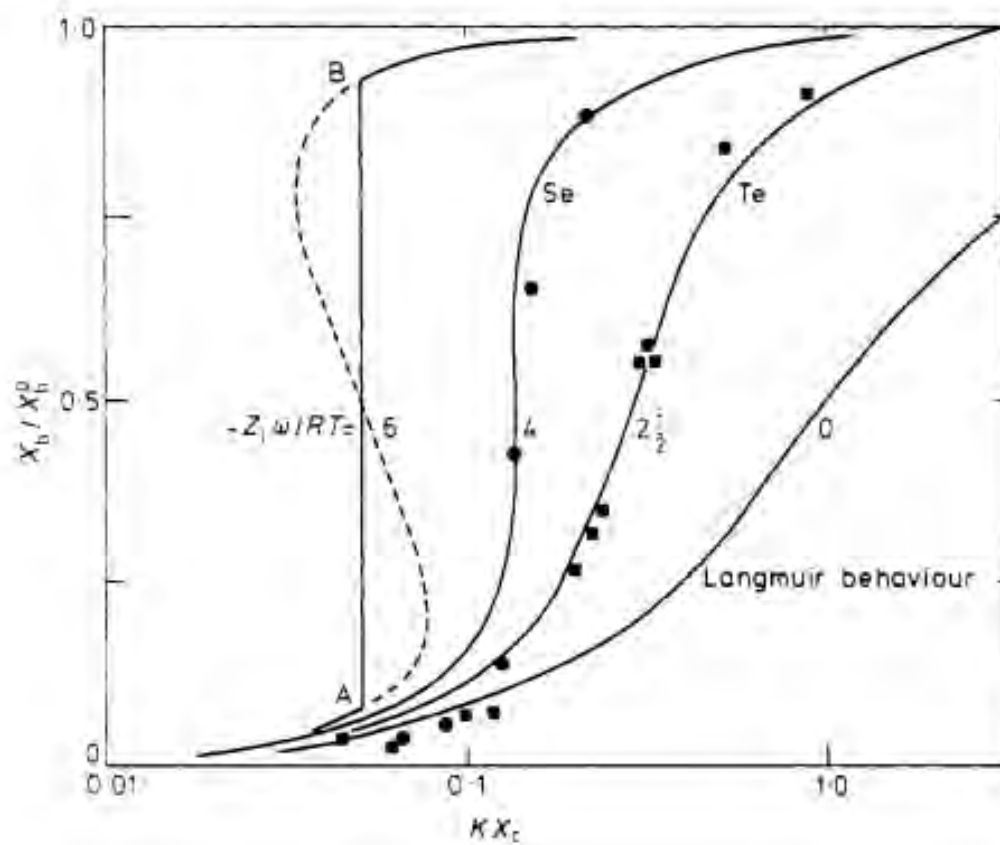


**Figure 2.6: Fowler isotherm** The calculated Fowler adsorption isotherm for Se and Te in iron at different values of the interaction term  $-Z_1\omega/k_B T$ . The experimental data for Te (■) and Se (●) from [64] are plotted too. The Langmuir isotherm could not predict the experimental observations. Taken from [65].

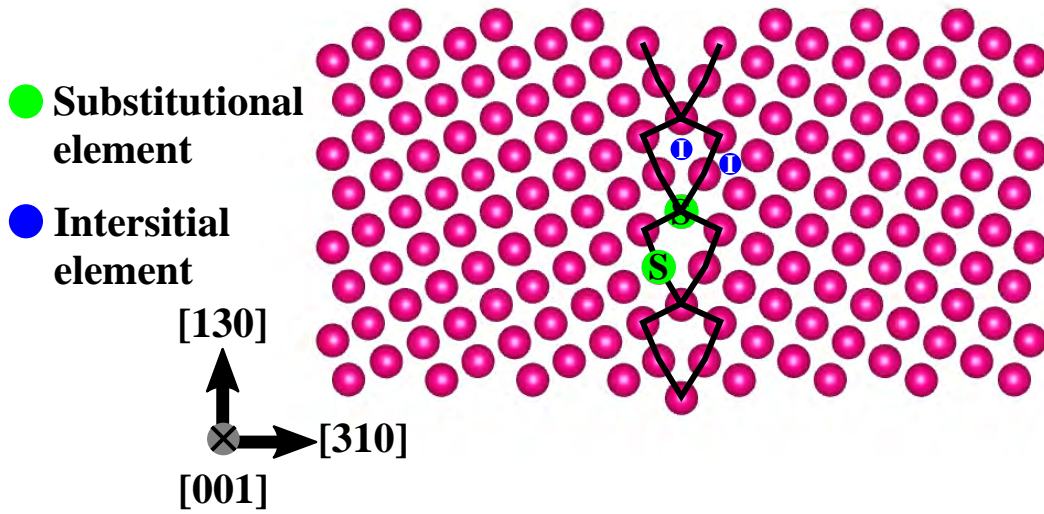


**Figure 2.7: GB segregation of foreign elements.** Structure of a bcc Fe  $\Sigma 5[001](310)$  GB with the kite-type SU. Examples of substitutional positions are marked in light green and interstitial positions in blue, respectively.

with two or more alloying elements and which typically contains impurity elements such as S, P, B and C in low concentrations stemming from the production process as well as raw material purity.

For the case that no interaction between the segregating elements occurs, the Langmuir-McLean model is still not fully valid. Site-competition effects have to be considered in Eq. 2.4. For a ternary system two equations are necessary for solute 1 and 2:

$$\frac{X_{b,1}}{X_b^0 - X_{b,1} - X_{b,2}} = \frac{X_{c,1}}{1 - X_{c,1} - X_{c,2}} \exp\left(-\frac{\Delta G_1}{k_B T}\right) \quad (2.11a)$$

$$\frac{X_{b,2}}{X_b^0 - X_{b,1} - X_{b,2}} = \frac{X_{c,2}}{1 - X_{c,1} - X_{c,2}} \exp\left(-\frac{\Delta G_2}{k_B T}\right) \quad (2.11b)$$

Site-competition can be applied to explain co-segregation behavior under two conditions: first, under high GB coverage and second when both segregants prefer to occupy the same position. Nevertheless, site-competition was used to explain segregation behavior of C and P [11] or S [67] in Fe, although the elements do not occupy the same site. Figure 2.7 shows the favored positions of C, P and S.

While C segregates interstitial, P and S preferentially segregate substitutional. Thus, site-competition alone can not be used to explain segregation tendencies. Whether substitutional or interstitial, in both cases the surrounding lattice can be

distorted and may cause elastic stresses. In the case of two solute elements occupying the same site in the matrix, site-competition would suggest only one of them to segregate the GB. However, experiments have shown that in some cases (e.g. Fe-Ni-Sb [68]) the segregation of one solute increases the segregation tendency of the other too. The reason for this behavior can only be explained with an attractive interaction potential between the solute elements.

Considering interaction effects, the free segregation energies  $\Delta G_1$  and  $\Delta G_2$  in Eqs. 2.11 depend on  $X_b$ . For  $X_c \ll X_b$  (dilute limit), they are:

$$\Delta G_1 = \Delta G_1^0 + \alpha'_{1,2} X_{b,2} \quad (2.12a)$$

$$\Delta G_2 = \Delta G_2^0 + \alpha'_{1,2} X_{b,1} \quad (2.12b)$$

with  $\Delta G_1 = \Delta G_1^0$  and  $\Delta G_2 = \Delta G_2^0$  the free segregation energies of the solutes without interaction and  $\alpha'_{1,2}$  the interaction coefficient in a regular solution. The segregation behaviour depends on the magnitude of  $\alpha'_{1,2}$ .

For  $\alpha'_{i,j} < 0$  the interaction is repulsive. Depending on the free segregation energies and bulk content (in Eq. 2.12) complete depletion of one solute can occur. For  $\alpha'_{i,j} > 0$ , i.e. attractive interaction between element  $i$  and  $j$  would result in GB segregation of both solutes. Experimental evidence for synergistic co-segregation of metalloid - transition metal was shown by Dumolin et al. [69]. Similar to the Fowler-Guggenheim model, when  $\alpha'_{i,j}$  or the bulk concentrations increases, the segregation level results in a discontinuity (see Fig. 2.6), where an  $(i + j)$ -rich 2D-phase compound forms (cluster or precipitate). Precipitation can also occur in the bulk if the interaction coefficient is too high. Thus, synergistic co-segregation and precipitation are in competition. It should be mentioned that the interaction coefficients  $\alpha'_{i,j}$  are deduced in the bulk, but at the GB the structure may be distorted and therefore change the segregation patterns. Intrinsic structural defects (e.g. voids, dislocations) also influence the interaction of solutes under equilibrium segregation since they can interact with the solute atoms.

Last but not least, it should be noted that all models described here are based on Gibbs' surface adsorption theory [57]. As we have seen before, the atomic structure of an internal interface such as a GB depends strongly on the orientation relationship of the adjacent grains. As shown in Fig. 2.8, the GB energy has minima (so called cusps) at specific tilt angles. These GBs are called special GBs. Segregation of a solute atom would change the GB energy such as shown by the solid line in Fig. 2.8.

According to our models the driving force of segregation is the reduction of the interfacial energy. Therefore, segregation is more prone to random high-angle GBs with misorientation angles between the cusps. Special GBs with a deep energy cusp are more prone to be segregated by foreign elements. On the other hand, GBs with shallow cusps were considered as not favorite for segregation as its GB energy vanishes. Watanabe et al. [70] studied the relationship between GB hardness and segregation in  $\alpha$ -Fe-1.08 at.%Sn bicrystals. He found out that GB segregation of Sn as well as the resulting hardening depend on the misorientation angle.

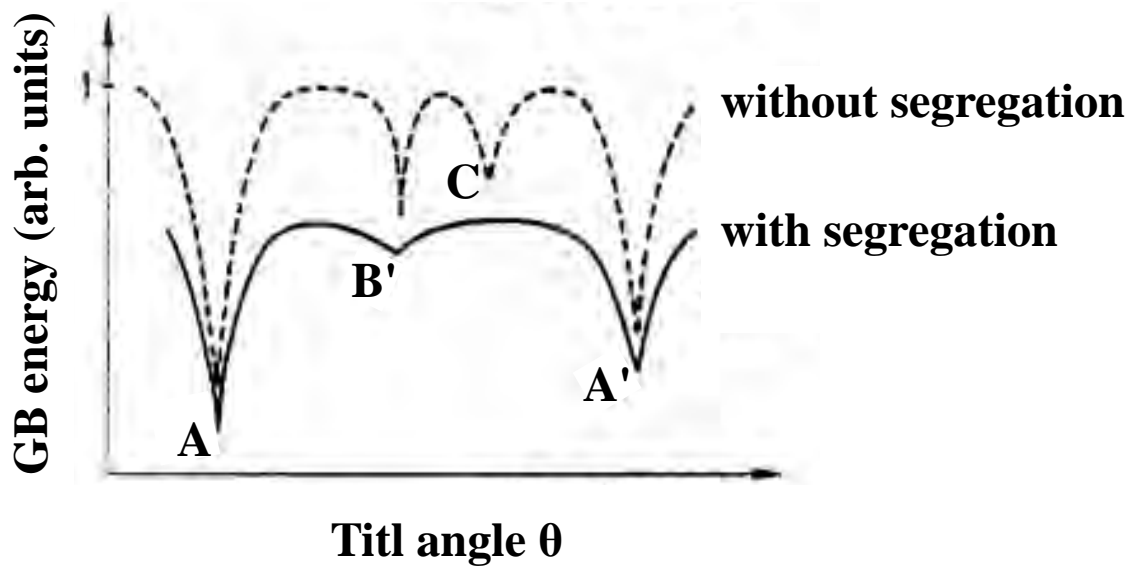


**Figure 2.8:** Segregation effect on GB energy vs tilt angle For a Fe-Sn solid solution (dashed line) the GB energy shows low energy cusps A, B', C, A' at specific tilt angles. Because of Sn segregation (solid line), the GB energy is reduced such that the initially shallow cusp C disappears, B' becomes shallow and the deep cusps A and A' remain unchanged. Redrawn from [71].

However, recent studies show that GB segregation can occur also for these boundaries. Rajagopalan et al. [72] used molecular statics simulations to calculate the GB segregation energy for various elements in different bcc Fe GBs. His calculations showed that the  $\Sigma 9[0\ 1\ 1](2\ 2\ 1)$  and  $\Sigma 3[0\ 1\ 1](1\ 1\ 1)$  GB having a shallow energy cusp are prone to segregation of P. The reason for this behaviour is the influence of the microscopic DOFs and the corresponding SU.

### 2.2.2 Non-equilibrium segregation

In contrast to equilibrium GB segregation, non-equilibrium segregation is an irreversible process. The effect of non-equilibrium segregation was first found by Westbrook et. al [73] in a quenched, dilute non-ferrous alloy. They detected a clear increase of the hardness near the GB, which was related to the GB segregation during fast cooling. This phenomenon was explained by Anthony et al. [74] as follows: at high temperature the density of vacancies increases. These vacancies are binding the solute atoms to vacancy-atom complexes. During quenching they tend to move towards the GB, which acts as a vacancy sink. This creates a gradient in vacancy concentration. If the interaction of the solute atom with the vacancy is attractive, the solute atoms follow the vacancies and they will be accumulated near the GB. This may explain the observations of Faulkner [75], who investigated GB segregation of titanium in quenched austenite steel with scanning transmission electron microscopy (STEM). Three times higher titanium concentration than in the matrix were detected over a range of 100 – 300 nm away from the GB. One important parameter is the cooling rate. Huang et al. [23] investigated B segregation in Ni-based superalloy 718 at different cooling rates using secondary-ion mass spectroscopy (SIMS). For 400°C/s (water quenching) non-equilibrium segregation was suppressed, while a lower cooling rate of 20°C/s enhanced the non-equilibrium segregation. This was explained with the diffusion time of the vacancy-solute complex. Similar observations were done in austenite 316-steel GBs, where B segregation was observed at a cooling rate of 50 K/s, while at a higher cooling rate of 500 K/s no segregation occurred even so the initial temperature was the same [76]. Therefore, non-equilibrium segregation can be avoided (or at least minimized), if the material is heat treated at low temperature and high cooling rate. On the other hand, if the solute-vacancy interaction is weak, the solute atom would diffuse away from the GB and the region around the GB would be depleted (no drag effect of the vacancy) [77].

Non-equilibrium segregation can also be explained with the *reverse Kirkendall effect* [78]. When a vacancy moves towards the GB, the atoms (solutes as well as solvents) near the interface has to diffuse out. If the diffusivity of the solvents and the solutes is equal, no gradient of solutes is formed. However, if the diffusivity of the solutes is larger than that of the solvent, a depletion or desegregation of solutes around the GB will be observed. For the reverse case, i.e. when the diffusivity of the solute is smaller than for the solvent, the GB region will be enriched by the

solute atoms.

Besides thermally induced non-equilibrium segregation, there are also radiation-induced, stress-induced and recently GB migration induced non-equilibrium segregation [10, 79–81], where the velocity and distance of the migrating GB are important parameters [80]. He et al. studied the influence of B segregation in austenite steel on recrystallization using SIMS. They concluded a direct relationship between non-equilibrium segregation of B during the formation of new boundaries (recrystallization) and the motion of the GBs during annealing. This phenomenon is explained by the increase width of the boundary during migration [82].

### 2.2.3 Diffusion induced grain boundary migration

A GB is known to move during recrystallization and grain growth. Both are thermally-assisted processes. However, GB migration can also occur during the diffusion of solute elements. This special type of process is referred to as “diffusion-induced grain boundary migration (DIGM)”. As shown in Figure 2.9 [83], in bulk samples with thicknesses larger than the diffusion length, the GB migrated in the region close to the surface while the region further away remains unchanged. There is a change of alloy content when a GB migrates. This creates a solute enriched or solute depleted zone, depending on the diffusivity of the solute atoms moving in or out [84]. DIGM was first observed by Rhines and Montgomery [85] in zinc diffused copper bicrystals. They found the GB “disturbed within the zone of Zn penetration”, but did not identify it as grain boundary migration. In 1972 den Broeder [86] was the first who identified DIGM in Cr-W diffusion couples. Since that time several researchers investigated DIGM in different aspects to understand the driving force [84, 87–90]. However, the question why it occurs remained unanswered.

Regarding the atomistic mechanism of DIGM, Sulonen [91] suggested that the solute atoms cause a coherent strain in the lattice of the solvent material. This is due to size differences causing lattice mismatch. In case of GB diffusion the GB moves to decrease the imposed strain energy. This coherent strain energy was regarded as the driving force for migration of interfaces. It should be noted that this model was proposed for discontinuous precipitation, i.e. formation of precipitates in combination with the growth of one grain into the other. In analogy to the work of Sulonen, Hillert et al. [92] developed a mathematical model to include coherency strain for DIGM. For an elastically isotropic material the driving force of motion



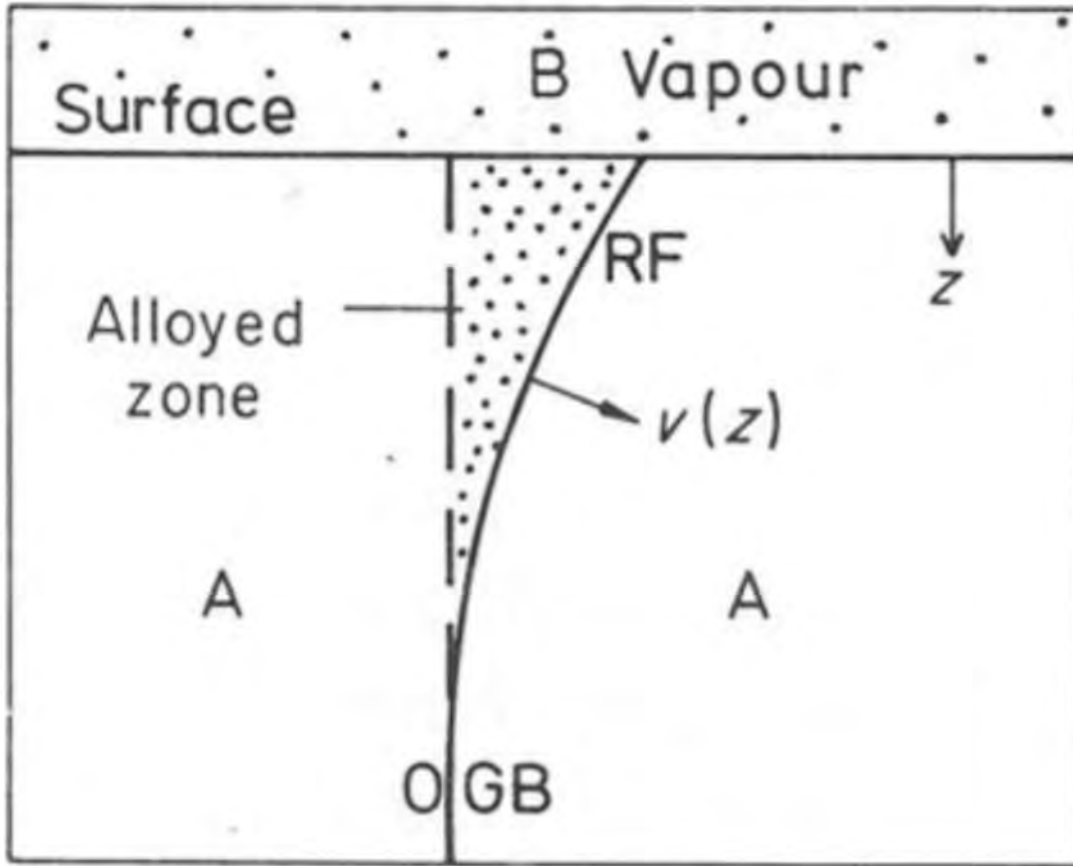


**Figure 2.9: Schematic representation of DIGM in bulk samples** The diffusion of vaporized B atoms diffuse from the top surface of the bulk sample containing element A. The GB starts to migrate with velocity  $v$ . The displacement is stronger at the A-B interface. Taken from [83].

per unit area of the GB is given by [93]

$$\Delta G_m = \frac{E\eta^2}{1-\nu}(X_+ - X_-)^2 \quad (2.13)$$

with  $E$  is the Young's modulus,  $\nu$  is the Poisson ratio,  $\eta$  is the lattice misfit parameter and  $X_+$ ,  $X_-$  the solute concentrations (in mole fraction) in front of and behind the GB. One important parameter for the validity of the coherency strain model is the thickness of the solute enriched layer given by  $\frac{D_{bulk}}{v}$  with  $D_{bulk}$  the bulk diffusion coefficient and  $v$  the velocity of the migrating boundary. The elastic coherency strain can be regarded as the driving force only for temperatures at which bulk diffusion occurs forming therefore an enriched solute layer. This model was used to explain

the increase of GB curvature during DIGM of Cu in Mo-Ni alloy [94].

For low temperatures, i.e.  $T \leq 0.5T_m$  ( $T_m$  the melting temperature) or if the size difference between solute and solvent atoms are negligible, Balluffi and Cahn [90] proposed GB diffusion caused by a vacancy mechanism similar to the Kirkendall effect in the bulk. The concentration gradient of solute atoms creates a flux of vacancies moving in the opposite direction. In order to accommodate more solute atoms in the GB and to maintain the equilibrium, state of the GB, more vacancies have to be generated. This is achieved through GB dislocations (GBDs), which act as sources/ sinks for vacancies similar to bulk dislocations during bulk diffusion processes. Vacancies are emitted by GBD during climbing. Since GBDs can cause steps in the boundary, a climb of GBDs means that the step will move parallel to the boundary plane. Figure 2.10 exemplary illustrates this process for a  $\Sigma 5[001]$  GB with a disconnection (GBD + step). The question could arise, where GBD come from? As described in the previous chapter, deviations from the ideal CSL boundary geometry can be compensated by the formation of an array of GBDs (similar to low-angle GBs). Additionally, non-equilibrium vacancy concentrations may produce GBD loops. More details about the model can be found in the work of Balluffi et al. [90] and Smith et al. [95].

### 2.2.4 Liquid metal embrittlement

Considering a liquid metal in contact with a solid material containing a GB. Due to GB diffusion, the liquid metal penetrates along the boundary and reduces its cohesion strength. When an external stress is applied, the solid material fractures along the dewetted boundaries in a brittle manner. This phenomenon is called “liquid metal embrittlement” (LME). It was observed in several binary system, such as Cu-Bi [96, 97], Fe-In [97], Al-Ga [98–100], Ni-Bi [101] as well as Fe-Zn [102–106]. Yu et. al [101] discovered that the phenomenon is not limited to only special GBs (CSL-type boundaries) but can also affect general GBs since the inclination of the GB plays a determining factor. Interesting is the work of Nam et al. [107], where the driving force behind LME in Al-Ga was studied. They concluded that the very high stresses caused by Ga diffusion nucleates GBDs in the Al polycrystal. The chemical potential changes abruptly at the GBD. Thus, the Ga atoms has to jump across the GBD and cause a stress discontinuity, which is preserved by GBD climb. The GBD climbing model was well agreeing with experimental observations of [108]. However, the mechanism for GB decohesion is still under debate and not

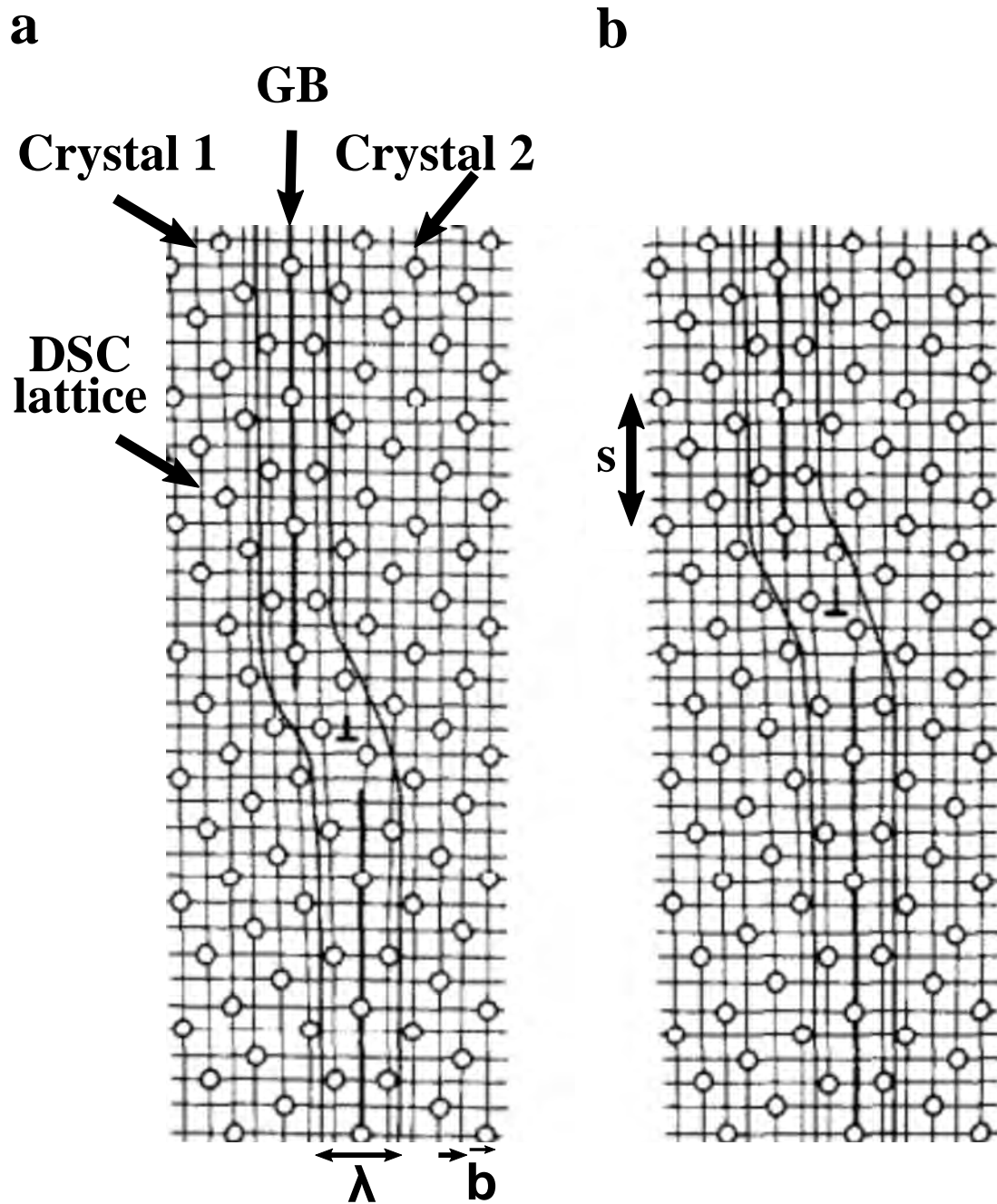


**Figure 2.10: GB dislocation climbing.** **a** The intrinsic state of a simple cubic  $\Sigma 5[001]$  tilt GB with core width  $\lambda$  containing an edge GBD with a Burgers vector  $\vec{b}$  of the DSC lattice. **b** Climb of GBD by distance  $s$  causes migration of the boundary. Image taken from [90].

well understood. Schweinfest et al. [109] studied the Cu-Bi system and found that the larger Bi-atoms increase the Cu-Cu bond length at the GB, i.e. reducing the

bonding strength. However, the model can not explain why LME also occurs in Fe-Zn, where the size difference is negligible. Peng et al. investigated the influence of Zn in a bcc-Fe  $\Sigma 5$  GB. Their analysis showed a slight increase of the Fe-Fe bond induced by Zn segregation. This could not explain the LME effect of Zn on Fe GBs. Their studies showed a modification of the charge distribution. It should be taken into account that both models are based on atomic scale processes. Therefore, to understand LME as well as DIGM, it is necessary to study the structure and composition of GBs down to the atomic scale.

It should be noted, that the segregation level exceeds a certain value, a secondary phase can form as a result of supersaturation of the GB solid solution [10].

### 2.2.5 Grain boundary precipitation

The nucleation of precipitates at GBs occurs usually heterogeneously, because GBs are regions of higher free energy compared to the bulk [45, 47]. In order to replace a GB area by a precipitate, the corresponding area has to be destroyed. Therefore, the destruction of GB area within the  $\alpha$ -phase matrix by the formation of a nucleus would release the destruction free energy  $\Delta G_d = A_{\alpha\alpha}\gamma_{\alpha\alpha}$  - reducing the total free energy for heterogeneous precipitation  $\Delta G_{het}$  given by: [110]

$$\Delta G_{het} = -V\Delta G_V + A_{\alpha\beta}\gamma_{\alpha\beta} - \Delta G_d \quad (2.14)$$

where  $V\Delta G_V$  is the volumetric free energy and  $A\gamma_{\alpha\beta}$  is the interfacial free energy. For precipitation, the first term has to be negative because it describes the free energy reduction due to the creation of a volume  $V$  of  $\beta$ -phase. The second term is always positive, describing the free interfacial energy increase for the creation of an area  $A_{\alpha\beta}$ . It should be noted that Eq. 2.14 does not take into account any misfit strain energy. The optimum nucleus shape is achieved through the minimization of the total free energy. For an incoherent GB nucleus the optimum shape are two spherical caps (shown in Fig. 2.11 a), symmetrical with respect to the GB plane. It can be seen that the shape of the nucleus can be defined by the angle  $\rho$  and the radius  $r$ . For a critical radius  $r^*$  the nucleus is energetically stabilized and its growth is favored. It is [45]

$$r^* = \frac{2\gamma_{\alpha\beta}}{\Delta G_V} \quad (2.15)$$

The angle  $\rho$  influences the activation energy barrier for heterogeneous nucleation  $\Delta G_{het}^*$ , which is usually lower than for homogeneous nucleation. In analogy to the solidification of a liquid on a solid substrate,  $\cos(\rho) = \frac{\gamma_{\alpha\alpha}}{2\gamma_{\alpha\beta}}$  is the dewetting parameter [45], i.e. the value of  $\rho$  depends on the GB energy and the interfacial energy. We have seen in Eq. 2.4, section 2.1.4 that the GB energy depends on the type of interface and the underlying atomic structure. There are three types of interfaces: coherent, semi-coherent and incoherent [45].

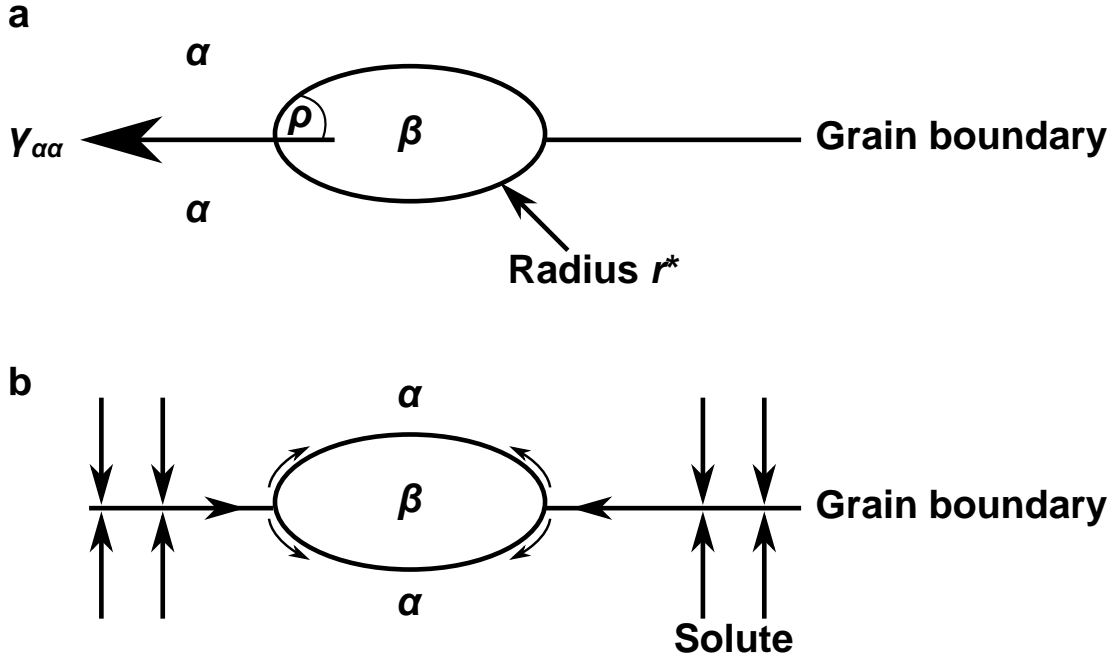


**Figure 2.11: GB precipitation and its growth** **a** Nucleation of an incoherent  $\beta$  precipitate at a  $\alpha/\alpha$  GB. The critical radius  $r^*$  and the dewetting angle  $\rho$  determine the shape of the precipitate. **b** GB diffusion induced growth of an incoherent precipitate according to the collector-plate mechanism. Images were adapted from [110]

To determine the shape of the precipitate, the Wulff construction is used to evaluate the minimum surface energy of a precipitate with a fixed volume. For coherent interfaces, i.e. the  $\beta$  precipitate has the same crystal structure with a similar lattice parameter than the  $\alpha$  matrix, the interfacial energy  $\gamma_{\alpha\beta}$  is usually isotropic with a preferential orientation relationship between the two phases. However, if the atomic size between precipitate and matrix is much larger, elastic strain energy becomes more important than the interfacial energy in determining the shape. For a semi-coherent interface the two phases have the same crystal structure but with large difference in the lattice parameters. Dislocations are introduced to compensate for the lattice misfit. Similar to low-angle GBs, the distance between the dislocations

## 2 Theory

gets smaller with increasing misfit until the dislocation cores overlap. Finally an incoherent interface describes the random orientation relationship between the two phases with different lattice parameter and its shape is elliptical, called “allotriomorph” [45, 110].

The final shape of a GB precipitate can change during the growth process. Figure 2.11 b shows the growth of an incoherent GB precipitate by the collector plate mechanism. The growth occurs in three steps:

1. volume diffusion of solute atoms towards the GB
2. diffusion of solutes along the GB (GB diffusion)
3. diffusion of solutes along the  $\alpha/\beta$  interfaces

This growth process becomes more relevant for substitutional solutes. Examples and more details on GB precipitation can be found in [45, 110, 111].

## 3 Experimental Methods

In this chapter the methodologies used in this thesis are presented - starting from the global micrometer scale down to the atomic scale. The chapter is structured as follows: the first part describes the growth of Fe-4at.%Al bicrystals by a modified Bridgman method. Next, the techniques used to investigate the GB structure and composition are introduced, starting with a brief depiction of the scanning electron microscopy (SEM) to characterize the global structure of the GBs. Since the main focus of this work is to describe the atomic arrangement as well as composition of the interfaces, the operation mode of scanning transmission electron microscopy (STEM) as well as atom probe tomography (APT) will be explained in more detail.

### 3.1 Fabrication of bicrystals

In this work, the study of special tilt GBs was performed using well oriented bicrystalline samples. The method of growing bicrystals from the melt by directional solidification in a vertical crucible was originally developed by *Williams Bridgman* [112]. The main idea is to solidify a molten material by moving heating coils along the sample. This allows the growth of single crystalline material. To grow a bicrystal containing a tilt GB, two seed crystals with a certain misorientation along a common axis are required. Figure 3.1 shows schematically the set up of the Bridgman technique.

Two Fe-4at.%Al single crystals (ingots) are attached to a cylindrical Fe-4at.%Al polycrystal. The relative orientation of the single crystal seeds to each other along a common axis define specific tilt boundaries. To stabilize the cylindrical shape during solidification, the material is placed in an alumina crucible and filled with alumina powder. In the Bridgman oven the bottom part of the polycrystal is heated to  $1600^{\circ}\text{C}$  to ensure complete melting. The heating coils of the oven are slowly moved upwards. In this way the molten mass solidifies in a defined way and a single tilt grain boundary grows. The required growth speed is material specific. Carrying out

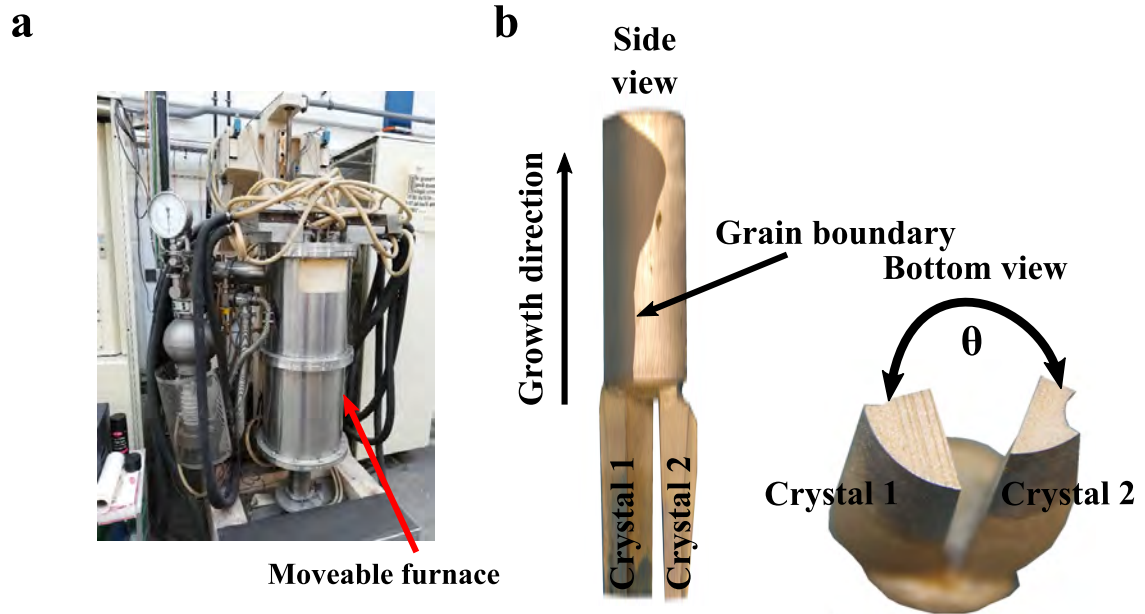


**Figure 3.1: Bicrystal growth in a Bridgman oven** a Overview photograph of the in-house Bridgman oven. The oven is connected to a turbo pump as well as an Ar-gas bottle to flush the sample chamber and to operate either under Ar-gas environment or high vacuum condition. The furnace can move upwards. b A photo of a Fe bicrystal. The two single crystals 1 2 are attached at the bottom of the initial polycrystal. The GB grew initially straight, but shows a wavy shape towards the end. The bottom view image shows that the two single crystals enclose a tilt angle  $\Theta$ , which defines the CSL GB type as well as the symmetry.

solidification too rapidly could result in the nucleation of new grains. The reason for the low content of Al in Fe is to stabilize the bcc phase throughout the complete temperature range (from the melting to room temperature) [40].

## 3.2 Scanning electron microscopy

A scanning electron microscope (SEM) is an instrument used for observing and analyzing the surface microstructure of a bulk sample using a focused electron beam. Figure 3.2 depicts the working principle of a SEM. A SEM consists of an electron source, which produces a fine beam of high energy electrons. The electron source may either be a thermionic filament or a field emission gun (FEG). The emitted electrons are accelerated through an oppositely arranged anode. Typical acceleration voltages are  $E_0 = 1 - 30 \text{ kV}$ . Below the electron gun, a two-stage lens combining condenser and objective lens is located to adjust the electron beam diameter. A beam-limiting aperture is placed between the condenser lens and the objective lens. The aperture is



a Cu plate with a hole and is called condenser aperture. Electrons passing through the hole will reach the objective lens and therefore the sample. If the condenser lens strength is increased, the focal length of the lens is reduced. This causes most electrons to be blocked by the aperture and the number of electrons reaching the sample reduces. That is, the size of the objective aperture and the condenser lens strength determine the probe current. The objective lens is used to focus the beam onto the sample. It determines the probe size. We will see later in section 3.3.2 that the probe diameter cannot be reduced infinitely. When the electrons reach the sample, they interact with it. Deflection coils scan the focused beam in a raster pattern over the sample to excite the atoms in the sample at each position. The generated signals are collected in synchronization to construct an image [113]. In

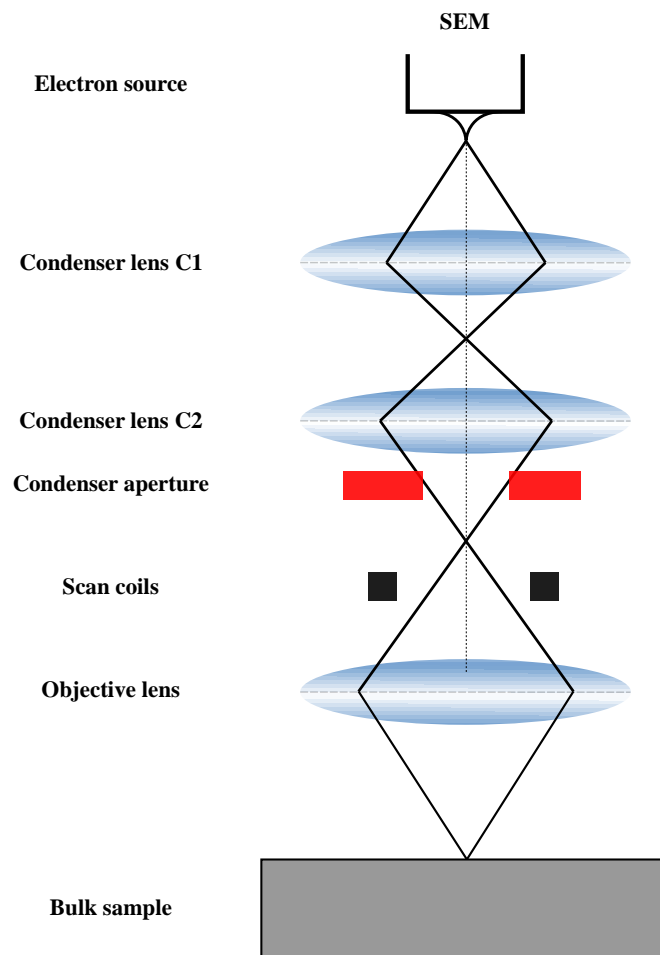


**Figure 3.2: Principle of a SEM.** Electrons emitted from the electron source pass through two condenser lenses, which reduce the electron beam diameter. The condenser lens aperture determines the beam current which reaches the sample. The objective lens focuses the electrons onto the sample surface.

the following the most relevant signals, their origin and detection are discussed.

#### 3.2.1 Secondary electrons and their detection

Electrons with high energy can produce detectable effects when they hit onto atoms. If the incident electron beam interacts inelastically with the weakly bonded valence or conduction electrons of the sample atoms, these electrons can be emitted from the sample. They are referred to as “secondary electrons” (SE). The energy transfer for emitting SEs is relatively low. It is  $E \leq 50 \text{ eV}$ . This low kinetic energy of SEs is responsible that only those who were produced close to the sample surface will have sufficient energy to leave the sample and reach the detector. Those emitted at deeper regions are absorbed by the sample after a few nm of free path length. Thus the information depth of the SE is in the range of a few nm. As a consequence of the low escape depth tips or hills appear brighter, where the probability of SE emission is larger compared to flat surfaces. This is due to the edge effect, where more SEs are generated at tips and surface edges. Additionally, SE emission depends on the incidence angle between electron beam and sample surface. Therefore, imaging with SE reflects the topography of the sample [113].

To most common used detector to collect SE is the Everhart-Thornley detector. It consists of a collector electrode, a scintillator and a photomultiplier. The collector is biased with a negative potential of few hundred volts. This value of that potential controls the number of collected SE reaching the scintillator. The scintillator converts the SE into photons. The photons are guided through a light tube towards the photomultiplier. The principle of the photomultiplier is to multiply the number of SE. The incident photons generate  $N_{Ph}$  photoelectrons (photoelectric effect), which are accelerated onto the first dynode (a positively charged anode), which emits SE. The number  $\nu$  of SE depends on the acceleration voltage. These SE are then further accelerated to the next dynode, where they produce  $\nu^2 N_{Ph}$  SE. Thus a photomultiplier with  $m$  dynodes generates  $\nu^m$  SE per photoelectron. This large number of electrons cause a voltage pulse and can be detected as an electrical signal. More details are provided in [113].

#### 3.2.2 Energy dispersive X-ray spectroscopy

We have seen that an incident electron can transfer part of its kinetic energy to the conduction or valence electrons in the sample. Additionally, there is a probability

to inelastically scatter with an inner shell electron of the atom. In this case, the inner shell electron would undergo a transition to a higher unoccupied energy level (orbit) above the Fermi energy, leaving a positive hole (electron vacancy) back. The atom is thereby in the excited state. To return to its ground state, a weakly bound electron from an outer shell has to fill the vacant position. To do so, the electron has to release energy in form of a photon (relaxation process) with energy

$$E_{Ph} = E_u - E_l \quad (3.1)$$

where  $E_u$  is the upper and  $E_l$  the lower energy level of the electron. This characteristic X-ray photon is related to the atomic number  $Z$  and the quantum numbers  $(n, l, j)$ , where  $n$  is the principal quantum number,  $l$  the angular momentum quantum number and  $j$  the total angular quantum number. The characteristic X-ray energy increases with  $Z$  because of the increase of binding energies between electrons and nucleus. It should be noted that some transitions are forbidden. A transition occurs, when the optical transition rule [113]

$$\Delta l = \pm 1 \quad \text{and} \quad \Delta j = 0, \pm 1 \quad (3.2)$$

is fulfilled. Figure 3.3 shows an energy dispersive X-ray spectrum (EDS) from a Fe sample obtained from primary electrons with  $E_0 = 30 \text{ keV}$ . The notation of the characteristic peaks is as follows: The first letter corresponds to the quantum number  $n_l$ . It is K for  $n_l = 1$ , L for  $n_l = 2$ . The following greek letter represents the value of  $\Delta n = n_u - n_l$ , where  $\alpha$  denotes  $\Delta n = 1$  and  $\beta$  denotes  $\Delta n = 2$ . Figure 3.3 shows that the heavy elements (large Z-number) such as Fe and Zn show multiple X-ray peaks. This is because of the larger number of shells. Further, the number of detected high-energy photons (K-peaks) is larger than the low-energy photons. This can be explained with the absorption of the photons by the sample before they reach the detector.

The spectrum of the characteristic X-rays is superimposed with the continuous Bremsstrahlung. Its origin is the deceleration of the primary electrons (deflection from propagation direction) in the Coulomb field of the nucleus. It has a continuous intensity distribution and is considered as background signal of the characteristic X-rays [114]. The number of Bremsstrahlung photons is given by Kramer's rule

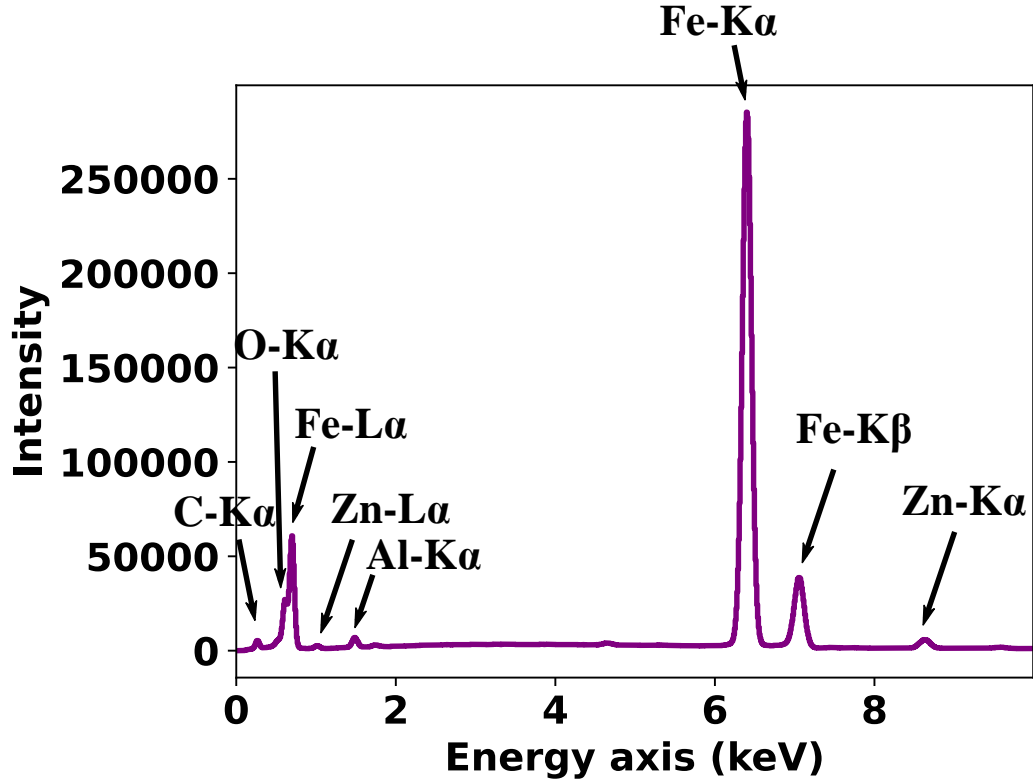


**Figure 3.3:** Energy dispersive X-ray spectrum of Fe. Detected X-ray photons emitted from a bulk sample showing characteristic peaks of C, O, Fe, Al and Zn. The spectrum shows that more electrons which undergo a K-transition were detected than those that undergo an L-transition.

[115]:

$$I_{Brems} = KZ \frac{E_0 - E_{Ph}}{E_{Ph}} \quad (3.3)$$

where  $K$  is the Kramers constant, which takes into account the collection efficiency of the detector and absorption processes in the sample [115]. A typical X-ray detector is a silicon (Si) single crystal doped with lithium (Li). The X-rays enter the detector and create electron-hole pairs (transition from valence band to conduction band), where  $3.8 \text{ eV}$  is necessary in Si. As we saw in Fig. 3.3 characteristic X-rays have energies of the order of keV and therefore generate thousands of electron-hole pairs in the Si detector. Note that the number of electron-hole pairs is proportional to the energy of the incoming X-ray. Since the penetration depth of high-energy photons is large, a thick  $3 - 5 \text{ mm}$  Si crystal is used. The backside of the crystal is coated with a  $\approx 20 \text{ nm}$  gold (Au) collector electrode (anode). Applying a high voltage

between the entrance and the anode separates the electron-hole pairs, where the electrons travel towards the anode. However, Si is due to remaining impurities a p-type semiconductor, i.e. it contains a high fraction of holes. These holes can trap the electrons traveling towards the anode. To prevent this and to make the Si crystal intrinsic, it is doped with Li. The applied reverse biasing increases the volume of the intrinsic layer until a thin p- and n-type layers remain at the entrance and the backside of the crystal. Using a Si(Li) detector requires to operate the detector at liquid nitrogen  $N_2$  temperature, because at room temperature the Li atoms would diffuse and destroy the intrinsic layer. Additionally, the advantage of cooling is that thermal noise and dark current are reduced. However, the cooling with liquid- $N_2$  may cause contamination and formation of an ice layer at the entrance plane absorbing the low energy X-rays. To avoid this a beryllium (Be) window is used to separate the detector from the vacuum column. The resolution of a Si(Li) detector is in the range of  $130 - 140 eV$ . It is measured from the full-width-half-maximum (FWHM) of the manganese (Mn)  $K_\alpha$  peak. The collected electrons correspond to current pulses, which are converted and amplified to voltage steps with a field-effect transistor. A pulse processor converts these voltage steps into signal pulses, which are stored in a multi-channel analyzer [115].

In order to increase the count rate and the processing speed of the electric signal, the Si(Li)-detector is replaced by Si-drift detectors (SDD) in newer electron microscopes. A SDD consists of a disc-shaped Si single crystal, where the front side (where the X-ray photons enter) has a negatively biased electrode (cathode) and its backside contains a small positively biased collector anode surrounded by annular electrodes (with stepped negative bias). When electron-hole pairs are generated, the electrons move towards the anode as well as the annular electrodes. A voltage is applied between the annular electrodes and the anode, whose strength increases from outer to inner electrode. The holes are moving towards the cathode. Thus, the SDD can be regarded as a capacitor with capacitance  $C$  causing a measurable voltage  $V$ . From the relationship  $V = \frac{Q}{C}$  one obtains the electric charge  $Q = Ne$ , i.e. the number of electrons generated from one photon. This number depends on the energy of the X-ray photon, which in turn is element-specific. Because of the smaller anode size, the capacitance is smaller than in a Si(Li)-detector. This increases the count rate and improves the signal-to-noise ratio. Further, the detector does not need to be cooled with liquid  $N_2$ . Its energy resolution is similar to a Si(Li)-detector [113, 115].

### 3 Experimental Methods

For quantification of element concentrations several factors need to be considered. It is known that the number of generated photons with energy  $E_{Ph}$  is proportional to the number of atoms of a specific element. However, the ionization cross-section  $\sigma$ , i.e. the probability that an atom was excited is an factor. It is given by an empirical equation of Bethe for K-shell electrons [115]:

$$\sigma = \frac{\pi e^4}{E_0 E_c} m b \ln \frac{c E_0}{E_c} \quad (3.4)$$

with  $E_c$  the ionization energy,  $m$  the number of electrons on the ionized sub-shell and  $b, c$  fitting parameters. The ionization cross-section depends on the overvoltage  $U = E_0/E_c$ . Ionization is most probable for  $E_0 \approx 5E_c$ . This becomes more important in a SEM, when the primary beam energy is small and high energy X-ray K-lines are not excited. In this case the intensity of the L-line is much high than the corresponding K-line and the quantification cannot be done correctly. Another important feature is the fluorescence yield  $\omega$ , which takes into account that not all inner shell excitation result in the emission of a X-ray photon. Instead the atom can relax through the emission of an Auger electron. The probability for Auger electron emission is larger for light elements. Finally, it should be considered that not all emitted X-ray photons are detected. Depending on the collection efficiency of the detector only a fraction of the X-ray photons will be detected [115]. In a SEM there are some more factors that need to be considered. As discussed before, a bulk sample is used in a SEM. This causes absorption processes, which influence the quantification. Therefore a SEM samples should have a flat surface and a absorption correction has to be applied before quantification. The absorption of the high-energy X-ray photons can also generate lower-energy photons changing the intensity of certain characteristic peaks [113].

#### 3.2.3 Backscattered electrons: Imaging and diffraction

Besides inelastic processes, the primary electrons can also elastically scatter. This occurs between the light incident electrons and the electric field of the heavy nucleus in the sample. After the elastic scattering the trajectory of the electron changes but its energy remains constant. An electron which is ejected backwards is referred to as backscattered electron (BSE). Since the BSE has a high energy, the escape depth is about two order of magnitude larger than for SE (for  $E_0 = 3 \text{ keV}$  it is few hundred nm) [114]. Therefore the BSE yield is a function of the atomic number  $Z$ . In

comparison to EDS, it does not give information on the exact composition but only variations of the chemical composition. Since the escape depth of BSE is smaller than for characteristic X-ray photons, the spatial resolution is increased. The BSE is mainly collected using an axial solid-state detector (silicon p-n diode) just below the objective lens. In comparison to the Everhart-Thornley detector, where also BSE electrons can be collected to form a BSE image, the position of the BSE detector prevents the collection of SE electrons and topographic contrast is negligible. The silicon solid-state detector is a p-i-n diode. When BSE are collected, they generate electron-hole pairs in the intrinsic layer. The applied voltage between the p- and n-type layer causes an electric current (electrons flow towards the n-type layer and holes towards the p-type layer). This current is used as a signal to form a BSE image. As the backscattering coefficient increases with atomic number  $Z$ , regions with higher  $Z$ -number result in a larger current and appear bright in the BSE image. In comparison to the Everhart-Thornley detector, there is no voltage necessary to collect BSE. Usually the detector is split into 2 – 4 quadrants. Adding the signals from the different segments would give rise to a  $Z$ -contrast, while subtraction would enhance the topographic contrast.

The backscattering cross-section, i.e. the probability of electrons to backscatter is related to the distance of the primary electron to the nucleus. In certain orientations of the crystalline sample the electrons can travel parallel to the atomic planes, which would increase the BSE yield. This is known as **channeling effect**. Therefore differences in orientation would also result in a change of the contrast. Part of these BSEs can leave the sample surface in exact Bragg angle  $\Theta$  and form the electron backscattered diffraction (EBSD) pattern, sometimes called Kikuchi pattern. The Kikuchi pattern are used to identify the crystal structure and the crystallographic orientation of the sample. This becomes important when analyzing the microstructure of GBs, where it is possible to identify the misorientation angle between the grains and the GB plane normal vectors. The latter one can be deduced assuming that the GB plane normal is perpendicular to the sample surface. As shown in Figure 3.4 a) the primary electrons (elastically and inelastically) are scattered towards an angle  $\Theta$ , which fulfill the Bragg condition

$$2d \sin \Theta = n\lambda \quad (3.5)$$

are diffracted and would produce a diffraction spot. Here,  $d$  denotes the distance

### 3 Experimental Methods

between the lattice planes ( $hkl$ ),  $n$  is an integer number and  $\lambda$  is the wavelength of the primary electron. While fulfilling Bragg's law, the diffracted electron can also travel in different azimuthal directions  $\phi$  forming a Kossel cone (named after Walther Kossel). Intersection of the Kossel cones with the phosphorous screen of the detector results in diffraction lines referred to as "Kikuchi lines". Different orientation of the lattice planes would produce different Kikuchi lines. Superimposing all possible Kikuchi lines would result in a EBSD pattern. Figure 3.4 b shows an exemplary EBSD pattern for ferritic iron. The intersection of the bands corresponds to a pole or zone axis. As in a SEM the beam scans over the sample, the orientation data is obtained at each beam position. The width of the Kikuchi band (two corresponding Kikuchi lines) is inversely proportional to the interplanar spacing  $d_{hkl}$  of the diffracting  $hkl$  planes. To increase the intensity of the EBSD pattern, it is necessary to reduce the path length of the BSEs. For that the sample is tilted to  $70^\circ$  with respect to the horizontal plane in order to reduce the angle between the incident electron beam and the sample surface. The fluorescent screen is placed in front of the tilted sample. Behind the fluorescent screen is either a charge coupled device (CCD) or a complementary metal-oxide semiconductor (CMOS) detector. The crystal orientation is determined from the exact location of the Kikuchi bands. This is done by a Hough transformation (parametrisation). Each Kikuchi band corresponds to a point in the Hough space, where the peak height is related to the brightness of the band. Once the location of the bands is known, it is possible to determine the angles between the bands. Comparison with simulated structures would give the orientation of the crystal structure. Scanning the electron beam results in an orientation map. In the case of a bicrystal with a GB, the Hough space contains a peak corresponding to a band in one grain but not in the other grain [116, 117].

The physical spatial resolution of EBSD depends on many factors such as the working distance WD (distance between sample and the objective lens), the acceleration voltage, the beam current (probe size), the material ( $Z$ -number) and the sample tilt angle [117]. The latter one would result in an elliptical profile of the incident beam and the spatial resolution has to be distinguished perpendicular and parallel to the tilt axis. In Fe-3%Si bicrystal investigated at  $E_0 = 15 \text{ keV}$ ,  $WD = 15 \text{ mm}$  and a sample tilt of  $70^\circ$  the spatial resolution were measured to be  $90 \text{ nm}$  in perpendicular and  $35 \text{ nm}$  in parallel direction [116]. It should be mentioned that reducing the beam current (probe size) would improve the spatial resolution but it would also decrease the quality of the recorded EBSD patterns. This complicates the compar-



ison with simulated patterns and reduces the *effective* resolution [118]. One way to improve the effective resolution is to use a Shottky emission gun because of its higher brightness or to improve the performance of the detector.

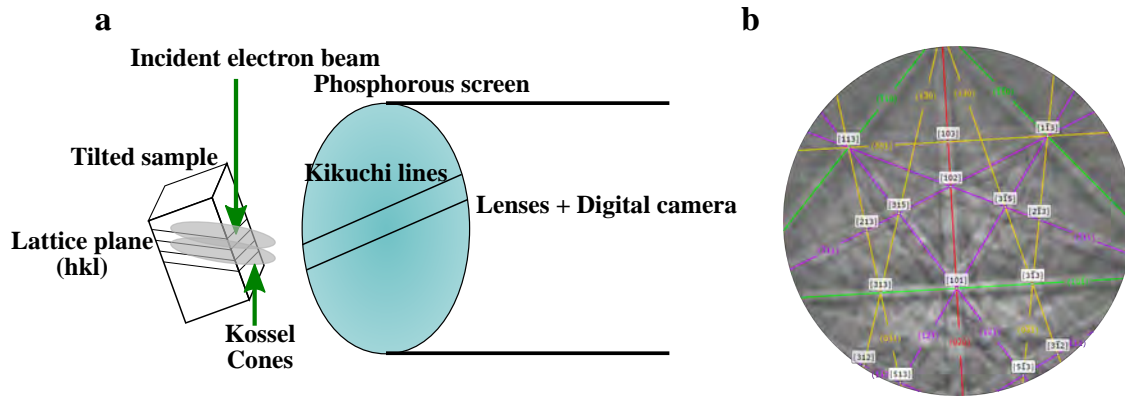


**Figure 3.4: Formation of EBSD pattern.** **a** Incident electron beam is diffracted by the lattice plane ( $hkl$ ) and produces the Kossel cones, which correspond to Kikuchi lines on the phosphorous screen. **b** Typical EBSD pattern of ferritic iron.

A typical EBSD detector consists of a fluorescent phosphor screen and a digital camera. The phosphorous screen is used to observe the EBSD pattern and adjust the exposure time since it converts the incoming electrons into photons. Lenses or optical fibres focus the photons onto a digital sensor. Standard digital sensors are CCDs. The image plane of a CCD detectors consist up to  $4096 \times 4096$  pixels, where each pixel can convert the incoming photon into electrical charge. The previous section described how such conversion is done using a Si p-i-n diode. Each pixel of a CCD is a p-i-n diode with a size of  $\approx 10\text{--}20 \mu\text{m}$ . Positively biased electrodes are used to create a potential well under each pixel. The generated charges are stored in these wells. The electrodes are also used to extract the electrical signal. The advantage of a CCD is that the sensitivity and acquisition speed can be increased through binning. However it should be noted that the pixel size determines the spatial resolution and increasing the pixel size through binning would decrease the resolution. Therefore the bin-size should be carefully chosen according to the speed, resolution and pattern quality. Recently, CMOS-based EBSD detectors are installed, which overcome the problems of the CCD. CMOS detectors allow high speed acquisition without any loss of resolution.

### 3.3 Scanning transmission electron microscopy

In order to reveal the structure and the compositional modulations that take place during (co-)segregation at a GB, two essential requirements are necessary: a high lateral resolution in the sub-nanometer range and the ability to carry out chemical analysis in these local dimensions with a high sensitivity. In this work, scanning transmission electron microscopy (STEM) is the key method for the characterization of the atomic structure and composition of the GB. After a general introduction in the principles of transmission electron microscopy (TEM), the focus will be on the image formation in a STEM and what conditions are essential for the analysis. Detailed information can be found in various textbooks such as [119–123].

#### 3.3.1 General description

The interaction of the primary electron beam with the sample generates various signals. As the name mentions in a TEM the forward scattered or transmitted electrons are used for imaging. For this the specimen needs to be electron transparent, i.e. a thickness of  $\leq 100\text{ nm}$  in the direction of the electron beam. This has the advantage over the SEM that the interaction volume is significantly reduced and the spatial resolution improved. The spatial resolution is further improved by using higher acceleration voltages, which would decrease their wavelength (according to deBroglie) [120].

A schematic of the TEM is shown in Fig. 3.5 a. At the top is the electron source, which emits the electrons. The electron source can be either a thermionic or a FEG as discussed before for the SEM. The advantage of a FEG over thermionic is its higher brightness, better coherency and lower energy spread.

Below the gun is a set of condenser lenses and apertures. Typically two or three condenser lenses are used, together with the minicondenser lens and the pre-field objective lens (upper objective lens), to control the illumination mode onto the specimen: a broad parallel beam for conventional TEM or a convergent beam for STEM (shown in Fig. 3.5 b). The condenser aperture below the C2 lens is used to block part of the electron beam, thus determines the coherency of the beam. A smaller aperture would create a more parallel and coherent beam. As can be seen, in TEM mode the minicondenser lens focuses the electron beam onto the front-focal plane of the upper objective lens, which results in a parallel illumination of the specimen. In STEM mode, the condenser lens C3 focuses the beam onto the front-

focal plane of the minicondenser lens, which in turn transfers a parallel beam to the upper objective lens. This results in a convergent beam with semi-convergence angle  $\alpha$  onto the specimen. It is clear that the size of the C2 aperture determines the semi-convergence angle. Below the specimen is the lower objective lens, which is the image forming lens in TEM. All following lenses (intermediate and projection lenses) will magnify the intermediate image formed by the objective lens and project it onto the screen/detector. This means that lens errors of the lower objective lens will be magnified, too. These errors need to be corrected to achieve a higher resolution in TEM.

In STEM (see Fig. 3.5b) the lenses below the specimen do not affect or limit the resolution due to the way how an image is magnified in STEM. Magnification in STEM is defined as the ratio between the scan size on the computer and the scan size on the specimen. At a constant scan size on the computer, a smaller scan area on the specimen would result in a higher magnification. Therefore, in a dedicated STEM there are no lenses below the specimen needed to form an image. In an instrument, which can switch between TEM and STEM and is equipped with the twin objective lens system, the lower objective lens creates diffraction discs in its back focal plane, i.e. convergent beam electron diffraction (CBED) pattern. It should be noted that the diameter of the disc is dependent on the semi-convergence angle  $\alpha$  of the primary beam, which is usually larger than the Bragg angle  $\Theta_B$ . A large semi-convergence angle would result in larger discs. This is the reason, why the diffracted disc (red) overlaps with the undiffracted disc (green). The intermediate lenses together with the projection lens are used to adjust the camera length, i.e. the effective distance between specimen and detector plane. It (de-)magnifies the CBED pattern onto the screen/detectors. The electrons are collected by annular shaped detectors, whose position and size determines the collection angle. The role and what information each detector provides will be later discussed.

In the following we will discuss how an image is formed and what are the lens aberrations that limit the resolution in TEM and STEM.

#### 3.3.2 Image formation in TEM

The main goal in high resolution imaging is to directly image the atomic structure of the specimen. For that the incident electron beam must be oriented parallel to a low- index crystal orientation (zone axis) of the specimen (typically  $[100]$ -,  $[110]$ - or  $[111]$ - directions). Low-index orientations have larger distances between atom

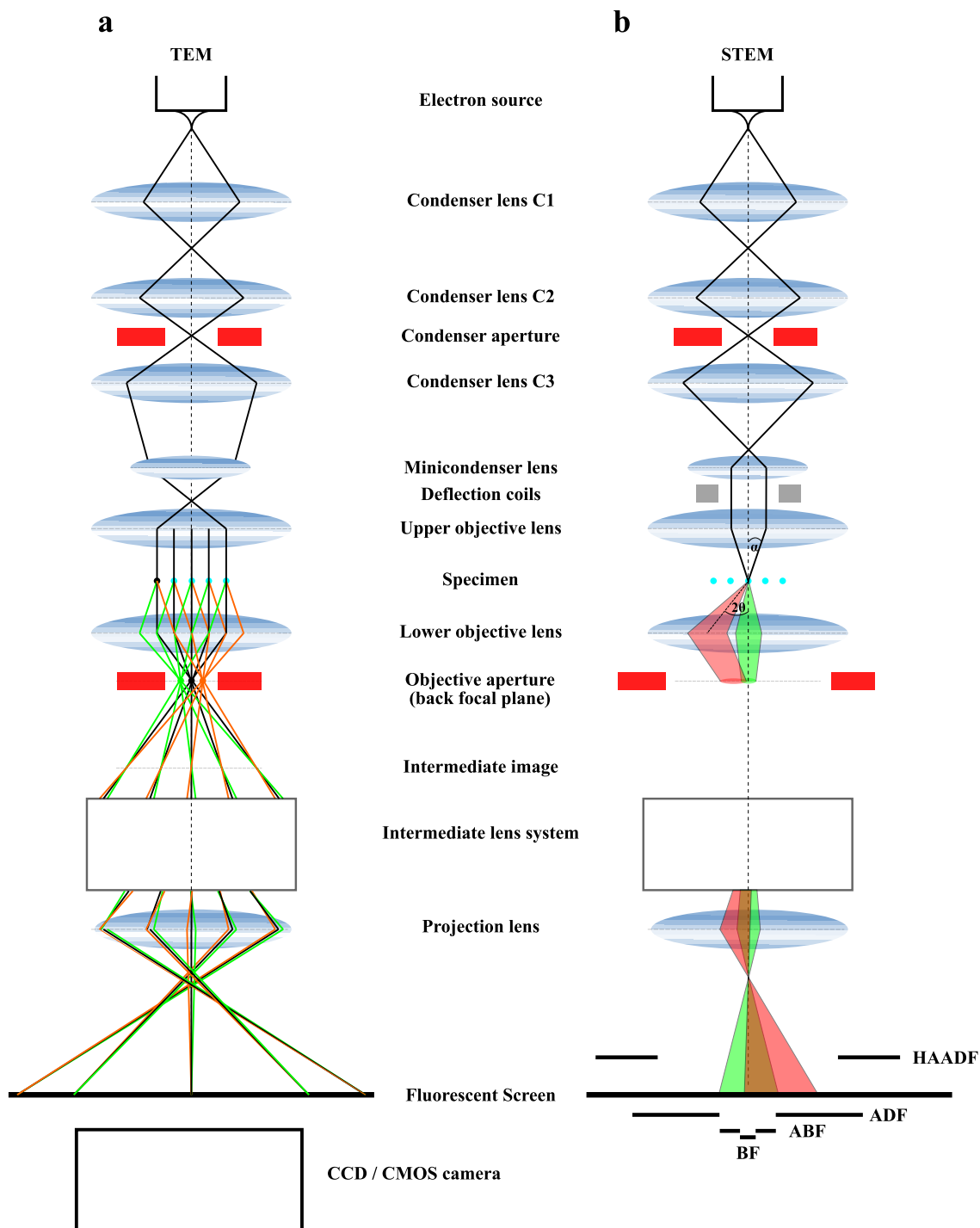


**Figure 3.5: Ray diagram for a TEM and STEM.** **a** In TEM mode the specimen is illuminated with a parallel beam and the lower objective lens forms a diffraction pattern and an intermediate image. This intermediate image is further magnified and projected onto the fluorescent screen or CCD/ CMOS camera. **b** In STEM mode the electron beam is converged to a spot with a semi-convergence angle  $\alpha$  onto the specimen by the upper objective lens. The diffracted discs (scattering angle  $\theta$ ) are projected onto annular shaped ABF, ADF and HAADF detectors. The abbreviations are explained in the text.

columns. To observe the atom columns, the resolution must be better than the distance between the columns. As mentioned before, in TEM a coherent parallel electron beam illuminates the specimen. Because of the electron transparency of the TEM specimen, a small portion of the electrons will be scattered elastically or inelastically, while the majority of electrons will traverse without undergoing a scattering process. Inelastic scattering processes play a major role in spectroscopy such as EDS or electron energy loss spectroscopy (EELS). The elastically scattered electrons are used for image formation. Elastic scattering is divided into low-angle scattering (Coulomb interaction with the electron cloud of the specimen) and high-angle scattering (Coulomb interaction with the nucleus). The low-angle scattered electrons ( $\theta \leq 3^\circ$ ) are mainly coherent and can fulfill the Bragg diffraction condition. The high-angle scattered electrons are incoherent and do not form diffracted beams. They depend strongly on the atomic number  $Z$ .

To better understand the image formation for high-resolution TEM (HRTEM) by low-angle elastic scattered electrons, it is better to consider electrons as waves. The incident electron wave function  $\psi_{in}(\vec{r}) = \exp -2\pi i(\vec{k} \cdot \vec{r})$ , where  $\vec{k}$  is the wave vector and  $\vec{r} = (x, y, z)$  the real-space vector, experiences an amplitude and a phase modulation as it passes through the specimen of finite thickness  $t_{tot}$ . This modulation corresponds to the potential distribution  $V(\vec{r})$  of the specimen's atoms. Remember, for electron transparent specimen the amplitude is constant and the specimen can be regarded as a phase object. The situation can be further approximated by assuming that the specimen is very thin and consists of light atoms. In this case the specimen acts as a weak phase object and the exit wave function is [124]:

$$\psi_{exit}(\vec{r}) = \psi_{in}(\vec{r})(1 + i\sigma V_p) \quad (3.6)$$

with  $\sigma = \frac{2\pi m e \lambda}{h^2}$  the interaction constant ( $h$  is the Planck constant) and  $V_p = \int_0^{t_{tot}} V(\vec{r}') d\vec{r}'$  the projected atomic potential. From Eq. 3.6 it can be seen that the phase shift between incident wave and scattered wave is  $90^\circ$  (indicated by  $i$ ) and that the imaginary part contains information about the atomic positions. For thicker specimen, there are two ways to calculate the exit wave function: the Bloch wave approach and the multislice approach. The former one solves the time-independent Schrödinger equation by a linear combination of Bloch waves  $b_i(\vec{q}, \vec{r})$  (sometimes

### 3 Experimental Methods

called Bloch states)

$$\psi(\vec{r}) = \sum_i a_i b_i(\vec{q}_i, \vec{r}) \quad (3.7)$$

with  $a_i$  the Bloch wave excitation coefficients. The Bloch states have the form

$$b_i(\vec{q}_i, \vec{r}) = \sum_{\vec{g}} C_{\vec{g},i} \exp[i(\vec{q}_i + \vec{g}) \cdot \vec{r}] \quad (3.8)$$

with  $\vec{g}$  the reciprocal lattice vector. To determine the Bloch wave coefficients  $C_{\vec{g},i}$  and wave vectors  $\vec{q}_i$ , the Eigenwert problem has to be solved. The Bloch waves are excited due to electron scattering events inside the specimen. The advantage of this method is that it relies on the symmetry of the specimen, but for crystal defects, such as dislocations or GBs, the number of possible Bloch waves increases due to larger number of atoms and with that also the computation time. Alternatively, the multislice method developed by Cowley and Moodie [125] is a fast approach to simulate complex crystal structures and defects. In the multislice method the specimen is subdivided into multiple thin layers along beam direction. Each layer is thin enough to be considered as a weak phase object. Because of the projected atomic potential, each slice can be characterized by a phase grating. The calculation is done in two steps. First, the interaction of the incident plane wave with the thin layer using the weak phase object approximation. Second, propagation of the electron wave through vacuum layer to the consecutive layer. The mathematical description of the propagation is given by the Fresnel propagator, which uses the fact that each point in the phase grating plane can be regarded as a source for spherical waves (Huygens-Fresnel principle). The final exit wave function is the convolution of the scattered wave function (through the slices) and the propagator. To minimize the computational time, the calculation is done in Fourier space (convolution in real space is replaced by multiplication in the Fourier space). [120, 124].

Up to now, it was considered that the exit wave function in Eq. 3.6 will be recorded in the image plane. From the different colors of the scattered electron waves in Fig. 3.5 a), it is clear that the lower objective lens sorts the electrons according to their diffraction angle  $\Theta$  and focuses them in the back focal plane to form the electron diffraction pattern. Each spot corresponds to a specific reciprocal lattice vector. Mathematically, the objective lens does a Fourier decomposition of the exit

wave function [120]

$$\psi_{diff}(\vec{q}) = \mathcal{F}(\psi(\vec{r})) \quad (3.9)$$

with  $\vec{q}$  the reciprocal vector. However, a real objective lens is not perfect. It has aberrations, i.e. deviations from an ideal lens, which can affect the wave function  $\psi_{diff}$  in the diffraction plane as shown in Fig. 3.6. Electron waves, which enter the

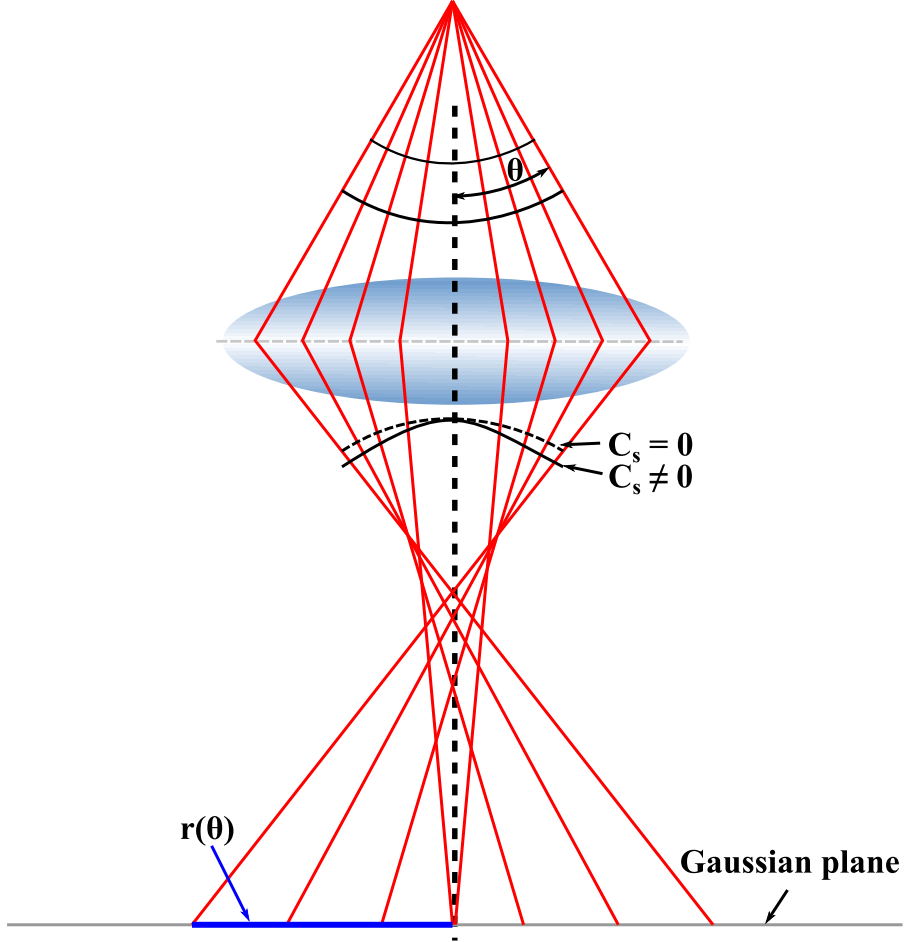


**Figure 3.6:** The effect of the spherical aberration of a real lens. Electron rays (red lines) are focused at different points. While paraxial rays are focused onto the Gaussian plane, marginal rays are focused closer to the lens. The wavefronts (black lines) show a stronger curvature, when  $C_s \neq 0$ .

lens at an angle  $\theta = \lambda \vec{q}$  will be focused to a shorter focal point by the objective lens. Thus, a point source will be imaged in the Gaussian image plane (image plane for paraxial rays) as a disk of radius [122]

$$r(\theta) = C_s \theta^3 \quad (3.10)$$

### 3 Experimental Methods

with  $C_s$  the third order spherical aberration coefficient. This stronger curvature of the wavefront with larger  $\Theta$  yield in a displacement  $\delta$  and a phase shift  $\chi(\Theta)$  [122].

$$\chi(\Theta) = \frac{2\pi}{\lambda} \delta \quad (3.11)$$

$$= \frac{\pi}{2\lambda} (C_s \Theta^4 - 2\Delta f \Theta^2) \quad (3.12)$$

with  $\Delta f$  the defocus defined as the difference between the real specimen plane and the “in-focus” specimen plane. Scherzer [126] had the idea to partially compensate the spherical aberration by defocusing the objective lens by  $\Delta f_{sch} = -1.15\sqrt{C_s\lambda}$ ,  $\Delta f_{sch}$  is called “Scherzer defocus”. With the definition of  $\Theta$ , we obtain the *spherical aberration function*  $B(\vec{q})$  [120]

$$B(\vec{q}) = \exp(-i\chi(\vec{q})) = \cos \chi(\vec{q}) - i \sin \chi(\vec{q}) \quad (3.13)$$

The spherical aberration function has to be convoluted with the exit wave function to obtain the final wave function in the image plane. For a weak phase object and with Eq. 3.9 it is

$$\psi'_{diff}(\vec{q}) = \psi_{diff}(\vec{q})B(\vec{q}) \quad (3.14)$$

$$= \delta(0) + i\rho'(\vec{q}) \exp(-i\chi) \quad (3.15)$$

with  $\rho'$  the Fourier transform of the exit wave function phase. The recorded intensity in the image plane can be expressed as [122]

$$I = \psi_{image}(\vec{r})\psi_{*image}(\vec{r}) \quad (3.16)$$

$$= 1 + 2\mathcal{F}^{-1}(\rho'(\vec{q}) \sin \chi) \quad (3.17)$$

where  $\sin \chi(\vec{q})$  is the phase contrast transfer function (PCTF), which describes the effect of phase shift on the image for a weak phase object. From this, it is clear that the optimum phase contrast is achieved for 90° phase shifts (analogy to the  $\lambda/4$  phase plate in optical microscopy).

Figure 3.7 shows the PCTF at Scherzer defocus  $\Delta f_{Sch}$ . For higher spatial frequencies  $\vec{q}$ , the PCTF oscillates, which means that the image contrast (Eq. 3.17) also oscillates and it is not possible to interpret the HRTEM image. Therefore the point resolution is given by the maximum spatial frequency, for which the PCTF has unique sign. An objective aperture with a proper size can be used to cut-off the



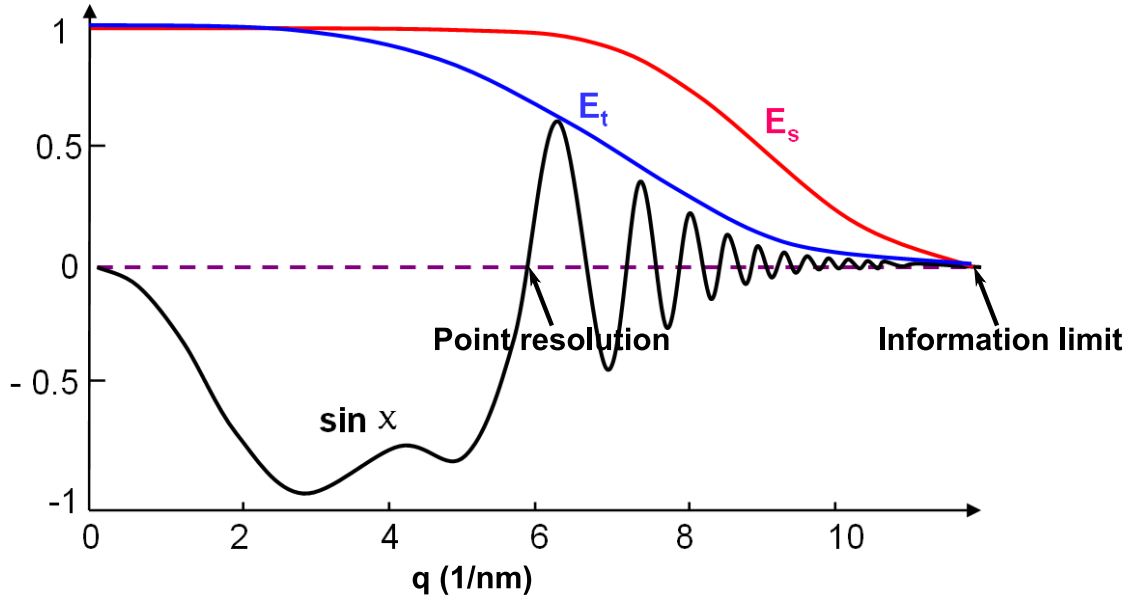


**Figure 3.7: Contrast transfer function of a TEM at Scherzer defocus.** The phase contrast transfer function  $\chi(\vec{q})$  for a negative  $C_s$ . Two arrows mark the point resolution, where the PCTF changes its sign and the information limit of the microscope. The amplitude of modulation decreases with increasing spatial frequencies because of the temporal ( $E_t$ ) and spatial ( $E_s$ ) incoherency of the electron waves. Image taken from [127].

modulated frequencies. According to Eq. 3.17, the oscillation of the PCTF should continue, but this is only valid for a fully coherent electron beam. However, partial spatial ( $E_s$ ) and temporal ( $E_t$ ) coherencies damp the PCTF oscillation in the large spatial frequency region. The origin of the partial spatial incoherence is the curvature of the incident electron wave. The origin of the partial temporal coherence is the instability of the acceleration voltage since not all electrons have the same kinetic energy. These two envelope functions limit the information transfer of the microscope [120, 122].

Besides the spherical aberration and the defocus, there are also other lens aberrations, which can affect the resolution. The most common ones are astigmatism and coma. Axial astigmatism or called two-fold astigmatism occurs because of a deviation of the objective lens field from the ideal rotational symmetry. This can happen either because of microstructural inhomogeneities of the pole pieces or by charging of the objective aperture due to contamination or charging of the specimen (non-conductive). Thus the Lorentz force is different for the electron waves in two orthogonal planes - sagittal and meridional planes. Axial astigmatism broadens the beam and the disc diameter of least confusion is given by  $d_a = \Delta f \alpha$ , with  $\Delta f$  the

difference of focal lengths for the two orthogonal planes. Axial astigmatism can be simply corrected by using a pair of quadrupoles below the objective lens. [120].

Coma (originated from comet) occurs when the electrons enter the objective lens at a distance away from the optical axis and under a certain angle (non-parallel to optical axis). These off-axis electrons do not focus onto one point in the image plane but form a comet-shaped image. Coma can be corrected using a pair of dipoles. More details on aberration correction will be given in the next section.

#### 3.3.3 Image formation in STEM

In contrast to TEM, where the image is generated by parallel illumination, in STEM the image is serially acquired with a convergent electron beam (probe). As already discussed in sec. 3.3.1, STEM is operated in diffraction mode, where the projection lens magnifies the back focal plane of the lower objective lens onto the screen/detectors, i.e. it adjusts the camera length. To form a STEM image, annular shaped detectors are used to collect the electrons that scatter up to a specific angular range. These detectors are of the same type as the SE/ BSE detectors in a SEM (see sec. 3.2.3). Figure 3.8 shows the arrangement of the detectors and how the camera length determines their collection angle. The circular bright-field detector collects the central portion of the direct, unscattered cone (up to few  $mrad$ ). These electrons would form a bright-field (BF) image, where the atoms may appear dark. BF-STEM can be used to image light elements with atomic number  $Z < 8$ . Similar as the HRTEM images, the intensity in BF-STEM images is sensitive to sample thickness and defocus (theorem of reciprocity for HRTEM and BF-STEM). This contrast reversals is due to the interference of the unscattered and diffracted discs [121]. In contrast, an annular shaped detector positioned in the outer area of the BF-detector is more robust to sample thickness and defocus. The inner collection angle of this annular bright-field (ABF) detector is limited by the size of the BF-detector, while its outer collection angle is  $\approx \alpha$ , the semi-convergence angle of the probe. ABF-STEM allows to image light and heavy atoms in the same time. Both types of atoms will appear as dark spots and does not change over a large defocus and specimen thickness because of the minimized interference effect. In order to understand the contrast formation in ABF-STEM (and in general in STEM), it is important to understand the propagation of the incident electron wave inside the specimen. Pennycook et al. [128] explained the STEM image intensities in terms of tightly bound Bloch waves. It was shown before that a linear combination of a set of

Bloch waves describes the propagation of the wave function inside a crystal. In zone axis the atoms in a crystalline specimen are arranged in columns. Their positive nucleus forms a channel trapping the incoming electron wave. When the electron probe is positioned between two atomic columns, the scattering cross-section (probability for scattering) with the atoms is very low. These electrons will form the background signal, when they hit onto the ABF detector. When the electron probe is positioned onto a column of light atoms, 1s Bloch waves are excited, which are strongly localized states. Thus, the electrons are stronger scattered forwards and will be transmitted through the hole of the ABF detector. Therefore, light elements will appear dark. When the electron probe is on top of a column consisting of heavy elements, most electrons will be scattered to angles outside the range of the ABF detector and these elements will appear dark, too. It should be mentioned, that the ABF signal is partially coherent, therefore STEM image simulations are necessary to identify the atom positions [121, 129]. To further minimize the interference problem and with that the diffraction contrast, the camera length can be reduced to detect electrons, which scatter to larger angles than the semi-convergence angle. Instead of changing the camera length, a further annular detector above the ABF can be used. For a small inner collection angle the annular dark-field (ADF) detector will collect a mixture of Bragg diffracted and incoherently scattered electrons. The resulting low-angle ADF (LAADF) STEM image is mainly used to image strain fields. This can be explained by the channeling effect. A strain field around defects (e.g. interfaces, GBs, dislocations) occurs due to (partly) displacement of atomic columns. This displacement will change the scattering angle. If the inner collection angle is more than  $50 \text{ mrad} \approx 3^\circ$  [120] the majority of the signal can be considered as incoherent. The image formed is known as high angle annular dark-field (HAADF) image, where atoms appear bright. HAADF-STEM is the most widely used imaging mode because the incoherence allows directly imaging the structure in terms of atomic number  $Z$ . The lack of coherence is due to the thermal diffuse scattering of electrons (with phonons) similar to Rutherford scattering. The differential cross-section for Rutherford scattering is known to be [121]

$$\frac{d\sigma}{d\Omega} = \frac{Z^2 e^4}{16E_0^2 \sin^4 \Theta} \quad (3.18)$$

with  $E_0$  the kinetic energy of the incident beam. This  $Z^2$ -dependence is the reason, why HAADF-STEM images are referred to as  $Z$ -contrast images. However, it should

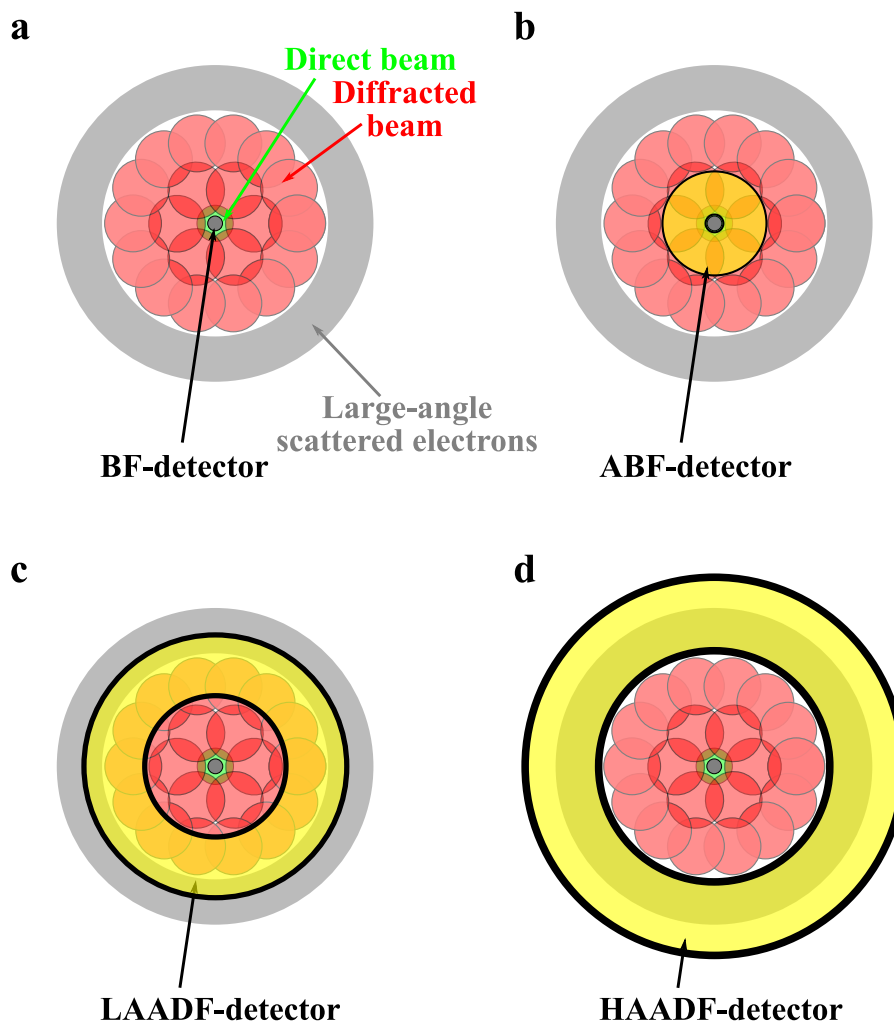


**Figure 3.8: Schematic representation for STEM imaging** **a** The bright-field (BF) detector is placed in the center of the undiffracted, direct cone of the electron beam (green) to form a BF-STEM image. It collects electrons up to an angle of  $\approx 10 \text{ mrad}$ . **b** The Bragg diffracted electron at the vicinity of the direct beam partially overlap with the latter one. An annular bright-field (ABF) detector, whose inner angle is determined by the size of the BF detector, collects these electrons to form an ABF-STEM image. Its outer collection angle is  $\approx \alpha$ , i.e. the collection range of the ABF detector is  $10 - 25 \text{ mrad}$ . **c** The low-angle annular dark-field (LAADF) detector collects a mixture of Bragg diffracted and incoherently scattered electrons, forming a LAADF-STEM image. The collection range here is  $25 - 70 \text{ mrad}$ . **d** The high angle, incoherently scattered electrons are collected by the HAADF detector. Typical collection ranges are  $70 - 200 \text{ mrad}$ .

be noted that the screening effects of the electron cloud reduce the exponent to 1.6 – 1.8 [121].

In comparison to HRTEM, high-resolution HAADF-STEM imaging has the advantage that the image contrast depends on the atomic number  $Z$  and the mass-thickness of the specimen. Therefore heavy elements can be imaged easily. However, since the scattering cross-section has a square dependency on  $Z$ , a weak signal is coming from light elements. The local image intensity for incoherent imaging is the convolution of the intensity distribution of incident electron beam  $|p(\vec{r})|^2$  (probe function) and the projected specimen potential  $V(\vec{r})$

$$I(\vec{r}) = |p(\vec{r})|^2 * |V(\vec{r})|^2 \quad (3.19)$$

The projected potential has peaks associated to the atomic columns. Therefore the HAADF-STEM image also has intensity maxima corresponding to the atomic columns. However, the image contrast is blurred because of the Gaussian intensity profile of the electron probe as shown in Figure 3.9 a with FWHM diameter  $d_t$ . The diameter  $d_t$  of the probe, which determines the resolution in STEM, is determined by at least three factors:

- *the gun brightness*: Assuming that the effective electron source has a Gaussian profile, than its demagnified diameter at FWHM is given by  $d_g = \frac{2}{\pi} \left( \frac{I_p}{\beta} \right)^{1/2} \frac{1}{\alpha}$ ,  $I_p$  the probe current on the specimen and  $\beta$  the gun brightness [121]. This equation also verifies the advantage of a FEG over a thermionic gun. A FEG has a higher brightness and would automatically enhance the resolution.
- *the diffraction limit*: According to the Rayleigh criterion diffraction at the illumination aperture (here C2 aperture) will cause an Airy disk with a diameter  $d_d = 1.22 \frac{\lambda}{\alpha}$  [121].
- *the spherical aberration*: The difference in focal length between paraxial and marginal electron waves the diameter of electron probe is (from Eq. 3.12)  $d_s = 2C_s \alpha^3$ .

The contributions of these three factors are shown in Fig. 3.9 b. For an ideal lens, the probe diameter  $d_t$  can be reduced by increasing the semi-convergence angle. However, in a real lens with geometric aberrations, the probe diameter increases with increasing the convergence angle  $\alpha$ . The optimum value for  $d_t$  is achieved through balancing the different factors. Two points should be highlighted: first, the probe

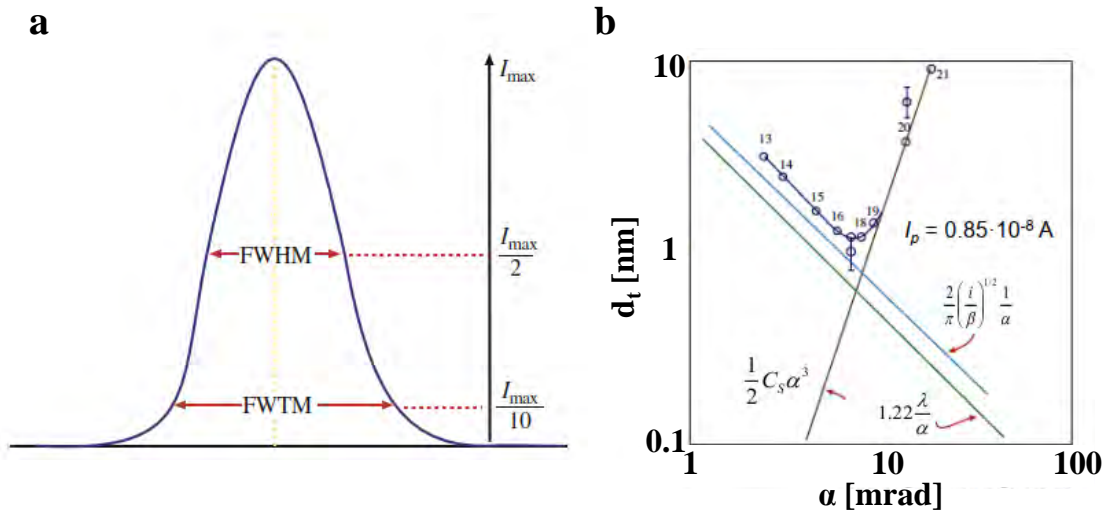


**Figure 3.9: Resolution in STEM.** **a** The intensity distribution of the electron probe can be described as a Gaussian function. The full width half maximum (FWHM) can be used to define the probe diameter  $D_t$ . **b** The probe diameter  $d_t$  as a function of the semi-convergence angle  $\alpha$ . Three factors limit the probe diameter with increasing semi angle. The spherical aberration (red curve), the diffraction limit (green curve) and the gun brightness (blue curve) are drawn at a probe current of  $I_p = 0.85 \cdot 10^{-8} \text{ A}$ . Images taken from [120].

diameter was defined here as the FWHM of the Gaussian function. This definition is not distinct. Second, the probe intensity distribution is not an ideal Gaussian function and misalignments and higher order aberrations (especially astigmatism) would result in a deviation from the Gaussian profile [121]. To improve the resolution, it is necessary to identify, measure and correct the aberrations of the probe-forming lens.

### 3.3.4 Aberration correction

The most common technique to identify the aberrations is the “Zemlin tableau” approach [130]. In TEM the approach uses the power spectra (fast Fourier transform FFT) of a high magnified under-focused image of a thin amorphous carbon specimen. The aberrations are measured by changing the azimuth and tilt angle of the incident electron beam. It is important to have an under-focused HRTEM image to see the Thon rings. These rings are the effect of the modulation of the PCTF, where bright rings correspond to contrast transfer and dark rings to no contrast transfer. Therefore the PCTF can be considered as a complex band-pass filter. From the shape and symmetry of the FFT the geometric aberrations (astigmatism, spherical aberration, star aberration, coma) are detected and corrected, accordingly. Hereby,

the distortions of the FFT pattern depends on the magnitude of corresponding aberration. After correction, the power spectra will show symmetric, round Thon rings at very high spatial frequency. A proper objective aperture can be used to exclude these higher spatial frequencies.

In STEM the situation is a bit different. To determine the aberration, the probe function has to be extracted from an image at Gaussian focus. As a specimen gold nanoparticles deposited on a supporting film are used due to their high contrast in HAADF-STEM. By deconvolution of an under and overfocused image the probe shape is calculated for different azimuth and tilt angles. Like in TEM, the modulated part of the PCTF can be cut-off using a proper condenser aperture size. To correct the aberrations, Scherzer [131] proposed to use non-rotational symmetric lenses. Commercial correctors consist of several multipoles (quadrupole, hexapole, octupole, dodecapole) and transfer lenses. Because of the higher order aberration correction it is possible to use a larger semi-convergence angle to reach sub-Å resolution. Besides the spatial resolution improvement, the chemical resolution is also enhanced, because of the higher current of the probe. This is important, when operating in high-resolution STEM (HRSTEM) mode, where it is useful to combine imaging with spectroscopic techniques. Detecting the EDS as well as the EELS signal at each probe position would give chemical and structural information of the specimen at the atomic scale. We will see in the following section the differences between STEM-EDS and SEM-EDS [114, 120–122, 132].

### 3.3.5 STEM-EDS vs. SEM-EDS

The EDS signal is the result of inelastic scattering processes. The main advantage of SEM-EDS (see 3.2.3) is to acquire relatively easy an elemental map of a large area ( $\mu\text{m}^2 - \text{mm}^2$ ) of the bulk sample. However, we have also seen some disadvantages, which can be summarized as:

1. **Low signal-to noise ratio:** The origin of the background signal is the Bremsstrahlung, i.e. the deceleration of the incident electron beam. This continuous signal gets larger for thicker samples reducing the sensitivity to quantify low concentrations. The signal  $I_t$  has to be three times larger than the standard deviation of the background signal. For Gaussian distribution this is  $I_t \geq 3I_t^{\text{background}}$ .
2. **Overvoltage:** The overvoltage is the ratio between the energy of the incident

electron beam  $E_0$  and the ionization energy of a an element  $E_i$ . For accurate quantification using the K-edge, it is important to use a overvoltage of  $> 3$ , i.e. the incident beam should have an energy three times larger than the K-edge of the element.

3. **Low spatial resolution:** Using bulk samples, the absorption and fluorescence yield play a major role in the detection process. The number of measured X-ray photons is not the same as the number of generated X-ray photons. These factors will also induce artifacts during acquisition. Additionally, the interaction volume depends on the acceleration voltage of the incident beam and the thickness of the sample. Thicker samples or a higher acceleration voltage decrease the spatial resolution due to the increased interaction volume. In SEM, the typical resolution is  $\approx 1 \mu m$ .
4. **Surface sensitivity:** For accurate SEM-EDS the surface of the sample has to be flat to avoid absorption.

In order to solve this issues it is beneficial to use a higher acceleration voltage and - to keep the interaction volume small - a thin foil. Both requirements are achieved in STEM-EDS. Typical specimen thicknesses of  $\leq 100 nm$  and acceleration voltages of several hundred  $kV$  improve the spatial resolution, the sensitivity and quantification, because of a decreased interaction volume, nearly no absorption and the overvoltage is much larger than 3. The spatial resolution in STEM-EDS can reach atomic scale. However, one disadvantage of STEM-EDS over SEM-EDS is sample drift. Drift can reduce the spatial resolution. To avoid the influence of the drift, the acquisition time has to be kept minimal. However, a low acquisition time would also mean a low count rate. Therefore, to keep a high count rate but at low acquisition time, the solid angle of the EDS detector has to be increased and/ or the acceleration voltage has to be reduced. The latter one would increase the ionization cross-section and in a aberration corrected STEM without loss of spatial resolution. Again, electron channeling can also induce artifacts and accurate quantification becomes challenging [113, 120, 122].

## 3.4 Electron energy loss spectroscopy

Transmitted electrons, which have undergone an inelastic scattering process lose part of their kinetic energy. This energy loss gives information about atomic composition,



the valence/conduction band and the electronic structure [114]. Figure 3.10 shows a typical EEL spectrum of the bcc-Fe bicrystal. The spectrum can be divided into three parts [114]:

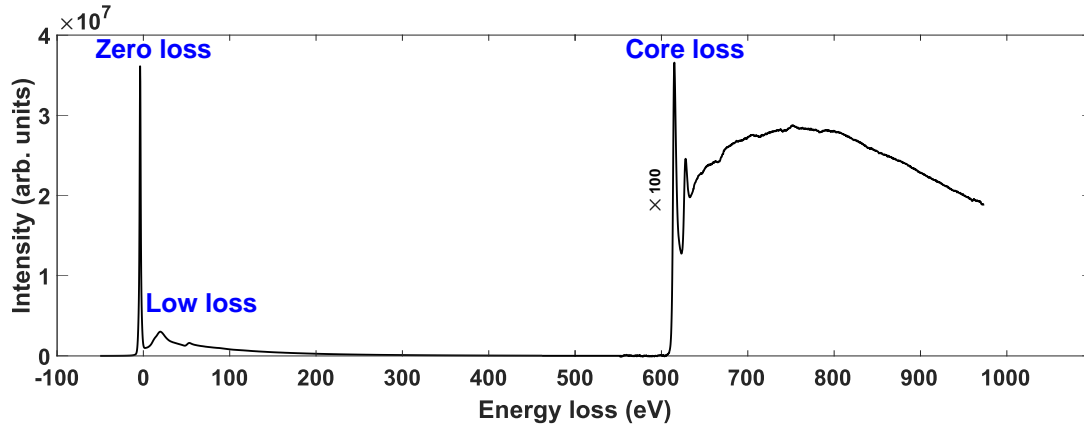


Figure 3.10: A typical EEL spectrum of the bcc-Fe sample acquired in this work.

- Zero loss: These electrons lost  $\leq 1\text{ eV}$  energy. Therefore, they are considered as quasi-elastically scattered electrons. The FWHM of the zero loss peak is related to the energy spread of the TEM.
- Low loss: When the incident electrons interact with the outer shell electrons of the atoms via Coulomb forces, they excite plasmons and interband transitions. The low loss region ranges from  $1\text{ eV}$  to  $50\text{ eV}$ .
- Core loss: When the electron inelastically interacts with inner shell electrons of the atoms, they will cause an ionization process. The ionization energy is element specific. As shown in Fig. 3.10 the Fe L ionization edge occurs at an electron energy loss of  $708\text{ eV}$ .

The element-specific ionization edges in the core loss region can be used to detect and quantify the concentration of the elements in the sample. Moreover, the energy loss near-edge structure (ELNES) can be used to get information about the electronic structure and the local coordination [114]. In this work, ELNES was used to identify the oxide phase.

To acquire an EEL spectrum, the transmitted electrons are passed through a magnetic prism, which deflects the electrons by  $90^\circ$  and focused them onto the dispersion plane. The magnitude of the deflection depends on the velocity or kinetic energy

of the electrons, i.e. the electrons are dispersed according to their energy. A spectrum is formed in the dispersion plane, which can be recorded with a CCD/CMOS detector [120].

## 3.5 Atom probe tomography

The chemical analysis of GBs, especially the segregation of tracer elements and very light elements, requires a very high level of sensitivity. As shown before, EDS analysis has its limitations regarding the atomic number  $Z$  and the quantification errors, which originate from specimen thickness or from dynamical scattering. On the other hand, atom probe tomography (APT) shows a very high chemical sensitivity down to ppm range (depending on the element). Spatially resolved, chemically quantitative analyzes can be carried out with the tomographic atom probe (TAP) with a resolution of up to  $0.2\text{ nm}$  in the depth and  $0.5\text{ nm}$  in the lateral direction. The APT is the further development of the field ion microscope with a position-sensitive time-of-flight (TOF) detector. The working principle of an APT is shown in Figure 3.11.

APT examinations require a needle-shaped tip from a conductive material with a radius of curvature  $R \approx 20 - 100\text{ nm}$ . The tip is cooled to a temperature  $\leq 100\text{ K}$  in a ultra-high vacuum chamber. A continuously adjustable, positive direct voltage up to approx.  $U_0 = 20\text{ kV}$  is applied to the sample. This voltage is just so high to reduce the work function, but insufficient to evaporate atoms from the tip. Opposed to the sample is a counter electrode. It has the shape of a hollow cone with a cut off upper part, which is moved very close ( $\mu\text{m}$ ) to the examined tip. Further, due to the short distance between needle and electrode a very strong electric field can be applied. An APT can be run in two modes, depending on how to trigger the field evaporation: voltage mode and laser mode. In the former one, high voltage pulses between sample and electrode are superimposed to the base voltage  $U_0$ . The pulses cause a controlled field evaporation of individual atoms from the tip surface. In the latter case, a pulsed laser with pulse rates in pico- to femtoseconds and a wavelength in the ultraviolet range is used to extract the atoms from the sample surface. Here, it is important that the laser is focused onto the tip apex. The use of a laser makes it possible to study also non-conductive materials with an APT. Once the evaporated atoms pass through the electrode they hit a position-sensitive detector, where the position of impact and  $(x,y)$  and the corresponding TOF is detected. The

z-coordinate is determined from the evaporation sequence. It is assumed that atoms that later arrive at the detector were located deeper in the material. To measure the TOF, with each pulse (voltage or laser), a clock channel is started, which is stopped again when the ion hits the detector. Taking into account the energy conservation law, the specific mass, i.e. the ratio of mass to charge  $m/n$ , can be determined from the TOF  $t$

$$\frac{m}{n} = 2eU \frac{t^2}{L^2} \quad (3.20)$$

with  $m$  the mass of the ion,  $n$  is its charge state,  $e$  the charge of an electron,  $U$  the applied voltage and  $L$  the flight distance of the ion. From this equation the corresponding element can be identified using a mass-spectrometer. Figure 3.11 b) shows an example for a mass spectrum. It is noticeable that the measured ions are multiply charged. The prevailing explanation is that during the flight electrons from the singly ionized atom tunnel back into the specimen. This tunnel effect is related to the strength of the electric field.

Regarding GB segregation, APT is not only able to detect all elements and their 3D-distribution in the tip albeit their atomic number, it also offers an accurate estimation of the Gibbsian interfacial excess (IE)  $\Gamma$ . It is the number of solute atoms per unit area of an interface. The IE is calculated by counting the number of solute atoms with respect to the total number of atoms in the sample. In a perfect single crystal this two number would have a linear relationship  $N_{solute} = aN_{total}$ , with  $a$  the slope. However, when enrichment of the solute atoms, e.g. at a GB, occurs, there will be a change of  $a$  in the region of the GB. Knowing the IE is important as it is directly related to the interfacial energy, where a change of the GB energy can affect its properties such as cohesive strength.

Throughout the work, the APT was run in laser mode. Though, it is necessary to mention some problems that can occur during the experiments. A perfect 3D reconstruction of the tip is possible, if the trajectories of the ions are known. For that a uniform electric field is necessary. However, when the shape of the apex is not symmetric, this can lead to errors in the reconstruction. Since the laser beam is coming from a particular side, a non-uniform heating will appear at the laser side. This means that this side has a stronger field evaporation and more ions are field evaporated from there. Further, laser induced diffusion can create clustering of certain elements. This effect depends on the diffusivity and is element type specific. Therefore, it is important to tune the parameters (temperature of sample, pulse, power of laser pulses etc.) to avoid or minimize this problems. Deeper information

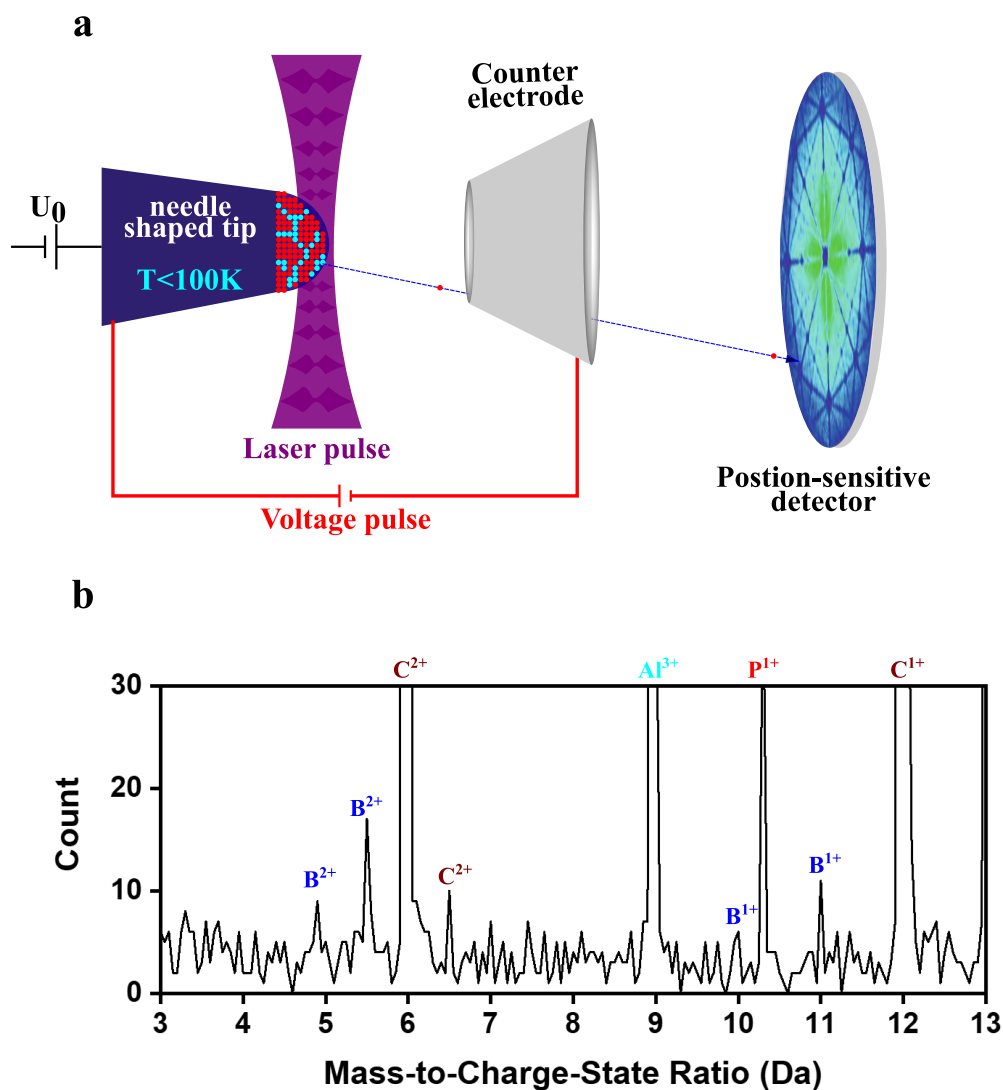


**Figure 3.11: Schematic representation of an APT** **a** The geometry of a typical APT. A needle-shaped sample is connected to a constant voltage  $U_0$  and placed in front of a local electrode. Ions are field evaporated either by an applied pulse voltage or a laser. In voltage mode the electrode is negatively biased, while in laser mode it is grounded. Field evaporated ions reach after some time the position-sensitive detector. This time of flight is element specific. **b** The mass spectrum acquired during an APT experiment shows detection of carbon C and boron B ions in bcc-Fe.

can be found in [32].



## 4 Experimental details

This chapter gives insight into specific parameters used in next chapter 5. Detailed information are given on sample preparation as well as the experimental conditions in SEM, (S)TEM and APT. It should be mentioned that the APT experiments and data analysis were done by Dr. Xuayang Zhou at the Max-Planck-Institut für Eisenforschung. All DFT and calculations were performed by Dr. Daniel Scheiber and Prof. Dr. Lorenz Romaner from Materials Center Leoben GmbH in Austria.

### 4.1 Bicrystal growth

For the growth of the bicrystals polycrystalline material made of electrolytic Fe with 2 wt.% ( $\approx 4$  at.%) Al in solid solution was used. The purity of the iron was 99.999% and the low concentration of Al ensures the  $\alpha$ - phase from the melting point down to room temperature. Two single crystal seed with this composition were aligned along the common [001]-direction. This was achieved by Laue diffraction with a coherent laser beam. Once the single crystals seeds were aligned, they are placed on the polycrystal. Afterwards, each single crystal is rotated by  $\approx 19^\circ$  along the [001]-axis. This results in a total misorientation of  $\Theta \approx 38^\circ$ . In this way a symmetric CSL  $\Sigma 5[001]$  GB can be grown. The single crystals are glued with the polycrystal and placed into a alumina crucible. In order to maintain the shape, the crucible is filled with alumina powder. The raw material with the seed crystals are placed into the Bridgman oven chamber, which was flushed several times with Ar. The position of the heating coils are placed such that the liquidus zone ranges from about 1/3 of the seeds up to the whole polycrystal. The temperature is increased to  $1600^\circ\text{C}$  in high vacuum ( $p \approx 10^{-6}$  mbar). This temperature is kept for 0.5 hour to ensure that the whole material is liquefied. The heating coils are moved upwards (along the polycrystal) with a speed of 2 mm/hour and the molten polycrystal resolidifies adapting the misorientation given by the single crystal seeds. After the growth process the oven is turned off and the temperature of the bicrystal will decrease to

## 4 Experimental details

room temperature after  $\approx 24$  hours. The final cylindrical bicrystal has a diameter of 20 mm and a length of 100 mm. A 2 mm thick slice was cut by spark erosion to perform wet chemical analysis using the inductively coupled plasma atomic emission spectroscopy. The measured concentrations are summarized in Table 4.1. Besides

Element	Al	C	B	O	P	S	Si
Content (at.%)	4	0.05	0.001	0.22	< 0.003	0.001	0.005

**Table 4.1: Wet chemical analysis of the Fe bicrystal showing the bulk concentrations.**

the 4 at.% Al to stabilize the bcc phase [40], the wet chemical analysis of the bulk sample revealed a content of 0.001 at.% B and 0.05 at.% C.

## 4.2 Diffusion couple

For the experiments on the segregation of Zn, the bicrystal was cut into a  $15 \times 11 \times 1$  mm rectangle with the GB in the center (see Fig. 4.1a). All sides of the sample were mechanically grinded with SiC papers and chemically polished using a solution of 6% HF, 14% H<sub>2</sub>O and 80% H<sub>2</sub>O<sub>2</sub>. Immediately afterwards, the sample was immersed into a 99.999% Zn bath for 300 s. The temperature of the Zn bath was kept at 467°C as shown in Fig. 4.1b. After the coating, the sample was mechanically grinded to remove the Zn from the large (001) surfaces as well as the large edges. Zn was left only at the short edges parallel to the GB plane normal. Finally, the sample was encapsulated in a quartz tube under vacuum ( $p \approx 10^{-3} - 10^{-4}$  mbar) and annealed at 800°C for 80 hours.

For the segregation studies of Mn, the top (001) surface of a 2 mm thick bicrystal was mechanically grinded and polished until a mirror-like surface was achieved. The polishing was done with diamond suspensions with particle sizes of 3  $\mu$ m and 1  $\mu$ m and finally with an oxide polishing suspension with particle size of 50 nm. Electron beam deposition of 250 nm Mn onto the the sample was done in a ultra high vacuum chamber at room temperature. The partial pressure pressure during deposition was set to  $2.3 \cdot 10^{-7}$  mbar and the evaporation rate was 5 Å/s. The deposition time was 15 minutes. After the deposition the sample was annealed under a high vacuum of  $p \approx 10^{-5}$  mbar at 700°C for 72 hours.



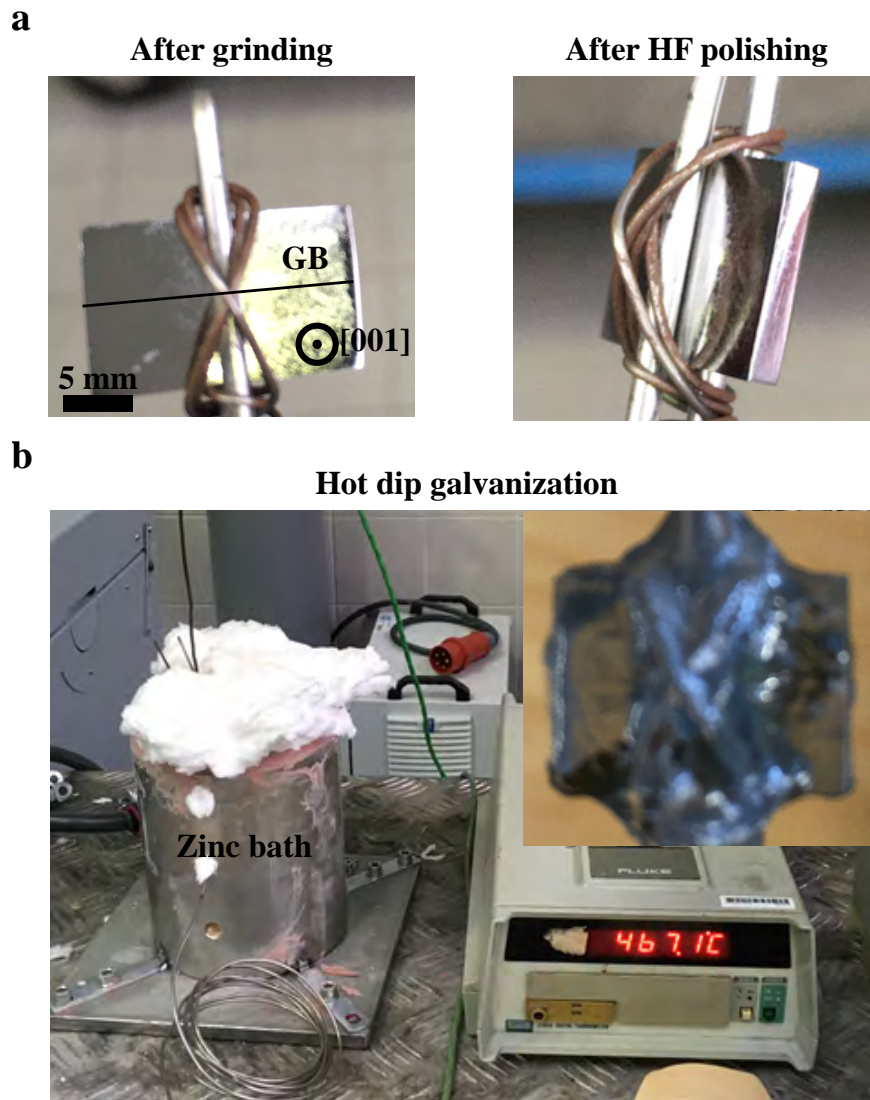


**Figure 4.1: Zn diffusion into the Fe bicrystal.** **a** Mechanically grinding the bicrystal up to 1200 SiC grit paper and subsequent chemical HF polishing. The GB is indicated by a black line.. **b** The polished sample was immersed into a liquid Zn bath. The temperature of the bath was measured with a thermocouple to be  $467^{\circ}\text{C}$ . The inset shows the bicrystal completely coated with Zn.

### 4.3 Sample preparation and characterization in SEM

After mechanically grinding and polishing the samples were etched for 5 s using a solution of 10%  $\text{HNO}_3$  and 90% ethanol to visualize the GB. SEM-EBSD and EDS experiments were done in ThermoFisher Scios 2 dual beam SEM/FIB equipped with the EDAX Velocity Plus EBSD camera and the EDAX Octane Elite Super EDS detector. The EBSD camera is a high-speed CMOS detector with up to 3000

## 4 Experimental details

indexed points per second [133]. The EDS detector is a SDD detector with a  $\text{Si}_3\text{N}_4$  window, which offers a better sensitivity to light elements and low-kV microanalysis as a polymer window [134].

For SEM-EBSD acquisition, the acceleration voltage of the SEM was set to 20 kV with a current of 13 nA. The sample was tilt to  $70^\circ$  and had a working distance of 14 mm. The step size of electron beam was 50 nm.

For SEM-EDS experiments the acceleration voltage was set to 30 kV and a current of 13 nA was used to get a dead time of 20 – 25% for the detector. The stage was at  $0^\circ$  tilt and the working distance was 7 mm.

### 4.4 Sample preparation for TEM and APT

Plane-view TEM specimens from the pre-characterized GB (via EBSD and EDS) were prepared using the ThermoFisher Scios 2 and the Helios 600(i) dual beam SEM/FIB. After liftout, the chunk was thinned with the  $\text{Ga}^*$ -FIB starting with a current of 100 pA at 30 kV until a thickness of  $\approx 800$  nm was reached. The acceleration voltage was reduced to 16 kV and the milling was continued until a thickness of  $\approx 250$  nm was reached. The the acceleration voltage was further reduced to 5 kV and a cuurent of 48 pA was chosen to mill the sample down to  $\approx 100$  nm. Final low-kV milling was done at 2 kV and 27 pA so that the final sample thickness was below 50 nm (confirmed later by STEM-EELS).

APT specimen (cross-sectional and plane-view) were prepared by mounting  $2 \times 2$  mm large chunks onto the tip of a Mo-grid. The GB is either placed horizontally or vertically in the chunk. For milling a circular pattern was placed onto the chunk such that the final shape of the specimen is like a needle. Starting with 30 kV and 100 pA until a diameter of 1  $\mu\text{m}$  was reached, the current was reduced to 500 pA. The milling is contuend until a diameter of 100 nm is reached. Final polishing was done at 5 kV and 48 pA so that the GB is about 50 – 100 nm away from the apex.

### 4.5 (S)TEM and APT characterization

STEM images were conducted using a  $C_s$  probe-corrected FEI Titan Themis 60–300 operated at 300 kV. The semiconvergence angle was chosen to be 17 mrad and a camera length of 100 mm resulted in a semicollection angle of 0 to 7 mrad for the BF-detector, 10 to 16 mrad for ABF-detector, 18 to 73 mrad for the ADF-detector

and 78 to 200 *mrad* for the HAADF-detector. To prevent beam damage the probe current was set to 80 *pA*. Typically, STEM images were acquired in a series of 30 frames each recorded with a dwell time of 5  $\mu$ s. These frames were stacked by means of cross correlation using the FEI Velox 2.8 software.

For STEM-EDS the acceleration voltage was reduced to 120 *kV* to improve the STEM-EDS map resolution by reducing the measurement time. The X-rays were collected with the ChemiSTEM SuperX detector.

STEM-EELS experiments were usually done to determine the thickness of the specimens. For that the camera length was increased to 310 *mm* to achieve a semi-convergence angle of 5.4 *mrad*. A post-column Gatan Quantum ERS/966P spectrometer was used with a dispersion of 0.25 *eV/channel* and a FWHM of the zero loss peak of 0.9 *eV*. Typically thicknesses of  $\approx 30 - 40$  *nm* were measured.

High-resolution TEM imaging was performed in a  $C_s$  image-corrected FEI Titan Themis 60 – 300 operating at 300 *kV* under negative  $C_s$  condition (with  $C_s \approx -10$  to  $-15$   $\mu$ m). For that the CETA high-speed 16M CMOS detector was used.

APT experiments were done by Dr. Xuyang Zhou using the CAMECA LEAP 5000XR as well as LEAP 5000XS in laser-pulsed mode. The pulse rate was 200 *kHz* with an energy of 30 *pJ* and the temperature of the specimen was 40 *K*. The laser energy was increased for the Fe-Zn experiments, since at lower laser energies the APT tip was fracturing.

## 4.6 Atomistic simulations

First principles DFT calculations were performed by Dr. Daniel Scheiber and Prof. Dr. Lorenz Romaner from Materials Center Leoben GmbH using the Vienna Ab-initio Simulation package (VASP), which employ projector augmented wave functions [135–138]. The PBE exchange-correlation functional [139, 140] was chosen as it has been shown that it is suited best to describe Fe [141]. The k-point density for all involved simulation cells was set as close as possible to 40 *k*-points/Å and the energy cutoff to 400 *eV*. As a result, the lattice parameter of Fe was determined as 2.8386 Å, which is in accordance with DFT literature [142, 143]. The simulation cells for GBs are build up of two slabs that are misoriented to each other so that they form a GB where they join. On the other side, the slabs are separated by a vacuum layer of at least 8 Å that proved to be large enough to prevent interactions of the two surfaces. With this setup, the simulation cell is constructed along the

#### 4 Experimental details

lattice vectors  $[001] \times [1-31] \times [310]$  with  $5.677 \times 4.708 \times 44.883 \text{ \AA}^3$  and contains 78 Fe atoms. For ionic relaxations a convergence criterion of  $0.01 \text{ eV/\AA}$  is employed.

Segregation energies are computed using

$$E_{seg,i}^x = \left( E_{gb,i}^x - E_{gb} \right) - \left( E_{bulk}^x - E_{bulk} \right) + \delta_{i-s} E_{Fe}, \quad (4.1)$$

with  $E_{gb}$  being the total energy of a GB without solute  $x$  while  $E_{gb,i}^x$  denotes the total energy of the same cell but with the solute  $x$  at GB site  $i$ . For the reference of the solute in the bulk, the difference is computed between a bulk cell of 128 atoms without solute  $x$  and with solute  $x$ ,  $E_{bulk}$  and  $E_{bulk}^x$ , respectively. For considering the change of interstitial B in the bulk to a substitutional site at the GB,  $\delta_{i-s} = 1$  and  $E_{Fe}$  corresponds to the total energy of a single Fe atom in its bulk structure [144]. Segregation energies are connected to the solute enrichment at GBs via the White-Coghlan segregation isotherm [27] extended to multiple solutes, see e.g. Ref. [145].

The work of separation was computed by separating the GB at possible GB planes by at least  $8 \text{ \AA}$  and computing the difference of the total energies for separated and joined GB slabs in the simulation cell [146, 147].

The simulated DFT cells of the GB structure were used as input files for STEM simulations using the Prismatic Software package [148]. The multi-slice simulation was done for a  $\approx 40 \text{ nm}$  thick cell choosing a slice thickness of  $1.7 \text{ \AA}$ . The pixel size was set to  $0.01 \text{ \AA}$  resulting in a maximum semi-collecion angle of  $492.187 \text{ mrad}$ . The semi-convergence angle was chosen to be  $17 \text{ mrad}$  and the lens aberrations (defocus and spherical aberration) were set to  $0 \text{ \AA}$ . Finally, the number of frozen phonons was at 8.

## **5 Results and Discussion**

## 5.1 Aluminum depletion induced by co-segregation of carbon and boron in a bcc-iron grain boundary

This section is based on:

A. Ahmadian, D. Scheiber, X. Zhou, B.Gault, L. Romaner, C. H. Liebscher and G. Dehm “Aluminum depletion induced by co-segregation of carbon and boron in a bcc-iron grain boundary”, *Nature Communications* 12, 6008 (2021)

## 5.2 Introduction

Segregation of solutes and impurity atoms to grain boundaries (GBs) have been studied extensively in the last decades because of their strong influence on the macroscopic physical and mechanical properties of materials [14, 21, 22, 28, 29, 149–153]. Typically, GB segregation is studied in binary alloys serving as model systems to discern segregation tendencies of individual solutes [14, 149, 152, 153]. However, technologically relevant alloy systems adopt a complex composition, which is tailored to maximize their mechanical properties. The interplay of different solutes in ternary or higher order systems on grain boundary segregation is far less understood [65, 154]. Xing et al. [154] developed a simple thermodynamic model to capture the competing mechanisms in ternary alloys that decrease, increase or do not affect GB segregation. However, this model has limited applicability when non-metallic elements are involved, which play a critical role in understanding embrittlement effects in iron-based alloys or steels [66, 151]. Furthermore, co-segregation effects have also been observed to play an important role in other material systems such as ceramic and oxide materials [155, 156]. Wang et al. [156] observed complex co-segregation patterns of Ca and Ti at MgO  $\Sigma 5(310)[001]$  GBs by atomic resolution imaging, which strongly affect the electronic structure of the GB and stabilize it.

Grain boundary segregation in iron (Fe) is often characterized by Auger electron spectroscopy (AES) providing excellent chemical sensitivity, but limited spatial resolution leaving the structure of the GB elusive. However, it could be shown that

sulphur (S) and phosphorous (P) are segregating to GBs [157, 158] in  $\alpha$ -Fe promoting embrittlement of the material. To prevent this detrimental tendency, carbon (C) or boron (B) can be introduced, which hinder the diffusion of S and P to GBs and therefore enhance their cohesive strength [15, 159, 160].

The isolated role of B on increasing GB cohesion has long been anticipated in a range of material systems [16, 160–165] and it has been shown that the addition of small amounts of B partially suppresses intergranular fracture in brittle intermetallic FeAl alloys [21, 22, 166]. It is generally also assumed that C acts as a GB cohesion enhancer and recent ab-initio calculations found that the theoretical fracture strength of  $\Sigma 5$  tilt GBs increases with increasing C excess concentration [19, 20, 167].

Aluminum (Al) is an important alloying element in Fe and especially light weight steels, where a reduction in density on the order of 7.5% can be achieved by additions of up to 7 wt.% Al (16 at.%) [168]. Hence, it is of great scientific and technological interest, but studies exploring the effect of Al on GB properties are rare [169, 170]. Yuasa et al. [169] concluded from density functional theory (DFT) calculations that Al grain boundary segregation will increase the GB energy and weaken the boundary strength due to a change from metallic to covalent-like bonding. However, Geng et al. [170] showed a slight decrease in GB energy by Al addition through first-principal calculations, which is also in agreement with the Rice-Wang thermodynamic model [171]. It should be noted that only binary Fe-Al systems were considered in the previously mentioned studies and insights into the impact of co-segregation effects are missing. For example, Rellick et al. [172] concluded from fracture tests upon quenching that small quantities of Al would hinder the segregation of residual oxygen (O) to GBs, which impedes intergranular fracture. But the low C content could also be responsible for mitigating embrittlement and the role of Al on GB properties remains elusive, since the GB structure and composition could not be determined. Therefore, it is of great interest to investigate GB segregation of Al in Fe and to explore the impact of prominent impurity elements such as C and B on segregation thermodynamics since all three elements are common alloying elements in Fe and high performance steel.

Deciphering co-segregation phenomena requires a complete understanding of the atomic grain boundary structure and composition as well as description of the interaction between impurities [10, 66]. The correlation of atom probe tomography (APT) and transmission electron microscopy (TEM) has paved the way to obtain

insights into the segregation behavior of solutes even in GBs of complex alloys [173]. However, the underlying atomistic effects and the interplay of elements on the grain boundary segregation behavior are often uncharted.

The discrete atomic GB structure and the presence of defects at the GB are additional factors impacting the segregation behavior. It is known that C and B tend to segregate to sites of high stress fields such as dislocation cores [174]. Therefore it is indispensable to resolve the GB structure and composition at atomic resolution to relate the underlying segregation mechanisms by ab-initio calculations. For example, Medlin et al. [175] investigated an asymmetric  $\Sigma 5$  GB in pure Fe using scanning transmission electron microscopy (STEM). They found that the GB adopts a complex topography by dissociating into nanofacets consisting of (210) and (310) facets, which are separated by GB facet junctions. However, connecting such complex GB structure and the segregation of minor impurities like S, P, C and B, which are even relevant in pure Fe, is challenging by STEM alone. Besides using AES to study GB segregation in ferritic Fe and steel [14, 30, 160], APT [152, 153] is capable of providing 3D compositional information with high elemental sensitivity. Aberrations arising from the field evaporation process [176, 177] limit the spatial resolution of APT effectively to approx. 0.5nm [178] for precipitates. For grain boundary structure and other crystalline defects, the spatial resolution is expected to be in a similar range or better [179]. Ultimately, the combination of atomic resolution STEM and APT provides structural as well as compositional information of the GB with the highest spatial and elemental resolution [180–185].

In the present work, we correlate atomic resolution STEM, energy-dispersive X-ray spectroscopy (EDS) and APT measurements on a  $\Sigma 5(310)[001]$  tilt GB in  $\alpha$ -Fe-4 at.%Al to resolve the atomic GB structure and its local composition. The GB predominantly adopts a kite-type structural unit and the presence of GB defects is indicated. The Al concentration at the GB is observed to decrease, whereas the impurities B and C are clearly segregating. Complementary first-principles based DFT calculations are employed to elucidate the segregation tendencies of Al, B and C and shed light onto the impact of solute interactions on the co-segregation behavior. A kinetic model is employed to investigate the temperature and time dependent segregation of solutes for similar conditions as in the experiment.



## 5.3 Results

### Atomic GB structure

A low-magnification high angle annular dark-field (HAADF)-STEM image of the  $\Sigma 5(310)$  GB observed in  $[001]$  direction is shown in Fig. 5.1a. The local contrast in Fig. 5.1a is mainly attributed to changes in sample thickness and atomic mass. At a constant sample thickness the intensity is proportional to  $Z^{1.5-2}$ , with  $Z$  being the atomic number [121]. At this length scale the GB appears straight and the formation of GB defects, such as steps or facets can not be resolved. The dark contrast of the GB may be attributed to GB grooving, a lower atomic density or lattice strain, causing dechannelling of the electron beam. Figure 5.1b shows the simultaneously acquired low-angle ADF-STEM image revealing bright contrast along the GB, which may be attributed to the accumulation of strain fields at the GB [181]. The red square in Fig. 5.1 a indicates a segment of the boundary, which was imaged at atomic resolution with a local sample thickness of about 40 nm as determined by electron energy loss spectroscopy (EELS) measurements.

A representative atomic resolution HAADF-STEM image of the GB (Fig. 5.3)) shows the projected structural units of the  $\Sigma 5(310)[001]$  GB viewed along the  $[001]$  direction. The blue and red squares in the corresponding fast Fourier transform (FFT) shown in the inset of Fig. 5.3a highlight the  $\langle 110 \rangle$  type reflections of the lower and upper grains, respectively. Both grains are misoriented by  $\sim 38^\circ$  around the common  $[001]$  tilt axis. This observation is in good agreement with the EBSD analysis presented in Fig. 5.2. A Butterworth Fourier-filter was applied to the image to remove low-frequency noise and highlight the atom columns at the boundary as shown in Fig. 5.3b. A magnified view reveals the kite-type structural units of the  $\Sigma 5(310)[001]$  GB, which is consistent with the predicted structure of a pure bcc-Fe GB [175, 186]. However, it should be noted, that a weak signal is apparent in the open regions of the kites (indicated by yellow arrows). In addition, the kite-structure of the GB is distorted on the right-hand side in Fig.5.3b (indicated by a red dotted rectangle). These features and their origins will be discussed later.

Besides kite-type structural units, defects such as steps (see Fig. 5.4) or facets are present in other locations of the GB, which are introduced due to a local change in GB inclination. Figure 5.5a shows a HAADF-STEM image of a GB segment intersecting an  $\text{Al}_2\text{S}_3$  precipitate. The local GB curvature is increased in close vicinity of the precipitate as indicated by a black rectangle in Figure 5.5a. Atomic

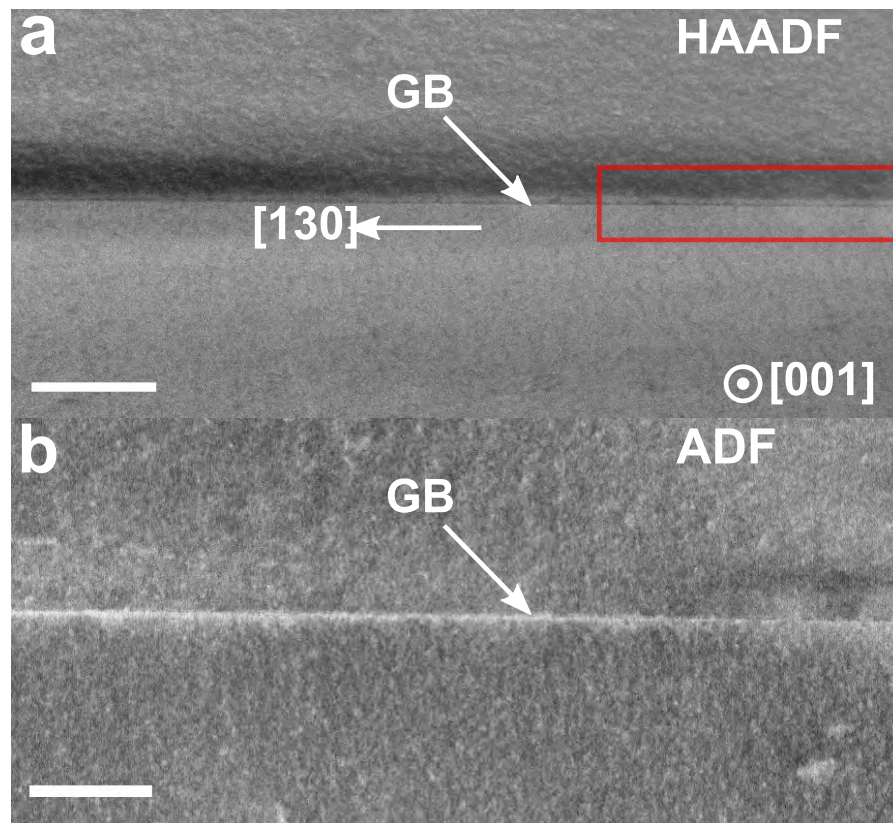


**Figure 5.1: Overview images of the  $\Sigma 5(310)[001]$  GB.** **a** HAADF-STEM image and **b** corresponding low-angle ADF-STEM image showing bright contrast at the GB core indicating an accumulation of strain fields at the GB. The red rectangle in **a** indicates regions, which were imaged at atomic resolution. The scale bar is 100 nm.

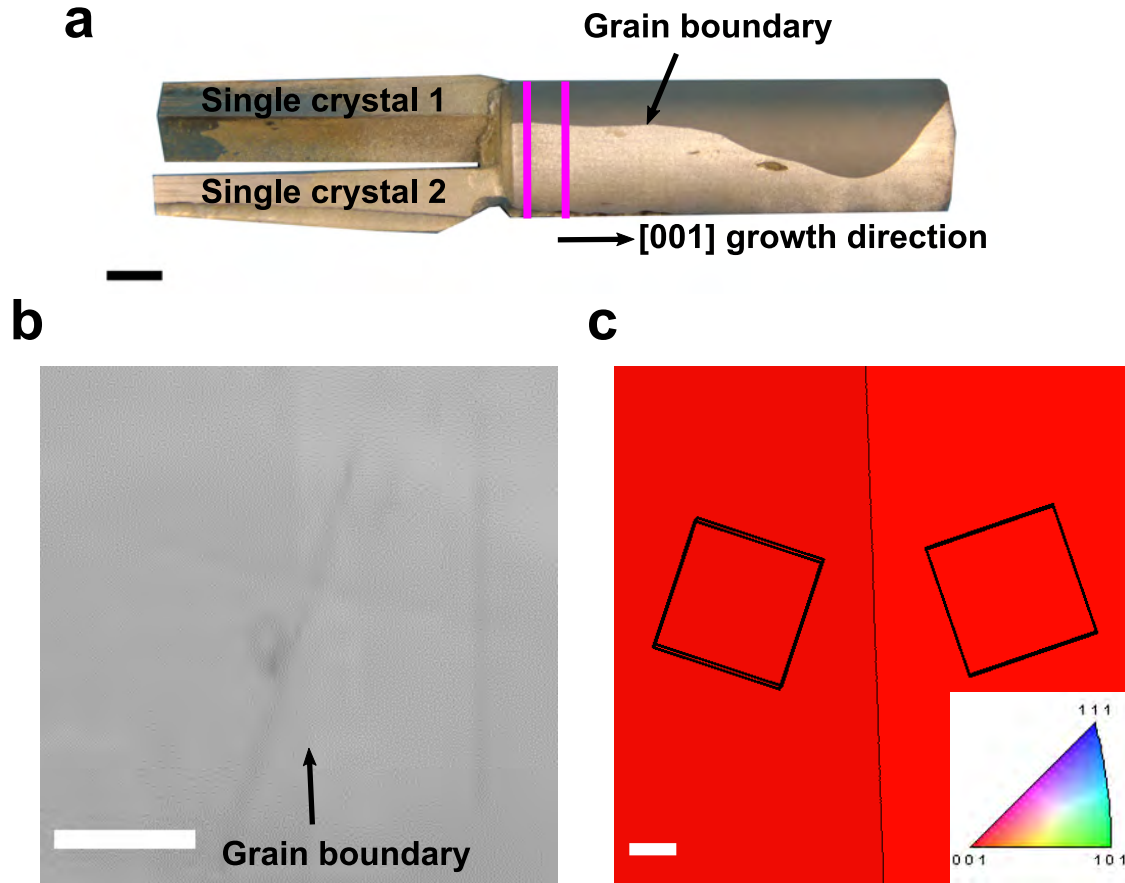


**Figure 5.2: Global characterization of the GB.** **a** Side view image of the bicrystal including the single crystal ingots to fabricate it. The growth direction is  $[001]$ . Samples were investigated from the initial part (labelled by magenta lines), where the GB started to grow. **b** SEM image of the bicrystal top surface (along the  $[001]$  tilt axis) after final polishing. The GB is indicated by the black arrow. The GB runs straight and shows no steps or curvatures at the micron scale. **c** EBSD scan of the bicrystal shows a clear  $[001]$  texture of both grains. In each grain the orientation of the unit cells is shown by the black rectangles indicating a symmetric misorientation of  $37.5^\circ$ . Further analysis of the polefigure the GB plane was obtained to be  $(310)$  into both grains. The Scale bar in **a** is  $10\text{ mm}$  in **b**  $5\ \mu\text{m}$  and in **c**  $1\ \mu\text{m}$ .

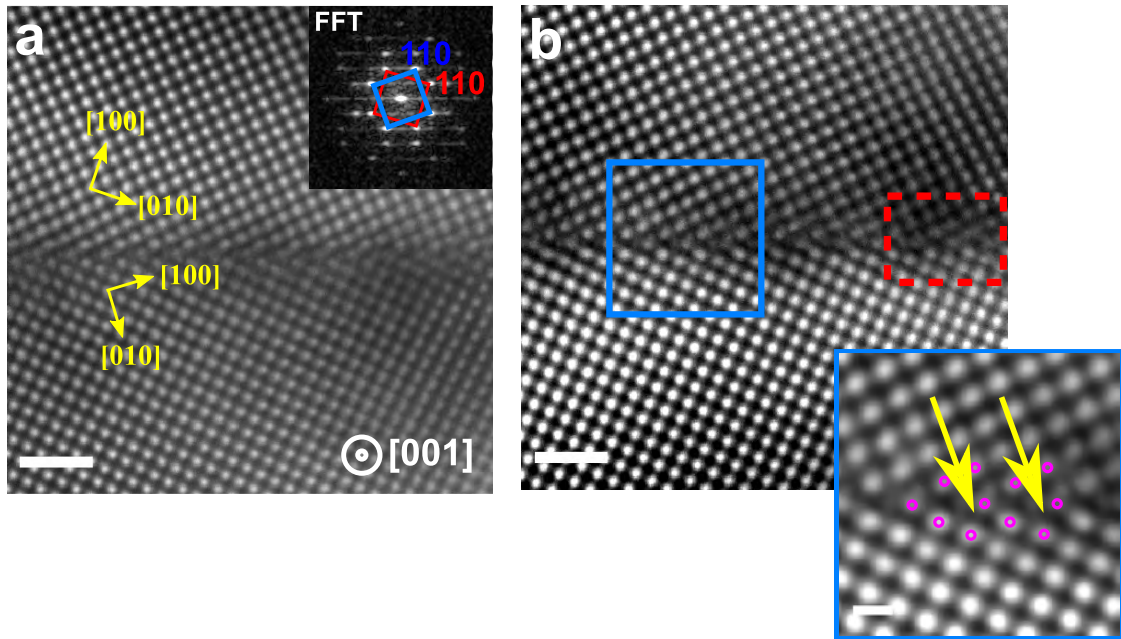


**Figure 5.3: Atomic structure of the  $\Sigma 5[001](310)$  GB in the Fe-4at.%Al bi-crystal.** **a** Raw HAADF-STEM image and corresponding FFT. From the FFT the misorientation angle is determined to  $38^\circ$ . **b** Fourier-filtered image of **a**. The inset shows a magnified view of the kite-type structural GB units highlighted by magenta dots. The yellow arrows indicate positions where weak contrast in the kite centers is observed. The scale bar in **a** and **b** is  $1\text{ nm}$ , while the inset has a scale bar of  $500\text{ pm}$ .

resolution imaging reveals a nano-faceted GB (Fig. 5.5b). It can be seen that while the lower grain is in  $[001]$  orientation, the upper grain is slightly off zone axis. The inclination angle of the GB with respect to the  $(310)$  plane is  $\approx 7^\circ$  and the GB facets are adopting the symmetric  $\Sigma 5(310)$  kite structure (blue box in Figure 5.5b). The magnified view of a step (red box in Figure 5.5b) reveals that it resembles a single kite structural unit, which is rotated by  $\sim 87^\circ$  with a height of  $\sim 0.46\text{ nm}$ . It should be mentioned that in the investigated TEM specimen only one  $\text{Al}_2\text{S}_3$  precipitate (see Fig. 5.6) was found, but even though a rather large GB curvature was introduced, the symmetric GB segments exhibit the kite-type structure.

## Grain boundary segregation

In parts of the GB, the atomic arrangement has shown slight deviations from the perfect kite structure and the presence of a GB precipitates indicates that impurity segregation could impact the GB structure. Besides  $\sim 4\text{ at.}\%$  Al, the as-grown bicrystal contains different impurities such as C, B, P, S, and Si in the lower ppm

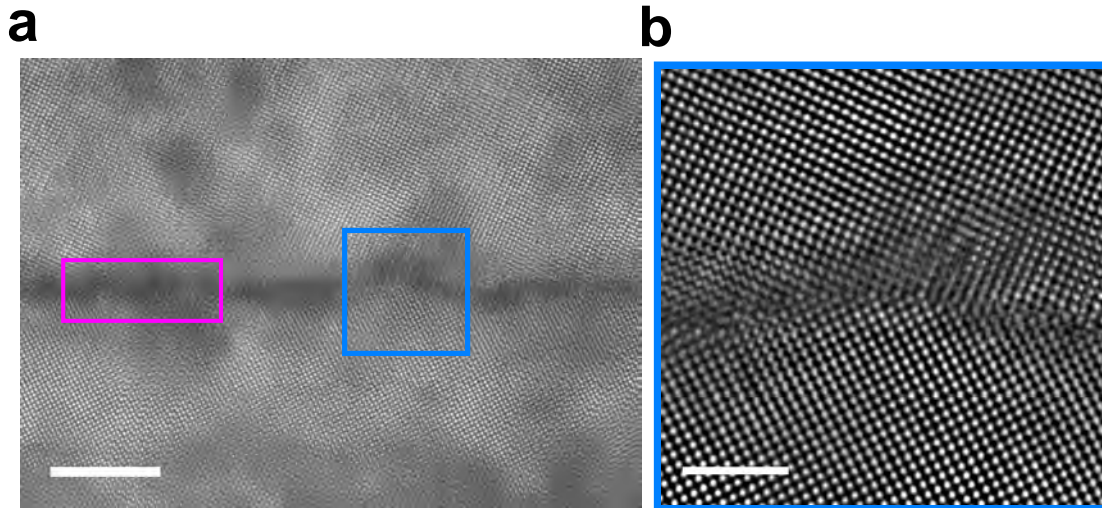


**Figure 5.4: High resolution imaging of distorted GB structure.** **a** HAADF-STEM image of the GB showing small steps (magenta rectangle), where the boundary plane shows facetting. Besides the small steps, large distortions are highlighted in the blue box and a higher magnified image is shown in **b**. The large step caused a large amount of strain - especially onto the upper grain. Thereby, the kite-structure is not visible anymore. The Scale bar in **a** is  $5\text{ nm}$  and in **b**  $2\text{ nm}$ .

range. Wet chemical analysis showed a bulk concentration of  $C_C \approx 0.05\text{ at.}\%$  and  $C_B \approx 0.001\text{ at.}\%$  for C and B (see Tab. 4.1). STEM-EDS elemental mapping was used to determine the GB composition as shown in Figure 5.7a. Here, the Al-K elemental map is superimposed on the simultaneously acquired HAADF-STEM image, where the dotted line highlights the position of the GB and the blue and red rectangles indicate regions where EDS spectra were integrated from. No Al enrichment at the GB is visible from the EDS map. To obtain a qualitative understanding of Al segregation, the spatial difference method was applied where the spectrum from within the grains (blue) is subtracted from the GB spectrum (red). Each integration window had an area of  $3 \times 10\text{ nm}^2$  in a region of constant thickness of  $40\text{ nm}$  as proved by STEM-EELS. The two spectra of the grain interior were averaged and for comparison all spectra were normalized according to the Fe- $K_\alpha$  edge as illustrated in Fig. 5.7b. The difference spectrum (orange curve) has a non-zero value at the Fe- $K_\alpha$  edge, which is not caused by a slight shape difference of the peaks within the grain and at the GB. Therefore, all peaks in the spectra were fitted by Gaussian peaks (solid lines). A magnified view of the Al- $K_\alpha$  peak is shown in Figure 5.7c. A decrease in Al intensity of  $\sim 5 \times 10^{-3}$  or 12% with respect to the grain interior is observed at the GB. The standard deviation of the noise level of the difference spectrum around

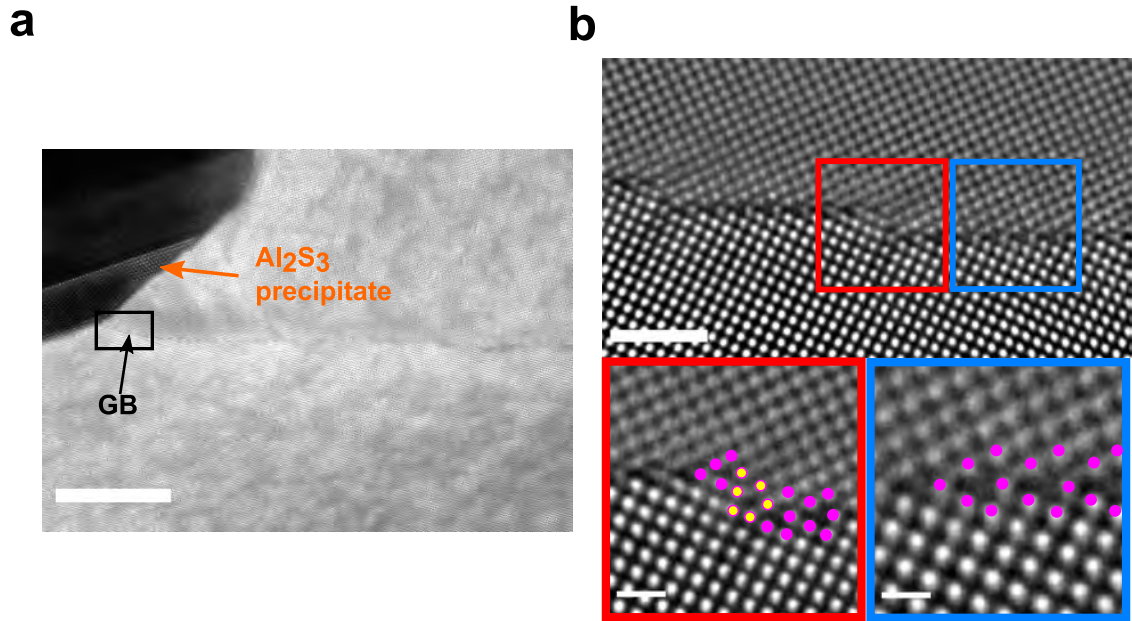


**Figure 5.5: Grain boundary nano-facetting in close vicinity to a GB precipitate.** **a** HAADF-STEM image taken near the  $\text{Al}_2\text{S}_3$  precipitate. The black rectangle indicates region where the boundary is bend. **b** Atomic resolution image of the region within the black rectangle showing nm-sized facets. The blue and red boxes indicate the symmetric facet and the step, respectively, as well as magnified views of the corresponding structural units. The scale bar is  $20\text{ nm}$  in **a** and  $1\text{ nm}$  in **b** and  $500\text{ pm}$  in the insets.

the  $\text{Al-K}_\alpha$  peak is  $\sim 1.3 \times 10^{-3}$ , which is nearly  $\times 5$  smaller than the peak maximum. This analysis suggests that Al is depleted at the GB, although first-principles calculations predicted a tendency for Al to segregate to substitutional sites at an idealized  $\Sigma 5(310)$  GB in bcc-Fe. Any sign of enrichment of other impurity elements were not revealed in the STEM-EDS data. Since measuring light elements is difficult in STEM-EDS, APT was used in addition to get a precise insight of the GB chemistry.

## Grain boundary composition

To obtain insights in the local distribution of Al and other impurity elements such as C and B at the GB with highest possible elemental sensitivity, we performed correlative STEM-APT investigations of the GB. Figure 5.8a presents a low magnification HAADF-STEM image of the needle shaped APT specimen containing the  $\Sigma 5$  GB at a distance of  $\sim 100\text{ nm}$  from the apex. From the width of the needle-shaped specimen, the thickness of the tip at the boundary region can be estimated

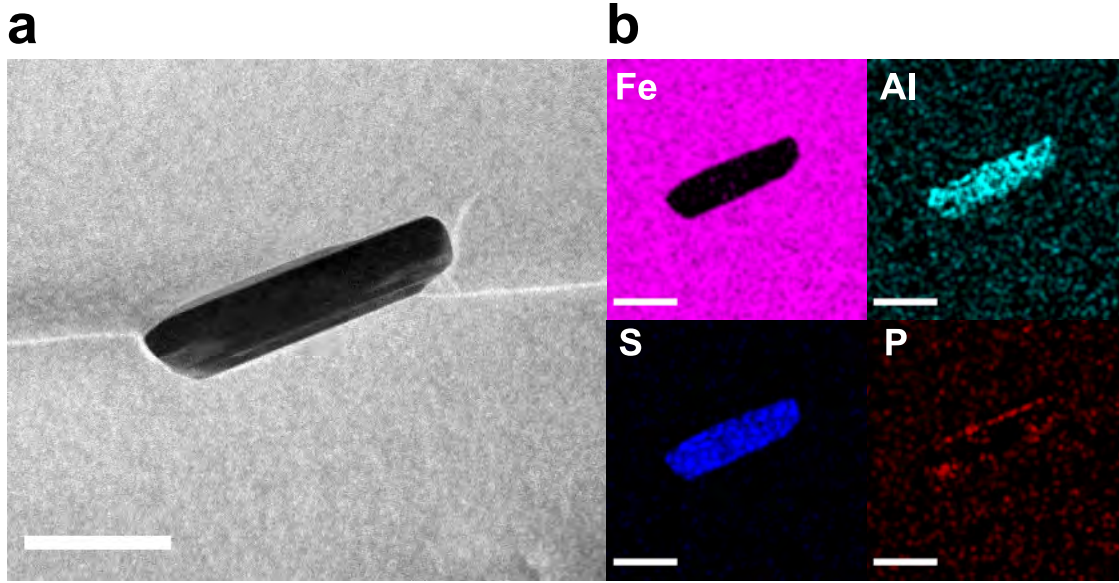


**Figure 5.6: Formation of precipitates at the GB.** **a** HAADF-STEM image of the GB intersecting with a large precipitate. **b** The corresponding EDS elemental maps for Fe, Al, S and P. The Scale bar in **a** and **b** is 100 nm.

to  $\sim 70$  nm. The viewing direction is along the  $[001]$  tilt axis. Figure 5.8b shows the distribution of Al, C and B atoms. In contrast to C and B enrichment at the GB, a depletion of Al is apparent. A linear 1D composition profile extracted from a cylindrical region with 20 nm in diameter (see Figure 5.8b) positioned perpendicular to the GB is shown in Figure 5.8c. The Al concentration decreases from  $\approx 3.8$  at.% in the bulk (which is in agreement to our wet chemical analysis) to  $\approx 2.4$  at.% at the GB. In contrast, the C and B concentration increase to 2.4 at.% and 1.8 at.%, respectively. A more profound analysis provides information about the Gibbs interfacial excess (IE)  $\Gamma_i$  of solute  $i$ , which describes the number of atoms per unit area at interfaces [152]. The measurements show that  $\Gamma_B \approx 2.4$  atoms  $\text{nm}^{-2}$  and  $\Gamma_C \approx 3.1$  atoms  $\text{nm}^{-2}$ , where  $\approx 8$  atoms  $\text{nm}^{-2}$  correspond to one monolayer. It should be noted that the IE value could increase when the diameter of the cylinder was reduced and placed across a solute enriched region within the GB, indicating that the elemental distribution is inhomogeneous. For Al a negative IE value of  $\Gamma_{Al} \approx -3.1$  atoms  $\text{nm}^{-2}$  was obtained.

For better understanding of C and B distribution, a second APT specimen was extracted from a location  $\sim 6$  mm apart from the previous STEM-APT observations. Figure 5.9a shows the reconstructed 3D volume of the needle shaped specimen, where this time the GB plane was chosen to be perpendicular to the evaporation

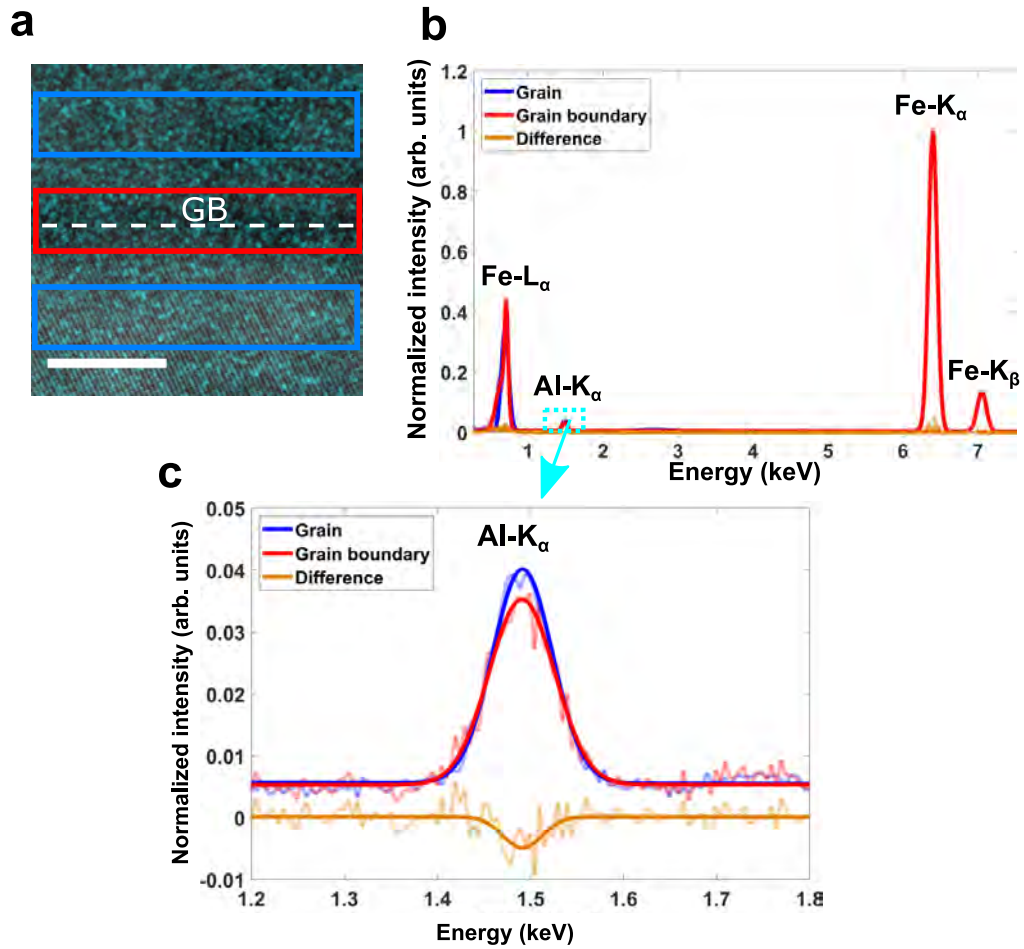


**Figure 5.7: Elemental distribution of Al at the  $\Sigma 5(310)$  GB.** **a** Overlay of the HAADF-STEM image and the Al-K elemental map taken across the  $\Sigma 5(310)$  GB. The colored boxes indicate the location where the spectra in **b** were summed. **b** Summed EDS spectra, which were normalized to the Fe- $K_{\alpha}$  peak, extracted from the grain interior (blue) and the GB (red). The corresponding difference spectrum is shown in orange. In order to minimize effects from differences in peak shapes, the spectra were fitted by a Gaussian function. **c** A magnified view of the Al- $K_{\alpha}$  edge indicates a slight decrease of Al at the GB. The semitransparent curves in **b** and **c** display the raw spectra, the solid lines the Gaussian fit. The Scale bar in **a** is 5 nm.



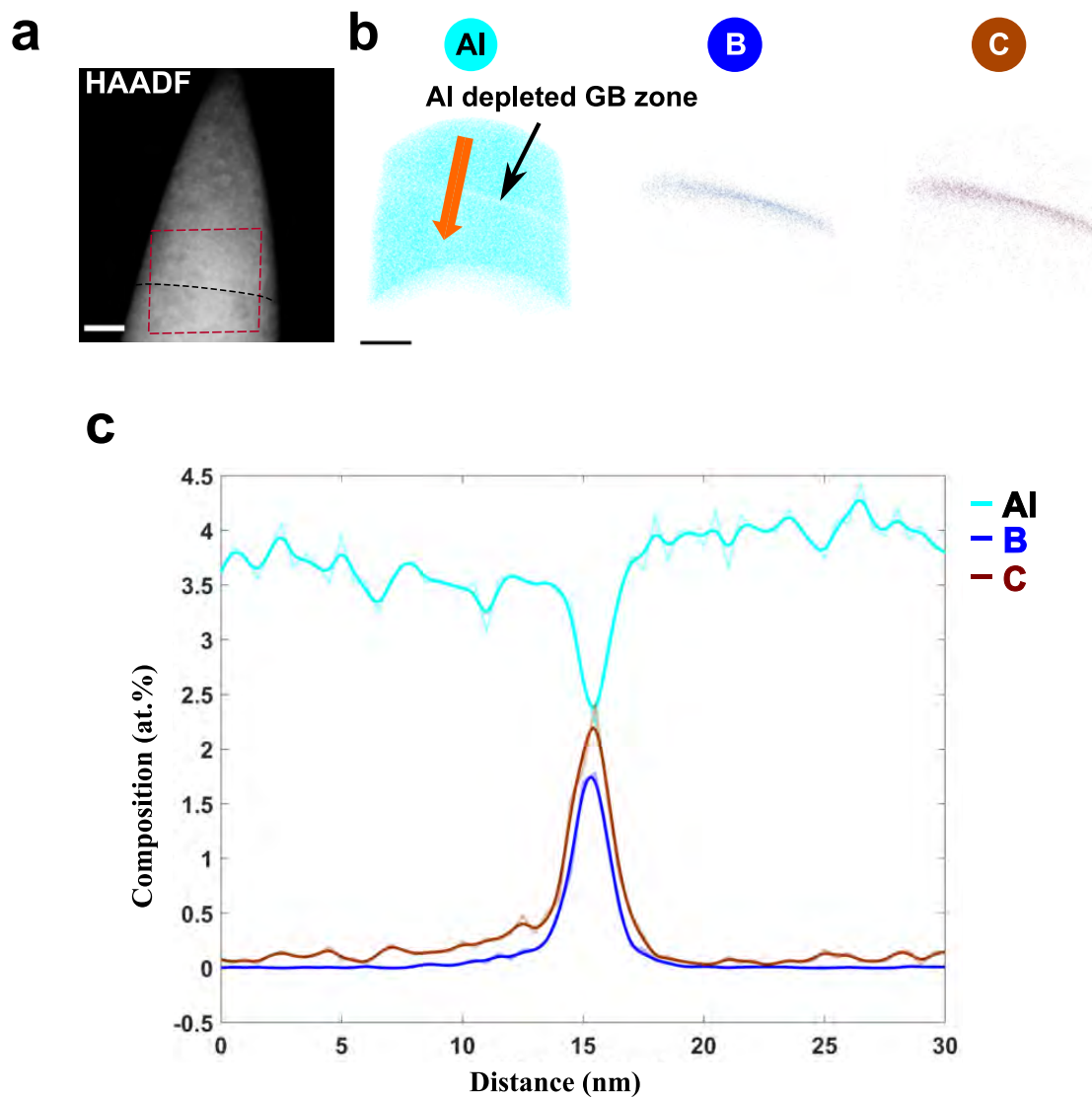


**Figure 5.8: Correlative STEM-APT study of the  $\Sigma 5$  GB.** **a** HAADF-STEM image of the needle shaped APT specimen with both grains in  $[001]$  orientation. The GB is labelled with a black dashed line. **b** The atom maps of Al, B and C reconstructed from the volume outlined by a red rectangle in **a**). At the GB, a depletion of Al and enrichment of B and C is observed. **c** The corresponding composition profiles extracted from a cylindrical region marked by an orange arrow in **b**) across the GB shows a decrease of Al and increase of B and C concentration at the GB. Scale bar in **a** is  $20\text{ nm}$  and in **b**  $10\text{ nm}$

direction ( $[001]$  points towards the evaporation direction). Again, a clear enrichment of C (brown) and B (blue) at the GB were observed, but no segregation of Al. Rotation of the reconstruction by  $90^\circ$  (see Fig. 5.9b) is showing the solute distribution along the GB plane, i.e. viewing along the  $[310]$  direction. The distribution of B and C within the GB plane seems to be different with C showing a rather periodic segregation pattern with C rich segments every 25 nm. The composition profile along the GB (green arrow in a)) is shown in Fig. 5.9c confirming a difference in the segregation behaviour between C and B. A modulating distribution of C with an amplitude of  $\sim 1$  at.% and a periodicity of 25 nm was obtained. On the other hand, the average content of B is  $\sim 1$  at.% with no significant modulation.

Although Al exhibits a high solubility of 4% at room temperature in bcc-Fe [40] a clear depletion at the GB was observed, which is in contradiction to previous computational [145, 169, 170] and experimental [187, 188] studies. The complex co-segregation of C and B revealed by APT in this study indicates that those interstitial elements might strongly affect the segregation behavior of Al.

## Computational results

We performed DFT calculations to explore the interaction of solutes at the  $\Sigma 5(310)$  GB and their effect on segregation energies. A particular focus was laid on the interaction of C and B with Al to elucidate the observed Al depletion. Furthermore, the segregation kinetics are investigated to obtain insights into the complex co-segregation during bicrystal fabrication.

The pristine  $\Sigma 5(310)[001]$  GB was modelled with 78 atoms in the unit cell and the ground state structure was determined using the  $\gamma$ -surface approach [142] at 0K. The present DFT calculations do not include temperature effects from thermal excitations, which have been shown to be minor for the considered temperatures [189, 190]. However, the effective segregation entropy that arises from averaging a multi-site GB excess to obtain a singular effective segregation energy [10, 27, 191] is included in the analysis. The resulting structure viewed along the  $[001]$  tilt axis is shown in Fig. 5.10.a. In a first step we have calculated the segregation energies of Al, C, and B at the GB using the equation

$$E_{seg,i} = (E_{gb,i}^x - E_{gb}) - (E_{bulk}^x - E_{bulk}) \quad (5.1)$$

where  $E_{gb}$  is the total energy of the pristine GB and  $E_{gb,i}^x$  denotes the total energy

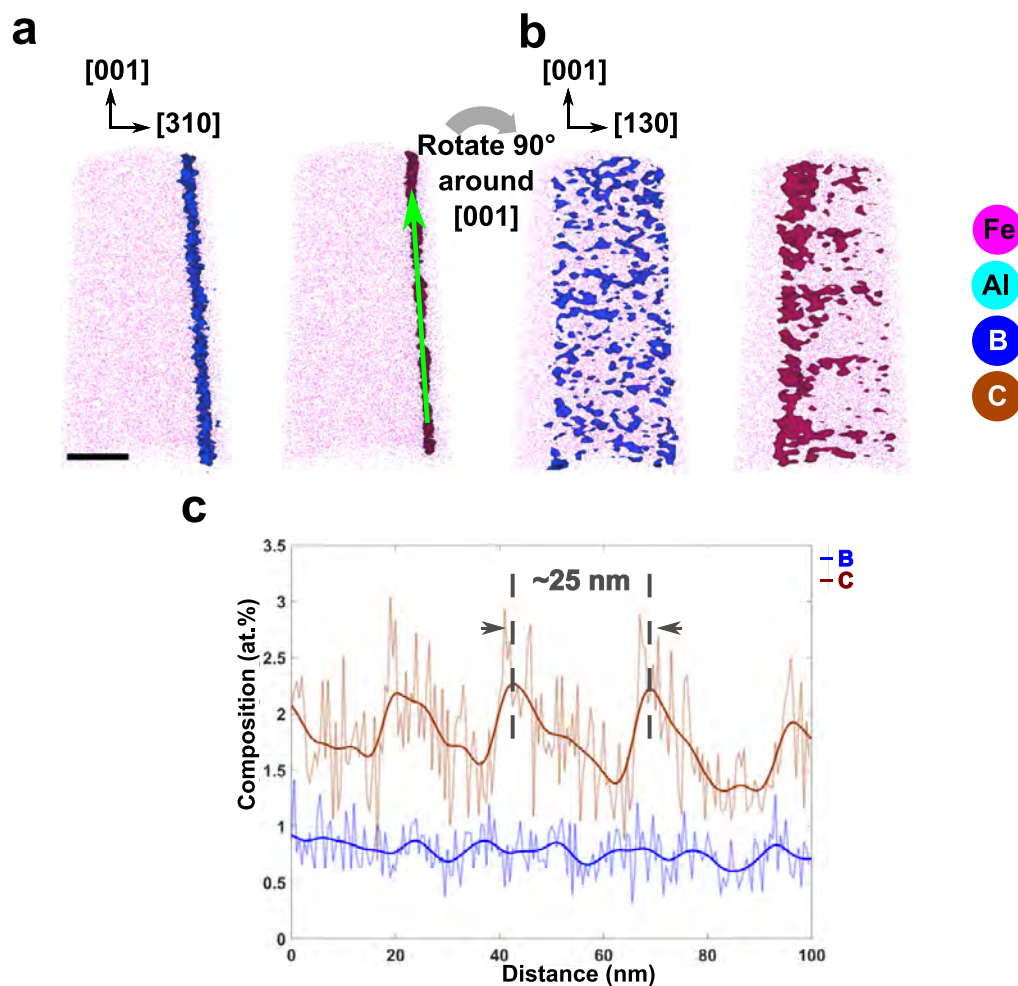


**Figure 5.9: Distribution of C and B along the  $\Sigma 5(310)$  GB.** **a** 3D APT reconstruction showing atom maps of Fe, Al, B, and C as well as isoconcentration surfaces of 1 at.% for C (brown) and B (blue) viewed perpendicular to the GB plane. **b** The same APT reconstruction rotated by  $90^\circ$  around [001] such that the viewing direction is along the (310) GB plane. **c** Corresponding composition profile of the GB extracted in a cylinder with 5 nm diameter along the green arrow in **a**. While the B concentration is nearly constant at  $\sim 1$  at.% along the boundary, the C concentration varies periodically. The average distance between the regions with a peak C concentration of  $\sim 2.3$  at.% is determined to  $25\text{ nm}$ . Scale bar in **a** is  $20\text{ nm}$

of the GB cell with the solute  $x$  at GB site  $i$ . The site  $i$  is varied over positions shown in Fig. 5.10a. The reference of the solute in the bulk is given by the energy difference of  $E_{bulk}$ , i.e. a cubic bulk cell that contains 128 Fe atoms, and  $E_{bulk}^x$ , which corresponds to the total energy of the bulk cell with solute  $x$  at its preferred position. The position in the bulk is substitutional for Al, while for C and B it is the octahedral interstitial site [192]. Because the atomic volume of B is in between typical substitutional and interstitial solutes, we consider B as both interstitial and substitutional at the GB. For the computation of the segregation energy, the number of atoms needs to be kept constant, which is the case in Eq. 5.1 if the site type is the same in the bulk and at the GB, i.e. either interstitial or substitutional. For placing B in a substitutional site at the GB and in an interstitial site in the bulk, the segregation energy needs to be compensated by the energy of a single Fe atom in the bulk  $E_{Fe} = E_{bulk}/128$ :

$$E_{seg,i} = \left( E_{gb,i}^x - E_{gb} \right) - \left( E_{bulk}^x - E_{bulk} \right) + E_{Fe} \quad (5.2)$$

A negative segregation energy of a solute indicates that the solute favours segregation to the GB.

We computed segregation energies at a coverage of 0.5 monolayers (ML) for Al to sites S1-S3, for C to sites I1-I4 and for B to all labeled sites in Fig. 5.10a. The resulting segregation energies for Al, B, and C are given in Fig. 5.10b. By far the strongest segregation tendency is observed for B with a segregation energy of  $-2.8$  eV to the interstitial site I1 at the GB center. The second strongest segregation tendency is found for the substitutional site S2 next to the GB center with  $-1.86$  eV. For C and Al the strongest segregation tendency is observed to the GB center with  $-1.7$  eV in the case of C for position I1 and only  $-0.38$  eV for Al for position S1, respectively. The segregation tendency decreases with increasing distance from the GB. When placing B at the segregation site I2, the B atom moved to site I1.

The segregation tendency of B to substitutional sites S2 and S3 at the GB is substantial, but it also introduces a strong displacement of the surrounding Fe atoms and hence a distortion of the kite structure as seen in Fig. 5.11. Especially for B at site S2, the B induced distortion is significant. This can be quantified by the mean squared displacement (MSD) of the atoms in the vicinity of B in a radius of  $5 \text{ \AA}$ . For B at site S1, S2, and S3 the MSD is  $0.14$ ,  $0.40$ , and  $0.59 \text{ \AA}$ , respectively. The corresponding simulated HAADF-STEM images using the Prismatic software [148, 193] are shown in the lower panels of Fig. 5.11. Here, the simulated HAADF

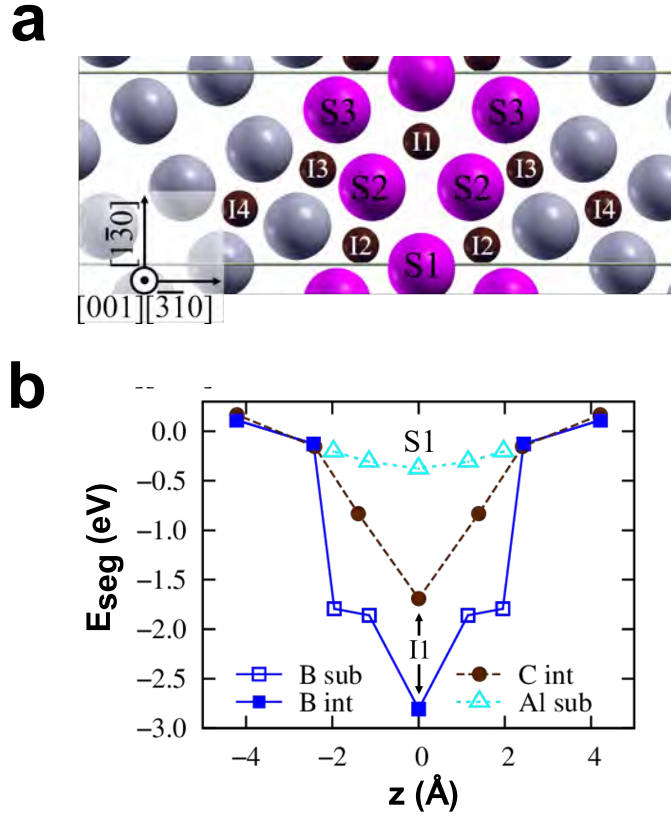


**Figure 5.10: Solute segregation energies at the GB.** **a** shows the GB (highlighted by the purple atoms) with the interstitial sites (I1-I4), where C and B were placed, and substitutional sites (S1-S3). **b** contains a plot of segregation energies of Al to substitutional sites (empty symbols), C to interstitial sites (solid symbols), and B to both substitutional and interstitial sites.

contrast predominately shows the Fe atomic columns and the B and/or C atoms are only indirectly visible. This can be seen in the slight decrease in intensity of the atomic columns in the kite tips when B is segregating to the substitutional site S1 (see Fig. 5.11a). When B is segregating to position S2 (Fig. 5.11b), the neighboring Fe atoms are displaced causing a smearing of the HAADF contrast and the individual columns are no longer resolvable. An even stronger displacement of the Fe atoms is introduced when B is located at site S3, as seen in the top panel of Fig. 5.11c, and here Fe dumbbells are observed at the kite tips in the simulated HAADF-STEM image (lower panel of Fig. 5.11c). Even placing B as well as C in the interstitial positions I1 and I2 (Fig. 5.11d) can have a slight distortion of the kite tips, where the Fe atoms are shifted perpendicular to the boundary plane.

So far, the computed segregation energies are obtained for individual solutes, but the interaction of solutes can have significant effects on the segregation tendencies

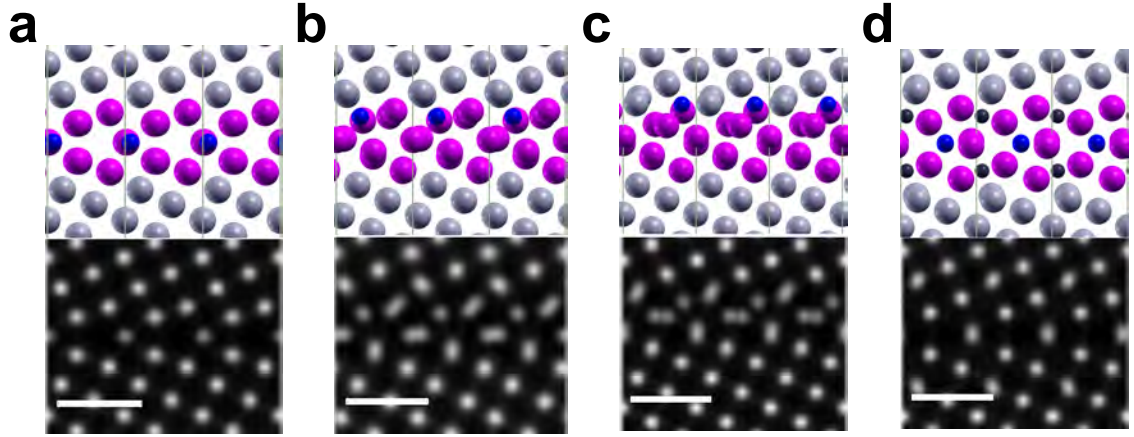


**Figure 5.11: Disorder at the GB for B at substitutional segregation sites.** The upper panels of **a**, **b** and **c** show the DFT calculated structures with B (blue) at substitutional sites 1, 2, 3. The lower panels are the corresponding HAADF-STEM simulated structures. Panel **d** shows the GB segregated with two B (in one column) and two C (brown) atoms from Fig. 5.12f (see below). The scale bar is 500 pm

when the binding energies are in the range of the segregation energies [146, 194]. In the following section, we explore the co-segregation behavior of Al with both C and B as a possible explanation for the observed depletion of Al from the GB. To that end, we have computed the binding energies of Al at its preferred site S1 in the GB center to B and C at vicinal interstitial segregation sites (I1-I4). The binding energy between Al and a solute  $x$  is defined as

$$E_{bind}^{Al-x} = (E_{Al} + E_x) - (E_{Al-x} + E) \quad (5.3)$$

where  $E_{Al-x}$  denotes the total energy of the GB cell with Al and the solute  $x$  present.  $E_{Al}$  and  $E_x$  are the energies of the same cell with either Al or solute  $x$  placed at their lowest energy segregation sites, respectively.  $E$  is the energy of the simulation cell not containing any solutes. For attractive interactions, the binding energy is positive, while repulsive interactions are associated with negative binding energies.

Figure 5.12a-d shows exemplary the calculated GB structure with B and C atoms placed in different interstitial (I1-I4) and substitutional (S1-S3) sites. The binding energies of Al in its preferred position and either B or C are shown in Fig. 5.12e. For Al and B in their lowest energy sites, S1 and I1, respectively, the binding energy is determined to  $-0.40$  eV, which is repulsive. If B is considered in one of the substitutional sites, the binding energy varies between  $-0.42$  eV (Al in S1 and B in

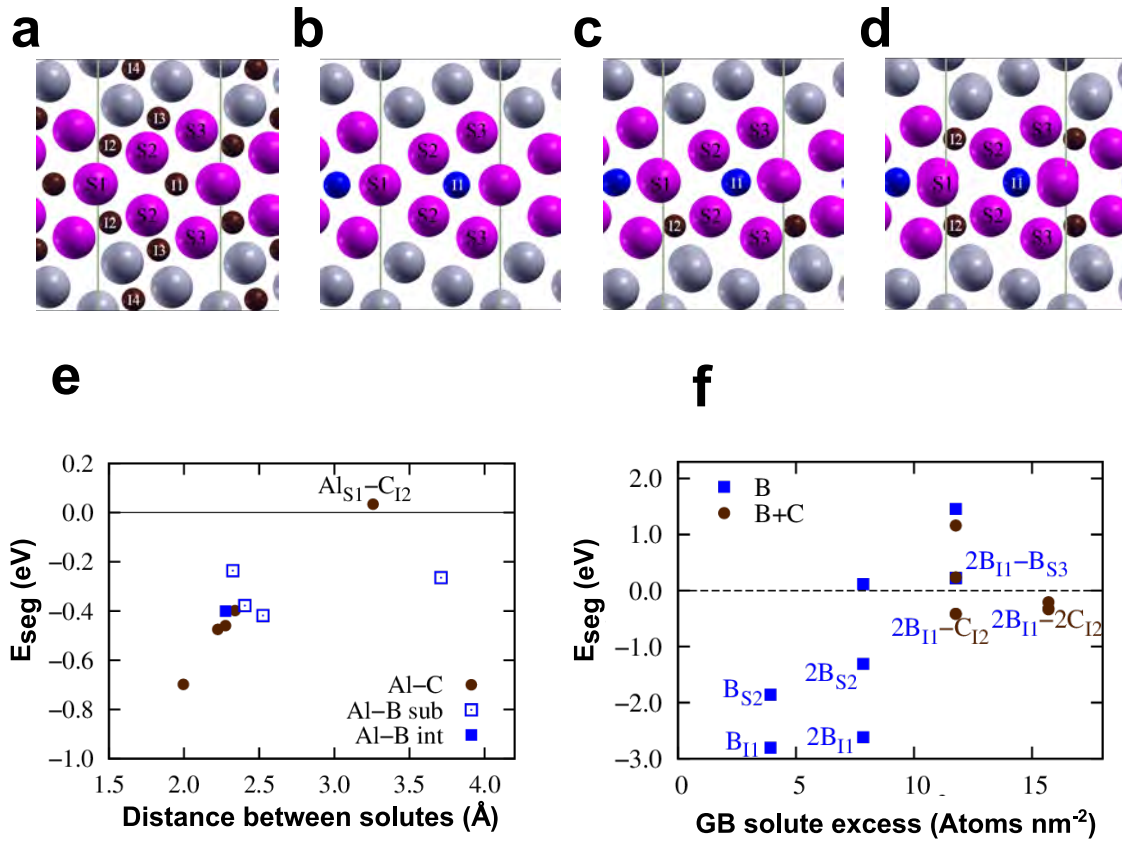


**Figure 5.12: Solute interactions at GB.** **a** GB structure with labelled substitutional (S1-S3) and interstitial sites (I1-I4). **b** The GB structure corresponding to configuration  $B_{I1}$  and  $2B_{I1}$  (the two B atoms are oriented in  $[001]$  direction and the structure cannot be distinguished from configuration  $B_{I1}$ ). **c** and **d** show the configurations  $2B_{I1} C_{I2}$  and  $2B_{I1} 2C_{I2}$ . In **e**, the binding energies of Al with B and with C are shown as a function of the distance between the solutes. Panel **f** presents the co-segregation energies of B and C atoms to the GB, where important configurations are named.

S2) and  $-0.24$  eV (Al in S1 and B in S3). For C, multiple repulsive constellations are found with binding energies in the range of  $-0.70$  to  $-0.40$  eV for small distances of  $<2.5$  Å between Al and C. For the constellation of Al at site S1 and C at site I2, with a distance of  $\sim 3.3$  Å, a slightly positive binding energy is obtained. However, this is not the site where C exhibits the strongest segregation tendency. For both C and B interaction with Al, the magnitudes of the binding energies are mostly larger than the segregation tendency of Al to the GB. The strong repulsive interactions of Al with either B or C imply that co-segregation of these elements is highly unlikely. This suggests that Al is repelled from the GB, since both C and B exhibit a much stronger segregation tendency in comparison to Al.

Another effect that comes into play with solute interactions is the coverage dependence, which refers to changes in the segregation energy with increasing coverage at the GB. This may be computed using Eqs. 5.1 and 5.2, where  $E_{gb,i}^x$  denotes the total energy of the structure with  $N+1$  solutes at the GB and  $E_{gb}$  the structure with  $N$  solutes at the GB. For the lowest solute coverage we take 0.5 ML which corresponds to the results shown in Fig. 5.10 and add atoms to preferential segregation sites. The resulting coverage dependent segregation energies are displayed in Fig. 5.12f. As B has by far the strongest segregation energy, the starting structure contains a B atom at the GB. Adding a second B atom leads only to a slightly lower segregation tendency for the interstitial positions ( $2B_{I1}$ ), whereas in the substitutional case, the decrease is somewhat stronger ( $B_{S2}$  to  $2B_{S2}$ ). Adding a third B atom, however, leads to a large decrease in segregation tendency to even positive values (the lowest energy configuration  $2B_{I1}$ - $B_{S3}$  is at  $+0.22$  eV). This means that additional B segregation above a coverage of 8 atoms  $\text{nm}^{-2}$  becomes unfavourable. When adding C to the GB to site I2 with already two B atoms present in position I1 gives a negative segregation energy of  $-0.42$  eV. Even for an additional C atom in I2, a negative segregation energy of  $-0.33$  eV is obtained. This indicates that although B shows strong segregation tendencies to different positions at the GB, at 1 ML coverage or about 8 atoms  $\text{nm}^{-2}$  a maximum enrichment is reached due to solute interactions.

The enrichment of solutes at GBs in equilibrium can be described with a modified McLean isotherm, but under experimental conditions kinetic processes often influence GB segregation. Therefore, we compute the enrichment of solutes at the GB by considering segregation kinetics via our recently published model [145, 195]. Note that the slow cooling rate during bicrystal growth minimizes non-equilibrium segregation effects as described by Faulkner [78] as possible origin for solute enrichment



at grain boundaries, and therefore, these effects are not included in our modeling approach. As input parameters we use grains with a radius of  $100\ \mu\text{m}$  that is further discretized into shells of  $1\ \mu\text{m}$  thickness. Although the bi-crystals are in the range of cm, the system size is sufficient because the diffusion length of all involved solutes is below  $100\ \mu\text{m}$  in the chosen heat treatment. The GB thickness is taken as  $0.8\ \text{nm}$ , which is the region where segregation energies are negative. The diffusion data is given in the Tab. 5.1 and for the heat treatment we consider cooling down from  $1800\ \text{K}$  with the experimentally informed [195] modified Newton's law of cooling. The cooling rate of  $r = 0.017\text{s}^{0.5}$  is chosen such that room temperature is reached

Solute	$D_0$ [m/s <sup>2</sup> ]	$E_a$ [eV]	Ref.
Al	$1.80 \times 10^{-4}$	2.364	[196]
C	$3.94 \times 10^{-7}$	0.831	[196]
B	$3.19 \times 10^{-7}$	2.310	[192]

**Table 5.1: Diffusion data employed for the segregation kinetics simulations.**

after 24 hours (see Fig. 5.13a) similar to the fabrication of the bi-crystal specimen. The bulk concentration of the solutes was taken from the wet chemical analysis. The segregation energies necessary were taken from the coverage dependence shown in Fig. 5.12f, i.e. for B site I1 is considered and for C the site I2. We want to point out that it is not possible to include the computed solute-solute interactions with classical approaches like the Guttman or Fowler isotherms [78] as these take as input only a single value, whereas we find that each configuration has its own individual interaction energy. Rather Monte Carlo Simulations would be required to link to the DFT data. Such calculations are beyond the scope of this study

The resulting time and temperature dependent enrichment of solutes at the GB is shown in Fig. 5.13. Due to the strong repulsive interactions of Al with B and C, we investigate Al segregating on its own in the center panel (Fig. 5.13b), while we consider mutual segregation for B and C in the bottom panel (Fig. 5.13c). The GB enriches with Al for temperatures above  $800\ \text{K}$ , but for temperatures below, segregation is kinetically limited. At this stage, the excess concentration of Al is  $22\ \text{atomsnm}^{-2}$ . Here it is important to note that for Al no coverage dependency was considered. For B, the GB enrichment takes place relatively fast at high temperatures because of the strong segregation tendencies and stops at a GB excess of  $7\ \text{atomsnm}^{-2}$  for temperatures below  $1200\ \text{K}$  due to kinetic reasons. This happens already for higher temperatures than for Al because the concentration in the bulk is much lower than for Al and for GB enrichment, B needs to diffuse from farther

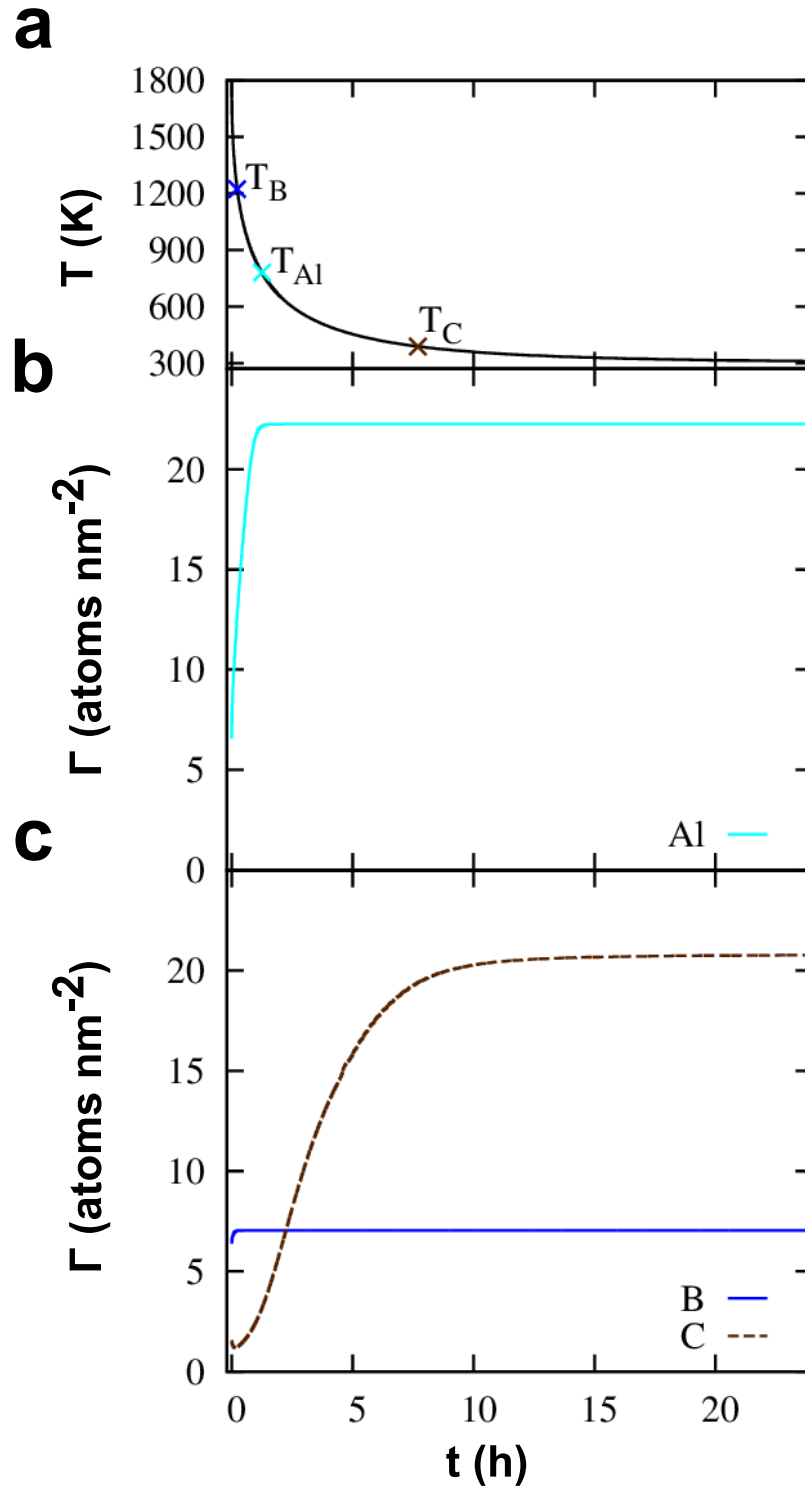


**Figure 5.13: Computed grain boundary segregation kinetics.** **a** Time-temperature curve during cooling with the temperatures  $T_{sol}$  marked at which segregation for the solutes is limited kinetically. **b** The resulting enrichment of Al atoms without interaction with other solutes. **c** Competing temperature dependent segregation of C and B while the bottom panel shows the enrichment for competing B and C segregation.

away from the GB. Contrary, C is able to enrich until temperatures of only 390 K due to faster diffusion and higher content in the bulk than for B so that a final GB excess of  $16 \text{ atoms nm}^{-2}$  is reached. The fact that B enriches already at higher temperatures than Al reduces the possibility of Al segregation even more because B is already present at the GB in a temperature range where Al segregation takes place.

## Discussion

In this study, the atomic structure, composition and co-segregation mechanisms of Al, C and B at a  $\Sigma 5 (310)[001]$  bcc-Fe GB were investigated by correlating aberration corrected HAADF-STEM observations, APT measurements and first-principles DFT calculations. The observed atomic structure of the  $\Sigma 5 (310)[001]$  GB consists of kite-type structural units and agrees to investigations by Medlin et al. [175]. Globally, the GB appeared straight and close to the symmetric orientation, but atomic resolved observations indicated the presence of defects such as steps or disconnections. Further, in close vicinity to a GB precipitate steps are incorporated into the GB to compensate the local curvature. Interestingly, this GB segment does not break up into  $\{210\}$  and  $\{310\}$  facets (as observed by Medlin et al. [175]), but retains the  $(310)$  kite-type structural units. The reason is that the inclination angle of only  $7^\circ$  from the symmetric orientation seems not to be sufficient to promote faceting.

Our compositional analysis of the GB revealed a depletion of Al at the interface, where locally the Al concentration reduces by  $\sim 1.5 \text{ at.}\%$  at the GB. This is in contradiction to first-principles calculations of Yasua et al. [169] and Geng et al. [170] as well as Scheiber et al. [145], who observed the segregation of Al. However, it should be mentioned, that they investigated a pure Fe-Al system. From our APT measurements, we were able to detect the segregation of B and C. Taking these elements into our calculations, we showed that both C and B have much stronger segregation tendencies than Al (Fig. 5.10), so that already simple site competition arguments suggest a depletion of Al due to competition with B for substitutional sites. Explicit calculation of solute interactions revealed strong repulsive interactions between Al-C and Al-B. By considering the kinetics of segregation, it is clear that B is the first solute to segregate to the GB, which prevented Al enrichment and explained the depletion of Al. The composition evaluated with the kinetic model

and first principles segregation energies is substantially higher than the composition observed with APT. This is attributed to co-segregation effects between B with itself, C with itself and B with C. In fact, evaluation of these co-segregation effects showed that increased coverage of B decreases the segregation tendency at coverages above 1 ML. It is not possible to implement these interactions into the current kinetic model, still, it can be inferred that co-segregation effects limit enrichment of B and C. The observed enrichment kinetics should hold true nonetheless, i.e. a first fast enrichment of B, followed by slower enrichment of C that continues on until lower temperatures. Even though co-segregation effects are known in general [11], they were not observed in the case of bcc-Fe-Al(C,B) and never explained in a comprehensive manner by combining atomistic simulations and experimental observations.

Another interesting finding is the observation of locally distorted kite structure. Its origin can be related to the presence of defects, which are aligned along the tilt axis, and to segregation of B to substitutional sites. The assumption that GB defects alter the projected structural units is supported by observations of a periodic distribution of C in our APT analysis. It is known that C preferentially segregates to highly distorted regions such as GB dislocation cores [197]. These defects could also be responsible for the extra contrast observed in the open volume of the kites (indicated by yellow arrows in Fig.5.3b). Hyde et al. [198] reported that by the formation of GB dislocation loops a metastable structure having extra Fe atoms in the kite center may appear. The distortion of the kites can also have a compositional origin. Our DFT simulations showed that different substitutional sites are also preferred positions for B segregation introducing strong displacements of Fe atoms from their equilibrium positions (Fig. 5.11). STEM image simulations of these structures - especially panel b of Figure 5.11 - closely resemble our observations in the red dashed line in Fig.5.3b even so the individual B atoms can not be localized. Furthermore, the formation of Fe dumbbells in the simulated images induced by B segregation could explain the weak contrast in the kite center observed in the experiments (see yellow arrows in the inset of Fig.5.3b. The weaker contrast originates that we do not have a full column of Fe atoms shifted, but partly. Therefore it is highly possible that defects in combination to the B segregation is responsible for the distorted structure of the GB.

## 5.4 Conclusion

Our results demonstrate that co-segregation effects in the presence of impurities leads to unexpected GB segregation effects and possible GB structural transformations. Considering the interaction of non-metallic elements, here B and C, with substitutional alloying additions, in our case Al, is indispensable to fully capture the entire segregation processes. We discovered that the presence of B and C impurities segregated to the GB is repelling Al from the GB by strong repulsive interactions. Furthermore, the competing mobilities of solutes critically influences the evolution of GB composition. We ultimately show that the presence of non-metallic impurity elements needs to be considered when studying GB segregation effects. Additionally, we expect similar trends in segregation of B and C even to general GBs in polycrystalline materials, which typically adopt complex structural arrangements and contain a high number of defects (such as disconnections and facets). This is supported by observations made by Janovec et al. [13] who compared segregation tendencies in Fe-Si-P polycrystal as well as in a bicrystal of the same composition. They even found a stronger segregation of P in general GBs. Moreover, Yu et al. [101] observed periodic segregation patterns even at general GBs in the Ni-Bi system and identified the GB plane normal as the driving force for the formation of such periodic enrichment of Bi in Ni polycrystals. Therefore, our work also paves the way for tailoring GB composition by tuning impurity additions.

## 5.5 Impurity segregation outweighs liquid metal embrittlement in iron

This section is based on:

A. Ahmadian, D. Scheiber, X. Zhou, B.Gault, L. Romaner, G. Dehm and C. H. Liebscher “Impurity segregation outweighs liquid metal embrittlement in iron”, *Unpublished*.

## 5.6 Introduction

Grain boundary (GB) properties such as cohesive strength or mobility can be significantly altered through segregation of alloying elements or impurities [10]. One of the most famous examples is zinc (Zn) diffusion and segregation into GBs of iron (Fe) and steel inducing GB migration [88, 102, 199] and intergranular brittle fracture [43, 103, 200–210]. The latter phenomenon is known as liquid metal embrittlement (LME), which is the loss of an initially ductile metal in the presence of a liquid metal.

LME limits the use of many high strength steel materials, which are coated with zinc (Zn) to prevent corrosion. Several models were proposed to explain the underlying mechanism leading to LME [211]. The most widely used model was simultaneously developed by Stoloff and Johnson [212] and Westwood and Kamdar [213] and is known as the Stoloff–Johnson–Westwood–Kamdar (SJWK) model. In their approach, the liquid metal adsorbs at the crack tip and promotes crack propagation under an applied stress by weakening the strength of the interatomic bonds. In contrast, the Krishtal-Gordon-An model [214] assumes that stress-assisted GB diffusion precedes the crack initiation and is the root cause for the increase in grain boundary brittleness. DiGiovanni et. al [215] investigated the diffusion of Zn in Fe by means of electron-probe microanalysis (EPMA) before and after thermomechanical loading of coated and uncoated TRIP steel. Their observations confirmed that stress-assisted diffusion in the vicinity of the crack tip is one of the dominant mechanism. It should

be mentioned that GB segregation induced phase transformation observed in Fe-Zn [43, 204, 206, 210] may also be regarded as the driving force for LME. Bauer et. al [104] performed ab initio DFT simulations to evaluate the change of GB energy of  $\Sigma 3$  (1 1  $\bar{2}$ ) and  $\Sigma 5$  (3 1 0) bcc-Fe GBs after Zn segregation. They concluded that the GB weakening depends on the mechanism, the underlying thermodynamical model (canonical Griffith model [216] or the grand-canonical Rice-Wang formulation [171]) and the choice of the chemical potential.

In order to avoid LME, it is possible to introduce cohesion enhancing alloying elements to the grain boundaries. Recently, Ding et. al [217] showed by first-principles based calculations on a  $\Sigma 5$  fcc-Fe GB that Ni can hinder GB weakening by Zn since it forms strong chemical bonds with Fe. The influence of other typical alloying elements such as Si and Al showed a similar behavior, however, the true paramagnetic state of fcc-Fe was not considered. Scheiber et. al [147] concluded from ab-initio calculations in combination with a Langmuir-McLean-type segregation model [218] that the embrittling effect of Zn at different symmetric bcc-Fe tilt GBs can be reduced by Al and Si. This is related to site-competition between Zn and Al as well as repulsive interactions between Si and Zn, respectively. However, since the tendency for Zn to segregate to grain boundaries is much larger than for Al or Si, it is technologically challenging to deplete Zn from the GB. A way to hinder the penetration of Zn into the metal was proposed by He et al. [219] by introducing an Al interlayer, which is capable of suppressing LME.

Another possible way to mitigate LME of Fe is to make use of cohesion enhancing trace impurities that are typically present in engineering Fe-based alloys or steels. While some candidate elements such as S and P are known to reduce GB cohesion [157, 158], C and B are GB cohesion enhancers. [15, 17–20, 22, 152, 159, 160, 167, 220, 221]. They may provide a natural source within the material to reduce the tendency for grain boundary failure. It has been shown that small amount of B can partially suppress GB weakening in intermetallic FeAl alloys [21, 22, 166]. This has not been considered for FeZn since the underlying co-segregation effects with Zn have not been explored. Miyazawa et al. for example showed by first-principles based tensile tests of a  $\Sigma 3$  symmetrical tilt GB that the increase in GB cohesion by C is due to the higher Fe-C bond mobility. Wachowicz et al. [167] studied the effect of B on the GB cohesion in  $\alpha$ -Fe using DFT calculations. They found out, that substitutional B would enhance the cohesion strength of the  $\Sigma 5$  (2 1 0) boundary because of stronger bonding with Fe atoms. This results are in good agreement to

previous calculations [163]. Therefore, it is of great interest to understand how trace impurities such as B and C impact the segregation behavior of Zn and how their interplay affects GB cohesion.

Here, we study the local atomic structure and composition down to the nanoscale in a  $\Sigma 5(310)[001]$  tilt GB in a bicrystal of body centered cubic (bcc) Fe at different levels of Zn segregation. By atomically resolved microscopic probing techniques, we systematically explore the local variation in Zn content at the GB in relation to the distribution of trace impurities B and C. We find that Zn forms nanometer sized segregation lines in a region preceding the former solid-liquid interface. Both B and C are homogeneously distributed across the GB plane, but their concentration profiles show a wide distribution extending away from the GB region. The atomic structure of the GB is largely distributed by GB defects and even shows local variations in GB habit plane distribution. The local Zn concentration is reaching levels of  $\geq 30 \text{ at.}\%$ , while only a weak sign of Zn segregation is measured in a region of  $\sim 30 \mu\text{m}$  away into the bulk bicrystal. We use ab-initio calculations in combination with thermodynamic segregation models to explore the impact of trace impurities on the segregation behavior of Zn and its effects on GB cohesion. A global observation of the obtained segregation energies, considering interaction between Zn and B, indicates that the presence of B is strongly reducing the tendency of Zn segregation. However, this effect is depending on the GB type and the specific site Zn occupies within the GB structure. Furthermore, the thermodynamic model suggests that B reduces the overall Zn concentration at the GB due to strong repulsive interactions even in regions with high bulk Zn concentration. The calculated work of separation of modeled GBs indicates that B compensates for the reduction in the work of separation even for high Zn concentrations of  $\sim 20 \text{ at.}\%$ . Our work suggests that trace impurities of B and C hinder the segregation of Zn into a  $\Sigma 5(310)[001]$  tilt GB in bcc-Fe and with this mitigate the embrittling tendency of Zn. These insights may provide pathways to make use of naturally occurring trace impurities in Fe alloys to prevent LME.

## 5.7 Results

### Global grain boundary structure

We use a bicrystal containing a  $\Sigma 5(310)[001]$  tilt GB with low amounts of impurity elements of B and C to study Zn segregation from the liquid state into the



GB and the interaction of Zn with the impurities [18]. We formed a diffusion couple of Zn and the bicrystal and subsequently annealed it at 800°C to liquefy the Zn reservoir and enable diffusion of Zn into the solid Fe bicrystal as schematically shown in Fig. 5.14a. The BSE-SEM image in Fig. 5.14b shows a two-phase region at the interface between the former liquid Zn reservoir and the Fe bicrystal consisting of  $\alpha$ -Fe (bcc) and  $\Gamma$ -Zn (see Fig. 5.15b). Here, we limit our observations to the GB below this two-phase region. We specifically focus on two different GB areas indicated as “Region 1”, which is Zn-rich with an average concentration of Zn determined by SEM-EDS of  $\sim 5.5$  at.%, and “Region 2” with an average Zn content of  $\sim 0.5$  at.% (see Fig. 5.14b). Region 1 is  $\sim 5$   $\mu\text{m}$  below the two-phase region and HAADF-STEM imaging along the [001] tilt axis reveals that the GB inclination is locally deviating from the exact (310) habit plane (see Fig. 5.14c). Corresponding STEM-EDS measurements shown in Fig. 5.14d demonstrate strong segregation of Zn to the GB and suggest that it is inhomogeneously distributed along the GB. The GB in Region 2, which is  $\sim 30$   $\mu\text{m}$  away from the two-phase region, is curved and exhibits a high density of local kinks as shown in Fig. 5.14e. Zinc is only slightly enriched at the GB in region 2 as shown in the elemental map in Fig. 5.14f.

### Near atomic scale zinc segregation

We performed near atomic resolution STEM-EDS elemental mapping in the Zn-rich Region 1 of the bicrystal. Figure 5.16 shows atomic resolution STEM images at 300 keV and 120 keV and the associated Zn distribution along the GB. The HAADF-STEM image in Fig. 5.16 reveals that the GB structure appears disrupted by a high density of GB defects. The corresponding Zn elemental map shows inhomogeneous distribution of Zn with a concentration peak of  $\sim 30$  at.%. The bulk Zn concentration was determined to  $\sim 5.5$  at.% and is in good agreement with our SEM-EDS analysis of Region 1 (see Fig. 5.14b). Reducing the acceleration voltage shows a better resolution, where Zn is forming a regular segregation pattern of Zn-rich ( $\sim 35$  at.%) and Zn-lean ( $\sim 10$  at.%) regions within the GB with a regular spacing of  $\sim 3$ -4 nm as shown in Fig. 5.16b. Although Zn ( $Z = 30$ ) has a slightly higher atomic number  $Z$  than Fe ( $Z = 26$ ), the corresponding HAADF-STEM as well as LAADF-STEM images do not show any indication of regions with higher intensity. Instead the ABF-STEM shows a higher intensity at the GB.

To obtain further insights into the 3D arrangement of the Zn segregation and its correlation to the distribution of the impurity elements B and C, we performed

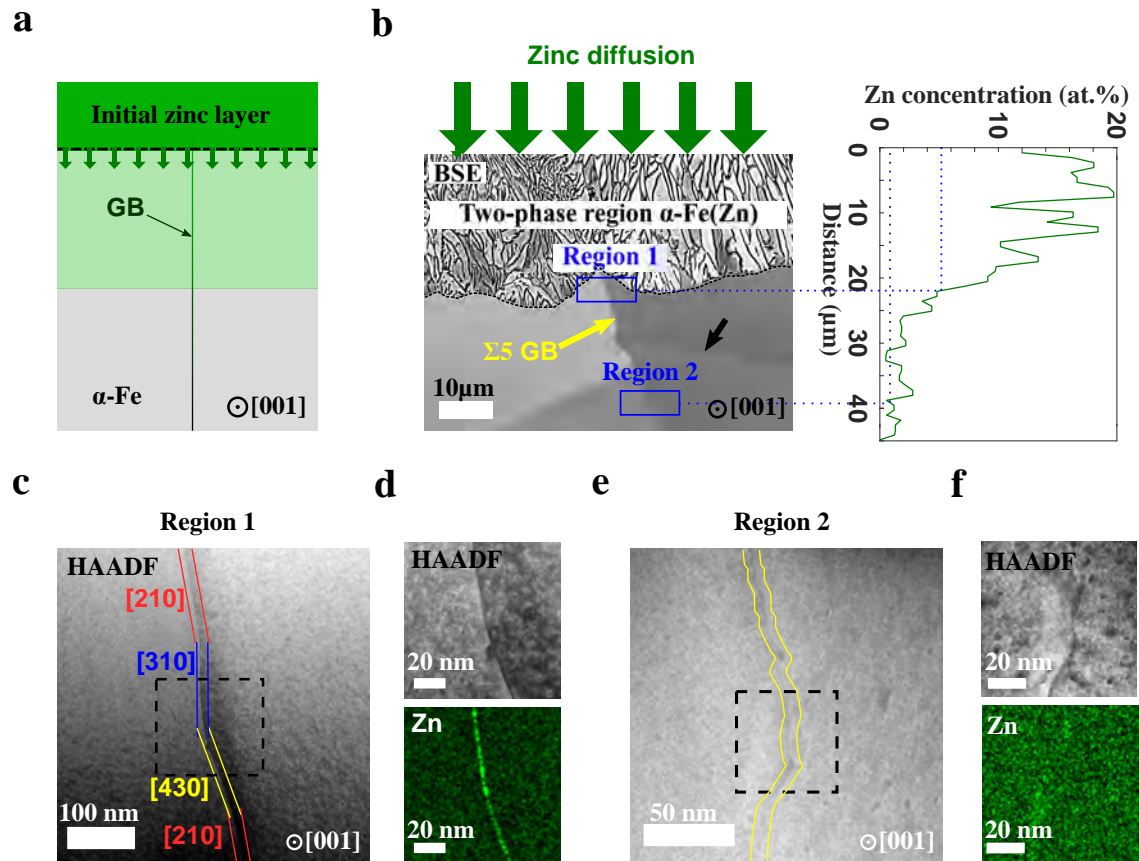


**Figure 5.14: Overview BSE images of the  $\Sigma 5$  [001] GB.** The diffusion of Zn results in the formation of a two-phase region containing  $\alpha$ -Fe and  $\Gamma$ -Zn phases. STEM specimens were extracted from two regions (indicated by blue rectangles). **a** Region 1 marks the area of the GB at the vicinity of the two-phase region. **b** Region 2 is  $\approx 30 \mu\text{m}$  away from the two-phase region. Further, in **b** is seen a low-angle GB (indicated by a black arrow) intersecting with the  $\Sigma 5$  GB and locally bending it. **c-d** Region 1: **c** HAADF-STEM image of the  $\Sigma 5$  viewed along the [001] tilt axis. The GB is inclined and the boundary plane can be divided into nearly symmetric (210), (430) and (310) segments. **d** STEM-EDS mapping of the region, which is indicated in **c** by a black dashed rectangle. The GB is enriched by Zn with a weak decrease from top to bottom. **e-f** Region 2: **e** HAADF-STEM image shows strong inclinations of the boundary. **f** Corresponding STEM-EDS map of the black dashed rectangle region shows no clear enrichment of Zn.

atom probe tomography (APT) experiments from the same regions as our STEM investigations.

### Grain boundary composition<sup>1</sup>

Figure 5.17a presents the reconstructed 3D-volume of the needle-shaped specimen viewed along the [001] tilt axis extracted from Region 1 (Zn-rich), where the GB is

<sup>1</sup>The APT data acquisition and analysis was done by Dr. Xuyang Zhou.

positioned at a  $45^\circ$  angle  $\sim 100\text{ nm}$  away from the apex. Besides the segregation of Zn, a clear indication of B and C segregation can be observed at the boundary. The 3D atom map of B shows a rather unusual behavior in the form of a tail that extends into the lower grain for nearly 50 nm. The concentration profile of B extracted across the GB in Fig. 5.17b verifies this observation, which will be discussed later. According to APT, the bulk concentration of Zn is  $\sim 5.5\text{ at.}\%$  in agreement with the STEM-EDS measurements (Fig. 5.16). The averaged GB concentration of Zn reaches a value of  $\sim 10\text{ at.}\%$ . Note, this concentration is lower than our STEM-EDS measurements, because the cylinder to extract the concentration has a diameter of  $30\text{ nm}$ . However, the Zn patches with concentrations  $\geq 30\text{ at.}\%$  are few nm big. Similar to our previous results on the Zn-free GB (see Sec. 5.1), the Al concentration decreases to  $\sim 2.7\text{ at.}\%$  at the GB due to the presence of B and C [18]. Both concentration profiles of B and C show a broadened and asymmetric shape with a tail towards the left side corresponding to the lower grain in the reconstruction (Fig. 5.17a). The peak concentration of B and C is reduced by a factor of  $\sim 4$  and  $\sim 10$ , respectively, compared to the initially investigated GB before Zn segregation [18]. A close inspection of the peak locations of the concentration profiles reveals an offset of the B peak of  $\sim 1\text{ nm}$  with respect to that of the Zn concentration peak. A similar behavior was obtained in a different APT specimen as shown in the Fig. 5.18. Deeper analysis allows information about the IE  $\Gamma_i$  of solute  $i$ , which describes the number of atoms per unit area at interfaces [152]. It is  $\Gamma_{\text{Zn}} \approx 16.2\text{ atoms/nm}^2$ , where  $8\text{ atoms/nm}^2$  would correspond to one monolayer at the  $\Sigma 5(310)$  GB.

Observations of the in plane distribution of Zn within the GB obtained by APT reveals that Zn is arranged in the form of segregation lines which are aligned along the  $[001]$  tilt axis, while B and C are homogeneously distributed within the GB as shown in Fig. 5.17c. A similar modulation in Zn concentration across these segregation lines as observed by STEM-EDS (Fig. 5.16) into Zn-rich and -lean regions is noticed by APT as shown in Fig. 5.17d.

APT investigations were also performed in Region 2 showing a much lower average bulk Zn content of  $\sim 0.5\text{ at.}\%$ , where STEM-EDS measurements only gave a slight hint for Zn segregation (see Fig. 5.14f). Figure 5.19a shows the 3D APT reconstruction of Zn, B and C in Region 2 of the bicrystal. The GB is clearly enriched in B and C with peak concentration values of  $\sim 1.8\text{ at.}\%$  and  $\sim 1\text{ at.}\%$ , respectively, shown in Fig. 5.19b. However, no clear sign of Zn segregation is found. In comparison to the Zn-rich Region 1 of Fig. 5.17b, the peak B and C concentration at the GB in

the Zn-lean Region 2 is nearly a factor of 4 higher, similar to values obtained in the initial as-grown bicrystal [18]. Furthermore, the concentration profiles of B as well as C adopt a symmetric shape, in contrast to that observed in Region 1 (Fig. 5.17b).

### Atomic grain boundary structure

To explore the underlying atomic GB structure in both Region 1 (Zn-rich) and 2 (Zn-lean), we used atomic resolution HAADF-STEM imaging as shown in Fig. 5.21. The HAADF-STEM overview image of the GB in Region 1 shown in the Fig. 5.20a reveals a slight curvature of the GB, which leads to the formation of different nanoscale GB facets with varying GB planes close to  $(3\ 1\ 0)$ . The atomic resolution images of Fig. 5.21a and b show that the GB structure is composed of kite-type structural units, which are disrupted by GB defects. Locally, the GB habit plane is modulating between  $((3\ 1\ 0))$ - and  $(2\ 1\ 0)$ -type as well as asymmetric GB segments.

The GB in Region 2 (Zn-lean) is composed of nanofacets with different GB plane inclinations (see Fig. 5.14e and Fig. 5.20b). Figure 5.18b shows an overview HAADF-STEM image of the GB in Region 2, where the GB alternates between symmetric  $(2\ 1\ 0)$  and asymmetric segments. The atomic GB structure shown in Fig. 5.21c shows a near  $(3\ 1\ 0)$  GB with kite-type structural units, which are interrupted by GB steps or dislocations (highlighted by dashed cyan circles) to compensate for deviations in GB inclination. In other areas in Region 2 the GB is dissociating into a nanofaceted structure (see Fig. 5.21d). This strong inclinations could only be explained with the diffusion of Zn. For comparison the same bicrystal but without Zn was annealed under the same conditions. The atomic structure of the GB does not show any inclinations (see Fig. 5.22).

### Co-segregation of Zn and B

In order to explore the interaction of B and Zn, their influence on segregation and cohesive energies, we performed first principles DFT calculations<sup>2</sup> of the  $\Sigma 5(3\ 1\ 0)$  as well as  $\Sigma 5(2\ 1\ 0)$  GBs. The GB structures with all possible segregation sites considered for Zn (green) and B (blue) atoms are displayed in Fig. 5.23a and b. The segregation energies of Zn  $E_{seg}^{Zn}$  with and without interstitial B for the  $\Sigma 5(3\ 1\ 0)$  and  $(2\ 1\ 0)$  GBs are shown in Fig. 5.23c and d. Zinc alone has a similarly high segregation energy for its lowest energy position at  $z = 0\ \text{\AA}$  in a substitutional site within the

---

<sup>2</sup>All DFT calculations were performed by Dr. D. Scheiber.

GB plane for both GBs of  $-0.57\text{ eV}$  and  $-0.58\text{ eV}$ , respectively. However, if B is present the overall segregation energies of Zn are strongly reduced (see the cyan triangles). For example, the presence of B lowers the segregation energy of Zn at the GB center position ( $z = 0\text{ \AA}$ ) by a factor of  $\sim 6$  to  $-0.09\text{ eV}$  for the  $\Sigma 5(310)$  GB. Only for Zn farthest away from the GB considered here at  $z = \pm 2\text{ \AA}$  a slightly higher  $E_{seg}^{Zn}$  of  $-0.30\text{ eV}$  is obtained. A similar trend is observed for the  $\Sigma 5(210)$  GB, where the segregation energies are reduced by a factor of  $\sim 2-3$  in the presence of B. A possible configuration with Zn at  $z = 0\text{ \AA}$  with nearly the same segregation energy as without B is found. This suggests that the  $\Sigma 5(210)$  GB shows a slightly higher probability for Zn to segregate with B being present than the  $\Sigma 5(310)$  GB.

Based on the calculated segregation energies, we estimate the enrichment of Zn at the GB at  $800^\circ\text{C}$  using the White-Coghlan isotherm [27]. This allows us to explore the influence of the bulk Zn concentration and the impact of B on the expected amount of Zn at the GB in the theoretical high temperature limit, which corresponds to the annealing temperature of the bicrystal diffusion couple. Since both the  $\Sigma 5(310)$  and  $(210)$  GBs show a similar minimum segregation energy of Zn alone, the Zn concentration is predicted to be nearly the same at both GBs. It increases monotonically with increasing Zn bulk content as shown in Fig. 5.23e (green dots). When B is also present at the GBs, a strong reduction of the maximum Zn content can be observed for both interfaces. For the  $\Sigma 5(310)$  GB (solid lines) a reduction in the Zn concentration from  $85\text{ at.}\%$  to  $30\text{ at.}\%$  is observed for a bulk Zn concentration of  $5.5\text{ at.}\%$ , which corresponds to the Zn-rich Region 1 in the experiments. A similar trend is observed for lower Zn bulk contents. The reduction in GB Zn concentration is less pronounced for the  $\Sigma 5(210)$  boundary as illustrated in Fig. 5.23e (dashed lines). These predictions indicate that B does not only strongly reduce the segregation energies, but with this also significantly lowers the maximum attainable Zn content at the GBs within the thermodynamic limit at the annealing temperature.

### Grain boundary cohesion

To assess the effects of co-segregation of Zn and B on GB cohesion, we calculated the theoretical work of separation  $W_{sep}$  for the  $\Sigma 5(310)$  and  $\Sigma 5(210)$  GBs as shown in Fig. 5.23f. Both GBs show very similar cohesive properties in the pure state without any solutes present resulting in a work of separation of  $3.5\text{ J/m}^2$ . With the addition of a single B atom (corresponds to a half monolayer), the co-

hesive energy increases to 4.3 and  $4 J/m^2$  for the  $\Sigma 5(310)$  and the  $\Sigma 5(210)$  GB, respectively. This is an enormous increase in cohesion by up to 23% in comparison to the unalloyed GB. We then investigated the effects of Zn additions to the GBs and found that the  $W_{sep}$  decreases almost linear for both GBs, albeit with a steeper slope for the  $\Sigma 5(310)$  GB. For the case when no B is present at the GBs, four Zn atoms lower the work of separation to  $2.3 J/m^2$  for the  $\Sigma 5(310)$  GB. It should be noted that from the total number of atoms in Fig. 5.23a, one Zn atom would correspond to 10 *at.%*. The reduction of  $W_{sep}$  is less pronounced for the  $\Sigma 5(210)$  GB with the same number of Zn atoms to  $3 J/m^2$ . However, as shown in Fig. 5.23b the number of substitutional atoms at the GB are higher and one Zn atom corresponds to 6.25 *at.%*. If both B and Zn are considered, it is found that the cohesion reducing effects of Zn are compensated by the presence of B. Even when three Zn atoms are added to both GBs, the work of separation is still higher than that of the pure interfaces. This shows that the effect of impurity atoms on GB cohesion is to a large extent purely additive.

From these observations clear implications can be established for GB-based alloy design to prevent LME. The natural abundance of B and other impurity elements as well as controlling their content through alloying strongly reduces the tendency for Zn segregation. The presence of cohesion enhancing elements such as B counteracts Zn embrittlement, while the reduction in Zn content through B by itself mitigates the detrimental properties of Zn.

## 5.8 Discussion

In this study, the nanoscale segregation behaviour of Zn in the presence of B and C at a  $\Sigma 5(310)[001]$  bcc-Fe tilt GB was investigated. It is found that Zn is forming a periodic, line-type segregation pattern with nanometer periodicity in regions with high Zn bulk concentration. This decomposition into Zn-rich and Zn-lean regions can be attributed to GB defects. Furthermore, it is observed that the impurity element B strongly reduces the segregation tendency of Zn to the GB and with this its maximum concentration at the interface. Boron is even capable of compensating for the tendency of Zn to embrittle the GB for relatively low B concentrations. These insights may provide novel pathways of utilizing impurity elements as a tool to prevent LME.

The observed modulations in Zn-rich ( $\sim 35 \text{at.}\%$ ) and Zn-lean ( $\sim 15 \text{at.}\%$ ) regions

along the GB may originate from the role of GB defects in the formation of this Zn segregation pattern. These Zn modulations alone would lead to local fluctuations in the work of separation along the GB, given the results obtained by DFT. Such local compositional variations at GBs have not been taken into account to explain the origins of LME or GB fracture [103, 204, 208, 222–231].

From APT it is observed that the impurity elements B and C are homogeneously distributed within the GB plane in the same area. However, their peak concentration is reduced compared to the as-grown bicrystal [18]. The asymmetric segregation profiles of B and C indicate that the GB has migrated during the annealing treatment either induced by Zn segregation [88, 102, 232] or through the triple line, where the GB connected to the liquid Zn reservoir during annealing [233].

Following our first-principles calculations, the strong repulsive interactions between B and Zn lead to a significant reduction in the segregation tendency of Zn in the presence of B. This ultimately leads to a reduction in the maximum Zn concentration at the GB, which by itself has a positive effect on GB cohesion [234, 235]. Furthermore, the trends in calculated cohesive properties of the GB clearly indicate that even lower levels of B comparable to those observed experimentally are capable to compensate for the embrittling effects of Zn. Since both B and C are known to enhance GB cohesion [17, 159, 160, 167], our calculated values for the work of separation only considering B are a lower bound and it is expected that C has a similarly positive effect on GB cohesion [20, 234, 236].

While LME is a complex, hierarchical process leading to material failure by the ingress of liquid metal along GBs, it has been indicated that GB composition and local co-segregation effects ahead of the crack tip are decisive in the underlying mechanisms [210, 215, 237]. Razmpoosh et al. [210] suggested that segregation effects on GB cohesion can be attributed to electronic structure modifications, which so far remain unexplored. However, we show that the evolving GB composition and intrinsic elemental interactions are crucial in understanding their effects on GB cohesion.

## 5.9 Conclusion

Our work emphasizes the role of cohesion enhancing impurity elements such as B and C and how they can be used to prevent GB failure induced during Zn induced LME. Impurity elements are typically scarce, but an abundant source in engineering alloys

that is rarely used for material engineering. Two regions of the  $\Sigma 5 [001] (310)$  GB with different Zn bulk concentrations (about 5.5 *at.*% and 0.5 *at.*%) were investigated with STEM-imaging, STEM-EDS and APT. The Zn-rich region showed nanometer size spaced Zn columns with concentrations of  $\geq 30$  *at.*%. This nanoscale segregation patterning can be due to the presence of GB defects. Our structural investigations showed nanofacetting of the GB with varying (310) and (210) as well as asymmetric planes. The SU at the GB is still kite-type, but they are more disrupted by GB defects as the Zn-free GB. On the other hand, the Zn-poor region was showing stronger facetting, with shorter facet lengths. Analysis on Zn segregation gave only a hint on a weak segregation of Zn. The ab-initio DFT calculations reveal that B hinders Zn segregation and compensates for its loss in GB cohesion. The results demonstrate that impurity segregation can mitigate the embrittling effects of Zn by hindering its segregation to GBs and leveling its reduction in GB cohesion.



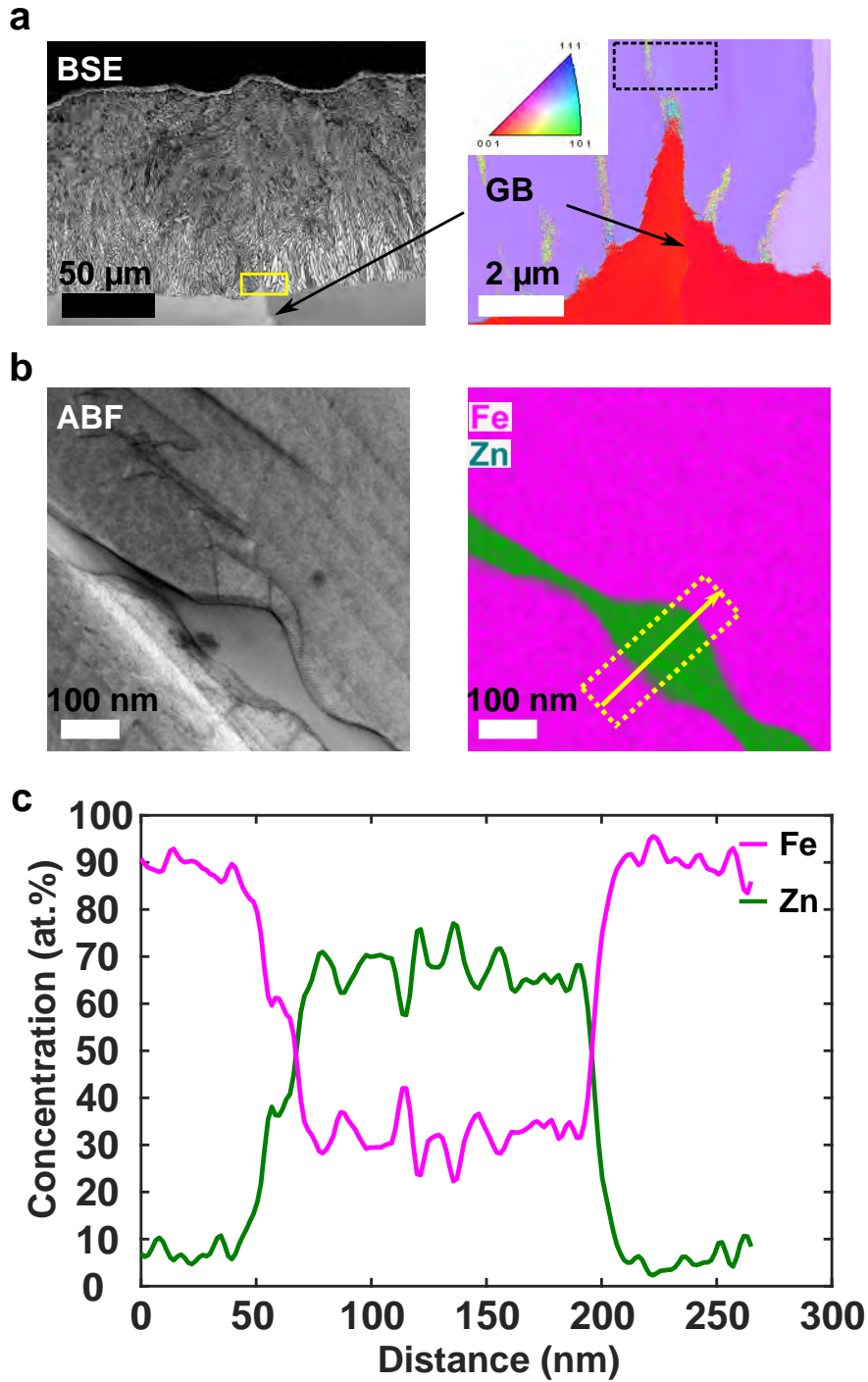


**Figure 5.15: Microstructural characterisation** **a** A BSE image shows the formation of a two-phase region, which extended up to  $\approx 150 \mu\text{m}$ . The out-of plane inverse pole figure shows orientation of the two-phase region to be close to  $[012]$ , while the  $\alpha$ -Fe region maintained the  $[001]$  direction. TEM specimen were extracted from the black dashed box. **b** ABF-STEM image and corresponding STEM-EDS mapping of the GB show the GB completely dewetted and transformed into a Zn-rich phase. The line profile in **c** shows a concentration of  $\approx 40 \text{ at.}\%$  Zn.

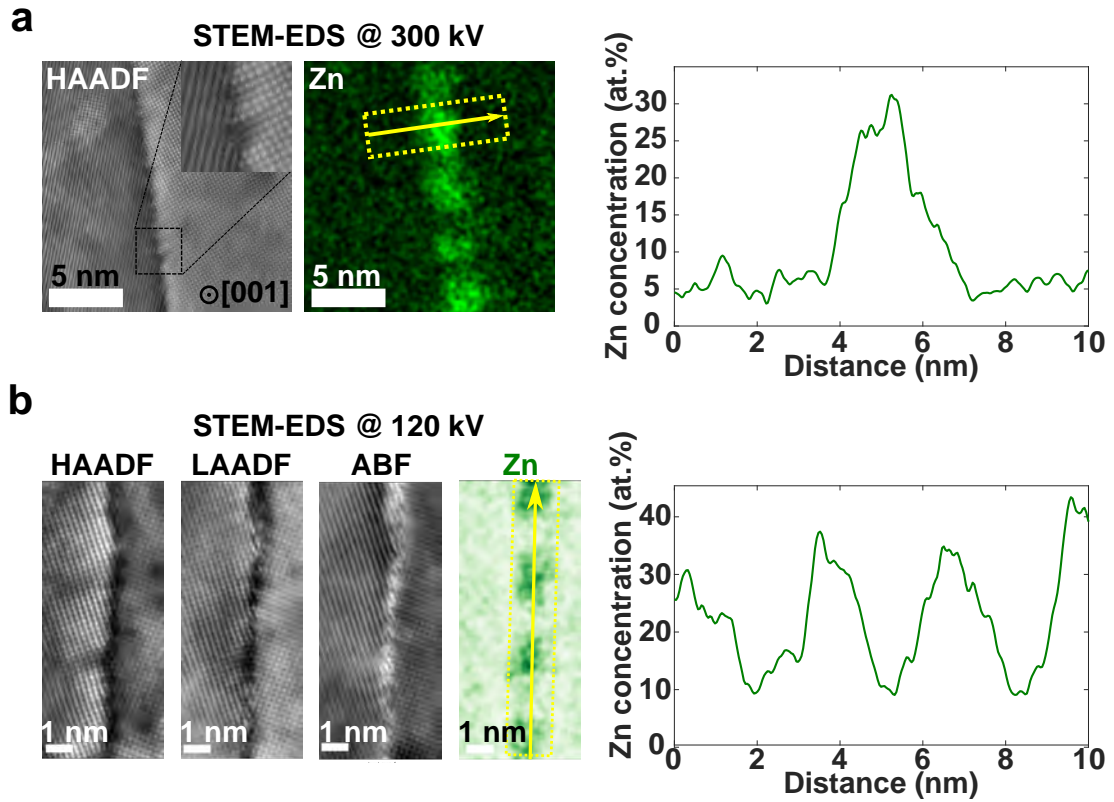


**Figure 5.16: High resolution STEM-EDS at different acceleration voltages.** **a** The HAADF-STEM and corresponding Zn elemental map show formation of Zn clusters with concentrations of  $\approx 30$  at.%. To improve the STEM-EDS resolution, the acceleration voltage was reduced to 120 kV as shown in **b**. The incident electrons are scattered to lower angles due to the presence of the Zn clusters resulting in a dark contrast in the HAADF- as well as LAADF-STEM image but a bright contrast in the ABF-STEM image. The Zn concentration profile along the GB shows a periodicity of 3 – 4 nm with concentrations varying from 10 at.% to 40 at.%.

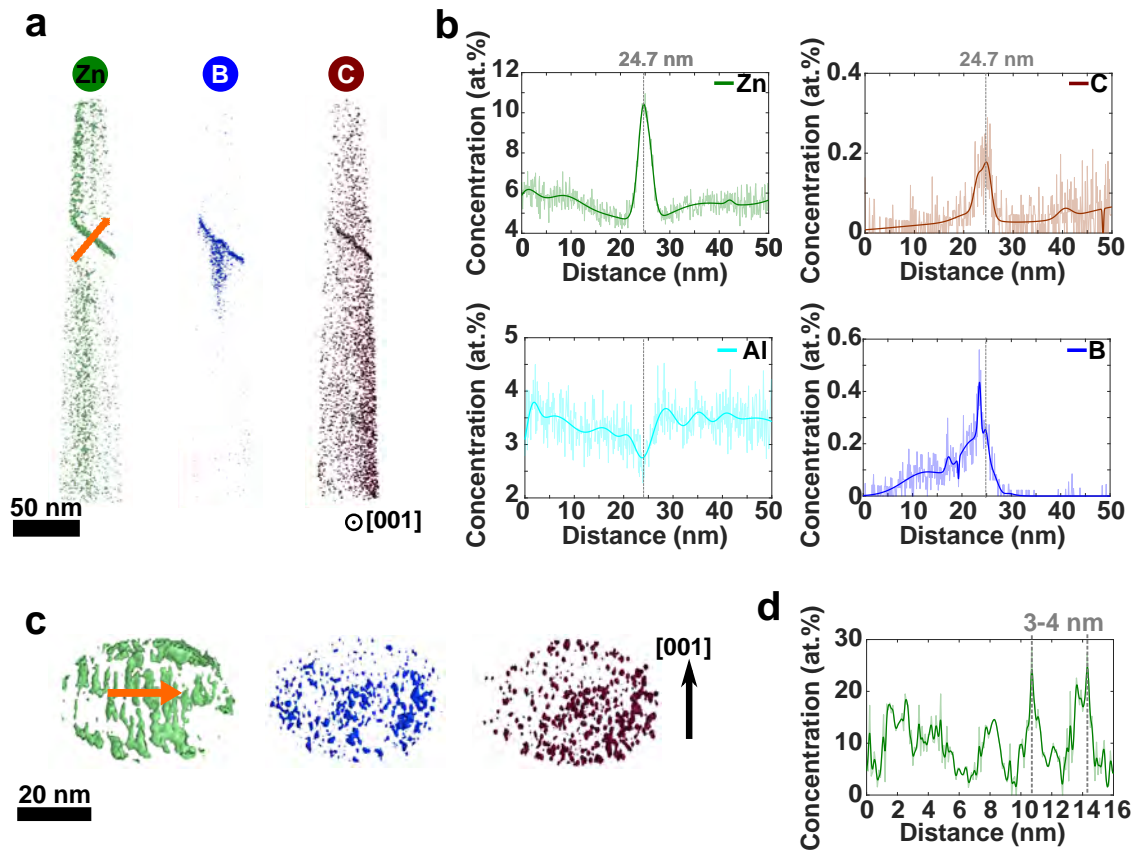


**Figure 5.17: Segregation of Zn, B, C and depletion of Al at the  $\Sigma 5$  [001] GB of region 1** **a** 3D APT reconstruction showing the distribution of Zn, B and C viewed along the [001] tilt axis. Using an iso-concentration value of 10 *at.%* for Zn, 0.5 *at.%* for B and 0.3 *at.%* for C highlights the segregation of these elements to the GB. **b** The composition profile extracted from a cylindrical region with diameter of 30 *nm* is extracted across the GB (shown as orange arrow in **a**). A clear increase of Zn, B and C is shown at the GB, while the concentration of Al decreases. The maximum concentration peak of Zn and C is at 24.7 *nm*, while B concentration reaches the maximum already at 23.5 *nm* same as the minimum of Al. The Zn concentration first decreases slightly at the vicinity of the boundary until it increases steeply. The C and B concentration do not show such decrease at the vicinity of the GB. The B concentration shows a continuous increase over a large range of several tens of *nm* before reaching the maximum value and then it decreases abruptly to nearly 0 *at.%*. **c** Rotation of the APT reconstruction in **a** such that the distribution of Zn, B and C onto the GB plane is shown, i.e. the viewing direction is along the GB plane. While B and C show no formation of patches, Zn forms columnar patches elongated along the tilt axis. **d** A concentration profile extracted along the orange arrow in **c** shows the concentration and distances of Zn columns.

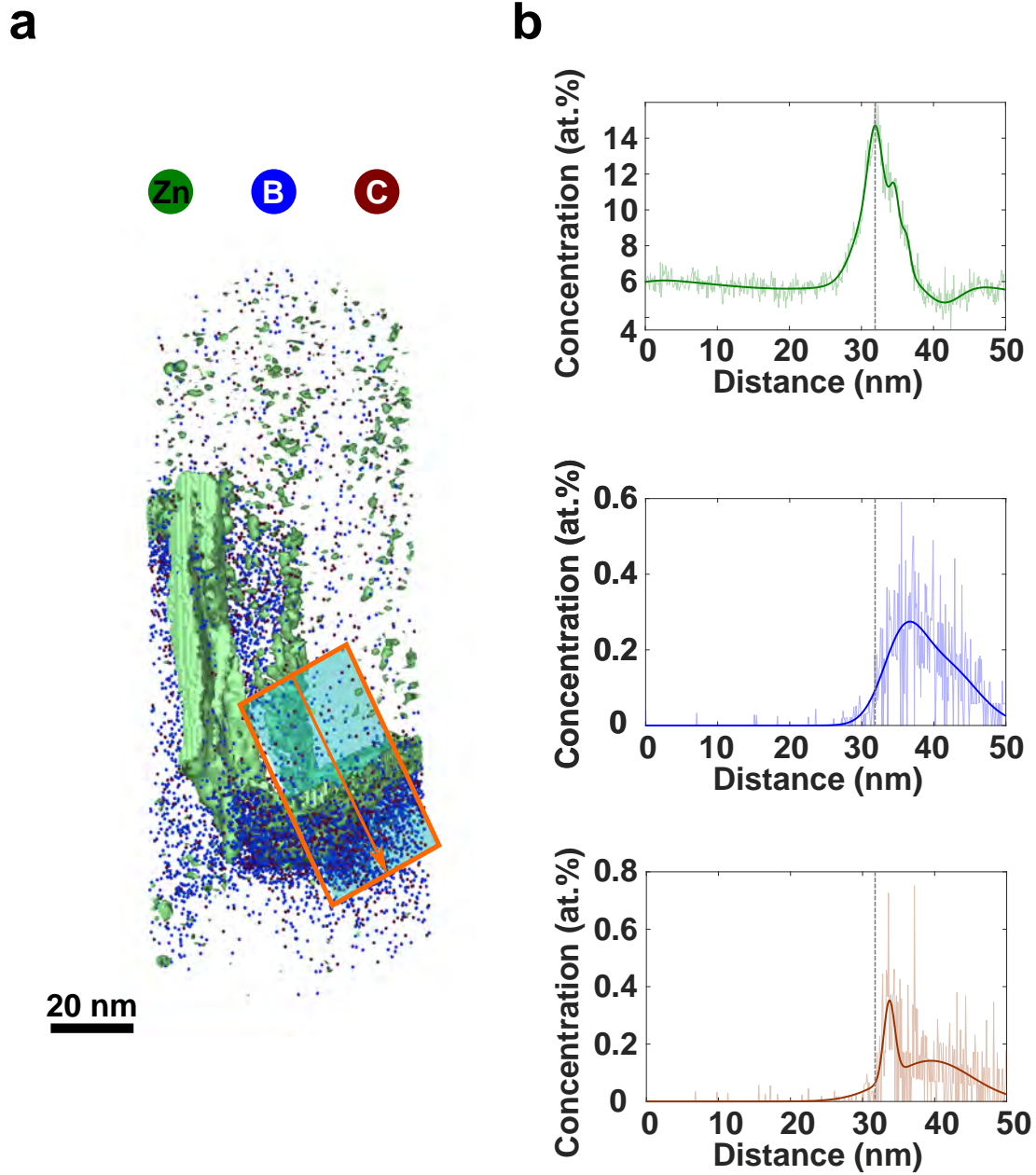


**Figure 5.18: Segregation of Zn, B and C at the  $\Sigma 5[001]$  GB of region 1** a 3D APT reconstruction of showing the segregation of Zn, B and C at the GB. The GB is split into two parts connected through a large step, which is also enriched with Zn A concentration profile across the bottom GB is shown in b. bStrong segregation of Zn and a moderate enrichment level of B and C of  $\leq 0.5$  at.%. The Zn distribution shows a stronger depletion into the right grain, where the concentration peak of B and C are located. The latter elements show a tail into the right grain.

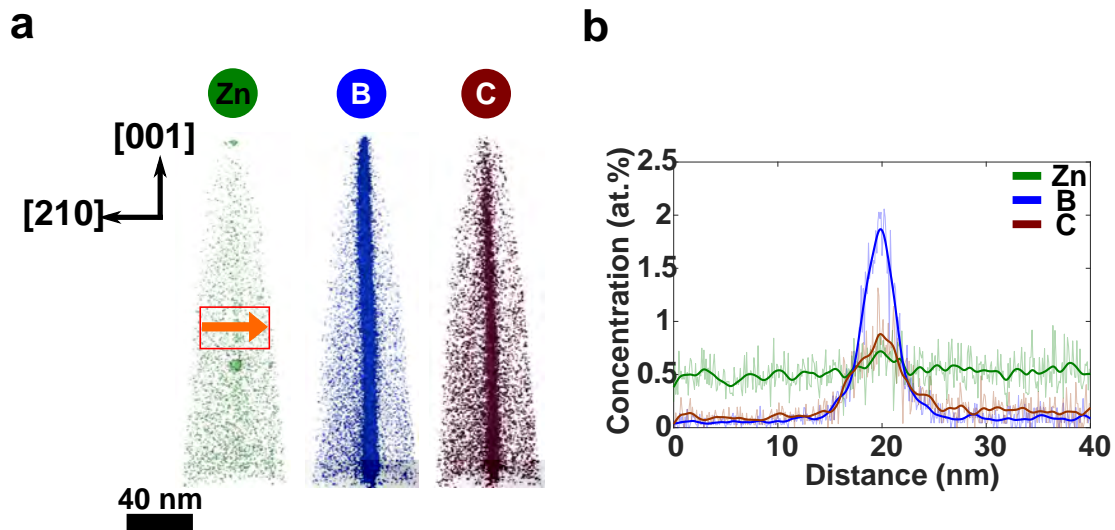


**Figure 5.19: Segregation of Zn, B, and C at the  $\Sigma 5$  [001] GB of region 2.** **a** 3D APT reconstruction showing the distribution of Zn, B and C. The [001] tilt axis shows upwards. Using an isoconcentration value of 0.5 at.% for Zn and B and 0.3 at.% for C highlights the segregation of these elements to the GB. **b** The composition profile extracted from a cylindrical region with diameter of 30 nm is extracted across the GB (shown as orange arrow in **a**). A clear increase of B and C is shown at the GB, while the concentration of Zn stays unchanged. The maximum concentration peak of B and C is at the same position of  $\approx 18.5$  nm. Both elements show a symmetric concentration profile.

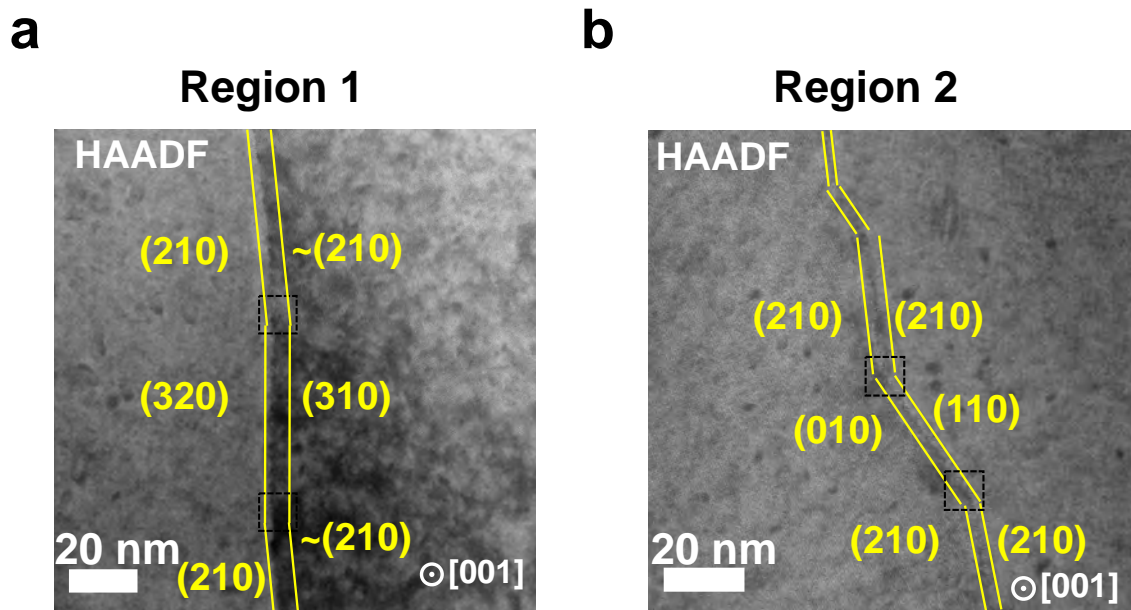


**Figure 5.20: HAADF-STEM of the  $\Sigma 5$  [001] GB from region 1 and 2** **a** Overview HAADF-STEM image showing the inclinations of the GB from nearly symmetric (210) into an asymmetric configuration of (320)/(310) boundary planes. The dashed square indicates the region analyzed at atomic level shown in Fig. 5.21a and b. **b** Overview HAADF-STEM image of the GB from the region 2. The GB inclines from symmetric (210) into an asymmetric configuration of (010)/(110) boundary planes.

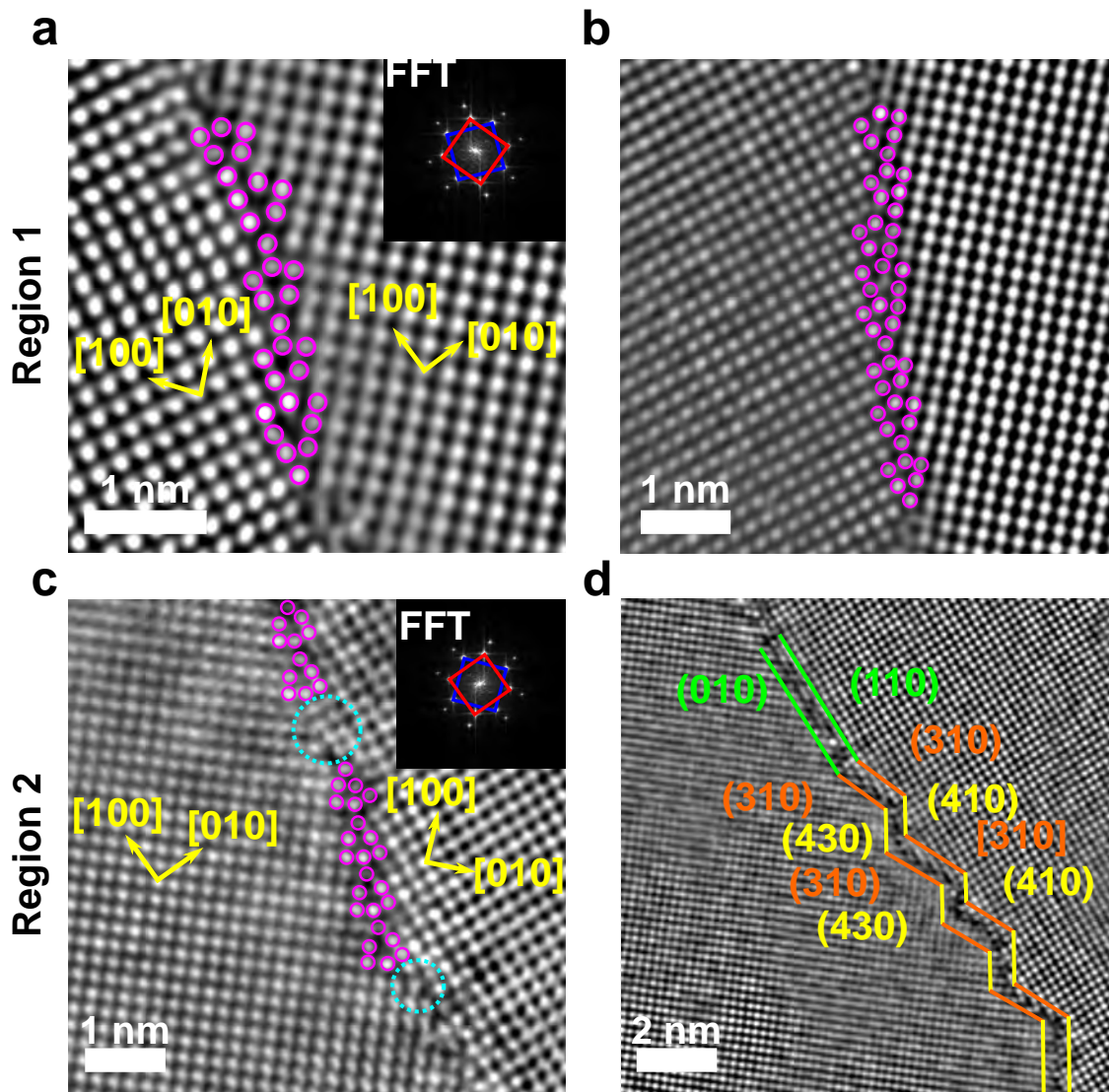


**Figure 5.21: Atomic structure of the  $\Sigma 5[001]$  GB in the Fe-4at.%Al bi-crystal.** **a,b** High-resolution HAADF-STEM images from region 1 shows the formation of kite-type structural units (purple color), where extra atoms are introduced to shift the SU parallel and perpendicular to the boundary plane normal. From the FFT in **a** the misorientation angle is determined to  $40^\circ$ . **c** High-resolution HAADF-STEM images from region 2 of the area marked by the upper dashed square in 5.18b. The GB consists of perfect kite-type SU interrupted by GB defects, which result in the inclination of the boundary. **d** High-resolution HAADF-STEM image of the region marked by the lower dashed square in 5.18b. The GB is faceting into symmetric (310)/(310) and asymmetric (430)/(410). The scale bar in **a,b** and **c** 1 nm and in **d** 2 nm.

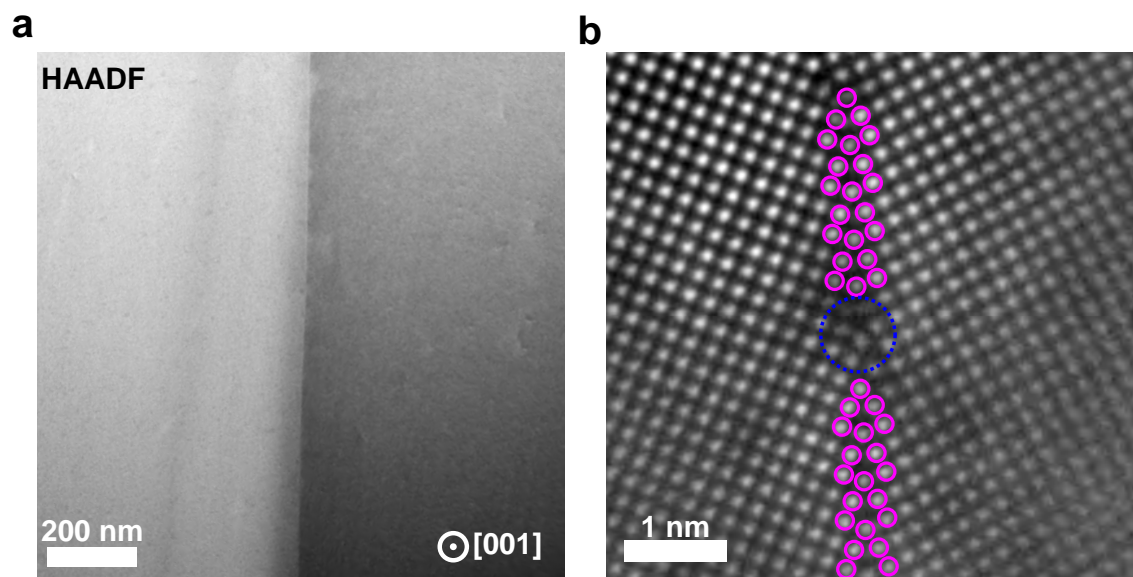


**Figure 5.22: Influence of annealing on GB structure** **a** HAADF-STEM overview image of the GB shows no inclinations of the GB. **b** The atomic-resolved HAADF-STEM image shows the kite-type SUs of the GB with a symmetric  $(310)$  boundary plane. The GB contains small defects highlighted by a blue dashed circle. The Scale bar in **a** is  $200\text{ nm}$  and in **b** it is  $1\text{ nm}$ .



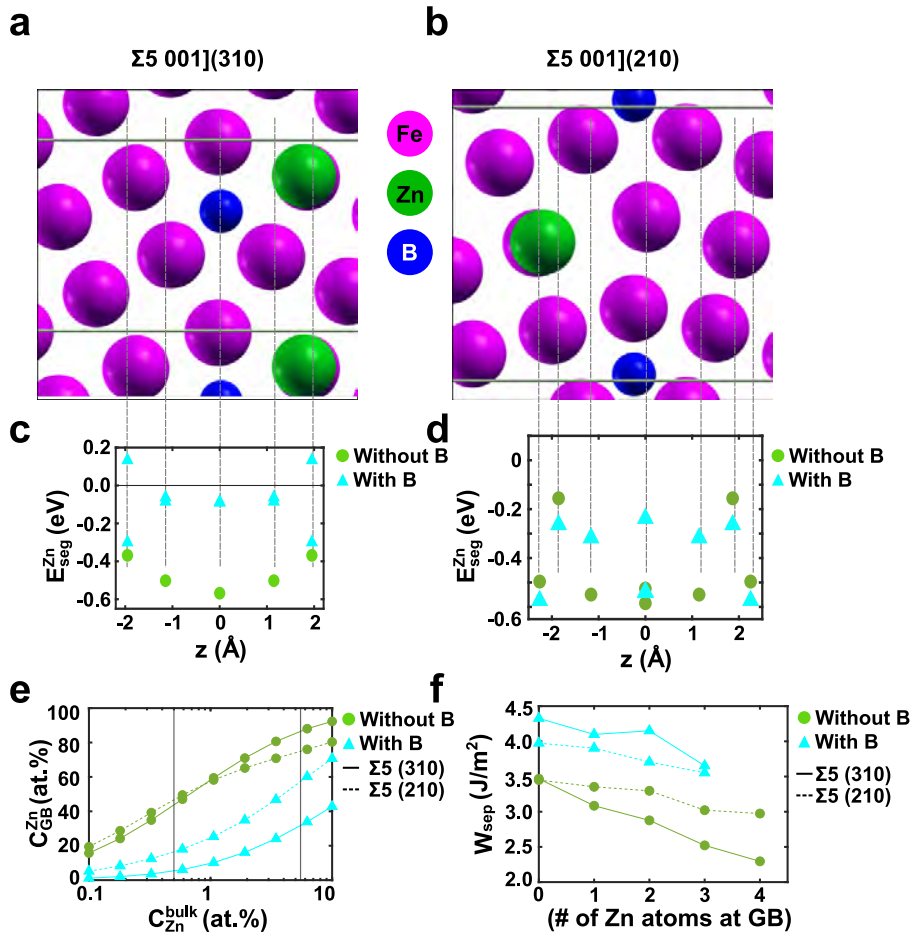


**Figure 5.23: Modelling of Zn segregation to  $\Sigma 5$  [001] GB with and without B.** Atomic structure of  $\Sigma 5$  [001](310) (a) and of  $\Sigma 5$  [001](210) GB with interstitial B (blue) and substitutional positions (purple = Fe, green = Zn). c Zn segregation energies from DFT for Zn to pure GB (green circles) and to GB when B is present (cyan triangles). d Zn segregation energies from DFT for Zn to pure GB (green circles) and to GB when B is present (cyan triangles). e Zn concentration at the GB as a function of the Zn bulk concentration modelled for  $\Sigma 5$  [001](310) (solid line) as well as  $\Sigma 5$  [001](210) (dashed line) GB. For both GBs the enrichment level was calculated with (cyan) and without (green) B. The vertical lines highlight the observed Zn concentrations in bulk - namely 0.5 at.% and 5.5 at.%. f Modelled GB cohesion for different number of Zn atoms at  $\Sigma 5$  [001](310) (solid line) and  $\Sigma 5$  [001](210) (dashed line) GB with (cyan) B and for GBs where B is not present (green).

## 5.10 Formation of nanocrystalline grain boundary oxides in a bcc-Fe-4 at.%Al bicrystal promoted by Mn diffusion

This section is based on:

A. Ahmadian, C. H. Liebscher and G. Dehm “Formation of nanocrystalline grain boundary oxides in a bcc-Fe-4 at.%Al bicrystal promoted by Mn diffusion”, *Unpublished*.

## 5.11 Introduction

In the past, the automotive industry has focused on the development of steels with high strength and ductility [238]. In recent years, however, the focus has been on reducing the weight of cars in order to minimize fuel consumption and emissions of greenhouse gases without any loss of ductility or strength [239]. Weight reduction is obtained either by reducing the size of the car bodies or their density. The latter one is achieved by incorporating lighter elements such as Al [38, 168, 239, 240]. Rana et al. [168] showed that addition of 6.8 wt.% Al in Fe decreases the density by 7.5%. This is due to an expansion of the crystal lattice. Recently, ferritic lightweight Fe-Al-Mn-C steels were developed containing low amount of Al and Mn to form a duplex ( $\alpha+\gamma$ )-phase microstructure. The low amount of Mn is used to enhance the deoxidizing effect of Al at low bulk concentrations [240–243]. Steels with a duplex phase microstructure are known to exhibit higher strength and ductility than single phase steels [244]. To obtain a duplex microstructure, the alloy is processed by several thermomechanical steps in oxygen (O) or water vapor environments, e.g. hot rolling [245]. These heat treatments can lead to the oxidation of the steel and hence, the formation of an outer oxide layer but even internal oxidation features. If the diffusivity of O into the material is higher than the diffusivity of the alloying elements such as Al or Mn to the free surface, internal oxides will form underneath

the surface [246].

Internal oxidation can occur inside the bulk or along grain boundaries (GBs) [247–250]. The latter case leads to a weakening of the GB [251, 252]. Therefore, GB oxidation needs to be prevented to avoid GB embrittlement and intergranular cracking. Phaniraj et al. [253] carried out SEM studies by means of EBSD and EDS on a polycrystalline ferritic stainless steel. They found out that  $\Sigma$  boundaries have a stronger resistance to oxidation than random GBs, whereby the angular deviation  $\Delta\Theta$  from the ideal  $\Sigma$ -boundary is an important key factor for the resistivity. The resistivity increases for smaller  $\Delta\Theta$ . Similar results were also found in the Ni-Fe alloys [254, 255]. It should be mentioned that the formation of oxides along the GB depends strongly on the underlying atomic structure of the boundary [83].

In the case of  $\text{Al}_2\text{O}_3$ , there are different metastable polymorphs besides the stable  $\alpha$ - $\text{Al}_2\text{O}_3$ . Depending on the arrangement of the O-anions, the metastable aluminas can be divided into a fcc or hcp packing [256]. The  $\text{Al}_2\text{O}_3$  structures based on fcc packing are  $\gamma$ ,  $\eta$ ,  $\Theta$  and  $\delta$ , while the phases  $\kappa$ ,  $\alpha$  and  $\chi$  are based on a hcp packing [257]. The difference of the  $\gamma$ -,  $\delta$  and  $\Theta$ - $\text{Al}_2\text{O}_3$  is the distribution of the  $\text{Al}^{3+}$  cations. For  $\Theta$ - $\text{Al}_2\text{O}_3$  it is well known that the  $\text{Al}^{3+}$  cations occupy in equal amounts octahedral and tetrahedral sites [258]. For  $\gamma$ - and  $\delta$ - $\text{Al}_2\text{O}_3$  the situation is more complex, because of their highly defective structure and coexistence. This phenomenon makes it challenging to analyse the crystallographic structure of the  $\gamma$ - and  $\delta$ - $\text{Al}_2\text{O}_3$  [257, 259–261]. Recently, Kovarik et al. [259] performed atomic-resolved HAADF-STEM imaging on the  $\delta$ - $\text{Al}_2\text{O}_3$  polymorph. Their studies show the appearance of two highly intergrown structures  $\delta_1$ - and  $\delta_2$ - $\text{Al}_2\text{O}_3$ , which have an orthorhombic (space group  $\text{P}2_1\text{P}2_1\text{P}2_1$ ) and a monoclinic (space group  $\text{P}2_1$ ) structure and lack in a long-range periodicity along one principal direction. Furthermore, they found out from DFT calculations that the  $\delta_1$ -,  $\delta_2$ - and  $\Theta$ - $\text{Al}_2\text{O}_3$  have similar enthalpy of formation. This is the reason, why these phases coexist simultaneously.

Due to the limited knowledge on the structure and composition of GB oxide phases, it is crucial to understand their formation mechanisms and impact on material properties. Hence, an atomic-scale characterization is needed, which was done for a special GB here. In this work, we study GB oxidation in a ferritic Fe-4.%Al bicrystal coated with Mn and high vacuum annealed at 700 °C for 72 hours. Previous studies on the bicrystal with a  $\Sigma 5$  [0 0 1] (3 1 0) GB showed a depletion of Al at the GB due to the segregation of B and C [18]. The formation of nanocrystalline oxides with a  $\text{Al}_2\text{O}_3$  core and a FeAlMnO shell were found by SEM-EDS and STEM-

EDS. Moreover, the oxide-free GB showed no Al and Mn and the atomic structure showed kite-type SUs.

## 5.12 Results

The diffusion couple of Mn and Fe-4 *at.*%Al bicrystal was annealed at 700 °C to allow the diffusion of Mn into the sample. Figure 5.24a schematically represents the setup of the diffusion process, where the [001] tilt axis is oriented upwards. As shown in the SE-micrograph in Fig. 5.24b the Mn diffused  $\approx 18 \mu\text{m}$  into the bicrystal. Figure 5.24c shows a closer look using the BSE signal of this region. Narrow secondary phases with lateral width of  $\leq 0.5 \mu\text{m}$  formed in the bulk as well as at the GB. The Al- and Mn-elemental maps from SEM-EDS indicate that these secondary phases are enriched with Al and Mn as shown in Fig. 5.24d. Cross-section TEM specimen were extracted from the region around the GB including the secondary phases to investigate the segregation level of Mn and Al at the GB.

Figure 5.25a shows an overview HAADF-STEM image, viewed along the common [001]-direction of the neighboring grains. The indicated GB (red line) as well as the grains are decorated with precipitates. The corresponding ABF-STEM image (Fig. 5.25b) shows a high density of dislocations around the precipitates. These dislocations are induced by the formation of the secondary phases. In order to understand the elemental distribution, STEM-EDS elemental maps shown in Figure 5.26a-d indicate that the precipitates are rich in Al, Mn and O but depleted in Fe. However, the distribution of these elements is not uniform within a single precipitate. Especially the precipitate center corresponding to a location close to the GB core here only contains Al and O, but no Mn ( see Fig. 5.26b and c). The concentration profile across the precipitate in Fig. 5.26e shows an increase of Mn from 0 *at.*% in the bulk to  $\approx 9 \text{ at.}\%$  in the outer shell of the precipitate. This concentration drops to zero in the precipitate core. The Al concentration also starts with a 0 *at.*% bulk concentration and increases to a maximum concentration of  $\approx 40 \text{ at.}\%$  in the precipitate core. The O concentration here reaches a value of  $\approx 60 \text{ at.}\%$ , while the concentration of Fe decreases to 0 *at.*% in the core. It should be mentioned that the absolute O content need to be approached with caution due to absorption effects on the corresponding low X-ray energy. However, these measurements indicate that an Al<sub>2</sub>O<sub>3</sub> formed at the GB that has a shell of a MnFe-oxide.

In order to determine the Al<sub>2</sub>O<sub>3</sub> phase, electron energy-loss near-edge structure

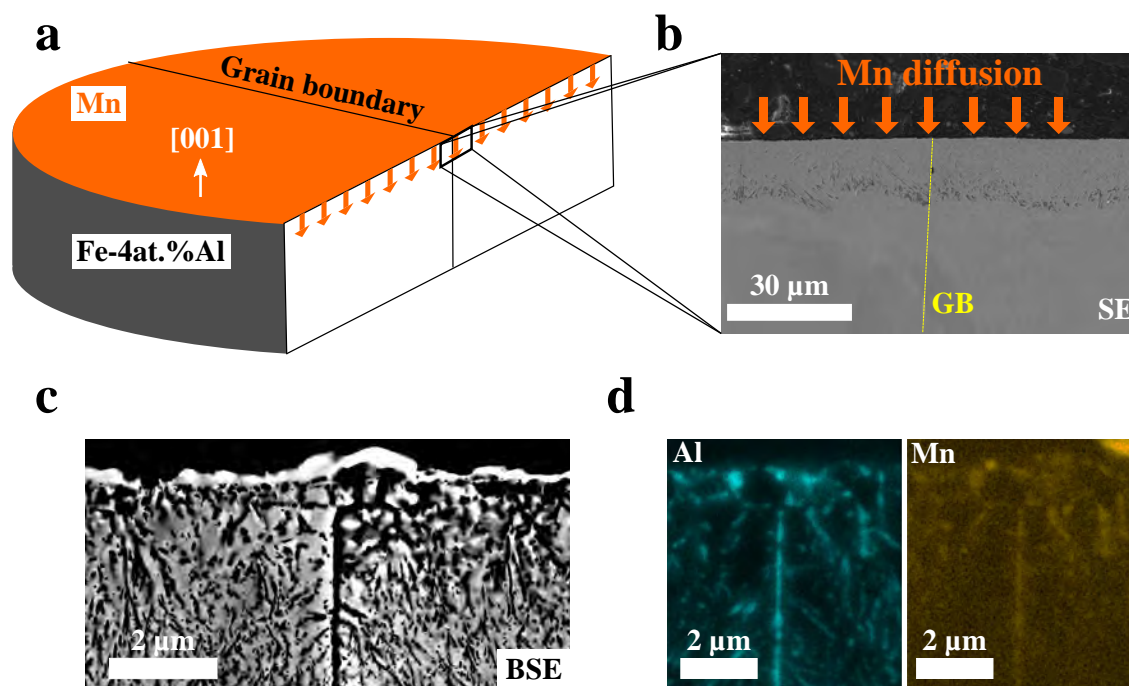


**Figure 5.24: SEM-EDS analysis of the  $\Sigma 5 [001] (310)$  GB.** **a** Schematic representation of the diffusion experiment, where the Mn layer was deposited onto the (001) surfaces of the bicrystal. By annealing the Mn atoms diffuse into the material. **b** SEM overview micrograph of the  $\Sigma 5 [001] (310)$  GB after Mn diffusion along the [001]-tilt axis. The GB is marked by a yellow line. **c** The BSE image near the surface shows formation of secondary phases. **d** The corresponding EDS elemental maps of Al and Mn show the enrichment of the GB as well as AlMn-rich secondary phases in the bulk. The scale bar in **b** is  $30 \mu\text{m}$  and in **c** as well as **d** is  $2 \mu\text{m}$

(ELNES) of the EEL spectra can be analyzed. Figure 5.27 shows the ELNES of the Al  $L_{2,3}$  and O-K edges recorded over a GB precipitate (blue). For comparison, Fig. 5.27 shows also the spectra of  $\alpha$ -,  $\gamma$ - and  $\delta$ - $\text{Al}_2\text{O}_3$  taken by Levin et al.[262]. For  $\alpha$ - $\text{Al}_2\text{O}_3$  the ELNES of the Al  $L_{2,3}$  edge is sharp (see Fig. 5.27a). In  $\alpha$ - $\text{Al}_2\text{O}_3$  the O- anions are arranged in a hexagonal close-packed lattice and the  $\text{Al}^{3+}$ -cations occupy two-third of the octahedral interstitial sites of the O sublattice. In contrast, the ELNES of the Al  $L_{2,3}$ -edge of the GB oxide shows a broadening of the intense peak similar to  $\gamma$ - and  $\delta$ - $\text{Al}_2\text{O}_3$ . Closer view on the  $\gamma$ - $\text{Al}_2\text{O}_3$  spectrum in Fig. 5.27a shows a weak shoulder at lower energy loss of the Al  $L_{2,3}$ -edge, which is missing in the  $\delta$ - $\text{Al}_2\text{O}_3$ . This shoulder corresponds to  $\text{Al}^{3+}$ -ions occupying tetragonal sites. Therefore, the measured spectrum of the GB oxide is in good agreement with the Al  $L_{2,3}$  edge of the  $\delta$ - $\text{Al}_2\text{O}_3$ . The corresponding ELNES of the O-K edges are shown in Fig. 5.27b. The O-K edge of the GB oxide shows no pre-edge, so that beam damage in form of radiolysis and/or formation of O-O bonds at the surface are not forming.

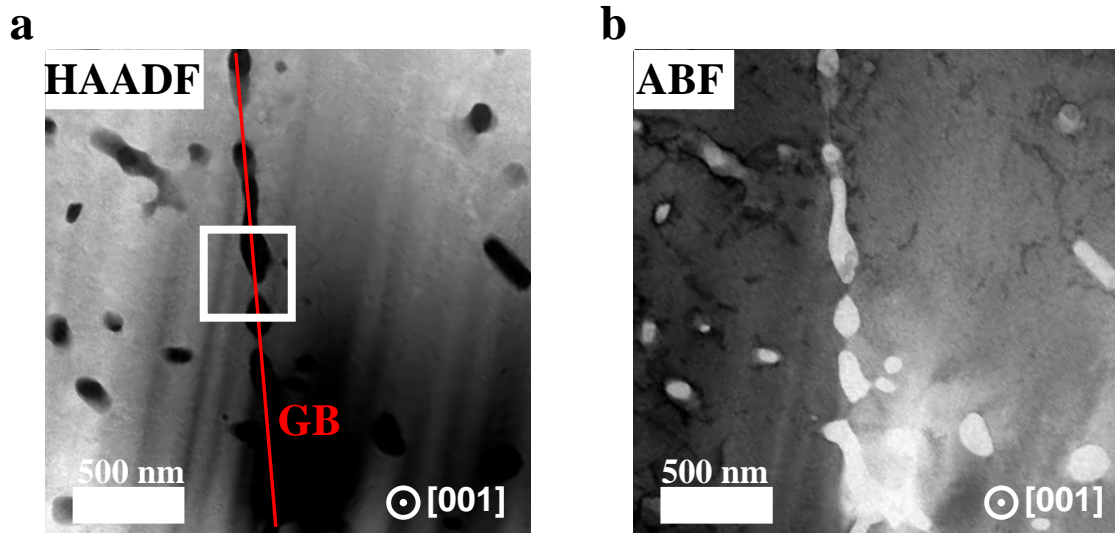


**Figure 5.25: Overview HAADF-STEM image.** **a** HAADF-STEM overview image of the GB indicated by a red line. The GB as well as the grains are decorated with secondary phases. The corresponding ABF-STEM image in **b** shows a higher fraction of dislocations around the secondary phases. Closer inspections were done on the region marked by a white box in **a**. The scale bar in **a** and **b** is 500 nm.

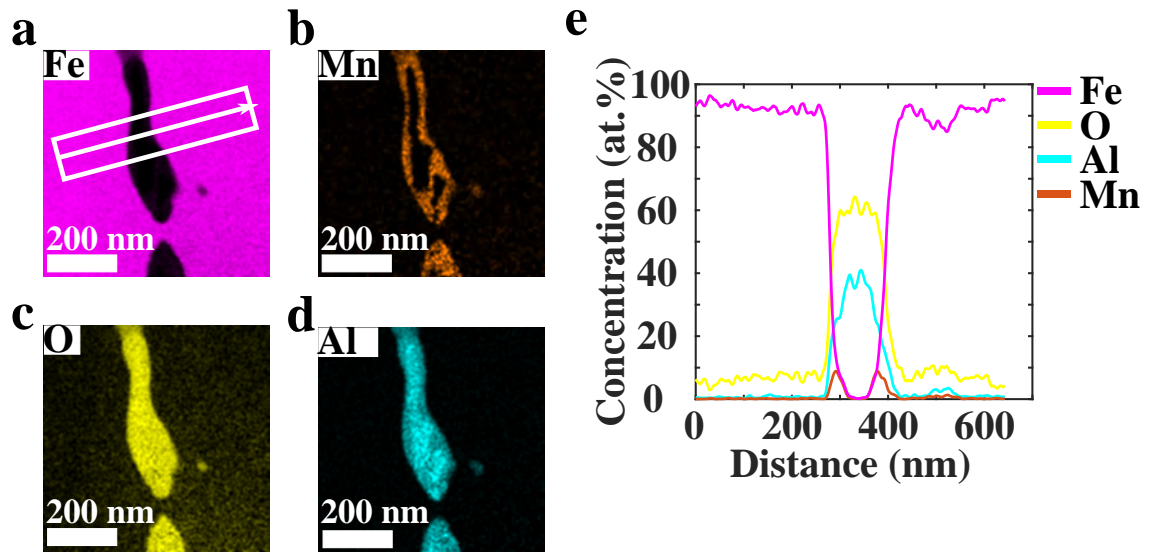


**Figure 5.26: STEM-EDS analysis of the GB precipitates.** **a-d** STEM-EDS elemental map for Fe, Mn, Al and O are show the enrichment of the core with Al and O, while Mn is enriched at the shell of the precipitate. **e** shows the corresponding concentration profile across the precipitate, which is indicated by a white arrow in **a**. Mn reaches a maximum concentration of  $\approx 9$  at.% at the shell, while Al and O reach a maximum of 40 at.% and 60 at.% at the center of the precipitate. The precipitate core is free of Fe. The scale bar in **a-d** is 200 nm.

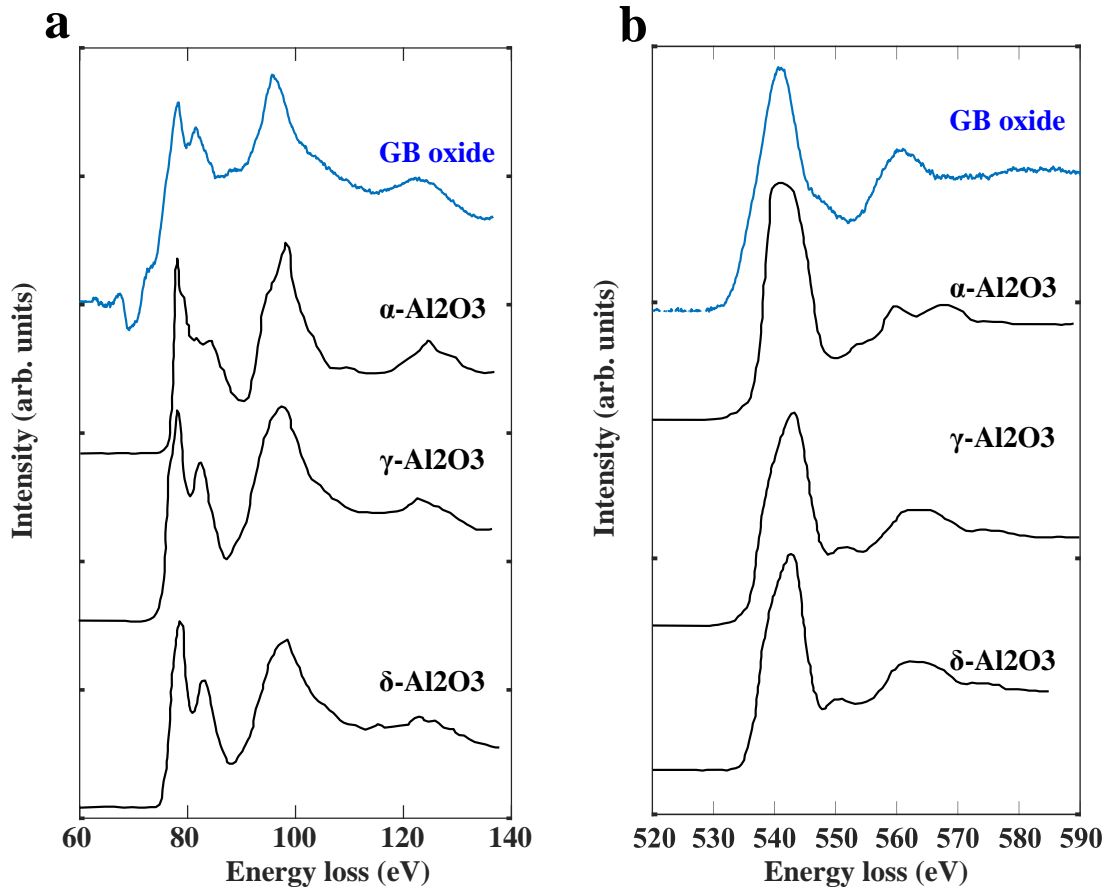


**Figure 5.27:** EELS analysis of GB oxide. **a** ELNES of Al  $L_{2,3}$ -edge and **b** O-K edge measured (blue spectrum) at the GB oxide. The black spectra were recorded from bulk  $\alpha$ -,  $\gamma$ - and  $\delta$ - $\text{Al}_2\text{O}_3$  by Levin et al.[262].

The shape of the broad peak appearing at around  $560\text{ eV}$ , which is also found in  $\gamma$ - and  $\delta$ - $\text{Al}_2\text{O}_3$  but not in  $\alpha$ - $\text{Al}_2\text{O}_3$ . However, the main intense peak at  $\approx 545\text{ eV}$  in  $\gamma$ - and  $\delta$ - $\text{Al}_2\text{O}_3$  is asymmetric, while our spectrum shows a symmetric peak similar to the  $\alpha$ - $\text{Al}_2\text{O}_3$ . Furthermore, the  $\gamma$ - and  $\delta$ - $\text{Al}_2\text{O}_3$  have a small peak at about  $560\text{ eV}$ , which is absent in the spectrum of the GB oxide.

In order to understand the structure of the GB oxide, HRTEM imaging as shown in Fig. 5.28a of the  $\text{Al}_2\text{O}_3$  core reveals domains with different orientations and grain sizes of  $\leq 20\text{ nm}$ . The corresponding FFT shown in Fig. 5.28b also confirms the nanocrystalline nature of the oxide. Additionally, the pattern in Fig. 5.28b suggest a complex superstructure of different phases with different lattice parameters.

Figure 5.29a shows the GB region between two oxides. Despite the GB inclination of  $\approx 8^\circ$  from the ideal  $(3\ 1\ 0)$ -plane, the arrangement of the atoms at the GB show of kite-type SUs (see Fig. 5.29). As already seen in Fig. 5.26, no Al and Mn is found

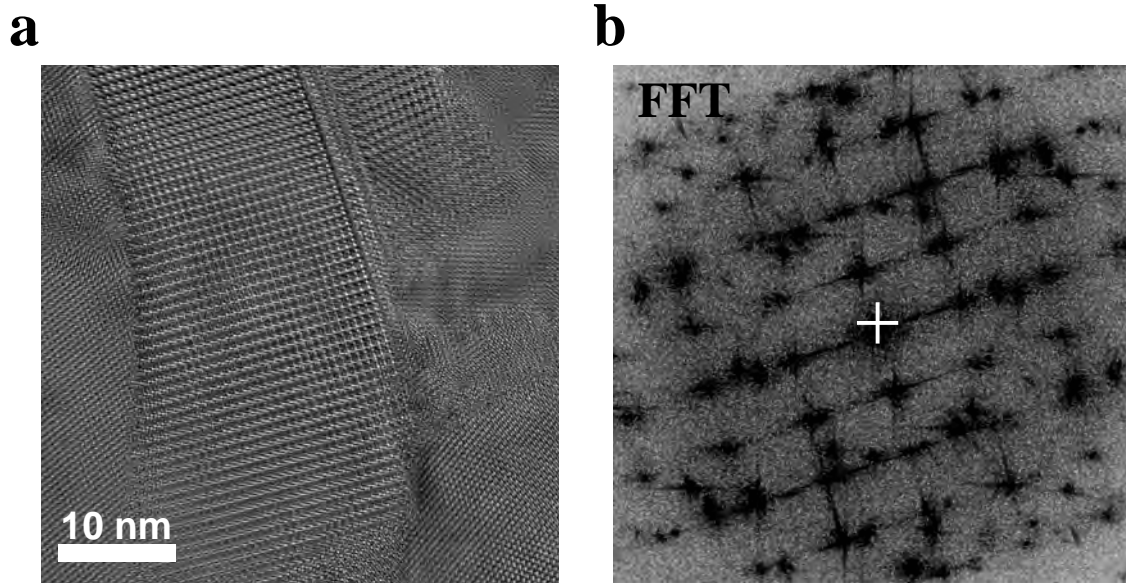


**Figure 5.28: HRTEM imaging and corresponding FFTs of the GB precipitate core**  
**a** HRTEM image of the GB core viewed along the  $[001]$ -axis of the  $\alpha$ -Fe grains shows different oriented domains. The corresponding FFT image in **b** confirms the nanocrystalline nature. The scale bar in **a** is 10 nm.

in this regions. This is confirmed by comparing the STEM-EDS spectra of two areas marked by blue and red rectangle in Fig. 5.29a. In Fig 5.29b the red spectrum shows the spectrum from the region around the GB and the blue spectrum from the oxide shell. No Mn- and Al-K peaks are detected at the GB region between the oxide precipitates, while a strong Al-K and Mn-K peaks as well as a decreased Fe-K peak are seen in the blue spectrum.

## Discussion

In this work the precipitation of oxides at a  $\Sigma 5 [001] (310)$  GB in  $\alpha$ -Fe-4 at.%Al was studied after diffusion of Mn. Both the grains as well as the GB show oxides, which range to a depth of  $\approx 18 \mu\text{m}$ . Auinger et al.[263] evaluated the internal oxidation of different Fe-based ternary alloys by annealing at  $700^\circ\text{C}$  for 1 hour in Ar/2.5 vol.%H<sub>2</sub>/0.94 vol.%H<sub>2</sub>O. For Fe-2.22 wt.%Mn-1.%Al, oxides formed at a depth of  $2.4 \mu\text{m}$  into the grains and  $8.2 \mu\text{m}$  along the GB. Extrapolating the oxidation depth for 72 hours would give  $20.4 \mu\text{m}$  oxidized length within the grains, which is a bit larger than our observations. However, it should be mentioned that our experiments were done in high vacuum with a pressure  $p \approx 10^{-5} \text{ mbar}$ , while the work



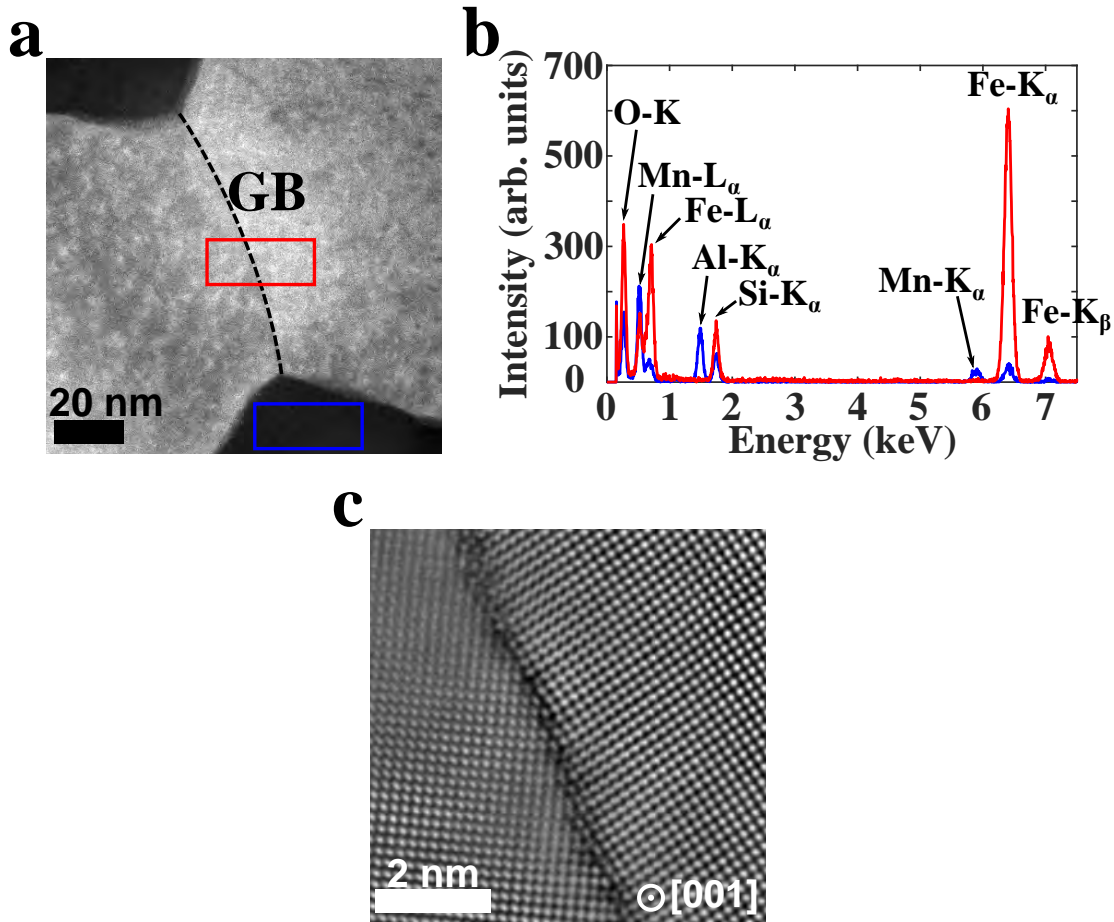


**Figure 5.29: Atomic structure of the GBa** HAADF-STEM image of the precipitate-free GB shows a slight inclination of  $\approx 8^\circ$  from the ideal  $(310)$  direction. STEM-EDS spectra taken from the oxide and outside the oxide around the GB are shown in **b**. The GB area shows no sign of Al and Mn. **c** High-resolution HAADF-STEM of the GB shows kite-type SUs. The scale bar in **a** is  $20\text{ nm}$  and  $2\text{ nm}$  in **c**.

of Ainger et al.[263] were done in a humid environment. Further, their analysis did not show whether Al or Mn or both oxidized. Our investigations showed the formation of  $\text{Al}_2\text{O}_3$  surrounded by a MnO shell at the  $\Sigma 5$  GB. The origin of the internal oxidation is not fully understood. Since the internal oxidation is limited to the area where Mn has penetrated, it can be assumed that there is a relationship between Mn diffusion and internal oxidation. This is supported by our previous studies, where the bicrystal without Mn was annealed at  $800^\circ\text{C}$  for  $80\text{ hours}$  in the same high-vacuum furnace and it showed no internal oxidation of the GB (see Fig. 5.22). One possible explanation is that Mn (hydr)oxidized before annealing, so that Mn was promoting the diffusion of oxygen or hydroxide into the bicrystal. The reason, why  $\text{Al}_2\text{O}_3$  core formed can be explained with the Ellingham-Richardson diagram

[264, 265]. At  $700^{\circ}\text{C}$  the  $\text{Al}_2\text{O}_3$  has a lower enthalpy of formation than for  $\text{MnO}$ . Therefore, the  $\text{MnO}$  will be reduced by the  $\text{Al}_2\text{O}_3$ .

The presented ELNES spectra of the Al  $L_{2,3}$  of the GB oxide corresponds well with the reported [262]  $\delta\text{-Al}_2\text{O}_3$  polymorph. The shoulder, which appears at about  $73\text{ eV}$  in Fig 5.27a corresponds to metallic Al. However, the same analysis on the O-K edge does not uniquely identify the  $\delta\text{-Al}_2\text{O}_3$ . It seems to be a superposition of the  $\alpha$ - and  $\delta\text{-Al}_2\text{O}_3$  phase. It should be mentioned that besides the polymorphs shown in Fig. 5.27, there are also other metastable phases such as  $\Theta$ ,  $\eta$  or  $\kappa$ . From the work of Kovarik et al. [259] it is known that different variants of the  $\delta\text{-Al}_2\text{O}_3$  structure and the  $\Theta$ -phase can coexist in a bulk oxide. This was confirmed by HRTEM images of the GB oxide core showing a complex nanocrystalline superstructure. It is known that in general the orientation of GB precipitates depend on the GB character (misorientation and inclination angle) and atomic structure [10]. Our results show that multiple orientations occur at GB oxides. Outside the oxides, the GB showed inclinations away from the ideal  $(3\ 1\ 0)$  plane. This inclinations could be responsible for the nanocrystalline structure of the oxides. Even with inclinations, the GB structure maintained the kite-type SUs [18] and no Al and Mn was left in the bulk or the precipitate-free GB because all Al and Mn atoms were bound in the precipitates.

### 5.13 Conclusion

GB oxidation at high temperatures has a detrimental effect on the strength of polycrystalline materials. The oxidation resistance of a GB depends on the misorientation of the adjoining grains and the inclination angle of the boundary with respect to the grains. Here, the diffusion of Mn into a symmetric  $\Sigma 5 [00\ 1]$   $(3\ 1\ 0)$  tilt grain boundary in  $\alpha\text{-Fe-4 at.}\%$  Al bicrystal is evaluated using SEM- and STEM-EDS. Nanoscale oxides formed along the grain boundary and show a core-shell structure. While the core consists of  $\text{Al}_2\text{O}_3$ , the shell is enriched with Mn. Because of the GB precipitated oxides, no Al and Mn was detected in the precipitate-free GB zone. Therefore, the focus was on deeper investigations of the oxide core using ELNES analysis, which showed similarities of  $\delta\text{-Al}_2\text{O}_3$  but there is a possibility of other coexisting phases such as  $\Theta\text{-Al}_2\text{O}_3$ . Furthermore, HRTEM imaging of this polymorphic oxide core was showing a nanocrystalline structure with grain sizes of  $\leq 20\text{ nm}$ . The origin of the nanocrystalline structure could be explained by the inclinations of the GB. Our

studies shed new light on the complex structure of GB oxides, which have not been studied, yet.



## 6 Summary and outlook

The aim of this work was to study the structure and composition of a bcc-Fe GB with respect to the following questions:

1. Why would the usually ductile bcc-Fe become brittle and show intergranular failure when it is alloyed with Al, Zn or Mn?
2. What is the GB segregation profile of these elements and how it would affect the GB structure?
3. How does co-segregation of B and C play a role in the segregation behavior of the solutes?

To answer these questions it is necessary to experimentally characterise the GB down to the atomic scale. For this purpose aberration-corrected (S)TEM imaging was carried out in combination with EDS, EELS and APT<sup>1</sup>. The experimental observations were complemented by first-principles based DFT calculations<sup>2</sup> to extract deeper information about the energy and the cohesive properties of the GB before and after segregation.

All investigations were done on a Fe-4 *at.%* Al bicrystal containing a symmetric  $\Sigma 5 [001](310)$  GB, which was grown in-house by the Bridgman method. In Ch. 5.1 the structure and composition of the GB were studied by means of Al segregation. Initially it was assumed by DFT calculations that Al would segregate to the GB. However, our in-depth experimental investigations of the composition revealed that instead of enrichment there was a depletion of Al at the GB. This depletion was due to the presence of B and C, which showed a repulsive interaction with Al. Since B and C have a higher GB diffusivity in bcc-Fe than Al, they will segregate to the boundary first and induce a depletion of Al. Even so, B and C segregated to the GB, the atomic structure of the  $\Sigma 5 [001](310)$  GB was similar to DFT calculations

---

<sup>1</sup>APT experiments were done by Dr. Xuyang Zhou from MPIE

<sup>2</sup>Performed by Dr. D. Scheiber and Prof. Dr. Lorenz Romaner from MCL Leoben

## 6 Summary and outlook

showing kite-type SUs with small disruptions due to GB dislocations and steps/disconnections. It should be emphasized that it was due to the experimental studies that could explain the depletion of Al and answer the above questions.

In Ch. 5.5 the segregation behaviour of Zn was studied. For that a diffusion couple of the Fe-4 *at.*%Al bicrystal and Zn was produced by hot-dip galvanization. The diffusion couple was sealed in a evacuated quartz tube and annealed at 800 °C for 80 hours. The annealing led to the formation of a two-phase zone consisting of  $\alpha$ -Fe and  $\Gamma$ -Zn. Two regions of the GB were further investigated and compared with each other. Region 1 was few  $\mu\text{m}$  below the two-phase zone with a high Zn concentration (5.5 *at.*%). In this region the GB was enriched with nanoscale segregation patterns of Zn. The concentration level of B and C reduced significantly and their distribution has broadened across the GB. This broadening is related to the Zn distribution and is explained by a Zn induced DIGM process. The structure of the GB showed a slight inclination away from the ideal (310) habit plane leading to the formation of nanoscale GB facets. Locally, the GB plane was varying between (310)-, (210) and asymmetric GB segments. The GB structure was composed of kite-type SUs disrupted by GB defects, which could be due to the segregation of Zn inducing structurally complex GB states. In order to understand the influence of Zn on the GB cohesion, DFT calculations were performed with and without the presence of B. The DFT calculations were done only for B because the effect of B and C are similar. With the DFT calculations it was possible to explain the detrimental effect of Zn on GBs by lowering its energy. Segregation of B reduced the tendency for Zn segregation and its concentration at the GB. The DFT calculated value agrees well with the concentration of the Zn clusters. Since B repulsively interacts with Zn, it will hinder the reduction of the GB cohesion strength by Zn. Furthermore, B itself is a cohesion enhancer, i.e. the segregation of B enhances the cohesion strength. Same studies were done on a second region 2, which was further away and showed a very low concentration of Zn (0.5 *at.*%). In this region there was no clear identification on Zn segregation. However, the B and C concentration increased to the values of the Zn-free GB in Ch. 5.1. As the bulk concentration was very low in this region and in combination with the presence of B and C, it can be concluded that Zn has a very low tendency for GB segregation. Interestingly, the structure of the GB had a higher fraction of GB defects and the facet lengths were shorter than in region 1. Comparing the two regions, our Experimental observations allowed to explain the effect of B and C on the segregation behavior of Zn. Depending on the

GB concentration level of B and C with respect to the bulk concentration of Zn, GB segregation of the latter one and thus GB embrittlement is avoided. In order to understand, whether the extracted work of separation is valid, mechanical test at room temperature and elevated temperatures has to be conducted to understand fully the LME process. Here, in-situ cantilever bending would be a good option to study the crack propagation.

In Ch. 5.10 the segregation behavior of Mn was studied. After annealing of the diffusion couple, Mn penetrated into the Fe-4 *at.*%Al bicrystal. However, due to the strong affinity of Mn to form an (hydr)oxide, the diffusion of Mn induced an internal oxidation of the GB. Deeper analysis of the GB oxides revealed a core-shell structure with a Al<sub>2</sub>O<sub>3</sub> core and a FeMnO-shell. Our investigations to study the phase of the oxide core showed a coexistence of different phases. The structure of the GB oxide core was determined to be nanocrystalline, which was not observed, yet. One explanation could be GB defects, which can act as nucleation sites for secondary phases. Our structural investigations of the oxide-free GB show curvatures of the boundary leading to the formation of GB dislocations or other defects. The nanocrystalline nature makes it more challenging to determine the phase of each grain. In order to be able to determine the phases, more profound analysis based on 4D-STEM (nanobeam diffraction) are necessary to extract the exact phases of the oxide core. Furthermore, APT investigations of the GB oxide would be necessary to clarify where and how B and C are distributed within the oxides.

Although, our studies were limited on a symmetric  $\Sigma 5 [001](310)$  tilt GB, the results can be qualitatively transferred to general, random GBs. This means, the impurities B and C - with ppm bulk concentrations - have a strong impact on the segregation behavior of Al and Zn. Al will be completely depleted from the boundary and Zn will form nanometer size spaced clusters when its bulk concentration is high enough. However, it should be noted that here the concentration of B and C exceeds 1 *at.*% but for a polycrystal the concentration of B and C will be lower because there are more possible segregation sites. Therefore, doping the GB with B and C is necessary to reach the same presented results.





# Bibliography

- [1] E. Hall, “The deformation and ageing of mild steel:II characteristics of the Lüeders deformation,” Proceedings of the physical society. Section B, vol. 64, no. 9, p. 742, 1951.
- [2] N. Petch, “The cleavage strength of polycrystals,” Journal of the Iron and Steel institute, vol. 174, pp. 25–28, 1953.
- [3] A. Cracknell and N. Petch, “Frictional forces on dislocation arrays at the lower yield point in iron,” Acta Metallurgica, vol. 3, no. 2, pp. 186–189, 1955.
- [4] P. J. Imrich, C. Kirchlechner, C. Motz, and G. Dehm, “Differences in deformation behavior of bicrystalline Cu micropillars containing a twin boundary or a large-angle grain boundary,” Acta Materialia, vol. 73, pp. 240–250, 2014.
- [5] J. R. Greer and J. T. M. De Hosson, “Plasticity in small-sized metallic systems: Intrinsic versus extrinsic size effect,” Progress in Materials Science, vol. 56, no. 6, pp. 654–724, 2011.
- [6] A. Sutton and R. Balluffi, Interfaces in Crystalline Materials. Oxford Classic Texts in the Physical Sciences, OUP Oxford, 2006.
- [7] H. Gleiter, “Observations suggesting a transformation in the structure of high angle grain boundaries in lead,” International Journal of Materials Research, vol. 61, no. 4, pp. 282–287, 1970.
- [8] E. W. Hart, “Two-dimensional phase transformation in grain boundaries,” 1968.
- [9] P. R. Cantwell, M. Tang, S. J. Dillon, J. Luo, G. S. Rohrer, and M. P. Harmer, “Grain boundary complexions,” Acta Materialia, vol. 62, pp. 1–48, 2014.
- [10] P. Lejček, Grain Boundary Segregation in Metals. No. 136 in Springer Series in Materials Science, Springer-Verlag, 2010.

## Bibliography

- [11] H. Erhart and H.-J. Grabke, "Equilibrium segregation of phosphorus at grain boundaries of fe-p, fe-c-p, fe-cr-p, and fe-cr-c-p alloys," Metal science, vol. 15, no. 9, pp. 401–408, 1981.
- [12] M. Guttman, P. Dumoulin, and M. Wayman, "The thermodynamics of interactive co-segregation of phosphorus and alloying elements in iron and temper-brittle steels," Metallurgical Transactions A, vol. 13, no. 10, pp. 1693–1711, 1982.
- [13] J. Janovec, M. Jenko, P. Lejček, and J. Pokluda, "Grain boundary segregation of phosphorus and silicon in polycrystals and bicrystals of the fe-2.6 si-0.055 p alloy," Materials Science and Engineering: A, vol. 462, no. 1-2, pp. 441–445, 2007.
- [14] P. Lejček and S. Hofmann, "Temperature Dependence of the Phosphorus Segregation at the Twin Boundary in an Fe-4 at.% Si Alloy," Surface and Interface Analysis, vol. 16, pp. 1–12, 1990-07.
- [15] C. Pichard, J. Rieu, and C. Goux, "The Influence of Oxygen and Sulfur on the Intergranular Brittleness of Iron," Metallurgical and Materials Transactions A, vol. 7, no. 12, pp. 1811–1815, 1976.
- [16] M. Yamaguchi, "First-Principles Study on the Grain Boundary Embrittlement of Metals by Solute Segregation: Part I. Iron (Fe)-Solute (B, C, P, and S) Systems," Metallurgical and Materials Transactions A, vol. 42, no. 2, pp. 319–329, 2011-02.
- [17] G. L. Krasko and G. Olson, "Effect of boron, carbon, phosphorus and sulphur on intergranular cohesion in iron," Solid State Communications, vol. 76, no. 3, pp. 247–251, 1990.
- [18] A. Ahmadian, D. Scheiber, X. Zhou, B. Gault, C. H. Liebscher, L. Romaner, and G. Dehm, "Aluminum depletion induced by co-segregation of carbon and boron in a bcc-iron grain boundary," Nature Communications, vol. 12, no. 1, p. 6008, 2021-10-14.
- [19] J. Wang, R. Janisch, G. K. H. Madsen, and R. Drautz, "First-Principles Study of Carbon Segregation in Bcc Iron Symmetrical Tilt Grain Boundaries," Acta Materialia, vol. 115, pp. 259–268, 2016.

- [20] R. Wu, A. J. Freeman, and G. B. Olson, “Effects of Carbon on Fe-Grain-Boundary Cohesion: First-Principles Determination,” Physical Review B, vol. 53, no. 11, pp. 7504–7509, 1996-03.
- [21] A. Fraczkiewicz, A.-S. Gay, and M. Biscondi, “On the Boron Effect in FeAl (B2) Intermetallic Alloys,” Materials Science and Engineering: A, vol. 258, no. 1, pp. 108–114, 1998-12.
- [22] A. Fraczkiewicz, “Influence of Boron on the Mechanical Properties of B2-Ordered FeAl Alloys,” Materials Transactions, JIM, vol. 41, no. 1, pp. 166–169, 2000.
- [23] X. Huang, M. C. Chaturvedi, N. L. Richards, and J. Jackman, “The effect of grain boundary segregation of boron in cast alloy 718 on HAZ microfissuring—A SIMS analysis,” Acta Materialia, vol. 45, no. 8, pp. 3095–3107, 1997-08-01.
- [24] D. McLean, Grain Boundaries in Metals. Clarendon Press, 1957.
- [25] J. W. Cahn, “The impurity-drag effect in grain boundary motion,” Acta Metallurgica, vol. 10, no. 9, pp. 789–798, 1962-09-01.
- [26] M. Hillert, “Solute drag in grain boundary migration and phase transformations,” Acta materialia, vol. 52, no. 18, pp. 5289–5293, 2004.
- [27] C. L. White and W. A. Coghlan, “The Spectrum of Binding Energies Approach to Grain Boundary Segregation,” Metallurgical and Materials Transactions A, vol. 8, no. 9, pp. 1403–1412, 1977-09.
- [28] P. Lejček, “Characterization of Grain Boundary Segregation in an Fe-Si Alloy,” Analytica Chimica Acta, vol. 297, no. 1-2, pp. 165–178, 1994-10.
- [29] P. Lejček and S. Hofmann, “Segregation Enthalpies of Phosphorus, Carbon and Silicon at {013} and {012} Symmetrical Tilt Grain Boundaries in an Fe-3.5 at.% Si Alloy,” Acta Metallurgica et Materialia, vol. 39, no. 10, pp. 2469–2476, 1991-10.
- [30] P. Lejček and J. Adimek, “Anisotropy of Grain Boundary Segregation in  $\Sigma=5$  Bicrystals of  $\alpha$ -Iron,” Surface Science, vol. 264, pp. 449–454, 1992-03.

## Bibliography

- [31] C. White and W. Coghlan, "Spectrum of binding energies approach to grain boundary segregation.," Metall Trans A, vol. 8 A, no. 9, p. 1403 – 1412, 1977. Cited by: 57.
- [32] B. Gault, M. P. Moody, J. M. Cairney, and S. P. Ringer, Atom Probe Microscopy, vol. 160 of Springer Series in Materials Science. Springer New York, 2012.
- [33] K. Babinsky, J. Weidow, W. Knabl, A. Lorich, H. Leitner, and S. Primig, "Atom probe study of grain boundary segregation in technically pure molybdenum," Materials characterization, vol. 87, pp. 95–103, 2014.
- [34] Z. Yu, Q. Wu, J. M. Rickman, H. M. Chan, and M. P. Harmer, "Atomic-resolution observation of hf-doped alumina grain boundaries," Scripta Materialia, vol. 68, pp. 703–6, 2013.
- [35] T. Nagano, K. Tamahashi, Y. Sasajima, and J. Onuki, "Cs-corrected stem observation and atomic modeling of grain boundary impurities of very narrow cu interconnect," ECS Electrochemistry Letters, vol. 2, no. 6, p. H23, 2013.
- [36] N. J. Peter, T. Frolov, M. J. Duarte, R. Hadian, C. Ophus, C. Kirchlechner, C. H. Liebscher, and G. Dehm, "Segregation-induced nanofaceting transition at an asymmetric tilt grain boundary in copper," Physical review letters, vol. 121, no. 25, p. 255502, 2018.
- [37] H. Schumann, "Metallographie," VEB Deutscher Verlag für Grundstoffindustrie, p. 608, 1980.
- [38] M. Palm, F. Stein, and G. Dehm, "Iron Aluminides," Annual Review of Materials Research, vol. 49, no. 1, pp. 297–326, 2019.
- [39] H. Bhadeshia and R. Honeycombe, Steels: microstructure and properties. Butterworth-Heinemann, 2017.
- [40] O. Kubaschewski, IRON —Binary Phase Diagrams. Springer Science & Business Media, 2013-03.
- [41] C. Briant, "Solid solubility and grain boundary segregation," Philosophical magazine letters, vol. 73, no. 6, pp. 345–350, 1996.
- [42] N. Wiberg, Lehrbuch der Anorganischen Chemie. De Gruyter, 2008-07.

- [43] M. H. Razmpoosh, A. Macwan, E. Biro, D. L. Chen, Y. Peng, F. Goodwin, and Y. Zhou, “Liquid metal embrittlement in laser beam welding of Zn-coated 22MnB5 steel,” Materials & Design, vol. 155, pp. 375–383, 2018-10-05.
- [44] M. H. Razmpoosh, A. Macwan, F. Goodwin, E. Biro, and Y. Zhou, “Role of Random and Coincidence Site Lattice Grain Boundaries in Liquid Metal Embrittlement of Iron (FCC)-Zn Couple,” Metallurgical and Materials Transactions A, vol. 51, no. 8, pp. 3938–3944, 2020-08.
- [45] L. Priester, Grain Boundaries, vol. 172 of Springer Series in Materials Science. Springer Netherlands, 2013.
- [46] M. Kronberg and u. F. Wilson, “Secondary recrystallization in copper,” JOM, vol. 1, no. 8, pp. 501–514, 1949.
- [47] G. Gottstein, Physikalische Grundlagen der Materialkunde: mit 28 Tabellen. Springer-Lehrbuch, Springer, 3. Aufl ed., 2007.
- [48] W. Bollmann, Crystal Defects and Crystalline Interfaces. Springer Berlin Heidelberg, 1970.
- [49] W. T. Read and W. Shockley, “Dislocation Models of Crystal Grain Boundaries,” Physical Review, vol. 78, no. 3, pp. 275–289, 1950-05.
- [50] D. G. Brandon, “The Structure of High-Angle Grain Boundaries,” Acta Metallurgica, vol. 14, no. 11, pp. 1479–1484, 1966-11.
- [51] A. P. Sutton, V. Vitek, and J. W. Christian, “On the structure of tilt grain boundaries in cubic metals I. Symmetrical tilt boundaries,” Philosophical Transactions of the Royal Society of London. Series A, Mathematical and Physical Sciences, vol. 309, no. 1506, pp. 1–36, 1983-03-17.
- [52] G. H. Bishop and B. Chalmers, “A coincidence — Ledge — Dislocation description of grain boundaries,” Scripta Metallurgica, vol. 2, no. 2, pp. 133–139, 1968-02-01.
- [53] A. Brokman and R. W. Balluffi, “Coincidence lattice model for the structure and energy of grain boundaries,” Acta Metallurgica, vol. 29, no. 10, pp. 1703–1719, 1981-10-01.

## Bibliography

- [54] A. P. Sutton and V. Vitek, “On the coincidence site lattice and DSC dislocation network model of high angle grain boundary structure,” Scripta Metallurgica, vol. 14, no. 1, pp. 129–132, 1980-01-01.
- [55] J. Han, V. Vitek, and D. J. Srolovitz, “The Grain-Boundary Structural Unit Model Redux,” Acta Materialia, vol. 133, pp. 186–199, 2017-07.
- [56] H. Gleiter, “The Structure and Properties of High-Angle Grain Boundaries in Metals,” Physica status solidi (b), vol. 45, no. 1, pp. 9–38, 1971-05.
- [57] J. W. Gibbs, Scientific Papers of J. Willard Gibbs, in Two Volumes, vol. 1. Longmans, Green, 1906.
- [58] J. C. Slater, “Introduction to chemical physics,” 1939.
- [59] E. D. Hondros and M. P. Seah, “The theory of grain boundary segregation in terms of surface adsorption analogues,” Metallurgica Transactions A, vol. 8, no. 9, pp. 1363–1371, 1977-09.
- [60] M. P. Seah, E. D. Hondros, and A. Kelly, “Grain Boundary Segregation,” Proceedings: Mathematical, Physical and Engineering Sciences, vol. 335, no. 1601, pp. 191–212, 1973-10.
- [61] S. Brunauer, L. S. Deming, W. E. Deming, and E. Teller, “On a theory of the van der Waals adsorption of gases,” Journal of the American Chemical Society, vol. 62, pp. 1723–1732, 1940-07/1940-12.
- [62] S. Takaki, N. Nakada, and T. Tsuchiyama, “Grain Boundary Carbon Segregation Estimated by McLean and Seah-Hondros Models,” in Advanced Steels (Y. Weng, H. Dong, and Y. Gan, eds.), pp. 81–86, Springer Berlin Heidelberg, 2011.
- [63] R. H. Fowler and E. A. Guggenheim, Statistical Thermodynamics: A Version of Statistical Mechanics for Students of Physics and Chemistry. Cambridge University Press, 1st ed., 1939.
- [64] C. Pichard, M. Guttman, J. Rieu, and C. Goux, “Ségrégation intergranulaire des éléments de la famille du soufre dans le fer pur,” Journal de physique colloques, vol. 36, no. C4, pp. C4-151–C4-155, 1975-10.

- [65] M. P. Seah, "Grain Boundary Segregation," Journal of Physics F: Metal Physics, vol. 10, no. 6, pp. 1043–1064, 1980.
- [66] M. Guttman, "Equilibrium Segregation in a Ternary Solution: A Model for Temper Embrittlement," Surface Science, vol. 53, no. 1, pp. 213–227, 1975-12.
- [67] S. Suzuki, S. Tanii, K. Abiko, and H. Kimura, "Site competition between sulfur and carbon at grain boundaries and their effects on the grain boundary cohesion in iron," Metallurgica Transactions A, vol. 18, no. 6, pp. 1109–1115, 1991-01-01.
- [68] P. Gas, M. Guttman, and J. Bernardini, "The Interactive Co-Segregation of Sb and Ni at the Grain Boundaries of Ultra-High Purity Fe-Base Alloys," Acta Metallurgica, vol. 30, no. 7, pp. 1309–1316, 1982-07.
- [69] P. Dumoulin and M. Guttman, "The influence of chemical interactions between metallic and metalloid solutes on their segregation in Alpha-Fe I: Co-segregation at free surface studied by Auger electron spectroscopy," Materials Science and Engineering, vol. 42, pp. 249–263, 1980-01-01.
- [70] T. Watanabe, S. Kitamura, and S. Karashima, "Grain boundary hardening and segregation in alpha Iron-Tin alloy," Acta Metallurgica, vol. 28, no. 4, pp. 455–463, 1980-04-01.
- [71] H. Sautter, H. Gleiter, and G. Bäro, "The effect of solute atoms on the energy and structure of grain boundaries," Acta Metallurgica, vol. 25, no. 4, pp. 467–473, 1977-04-01.
- [72] M. Rajagopalan, M. A. Tschopp, and K. N. Solanki, "Grain Boundary Segregation of Interstitial and Substitutional Impurity Atoms in Alpha-Iron," JOM, vol. 66, no. 1, pp. 129–138, 2014-01-01.
- [73] J. H. Westbrook, "Segregation at Grain Boundaries," Metallurgical Reviews, vol. 9, no. 1, pp. 415–471, 1964-01-01.
- [74] T. R. Anthony, "Solute segregation in vacancy gradients generated by sintering and temperature changes," Acta Metallurgica, vol. 17, no. 5, pp. 603–609, 1969-05-01.

## Bibliography

- [75] R. G. Faulkner, T. C. Hopkins, and K. Norrgård, “Improved spatial resolution microanalysis in a scanning transmission electron microscope,” X-Ray Spectrometry, vol. 6, no. 2, pp. 73–79, 1977.
- [76] T. M. Williams, A. M. Stoneham, and D. R. Harries, “The segregation of boron to grain boundaries in solution-treated Type 316 austenitic stainless steel,” Metal Science, vol. 10, no. 1, pp. 14–19, 1976-01-01.
- [77] R. E. Hanneman and T. R. Anthony, “Effects of non-equilibrium segregation on near-surface diffusion,” Acta Metallurgica, vol. 17, no. 9, pp. 1133–1140, 1969-09-01.
- [78] R. G. Faulkner, “Non-Equilibrium Grain-Boundary Segregation in Austenitic Alloys,” Journal of Materials Science, vol. 16, no. 2, pp. 373–383, 1981-02.
- [79] S. Watanabe, N. Sakaguchi, N. Hashimoto, M. Nakamura, H. Takahashi, C. Namba, and N. Q. Lam, “Radiation-induced segregation accompanied by grain boundary migration in austenitic stainless steel,” Journal of Nuclear Materials, vol. 232, no. 2, pp. 113–118, 1996-09-02.
- [80] M. B. Kasen, “Some observations on boundary segregation during grain growth annealing of ultrapurity aluminum,” Acta Metallurgica, vol. 20, no. 1, pp. 105–113, 1972-01-01.
- [81] M. Jahazi and J. J. Jonas, “The non-equilibrium segregation of boron on original and moving austenite grain boundaries,” Materials Science and Engineering: A, vol. 335, no. 1, pp. 49–61, 2002-09-25.
- [82] S. Zhang, X. He, and T. Ko, “Non-equilibrium segregation of solutes to grain boundary,” Journal of Materials Science, vol. 29, no. 10, pp. 2663–2670, 1994-05-01.
- [83] I. Kaur, Y. Mishin, and W. Gust, Fundamentals of Grain and Interphase Boundary Diffusion. John Wiley, 1995.
- [84] J. D. Pan and R. W. Balluffi, “Diffusion induced grain boundary migration in AuCu and AuAg thin films,” Acta Metallurgica, vol. 30, no. 4, pp. 861–870, 1982-04-01.



- [85] F. N. Rhines and A. M. Montgomery, "A New Type of Structure in the  $\alpha$ -Copper-Zinc Alloys," Nature, vol. 141, no. 3566, pp. 413–413, 1938-03.
- [86] F. J. A. Den Broeder, "Interface reaction and a special form of grain boundary diffusion in the Cr-W system," Acta Metallurgica, vol. 20, no. 3, pp. 319–332, 1972-03-01.
- [87] K. N. Tu, "Kinetics of thin-film reactions between Pb and the AgPd alloy," Journal of Applied Physics, vol. 48, no. 8, pp. 3400–3404, 1977-08-01.
- [88] M. Hillert and G. R. Purdy, "Chemically induced grain boundary migration," Acta Metallurgica, vol. 26, no. 2, pp. 333–340, 1978-02-01.
- [89] J. W. Cahn, J. D. Pan, and R. W. Balluffi, "Diffusion induced grain boundary migration," Scripta Metallurgica, vol. 13, no. 6, pp. 503–509, 1979-06-01.
- [90] R. W. Balluffi and J. W. Cahn, "Mechanism for diffusion induced grain boundary migration," Acta Metallurgica, vol. 29, no. 3, pp. 493–500, 1981-03-01.
- [91] M. S. Sulonen, "On the driving force of discontinuous precipitation and dissolution," Acta Metallurgica, vol. 12, no. 6, pp. 749–753, 1964-06-01.
- [92] M. Hillert, "On the driving force for diffusion induced grain boundary migration," Scripta Metallurgica, vol. 17, no. 2, pp. 237–240, 1983-02-01.
- [93] O. Penrose, "On the elastic driving force in diffusion-induced grain boundary motion," Acta Materialia, vol. 52, no. 13, pp. 3901–3910, 2004-08-02.
- [94] Y.-J. Baik and D. N. Yoon, "The effect of curvature on the grain boundary migration induced by diffusional coherency strain in mo-ni alloy," Acta Metallurgica, vol. 35, no. 9, pp. 2265–2271, 1987-09-01.
- [95] D. A. Smith and A. H. King, "On the mechanism of diffusion-induced boundary migration," Philosophical Magazine A, vol. 44, no. 2, pp. 333–340, 1981-08-01.
- [96] G. Duscher, M. F. Chisholm, U. Alber, and M. Rühle, "Bismuth-induced embrittlement of copper grain boundaries," Nature Mater, vol. 3, no. 9, pp. 621–626, 2004-09.

## Bibliography

- [97] L. Klinger and E. Rabkin, “The effect of stress on grain boundary interdiffusion in a semi-infinite bicrystal,” Acta Materialia, vol. 55, no. 14, pp. 4689–4698, 2007-08-01.
- [98] E. Pereiro-López, W. Ludwig, D. Bellet, and C. Lemaignan, “In situ investigation of Al bicrystal embrittlement by liquid Ga using synchrotron imaging,” Acta Materialia, vol. 54, no. 16, pp. 4307–4316, 2006-09-01.
- [99] H.-S. Nam and D. J. Srolovitz, “Effect of material properties on liquid metal embrittlement in the Al–Ga system,” Acta Materialia, vol. 57, no. 5, pp. 1546–1553, 2009-03-01.
- [100] M. Naderi, M. Peterlechner, E. Schafner, S. V. Divinski, and G. Wilde, “Kinetic, volumetric and structural effects induced by liquid Ga penetration into ultrafine grained Al,” Acta Materialia, vol. 99, pp. 196–205, 2015-10-15.
- [101] Z. Yu, P. R. Cantwell, Q. Gao, D. Yin, Y. Zhang, N. Zhou, G. S. Rohrer, M. Widom, J. Luo, and M. P. Harmer, “Segregation-induced ordered superstructures at general grain boundaries in a nickel-bismuth alloy,” Science, vol. 358, no. 6359, pp. 97–101, 2017-10-06.
- [102] E. Rabkin, B. B. Straumal, V. G. Sursaeva, L. S. Shvindlerman, R. Fournelle, and W. Gust, “High-Temperature Diffusion-Induced Grain Boundary Migration in an Fe-5 AT.% Al Bicrystal during Zinc Diffusion,” Materials Science Forum, vol. 126–128, pp. 321–324, 1993-01.
- [103] C. Beal, X. Kleber, D. Fabregue, and M. Bouzekri, “Liquid zinc embrittlement of twinning-induced plasticity steel,” Scripta Materialia, vol. 66, no. 12, pp. 1030–1033, 2012-06-01.
- [104] K.-D. Bauer, M. Todorova, K. Hingerl, and J. Neugebauer, “A first principles investigation of zinc induced embrittlement at grain boundaries in bcc iron,” Acta Materialia, vol. 90, pp. 69–76, 2015-05-15.
- [105] D. Bhattacharya, L. Cho, E. van der Aa, A. Pichler, N. Pottore, H. Ghassemi-Armaki, K. O. Findley, and J. G. Speer, “Influence of the starting microstructure of an advanced high strength steel on the characteristics of Zn-Assisted liquid metal embrittlement,” Materials Science and Engineering: A, vol. 804, p. 140391, 2021-02-15.

- [106] W. Peng, H. Peng, G. Wu, and J. Zhang, “Effect of zinc-doping on tensile strength of  $\Sigma 5$  bcc Fe symmetric tilt grain boundary,” Computational Materials Science, vol. 171, p. 109204, 2020-01-01.
- [107] H.-S. Nam and D. J. Srolovitz, “Molecular Dynamics Simulation of Ga Penetration along Grain Boundaries in Al: A Dislocation Climb Mechanism,” Physical Review Letter, vol. 99, no. 2, p. 025501, 2007-07-13.
- [108] R. C. Hugo and R. G. Hoagland, “The kinetics of gallium penetration into aluminum grain boundaries—in situ TEM observations and atomistic models,” Acta Materialia, vol. 48, no. 8, pp. 1949–1957, 2000-05-11.
- [109] R. Schweinfest, A. T. Paxton, and M. W. Finnis, “Bismuth embrittlement of copper is an atomic size effect,” Nature, vol. 432, no. 7020, pp. 1008–1011, 2004-12.
- [110] D. A. Porter and K. E. Easterling, Phase transformations in metals and alloys (revised reprint). CRC press, 2009.
- [111] J. W. Martin, R. D. Doherty, and B. Cantor, Stability of microstructure in metallic systems. Cambridge University Press, 1997.
- [112] P. W. Bridgman, “Certain Physical Properties of Single Crystals of Tungsten, Antimony, Bismuth, Tellurium, Cadmium, Zinc, and Tin,” Proceedings of the American Academy of Arts and Sciences, vol. 60, no. 6, pp. 305–383, 1925.
- [113] L. Reimer, Scanning Electron Microscopy: Physics of Image Formation and Microanalysis. No. 45 in Springer Series in Optical Sciences, Springer, 2., completely rev. and upyear ed ed., 1998. Hier auch später erschienene, unveränderte Nachdrucke.
- [114] R. F. Egerton, “Analytical Electron Microscopy,” in Physical Principles of Electron Microscopy: An Introduction to TEM, SEM, and AEM (R. F. Egerton, ed.), pp. 155–175, Springer US, 2005.
- [115] D. B. Williams and C. B. Carter, Transmission Electron Microscopy: A Textbook for Materials Science. Springer US, second ed., 2009.
- [116] S. Zaefferer, “On the formation mechanisms, spatial resolution and intensity of backscatter Kikuchi patterns,” Ultramicroscopy, vol. 107, no. 2, pp. 254–266, 2007-02-01.

## Bibliography

- [117] D. R. Steinmetz and S. Zaefferer, “Towards ultrahigh resolution EBSD by low accelerating voltage,” Materials Science and Technology, vol. 26, no. 6, pp. 640–645, 2010-06-01.
- [118] F. J. Humphreys, Y. Huang, I. Brough, and C. Harris, “Electron backscatter diffraction of grain and subgrain structures — resolution considerations,” Journal of Microscopy, vol. 195, no. 3, pp. 212–216, 1999.
- [119] E. J. Kirkland, “The Transmission Electron Microscope,” in Advanced Computing in Electron Microscopy (E. J. Kirkland, ed.), pp. 5–27, Springer US, 2010.
- [120] D. B. Williams and C. B. Carter, Transmission Electron Microscopy: A Textbook for Materials Science. Springer US, second ed., 2009.
- [121] S. J. Pennycook and P. D. Nellist, eds., Scanning Transmission Electron Microscopy. Springer New York, 2011.
- [122] L. Reimer and H. Kohl, Transmission Electron Microscopy: Physics of Image Formation. No. 36 in Springer Series in Optical Sciences, Springer, 5th ed ed., 2008.
- [123] R. Brydson, ed., Aberration-Corrected Analytical Transmission Electron Microscopy. RMS-Wiley, 2011.
- [124] E. J. Kirkland, “Calculation of Images of Thin Specimens,” in Advanced Computing in Electron Microscopy (E. J. Kirkland, ed.), pp. 77–113, Springer US, 2010.
- [125] J. M. Cowley and A. F. Moodie, “The scattering of electrons by atoms and crystals. I. A new theoretical approach,” Acta Crystallographica, vol. 10, pp. 609–619, Oct 1957.
- [126] O. Scherzer, “The theoretical resolution limit of the electron microscope,” Journal of Applied Physics, vol. 20, no. 1, pp. 20–29, 1949.
- [127] “<https://www.globalsino.com/em/page4165.html>.”
- [128] S. Pennycook and D. Jesson, “High-resolution z-contrast imaging of crystals,” Ultramicroscopy, vol. 37, no. 1, pp. 14–38, 1991.

- [129] E. J. Kirkland, “Atomic Potentials and Scattering Factors,” in Advanced Computing in Electron Microscopy (E. J. Kirkland, ed.), pp. 243–260, Springer US, 2010.
- [130] F. Zemlin, K. Weiss, P. Schiske, W. Kunath, and K.-H. Herrmann, “Coma-free alignment of high resolution electron microscopes with the aid of optical diffractograms,” Ultramicroscopy, vol. 3, pp. 49–60, 1978.
- [131] O. Scherzer, “Über einige fehler von elektronenlinsen,” Z. Physik, vol. 101, no. 9, pp. 593–603, 1936-09-01.
- [132] E. J. Kirkland, “Introduction,” in Advanced Computing in Electron Microscopy (E. J. Kirkland, ed.), pp. 1–4, Springer US, 2010.
- [133] “<https://www.edax.com/products/ebsd/velocity-ebsd-camera>.”
- [134] “<https://www.edax.com/products/eds/octane-elite-eds-system>.”
- [135] G. Kresse and J. Hafner, “Ab Initio Molecular Dynamics for Liquid Metals,” Physical Review B, vol. 47, no. 1, p. 558, 1993.
- [136] G. Kresse and J. Furthmüller, “Efficiency of Ab-Initio Total Energy Calculations for Metals and Semiconductors Using a Plane-Wave Basis Set,” Computational Materials Science, vol. 6, no. 1, pp. 15–50, 1996.
- [137] G. Kresse and J. Furthmüller, “Efficient Iterative Schemes for Ab Initio Total-Energy Calculations Using a Plane-Wave Basis Set,” Physical Review B, vol. 54, no. 16, pp. 11169–11186, 1996.
- [138] G. Kresse and D. Joubert, “From Ultrasoft Pseudopotentials to the Projector Augmented-Wave Method,” Physical Review B, vol. 59, no. 3, pp. 1758–1775, 1999-01.
- [139] J. P. Perdew, K. Burke, and M. Ernzerhof, “Generalized Gradient Approximation Made Simple,” Physical Review Letter, vol. 77, no. 18, p. 3865, 1996.
- [140] J. Perdew, K. Burke, and M. Ernzerhof, “Perdew, Burke, and Ernzerhof Reply,” Physical Review Letter, vol. 80, no. 4, p. 891, 1998.
- [141] P. Haas, F. Tran, and P. Blaha, “Calculation of the Lattice Constant of Solids with Semilocal Functionals,” Physical Review B, vol. 79, no. 8, pp. 1–10, 2009.

- [142] D. Scheiber, R. Pippan, P. Puschnig, and L. Romaner, “\emph{Ab Initio Calculations of Grain Boundaries in Bcc Metals},” Modelling and Simulation in Materials Science and Engineering., vol. 24, no. 3, p. 035013, 2016-03.
- [143] H. Jin, I. Elfimov, and M. Militzer, “Study of the Interaction of Solutes with  $\Sigma 5$  (013) Tilt Grain Boundaries in Iron Using Density-Functional Theory,” Journal of Applied Physics, vol. 115, no. 9, p. 093506, 2014.
- [144] A. S. Ebner, S. Jakob, H. Clemens, R. Pippan, V. Maier-Kiener, S. He, W. Ecker, D. Scheiber, and V. I. Razumovskiy, “Grain boundary segregation in ni-base alloys: A combined atom probe tomography and first principles study,” Acta Materialia, vol. 221, p. 117354, 2021.
- [145] D. Scheiber, T. Jechtl, J. Svoboda, F. Fischer, and L. Romaner, “On Solute Depletion Zones along Grain Boundaries during Segregation,” Acta Materialia, vol. 182, pp. 100–107, 2020.
- [146] D. Scheiber, L. Romaner, R. Pippan, and P. Puschnig, “Impact of Solute-Solute Interactions on Grain Boundary Segregation and Cohesion in Molybdenum,” Physical Review Materials, vol. 2, no. 9, p. 093609, 2018.
- [147] D. Scheiber, K. Prabitz, L. Romaner, and W. Ecker, “The influence of alloying on Zn liquid metal embrittlement in steels,” Acta Materialia, vol. 195, pp. 750–760, 2020-08-15.
- [148] C. Ophus, “A Fast Image Simulation Algorithm for Scanning Transmission Electron Microscopy,” Advanced Structural and Chemical Imaging/Struct Chem Imaging, vol. 3, no. 1, p. 13, 2017-05.
- [149] J. M. Papazian and D. N. Besherb, “Grain Boundary Segregation of Carbon in Iron,” Metallurgical Transactions, vol. 2, no. 2, pp. 497–503, 1971-02.
- [150] S. Suzuki, M. Obata, K. Abiko, and H. Kimura, “Effect of Carbon on the Grain Boundary Segregation of Phosphorus in  $\alpha$ -Iron,” Scripta Metallurgica, vol. 17, no. 11, pp. 1325–1328, 1983-11.
- [151] H. Hänsel and H. J. Grabke, “Grain Boundary Segregation of Phosphorus and Carbon in Ferritic Iron,” Scripta Metallurgica, vol. 20, no. 11, pp. 1641–1644, 1986-11.

- [152] B. Krakauer and D. N. Seidman, "Atomic Scale Observations of Solute-Atom Segregation at Grain Boundaries in an Iron (Silicon) Alloy," Materials Science Forum, vol. 126–128, pp. 161–164, 1993-01.
- [153] N. Maruyama, G. D. W. Smith, and A. Cerezo, "Interaction of the Solute Niobium or Molybdenum with Grain Boundaries in  $\alpha$ -Iron," Materials Science and Engineering: A, vol. 353, no. 1, pp. 126–132, 2003-07.
- [154] W. Xing, A. R. Kalidindi, D. Amram, and C. A. Schuh, "Solute Interaction Effects on Grain Boundary Segregation in Ternary Alloys," Acta Materialia, vol. 161, pp. 285–294, 2018.
- [155] S. Ohtsuka, Y. Shinoda, T. Akatsu, and F. Wakai, "Effect of Oxygen Segregation at Grain Boundaries on Deformation of B, C-Doped Silicon Carbides at Elevated Temperatures," J. Am. Ceram. Soc., vol. 88, no. 6, pp. 1558–1563, 2005.
- [156] Z. Wang, M. Saito, K. P. McKenna, L. Gu, S. Tsukimoto, A. L. Shluger, and Y. Ikuhara, "Atom-Resolved Imaging of Ordered Defect Superstructures at Individual Grain Boundaries," Nature, vol. 479, no. 7373, pp. 380–383, 2011-11.
- [157] H. J. Grabke, "Surface and grain boundary segregation on and in iron," Steel Res., vol. 57, no. 4, pp. 178–185, 1986.
- [158] H. J. Grabke, W. Paulitschke, G. Tauber, and H. Viefhaus, "Equilibrium surface segregation of dissolved nonmetal atoms on iron(100) faces," Surface Science, vol. 63, pp. 377–389, 1977-03-01.
- [159] G. Tauber and H. J. Grabke, "Grain Boundary Segregation of Sulfur, Nitrogen, and Carbon in  $\alpha$ -Iron," Berichte der Bunsengesellschaft für physikalische Chemie, vol. 82, no. 3, pp. 298–302, 1978-03.
- [160] C. M. Liu, T. Nagoya, K. Abiko, and H. Kimura, "Effect of Boron on the Grain Boundary Segregation of Phosphorus and Intergranular Fracture in High-Purity Fe-0.2 Pct P-B Alloys," Metallurgical and Materials Transactions A, vol. 23, no. 1, pp. 263–269, 1992-01.
- [161] C. T. Liu, C. L. White, and J. A. Horton, "Effect of Boron on Grain-Boundaries in Ni<sub>3</sub>Al," Acta Metallurgica, vol. 33, no. 2, pp. 213–229, 1985.

## Bibliography

- [162] G. S. Painter and F. W. Averill, “Effects of Segregation on Grain-Boundary Cohesion: A Density-Functional Cluster Model of Boron and Sulfur in Nickel,” Physical Review Letter, vol. 58, no. 3, pp. 234–237, 1987.
- [163] R. Wu, A. J. Freeman, and G. B. Olson, “First Principles Determination of the Effects of Phosphorus and Boron on Iron Grain Boundary Cohesion,” Science, vol. 265, no. 5170, pp. 376–380, 1994-07.
- [164] J. S. Braithwaite and P. Rez, “Grain Boundary Impurities in Iron,” Acta Materialia, vol. 53, no. 9, pp. 2715–2726, 2005-05.
- [165] Z.-Z. Chen and C.-Y. Wang, “First-Principles Study on the Effects of Co-Segregation of Ti, B and O on the Cohesion of the  $\alpha$ -Fe Grain Boundary,” Journal of Physics: Condensed Matter, vol. 17, no. 42, pp. 6645–6652, 2005-10.
- [166] P. Lejčėk and A. Fraczkiewicz, “Boron Segregation in Intermetallics: On the Possible Origins of a Low-Level Intergranular Segregation,” Intermetallics, vol. 11, no. 10, pp. 1053–1063, 2003-10.
- [167] E. Wachowicz and A. Kiejna, “Effect of Impurities on Grain Boundary Cohesion in Bcc Iron,” Computational Materials Science, vol. 43, no. 4, pp. 736–743, 2008-10.
- [168] R. Rana, C. Liu, and R. K. Ray, “Low-Density Low-Carbon Fe–Al Ferritic Steels,” Scripta Materialia, vol. 68, no. 6, pp. 354–359, 2013-03.
- [169] M. Yuasa and M. Mabuchi, “First-Principles Study in Fe Grain Boundary with Al Segregation: Variation in Electronic Structures with Straining,” Philosophie Magazin, vol. 93, no. 6, pp. 635–647, 2013-02.
- [170] W. T. Geng, A. J. Freeman, and G. B. Olson, “Influence of Alloying Additions on Grain Boundary Cohesion of Transition Metals: First-Principles Determination and Its Phenomenological Extension,” Physical Review B, vol. 63, no. 16, p. 165415, 2001-04.
- [171] J. R. Rice and J.-S. Wang, “Embrittlement of Interfaces by Solute Segregation,” Materials Science and Engineering A, vol. 107, pp. 23–40, 1989.



- [172] J. Rellick and C. McMahon, “Elimination of Oxygen-Induced Intergranular Brittleness in Iron by Addition of Scavengers,” Metallurgical Transactions, vol. 1, no. 4, pp. 929–&, 1970.
- [173] D. Raabe, M. Herbig, S. Sandlöbes, Y. Li, D. Tytko, M. Kuzmina, D. Ponge, and P. P. Choi, “Grain Boundary Segregation Engineering in Metallic Alloys: A Pathway to the Design of Interfaces,” Curr Opin Solid State Mater Sci, vol. 18, no. 4, pp. 253–261, 2014-08.
- [174] G. Da Rosa, P. Maugis, J. Drillet, V. Hebert, and K. Hoummada, “Co-Segregation of Boron and Carbon Atoms at Dislocations in Steel,” J. Alloys Compd., vol. 724, pp. 1143–1148, 2017-11.
- [175] D. Medlin, K. Hattar, J. Zimmerman, F. Abdeljawad, and S. Foiles, “Defect Character at Grain Boundary Facet Junctions: Analysis of an Asymmetric  $\Sigma = 5$  Grain Boundary in Fe,” Acta Materialia, vol. 124, pp. 383–396, 2017-02.
- [176] D. Larson, B. Gault, B. Geiser, F. De Geuser, and F. Vurpillot, “Atom Probe Tomography Spatial Reconstruction: Status and Directions,” Current Opinion in Solid State Materials Science, vol. 17, no. 5, pp. 236–247, 2013-10.
- [177] M. Ashton, A. Mishra, J. Neugebauer, and C. Freysoldt, “Ab Initio Description of Bond Breaking in Large Electric Fields,” Physical Review Letter, vol. 124, no. 17, p. 176801, 2020-05.
- [178] F. De Geuser and B. Gault, “Metrology of Small Particles and Solute Clusters by Atom Probe Tomography,” Acta Materialia, vol. 188, pp. 406–415, 2020-02.
- [179] B. M. Jenkins, F. Danoix, M. Gouné, P. A. Bagot, Z. Peng, M. P. Moody, and B. Gault, “Reflections on the Analysis of Interfaces and Grain Boundaries by Atom Probe Tomography,” Microscopy and Microanalysis Microanal., vol. 26, pp. 247–257, 2020.
- [180] X. Zhou, X. X. Yu, T. Kaub, R. L. Martens, and G. B. Thompson, “Grain Boundary Specific Segregation in Nanocrystalline Fe(Cr),” Scientific Reports, vol. 6, pp. 1–14, 2016.
- [181] C. H. Liebscher, A. Stoffers, M. Alam, L. Lymperakis, O. Cojocar-Mirédin, B. Gault, J. Neugebauer, G. Dehm, C. Scheu, and D. Raabe, “Strain-Induced

- Asymmetric Line Segregation at Faceted Si Grain Boundaries,” Physical Review Letter, vol. 121, no. 1, p. 015702, 2018-07.
- [182] C. H. Liebscher, M. Yao, P. Dey, M. Lipińska-Chwalek, B. Berkels, B. Gault, T. Hickel, M. Herbig, J. Mayer, J. Neugebauer, D. Raabe, G. Dehm, and C. Scheu, “Tetragonal Fcc-Fe Induced by  $\chi$ -Carbide Precipitates: Atomic Scale Insights from Correlative Electron Microscopy, Atom Probe Tomography, and Density Functional Theory,” Physical Review Materials, vol. 2, no. 2, p. 023804, 2018-02.
- [183] S. K. Makineni, A. Kumar, M. Lenz, P. Kontis, T. Meiners, C. Zenk, S. Zaef-ferer, G. Eggeler, S. Neumeier, E. Spiecker, D. Raabe, and B. Gault, “On the Diffusive Phase Transformation Mechanism Assisted by Extended Dislocations during Creep of a Single Crystal CoNi-Based Superalloy,” Acta Materialia, vol. 155, pp. 362–371, 2018-08.
- [184] A. Stoffers, J. Barthel, C. H. Liebscher, B. Gault, O. Cojocaru-Mirédin, C. Scheu, and D. Raabe, “Correlating Atom Probe Tomography with Atomic-Resolved Scanning Transmission Electron Microscopy: Example of Segrega-tion at Silicon Grain Boundaries,” Microscopy and Microanalysis Microanal., vol. 23, no. 2, pp. 291–299, 2017-04.
- [185] M. Herbig, “Spatially Correlated Electron Microscopy and Atom Probe To-mography: Current Possibilities and Future Perspectives,” Scripta Materialia, vol. 148, pp. 98–105, 2018-04.
- [186] M. Čák, M. Šob, and J. Hafner, “First-Principles Study of Magnetism at Grain Boundaries in Iron and Nickel,” Physical Review B, vol. 78, no. 5, p. 054418, 2008-08.
- [187] P. Lejček and S. Hofmann, “Solute Segregation at Grain Boundaries of a Par-tially Ordered Fe3Al Base Alloy,” Surface and Interface Analysis, vol. 36, no. 8, pp. 938–940, 2004.
- [188] B. Mintz and J. M. Arrowsmith, “Hot-Ductility Behaviour of C–Mn–Nb–Al Steels and Its Relationship to Crack Propagation during the Straightening of Continuously Cast Strand,” null, vol. 6, no. 1, pp. 24–32, 1979-01.

- [189] D. Scheiber, O. Renk, M. Popov, and L. Romaner, “Temperature Dependence of Surface and Grain Boundary Energies from First Principles,” Physical Review B, vol. 101, no. 17, p. 174103, 2020-05.
- [190] S. Schönecker, X. Li, B. Johansson, S. K. Kwon, and L. Vitos, “Thermal Surface Free Energy and Stress of Iron,” Scientific Reports, vol. 5, no. 1, p. 14860, 2015-10.
- [191] L. Huber, R. Hadian, B. Grabowski, and J. Neugebauer, “A Machine Learning Approach to Model Solute Grain Boundary Segregation,” npj Computational Materials, vol. 4, no. 1, pp. 1–8, 2018-11.
- [192] D. H. R. Fors and G. Wahnström, “Nature of Boron Solution and Diffusion in  $\alpha$ -Iron,” Physical Review B, vol. 77, no. 13, p. 132102, 2008-04.
- [193] A. Pryor, C. Ophus, and J. Miao, “A Streaming Multi-GPU Implementation of Image Simulation Algorithms for Scanning Transmission Electron Microscopy,” Advanced Structural and Chemical ImagingStruct Chem Imaging, vol. 3, no. 1, p. 15, 2017-10.
- [194] D. Aksyonov, T. Hickel, J. Neugebauer, and A. Lipnitskii, “The Impact of Carbon and Oxygen in Alpha-Titanium: Ab Initio Study of Solution Enthalpies and Grain Boundary Segregation,” Journal of Physics: Condensed Matter, vol. 28, no. 38, p. 385001, 2016.
- [195] D. Scheiber, L. Romaner, F. Fischer, and J. Svoboda, “Kinetics of Grain Boundary Segregation in Multicomponent Systems—The Example of a Mo-CBO System,” Scripta Materialia, vol. 150, pp. 110–114, 2018.
- [196] H. Mehrer and N. Stolica, “Diffusion in Solid Metals and Alloys,” vol. 26, Springer-Verlag, 1990.
- [197] E. Hristova, R. Janisch, R. Drautz, and A. Hartmaier, “Solubility of Carbon in  $\alpha$ -Iron under Volumetric Strain and Close to the  $\Sigma 5(310)[001]$  Grain Boundary: Comparison of DFT and Empirical Potential Methods,” Computational Materials Science, vol. 50, no. 3, pp. 1088–1096, 2011-01.
- [198] B. Hyde, D. Farkas, and M. J. Caturla, “Atomistic Sliding Mechanisms of the  $\Sigma=5$  Symmetric Tilt Grain Boundary in Bcc Iron,” Philosophie Magazin, vol. 85, no. 32, pp. 3795–3807, 2005-11.

## Bibliography

- [199] L. Chongmo and M. Hillert, “A metallographic study of diffusion-induced grain boundary migration in the Fe-Zn system,” Acta Metallurgica, vol. 29, no. 12, pp. 1949–1960, 1981-12-01.
- [200] M. Andreani, P. Azou, and P. Bastien, “Action of molten Zn on Ni steels,” COMPT REND ACAD SCI, vol. 263, no. 18, pp. 1041–1043, 1966.
- [201] T. Shinohara and K. Matsumoto, “Welding cracks of Zn-contaminated stainless steel pipe,” Corrosion Science, vol. 22, no. 8, pp. 723–737, 1982-01-01.
- [202] C. Dillon, “Liquid metal cracking of stainless steels in chemical plants,” MP-Materials performance, vol. 29, no. 11, pp. 54–55, 1990.
- [203] S. P. Lynch, “Failures of Structures and Components by Metal-Induced Embrittlement,” Journal of Failure Analysis and Prevention, vol. 8, no. 3, pp. 259–274, 2008-06-01.
- [204] L. Cho, H. Kang, C. Lee, and B. C. De Cooman, “Microstructure of liquid metal embrittlement cracks on Zn-coated 22MnB5 press-hardened steel,” Scripta Materialia, vol. 90–91, pp. 25–28, 2014-11-01.
- [205] R. Ashiri, M. A. Haque, C.-W. Ji, M. shamanian, H. R. Salimijazi, and Y.-D. Park, “Supercritical area and critical nugget diameter for liquid metal embrittlement of Zn-coated twinning induced plasticity steels,” Scripta Materialia, vol. 109, pp. 6–10, 2015-12-01.
- [206] C. W. Lee, W. S. Choi, L. Cho, Y. R. Cho, and B. C. D. Cooman, “Liquid-Metal-Induced Embrittlement Related Microcrack Propagation on Zn-coated Press Hardening Steel,” ISIJ International, vol. 55, no. 1, pp. 264–271, 2015.
- [207] J. Barthelmie, A. Schram, and V. Wesling, “Liquid Metal Embrittlement in Resistance Spot Welding and Hot Tensile Tests of Surface-refined TWIP Steels,” IOP Conference Series: Materials Science and Engineering, vol. 118, p. 012002, 2016-03.
- [208] R. Ashiri, M. Shamanian, H. R. Salimijazi, M. A. Haque, J.-H. Bae, C.-W. Ji, K.-G. Chin, and Y.-D. Park, “Liquid metal embrittlement-free welds of Zn-coated twinning induced plasticity steels,” Scripta Materialia, vol. 114, pp. 41–47, 2016-03-15.

- [209] H. Kang, L. Cho, C. Lee, and B. C. De Cooman, “Zn Penetration in Liquid Metal Embrittled TWIP Steel,” Metallurgical and Materials Transactions A, vol. 47, no. 6, pp. 2885–2905, 2016-06-01.
- [210] M. H. Razmpoosh, A. Macwan, F. Goodwin, E. Biro, and Y. Zhou, “Role of Random and Coincidence Site Lattice Grain Boundaries in Liquid Metal Embrittlement of Iron (FCC)-Zn Couple,” Metallurgical and Materials Transactions A, vol. 51, no. 8, pp. 3938–3944, 2020-08-01.
- [211] P. J. L. Fernandes and D. R. H. Jones, “Mechanisms of liquid metal induced embrittlement,” International Materials Reviews, vol. 42, no. 6, pp. 251–261, 1997-11-01.
- [212] N. S. Stoloff and T. L. Johnston, “Crack propagation in a liquid metal environment,” Acta Metallurgica, vol. 11, no. 4, pp. 251–256, 1963-04-01.
- [213] A. R. C. Westwood and M. H. Kamdar, “Concerning liquid metal embrittlement, particularly of zinc monocrystals by mercury,” The Philosophical Magazine: A Journal of Theoretical Experimental and Applied Physics, vol. 8, no. 89, pp. 787–804, 1963-05-01.
- [214] P. Gordon and H. H. An, “The mechanisms of crack initiation and crack propagation in metal-induced embrittlement of metals,” Metallurgical and Materials Transactions A, vol. 13, no. 3, pp. 457–472, 1982-03-01.
- [215] C. DiGiovanni, A. Ghatei Kalashami, E. Biro, and N. Y. Zhou, “Liquid metal embrittlement transport mechanism in the Fe/Zn system: Stress-assisted diffusion,” Materialia, vol. 18, p. 101153, 2021-08-01.
- [216] A. A. Griffith and G. I. Taylor, “VI. The phenomena of rupture and flow in solids,” Philosophical Transactions of the Royal Society of London. Series A, Containing Papers of a Mathematical or Physical Character, vol. 221, no. 582-593, pp. 163–198, 1921-01.
- [217] C. Ding, W. Peng, Z. Ma, Y. Zhao, H. Teng, and G. Wu, “Effect of Ni Doping on the Embrittlement of Liquid Zinc at  $\Sigma 5$  Fe Austenite Grain Boundary,” Metals, vol. 12, no. 1, p. 27, 2022-01.
- [218] D. McLean and A. Maradudin, “Grain Boundaries in Metals,” Physics Today, vol. 11, p. 35, 1958.

## Bibliography

- [219] L. He, C. DiGiovanni, X. Han, C. Mehling, E. Wintjes, E. Biro, and N. Zhou, “Suppression of liquid metal embrittlement in resistance spot welding of TRIP steel,” Science and Technology of Welding and Joining, vol. 24, no. 6, pp. 579–586, 2019-08-18.
- [220] N. Miyazawa, M. Hakamada, and M. Mabuchi, “Atomic bond-breaking behaviour during grain boundary fracture in a C-segregated Fe grain boundary,” Philosophical Magazine Letters, vol. 97, no. 8, pp. 311–319, 2017-08-03.
- [221] A. S. Kholobina, W. Ecker, R. Pippan, and V. I. Razumovskiy, “Effect of alloying elements on hydrogen enhanced decohesion in bcc iron,” Computational Materials Science, vol. 188, p. 110215, 2021.
- [222] H. Kim, D.-W. Suh, and N. J. Kim, “Fe–al–mn–c lightweight structural alloys: a review on the microstructures and mechanical properties,” Science and technology of advanced materials, 2013.
- [223] R. Frappier, P. Paillard, R. Le Gall, and T. Dupuy, “Embrittlement of steels by liquid zinc: crack propagation after grain boundary wetting,” in Advanced materials research, vol. 922, pp. 161–166, Trans Tech Publ, 2014.
- [224] G. Jung, I. S. Woo, D. W. Suh, and S.-J. Kim, “Liquid zn assisted embrittlement of advanced high strength steels with different microstructures,” Metals and Materials International, vol. 22, no. 2, pp. 187–195, 2016.
- [225] H.-H. Seok, J.-C. Mun, and C.-g. Kang, “Micro-crack in zinc coating layer on boron steel sheet in hot deep drawing process,” International Journal of Precision Engineering and Manufacturing, vol. 16, no. 5, pp. 919–927, 2015.
- [226] J. Mendala and P. Liberski, “Liquid metal embrittlement of steel with a coating obtained by batch hot dip method in a zn+ 2% sn bath,” in Solid State Phenomena, vol. 212, pp. 107–110, Trans Tech Publ, 2014.
- [227] M. Takahashi, M. Nakata, K. Imai, N. Kojima, and N. Otsuka, “Liquid metal embrittlement of hot stamped galvanized boron steel sheet—effect of heating time on crack formation—,” isij international, pp. ISIJINT–2016, 2017.
- [228] Y. Ikeda, R. Yuan, A. Chakraborty, H. Ghassemi-Armaki, J. Zuo, and R. Maaß, “Early stages of liquid-metal embrittlement in an advanced high-strength steel,” Materials Today Advances, vol. 13, p. 100196, 2022.

- [229] D. Scheiber, K. Prabitz, L. Romaner, and W. Ecker, “The Influence of Alloying on Zn Liquid Metal Embrittlement in Steels,” Acta Materialia, 2020.
- [230] E. Bitzek, J. R. Kermode, and P. Gumbsch, “Atomistic aspects of fracture,” International Journal of Fracture, vol. 191, no. 1, pp. 13–30, 2015.
- [231] J. J. Möller and E. Bitzek, “Fracture toughness and bond trapping of grain boundary cracks,” Acta materialia, vol. 73, pp. 1–11, 2014.
- [232] L. Chongmo and M. Hillert, “Diffusion induced grain boundary migration in CuZn,” Acta Metallurgica, vol. 30, no. 6, pp. 1133–1145, 1982-06-01.
- [233] J. S. Dohie, J. Cahoon, and W. Caley, “The grain-boundary diffusion of zn in  $\alpha$ -fe,” Journal of Phase Equilibria and Diffusion, vol. 28, no. 4, pp. 322–327, 2007.
- [234] A. Tahir, R. Janisch, and A. Hartmaier, “Hydrogen embrittlement of a carbon segregated  $\sigma_5$  (310)[001] symmetrical tilt grain boundary in  $\alpha$ -fe,” Materials Science and Engineering: A, vol. 612, pp. 462–467, 2014.
- [235] M. H. Kamdar, “Embrittlement by liquid metals,” Progress in Materials Science, vol. 15, no. 4, pp. 289–374, 1973-01-01.
- [236] S. Bechtle, M. Kumar, B. P. Somerday, M. E. Launey, and R. O. Ritchie, “Grain-boundary engineering markedly reduces susceptibility to intergranular hydrogen embrittlement in metallic materials,” Acta materialia, vol. 57, no. 14, pp. 4148–4157, 2009.
- [237] A. Ghatei-Kalashami, E. Ghassemali, C. DiGiovanni, F. Goodwin, and N. Y. Zhou, “Occurrence of liquid-metal-embrittlement in a fully ferritic microstructure,” Materialia, vol. 15, p. 101036, 2021.
- [238] D. K. Matlock, J. G. Speer, E. De Moor, and P. J. Gibbs, “Recent developments in advanced high strength sheet steels for automotive applications: an overview,” Jestech, vol. 15, no. 1, pp. 1–12, 2012.
- [239] R. Rana, “Low-Density Steels,” JOM, vol. 66, no. 9, pp. 1730–1733, 2014-09-01.

## Bibliography

- [240] S. Pramanik and S. Suwas, “Low-Density Steels: The Effect of Al Addition on Microstructure and Properties,” JOM, vol. 66, no. 9, pp. 1868–1876, 2014-09-01.
- [241] K.-G. Chin, H.-J. Lee, J.-H. Kwak, J.-Y. Kang, and B.-J. Lee, “Thermodynamic calculation on the stability of (Fe,Mn)<sub>3</sub>AlC carbide in high aluminum steels,” Journal of Alloys and Compounds, vol. 505, no. 1, pp. 217–223, 2010-08-27.
- [242] R. Rana, C. Liu, and R. K. Ray, “Evolution of microstructure and mechanical properties during thermomechanical processing of a low-density multiphase steel for automotive application,” Acta Materialia, vol. 75, pp. 227–245, 2014-08-15.
- [243] S. S. Sohn, B. J. Lee, S. Lee, N. J. Kim, and J. H. Kwak, “Effect of annealing temperature on microstructural modification and tensile properties in 0.35 C–3.5 Mn–5.8 Al lightweight steel,” Acta Materialia, vol. 61, no. 13, pp. 5050–5066, 2013-08-01.
- [244] J. Johansson, M. Odén, and X. H. Zeng, “Evolution of the residual stress state in a duplex stainless steel during loading,” Acta Materialia, vol. 47, no. 9, pp. 2669–2684, 1999-07-09.
- [245] P. Rawat, U. Prakash, and V. Prasad, “Phase transformation and hot working studies on high-al fe-al-mn-c ferritic low-density steels,” Journal of Materials Engineering and Performance, vol. 30, no. 8, pp. 6297–6308, 2021.
- [246] V. A. Lashgari, C. Kwakernaak, and W. Sloof, “Transition from internal to external oxidation of mn steel alloys,” Oxidation of metals, vol. 81, no. 3, pp. 435–451, 2014.
- [247] S. Matsnaga and T. Homma, “Influence on the oxidation kinetics of metals by control of the structure of oxide scales,” Oxidation of Metals, vol. 10, no. 6, pp. 361–376, 1976.
- [248] N. Appannagaari and S. Basu, “Modeling of o-18 tracer distribution during “double oxidation” experiments for inward growing scales,” Journal of applied physics, vol. 78, no. 3, pp. 2060–2069, 1995.



- [249] V. Trindade, U. Krupp, P. E.-G. Wagenhuber, and H.-J. Christ, "Oxidation mechanisms of cr-containing steels and ni-base alloys at high-temperatures—part i: The different role of alloy grain boundaries," Materials and Corrosion, vol. 56, no. 11, pp. 785–790, 2005.
- [250] J. Takada, S. Yamamoto, S. Kikuchi, and M. Adachi, "Internal oxidation of fe-al alloys in the  $\alpha$ -phase region," Oxidation of Metals, vol. 25, no. 1, pp. 93–105, 1986.
- [251] R. Bricknell and D. Woodford, "Grain boundary embrittlement of the iron-base superalloy in903a," Metallurgical Transactions A, vol. 12, no. 9, pp. 1673–1680, 1981.
- [252] T. Watanabe and S. Tsurekawa, "Toughening of brittle materials by grain boundary engineering," Materials Science and Engineering: A, vol. 387, pp. 447–455, 2004.
- [253] M. Phaniraj, D.-I. Kim, and Y. W. Cho, "Effect of grain boundary characteristics on the oxidation behavior of ferritic stainless steel," Corrosion Science, vol. 53, no. 12, pp. 4124–4130, 2011.
- [254] S. Yamaura, Y. Igarashi, S. Tsurekawa, and T. Watanabe, "Structure-dependent intergranular oxidation in ni-fe polycrystalline alloy," Acta Materialia, vol. 47, no. 4, pp. 1163–1174, 1999.
- [255] S.-i. Yamaura, S. Tsurekawa, and T. Watanabe, "The control of oxidation-induced intergranular embrittlement by grain boundary engineering in rapidly solidified ni-fe alloy ribbons," Materials Transactions, vol. 44, no. 7, pp. 1494–1502, 2003.
- [256] K. Wefers and C. Misra, "Alcoa technical paper no. 19," 1987.
- [257] I. Levin and D. Brandon, "Metastable alumina polymorphs: crystal structures and transition sequences," Journal of the american ceramic society, vol. 81, no. 8, pp. 1995–2012, 1998.
- [258] R.-S. Zhou and R. L. Snyder, "Structures and transformation mechanisms of the  $\eta$ ,  $\gamma$  and  $\theta$  transition aluminas," Acta Crystallographica Section B: Structural Science, vol. 47, no. 5, pp. 617–630, 1991.

## Bibliography

- [259] L. Kovarik, M. Bowden, A. Genc, J. Szanyi, C. H. Peden, and J. H. Kwak, "Structure of  $\delta$ -alumina: toward the atomic level understanding of transition alumina phases," The Journal of Physical Chemistry C, vol. 118, no. 31, pp. 18051–18058, 2014.
- [260] G. Paglia, E. S. Božin, and S. J. Billinge, "Fine-scale nanostructure in  $\gamma$ - $\text{Al}_2\text{O}_3$ ," Chemistry of Materials, vol. 18, no. 14, pp. 3242–3248, 2006.
- [261] G. Paglia, C. E. Buckley, A. L. Rohl, B. A. Hunter, R. D. Hart, J. V. Hanna, and L. T. Byrne, "Tetragonal structure model for boehmite-derived  $\gamma$ -alumina," Physical Review B, vol. 68, p. 144110, Oct 2003.
- [262] I. Levin and D. Brandon, "Metastable alumina polymorphs: Crystal structures and transition sequences," Journal of the American Ceramic Society, vol. 81, no. 8, pp. 1995–2012.
- [263] M. Auinger, V. G. Praig, B. Linder, and H. Danninger, "Grain boundary oxidation in iron-based alloys, investigated by  $^{18}\text{O}$  enriched water vapour—the effect of mixed oxides in binary and ternary  $\text{Fe}$ –{Al, Cr, Mn, Si} systems," Corrosion Science, vol. 96, pp. 133–143, 2015.
- [264] H. J. Ellingham, "Reducibility of oxides and sulphides in metallurgical processes," J. Soc. Chem. Ind., vol. 63, no. 5, pp. 125–160, 1944.
- [265] F. D. Richardson, "Thermodynamics of substances of interest in iron and steel making from  $0^\circ\text{C}$  to  $2400^\circ\text{C}$ ," JISI, vol. 160, pp. 261–270, 1948.

# Acknowledgement

Before I start to acknowledge all colleagues and friends, I would like to thank god, who was always helping me during my whole life!

I would like to express my deepest gratitude to **Prof. Dr. Gerhard Dehm** and **Dr. Christian H. Liebscher** for the opportunity to do my PhD work in their group and for the great supervision. Both of them were teaching me so many things. Counting them all would be another thesis. Nevertheless, I would like to mention at least few things. Due to all the fruitful discussions with Chris and Gerhard about my results I learned how to improve and become a better microscopist and scientists. They also learned from them how to be a good mentor. Chris was not only reviewing my papers and the thesis, he is someone who is very disciplined and I will always remember his critical comment about scientists behaving like in a Kindergarten. I really appreciated the freedom he gave me to develop own ideas and discuss new things. Gerhard has also his very special place in my life. I will never forget the handshake during my interview! He is a unique professor. A professor, who knows not only the names of his group members but also some stories and gossips about them. He treats all his students and postdocs like humans and this is very important. I am very thankful to have had such great scientists as my bosses. I know that both of them were worried about me - especially during the initial phase of the pandemic. I was very happy, when Chris allowed me to work in the office even during the Lock down. Probably, I would have become crazy at home. Gerhard was checking every Monday whether I am in the office or not. He never said a word but I knew why he was doing it. I really appreciated it and wish them all the best.

Further, I also would like to thank **Prof. Dr. Christian Kübel**, who invited me to his group to discuss my results. He gave me fruitful ideas and I am very happy that he agreed to be my second referee. I know Christian from my master's degree, where he was my supervisor. A great scientist is someone, who is not forcing his students to stay but give them the right to move to new places. He gave me the advise to choose positions, where the professor/group leader is a microscopist

and they should have good equipment. This is one of the reasons I choose Gerhard, Chris and the MPIE. I am happy to consider him as one of my fiends!

All the work I have done would not have been possible without the help and support of many people. Zuallererst möchte ich mich bei **Jürgen Wichert** bedanken, der die Bikristalle gezüchtet hat und für mich das Verzinken und die Auslagerungen gemacht hat. Wäre seine Arbeit nicht so gut gewesen, hätte ich nie die Doktorarbeit schaffen können. Vielen lieben Dank Jürgen! Weiterhin möchte ich mich bei **Markus Bormann** und **Eugen Trautenbach** bedanken, die mir einen Schleifhalter gebaut haben und mir die rheinländische Lebensweise beigebracht haben. Außerdem möchte ich mich auch bei **Tristan Wickfeld** und **Mario Bütow** bedanken für all die schnellen Arbeiten beim Funkerodieren meiner Proben. Ganz lieben Dank dafür! Außerdem würde ich auch gerne die damaligen Azubis nennen: **Simon Sprengel** (jetzt Festangestellter), **Fabian Holzhauer** und **Samy Soroush**. Sie haben mit mir einen Halter für Plan-view FIB Präparation gebaut. **Tobias Franken** hatte mir eine tolle Vakuumbbox ("die Handtasche für den Mann von morgen") aus Aluminium gebaut. Natürlich bin ich auch **Ralph Selbach**, **Jürgen Baseler**, **Mike Bauer**, **Rainer Lück**, **Jens Dose** und **Dominik Korbmacher** dankbar für all die schönen und politisch korrekten Gespräche.

Es ist bekannt, dass 75% der wissenschaftlichen Arbeit an die Probenpräparation und das Experimentieren gehen. Ich habe das große Glück gehabt, dass in unserem Institut so viele Helfer waren, die sich um die Instandhaltung der Geräte kümmern und Einweisungen geben. Als ich ankam, habe ich einen echt netten Jungen kennengelernt. Sein Name: **Leon Christiansen!** Leon hatte mir eine Einführung in die metallographische Präparation gegeben. Ich mochte ihn von Anfang an, da er gepflegt erschien. Nach einiger Zeit, hatte ich herausgefunden gehabt, dass er ein Problem mit körperlicher Nähe von Männern hat. Deswegen habe ich ihm etwas versprochen und werde ihm etwas nach meiner Verteidigung geben. Komme, was da wolle! Ich möchte auch gerne **Angelika Bobrowski** und **Jörg Thomas** danken für die Einweisung in klassische TEM Probenpräparation mittels Elektropolieren und der Benutzung des CM20 TEMs. Jörg war ein genialer TEM-Techniker und sein Erfahrungsschatz war unersetzlich. **Volker Kree** bin ich sehr dankbar für all die Hilfe beim JEOL TEM, aber auch für die tollen Restaurantempfehlungen. Er ist genau wie ich ein ledienschaftlicher Steak-Esser. Wenn man ein gutes Lokal wissen will, wo es gutes Essen zu guten Preisen gibt, dann ist Volker der richtige Ansprechpartner. Einen großen Dank auch an **Philipp Watermeyer**, der Nachfol-

ger von Jörg. Ich glaube, dass unsere Gruppe ein riesen Glück hatte einen jungen Mann wie ihn gefunden zu haben. Er kennt sich mit TEM sehr gut aus und lernte schnell neue Dinge. Zusammen haben wir am IC Titan trainiert. Außerdem hat er mir viele Dinge beigebracht, die sonst ein Doktorand nie lernen würde. So hat er mir am Telefon gesagt, wie ich die Spitze des Mikromanipulators wechseln kann. Unglaublich!!!! Zu guter letzt möchte ich mich auch bei **Simon Reckort** bedanken für die Probenpräparationen und die vielen Gespräche in der Raucherecke. Ich hoffe wirklich, dass du irgendwann weniger rauchen wirst!

I am highly thankful to **Dr. Xuyang Zhou (Rhett)** for all the discussions on Fe GBs. It was super cool to have someone working on the same material. I remember how patient Rhett was during the Fe-Zn experiments. So many tips failed to run in the APT, but I never wanted to give up. Rhett was continuing just for me. All the experimental observations could not have been understood without the amazing theoretical work of **Dr. Daniel Scheiber** and **Prof. Dr. Lorenz Romaner** from the Materials Center Leoben GmbH, in Austria. I really enjoyed the annual workshops in Seggau and Leoben, the group meetings and all the discussions on GB segregation. Especially the enthusiasm of Lorenz about my results was also infecting me and was an inspiration. Maybe it is not good to generalize things, but for me the Austrians are super nice people!

Besides all the above mentioned people, who directly contributed to my work, I would like to thank all the friends I found at MPIE. Without the positive environment, the work would have been much harder. First of all I would like to mention a girl/woman from Catalonia (not Spain!). I thought I am loud, talkative and like to gossip, but then I met her: **Dr. Alba Garzón Manjón**. Alba became my best friend at MPIE and we nearly shared everything with each other. It was Alba, who was running with me so that I reduced my weight. Even when she broke her toe, she run a 5 km race in Neuss with me. I will never forget one single moment we spent together. Not only the sports but also other activities such as gin tonic nights, Burger nights as well as our gossiping hours. Alba was there, when I was not feeling so good and I really appreciated it. Aside from that, she introduced me to very nice people. One of them was her cute son **Max Garzón Schwarz**. I was having a lot of fun with Max. He is like a sponge and learns everything I show him. He is my Mini-me!! We had many nice moments together especially with the gloves. I will not tell more. Top-top-secret!! I really miss both and hope I can see them soon. Alba also introduced me **Miquel Vega-Paredes**, who became a very close friend

## *Bibliography*

of mine. In the beginning, when he was a Bachelor student at our institute, I had little contact. This changed when I knew more about him and found that he is a honest and nice person. He was my second trainer after Alba trying to get me a sixpack. Unfortunately, he failed!!

I am also highly thankful to my office mates **Dr. Silas Woff-Goodrich** (from USA), whis now at Tata Steel, **Piyush Patil Pramod** (from India), **Jing Rao** (from China), **Jakub Nowak** (Germany/Poland), who is now at Bayer and recently **Shreehard Sahu**. With all of them I shared nice moments. Jing was the the first one I met in our department. We spent so many hours in the metallography lab in grinding and polishing our samples. During this hours I found out how many similarities our cultures have regarding the concept of family as well as the respect towards parents. I was very happy when she got pregnant and I wish her and her husband all the best. Silas came a bit later than me. When we met the first time, I could only look at his super curly hairs and strong body. I really loved Silas passion for nature. He removed so many biases I had about Americans. I was very sad when he left. Piyush came in January 2018 from Stuttgart and we went to many Indian parties together. I wish him all the best for his future. Jakub opened my view in many ways. He is a very disciplined person but with a lot of stress. Unfortunately, he left to Bayer without finishing his PhD thseis but i am confident that can handle both together.

Next, I would like to mention **Dr. Rajib Sahu**, a man from Bengal. I spent many nice events with Rajib lastly the New year's eve 2022. Here, I would like to mention the whole Indian community I came into contact: **Vivek Devulapalli**, **Shreehard Sahu**, **Dr. Hariprasad Gopalan**, **Mohammad Kamran Bhat**, **Dr. Prithiv Thoudden Sukumar**, **Faisal Waqar Syed** and **Dr. Lalithkumar Bhaskar** with whom I had nice food and game nights. Furthermore, I would like to mention **Dr. Subin Lee**, who is now a group leader at KIT. He is a stylish Korean man with a lot of knowledge on in-situ TEM characterizations. He gave me good advises regarding my future plans.

Ich möchte mich auch bei meinem "Buddha" bedanken: **Michael Kulse**. Das tägliche Streicheln seines Bauches hat so einiges bewirkt. Ich möchte mich auch bei den anderen deutschen Arbeitskollegen von SN, NG und MA bedanken: **Irina Wossack**, **Benjamin Breitbach**, **Andreas Jansen**, **Tanja Sondermann**, **Dr. Frank Stein**, **Dr. Martin Palm**, **Dr. Benedikt Distl**, **Christian Broß**, **Achim Kuhl**, **Berthold Beckschäfer**, **Till Freieck** und **Prof. Dr. Christoph Kirchlechner**

für die schönen Momente während der Kaffee-/Mittagspausen. Es war immer wieder interessant neue Dinge zu lernen. Speziell, Christophs schöne Anekdoten, Benjamins Wortgewandtheit, Benedikts Fahrradgeschichten und Irinas kostenlose Geschenke, die zufällig vom Laster gefallen waren.

Finally, I would like to thank all the old and new colleagues from MPIE: **Andrea Brognara, Angelika Gedsun, Swetha Pemma, Lena Frommeyer, Dr. Nico Peter, Dr. Thorsten Meiners, Jean-Baptiste Molin, Dr. Raphael Soler, Hanna Tsybenko, Dr. Juan Li, Martin Winkler, Dr. Chunhua Tian, Dr. Wenqi Guo, Dr. Wenjun Lu, Dr. Wenzhen Xia, Dr. Siyuan Zhang (Spark), Raquel Aymerich Armengol, Ruben Bueno Villoro, Thomas Gänsler, Rasa Changizi, Dr. Lamya Abdellaoui, Zahra Kahrobee, Farnaz Farzam, Dr. Steffen Brinckmann, Chanwon Jung, Robin Jentner, Hannah Bishara, Dr. Jiwon Jeong, Dr. Xukai Zhang, Dr. Sung-Gyu Kang, Martí López Freixes, Francisco José Gallardo Basile, Carola Merten, Dorothea Opitz, Sumith Sellahewage, Alexander Moll, Peter Zech, Julian-Alexander Sawitzki, Richard Drabinski and Prof. Dr. Christina Scheu.** I am sorry, if I have not written a long text about everyone of you. I like you all. I just have not the time to write a novel about all the stories we share with each other.

Last but not least, I would like to thank those who were praying for me all the time: my **family**. I hope they will not be disappointed the way I chose to live my life. They are the most important people for me and I will always love them - no matter what comes!

The author gratefully acknowledges the financial support under the scope of the COMET program within the K2 Center “Integrated Computational Material, Process and Product Engineering (IC-MPPE)” (Project No 886385). This program is supported by the Austrian Federal Ministries for Climate Action, Environment, Energy, Mobility, Innovation and Technology (BMK) and for Digital and Economic Affairs (BMDW), represented by the Austrian Research Promotion Agency (FFG), and the federal states of Styria, Upper Austria and Tyrol.

## Personal Information

---

Name	Ali Ahmadian
Date of Birth	10.05.1987
Place of Birth	Herat, Afghanistan

## Education

---

2017–Present	<b>Doctoral Studies</b>
Dissertation	<i>Atomic-scale characterisation of grain boundary structure and segregation in bcc-iron</i> Ruhr Universität Bochum – Fakultät für Maschinenbau Advised by: Prof. Dr. Dehm and Dr. Christian H. Liebscher
2015–2017	<b>Master Studies</b>
Thesis	<i>Structural analysis of metallic glasses and corresponding nanoglasses by transmission electron microscopy</i> Karlsruhe Institute of Technology, Karlsruhe – Department of Physics Advised by: Dr. Christian Kübel & Prof. Dr. Dagmar Gerthsen & Prof. Dr. Karine Masenelli-Varlot
2014–2015	<b>Erasmus student in Lyon, France</b>
2014–2015	<b>Bachelor studies</b>
Thesis	<i>Characterization of pop-ins during shear band initiation in metallic glasses</i> Georg-August-University Göttingen, Göttingen – Department of Physics Advised by: Dr. Robert Maaß & Dominik Tönnies